AN ABSTRACT OF THE DISSERTATION OF

Alyssa R. Deline for the degree of Doctor of Philosophy in Environmental Engineering presented on August 16, 2018.

Title: Examining the Environmental Behavior and Treatment Efficacy of Titanium Dioxide Nanomaterials in Complex Systems

Abstract approved:

Jeffrey A. Nason

Metal oxide nanoparticles (MONPs) are manufactured at the greatest rate of any class of nanomaterial due to their wide variety of industrial, commercial, and environmental applications. The sustainable use of MONPs requires a balance of careful consideration of their potential negative environmental impacts with the effective exploitation of their unique properties in situations where the benefit of their use outweighs the risk. Currently, the study of the environmental behavior and toxicity of MONPs, as well as the understanding of their efficacy in environmental remediation applications, would benefit from the understanding of how MONPs

behave in complex aquatic media. MONPs are particularly difficult to study in environmentally-relevant matrices like natural water samples or within organisms due to the presence of elevated levels of the naturally occurring metal oxide.

In this dissertation, I directly address this challenge through the development of gold core-labeled TiO_2 NPs (Au@TiO_2 NPs). These labeled NPs were characterized and compared to their unlabeled counterparts, and it was determined that the size, crystal structure, and stability in media up to 500 mM was not significantly changed by the presence of the gold core label. The Au@TiO_2 NPs were quantified at low concentrations in complex natural matrices containing elevated levels of background titanium, using both inductively-coupled plasma optical emission spectroscopy and instrumental neutron activation analysis.

To contextualize these Au@TiO_2 NPs within the broader context of the available MONP labeling strategies, I prepared a critical review of the current literature. Four major categories of labeling techniques are described: fluorescent dyes, radioactive isotopes, stable isotopes, and dopant and core/shell labels. The advantages and disadvantages of each technique are presented. Recommendations are made for characterization that should be performed on labeled and unlabeled MONPs to ensure mechanistic conclusions drawn in experiments are not affected by the presence of the label. Guidance is provided on choosing and applying a labeling strategy for a given study.

Finally, I examine the properties and behavior of TiO_2 NPs in water treatment applications. The relative influence of elemental surface composition, crystal structure, ROS generation capacity, aggregation state, and water chemistry on the photocatalytic degradation of methylene blue dye is presented. Due to sample contamination, no correlations were found between the molecular-level surface properties determined by x-ray photoelectron spectroscopy and overall treatment efficacy. The most important property determining the extent of decolorization of the dye solutions was the inherent ROS generation capacity of the TiO_2 NPs, which in this study was controlled by the crystal structure. Other important properties were the aggregation state of the TiO_2 NPs in solution, and the pH stability of the media during the treatment process.

Overall, this dissertation provides both justification and methodologies for the study of TiO_2 NPs in complex, environmentally-relevant aquatic matrices.

Examining the Environmental Behavior and Treatment Efficacy of Titanium Dioxide Nanomaterials in Complex Systems

by

Alyssa R. Deline

A DISSERTATION

submitted to

Oregon State University

in partial fulfillment of

the requirements for the

degree of

Doctor of Philosophy

Presented August 16, 2018

Commencement June 2019

Doctor of Philosophy dissertation of Alyssa R. Deline presented on August 16, 2018.

APPROVED:

Major Professor, representing Environmental Engineering

Head of the School of Chemical, Biological & Environmental Engineering

---

Dean of the Graduate School

I understand that my dissertation will become part of the permanent collection of Oregon State University libraries. My signature below authorizes release of my dissertation to any reader upon request.

Alyssa R. Deline, Author

ACKNOWLEDGEMENTS

First and foremost, I sincerely thank my advisor Dr. Jeff Nason for his mentorship and guidance throughout my Ph.D. It has been so inspiring to see you always striving to be a better researcher, teacher, and advisor, even though you are already excellent at all of those things. Special thanks also goes to Dr. Tyler Radniecki, who has been one of my biggest supporters even before my graduate school applications were submitted. I can’t thank you enough for all of the patience you have had with me and the advice you have given me. I would also like to thank the rest of my committee for all of the valuable time and feedback they have provided to this work: Dr. Stacey Harper, Dr. Greg Herman, Dr. Brady Gibbons, and Dr. May Nyman.

Thank you to all of the members of the Nason Lab past and present, for putting up with my weird side projects and always being the best conference buddies. Thanks especially to Will Young, who worked side by side with me for four years. I learned so much from you, and I know you are going to be a huge success in whatever you decide to do next.

This dissertation was also made possible by an amazing circle of friends and family that celebrated my successes and pushed me to continue on in the more difficult times.

I am grateful to National Science Foundation Awards 1255020 and 1314109-DGE for funding.

CONTRIBUTION OF AUTHORS

Dr. Jeffrey A. Nason assisted with the design of the research, interpretation of the data, and editing of all the manuscripts presented within this dissertation. In Chapter 2, William M. Young was responsible for instrumental neutron activation analysis data presented in the manuscript.

TABLE OF CONTENTS

Page

TABLE OF CONTENTS (Continued)

Page

TABLE OF CONTENTS (Continued)

LIST OF FIGURES

LIST OF FIGURES (Continued)

LIST OF TABLES

LIST OF TABLES (Continued)

1 Introduction

Nanoparticles (NPs) are broadly defined as materials that are smaller than 100 nm in at least one dimension. The small size of NPs gives rise to differences in properties and behaviors when compared to their bulk counterparts. Examples of these differences include greater antimicrobial activity[1,2], increased material strength and stiffness[3], and enhanced color brightness and purity[4,5]. The benefits of NPs have been exploited in numerous commercial and industrial applications, and over $25 billion has been invested by the United States government in the research and development of nanotechnology since 2001[6].

Metal oxide NPs (MONPs) have the highest production of any type of nanomaterial, with global production occurring on the order of thousands of tons per year[7,8]. The magnitude of the production and application of MONPs increases the amount that will be released into the environment, which has led to a growing body of research on the potential negative implications of these materials[9,10]. MONPs have been shown to have toxic effects on microorganisms, small aquatic invertebrates, and some human cell lines[11–14]. The study of MONPs in environmentally-relevant systems is complicated by the presence of naturally occurring metals and metal oxides that must be distinguished from the engineered MONP of interest. This challenge, and the analytical strategies that are used to overcome it, are discussed in detail in Chapter 3.

Although there are concerns about negative environmental effects of MONPs, some MONPs may be useful in environmental remediation applications. TiO_2 NPs in particular have been extensively studied for these purposes, with potential uses including the degradation of organic contaminants, the adsorptive removal of toxic heavy metals, and the inactivation of harmful viruses and microorganisms[15,16]. Advanced oxidation processes in water treatment enabled by TiO_2 NPs rely on the photocatalytic activity of the NPs, specifically their ability to generate reactive oxygen species (ROS).

The mechanism of TiO_2 photocatalytic activity is summarized in Figure 1.1. When TiO_2 NPs are irradiated with light (hν) that exceeds the band gap energy, electrons (e^-) are excited from the valence band to the conduction band, leaving behind a positively charged hole (h^+)[17,18]. Some of these free charges will diffuse to the TiO_2 surface and participate in redox reactions with the surrounding solution to form multiple types of ROS, most notably hydroxyl radicals ($^\bullet OH$) and superoxide ($^\bullet O_2^-$), and singlet oxygen ($^1O_2$)[17,18]. Alternatively, the e^- or h^+ may become trapped either on the surface or within the bulk, with movement is restricted due to the presence of impurities or defects in the TiO_2. The e^-/h^+ pairs may alsorecombine without producing ROS. These core photocatalytic processes are summarized in the following equations, where e^-_{TR} and h^+_{TR} represent the surface trapped charges and e^-_{CB} and h^+_{VB} represent the electrons excited to the conduction band and the holes remaining in the valence band, respectively[18].

$$\mathrm{TiO_2} + h\nu \rightarrow \mathrm{e^-}_{\mathrm{CB}} + \mathrm{h^+}_{\mathrm{VB}} \qquad (1)$$

$$\mathrm{O_2} + \mathrm{e^-}_{\mathrm{CB}} \rightarrow {}^\bullet\mathrm{O_2^-} \qquad (2)$$

$$\mathrm{OH^-} + \mathrm{h^+}_{\mathrm{VB}} \rightarrow {}^\bullet\mathrm{OH} \qquad (3)$$

$$\mathrm{e^-}_{\mathrm{CB}} \rightarrow \mathrm{e^-}_{\mathrm{TR}} \qquad (4)$$

$$\mathrm{h^+}_{\mathrm{VB}} \rightarrow \mathrm{h^+}_{\mathrm{TR}} \qquad (5)$$

Hydrogen peroxide (H_2O_2) can also be generated by the $^{\bullet}O_2^-$ disproportionation and reaction with dissolved protons (H^+). H_2O_2 then goes on to form additional $^{\bullet}OH$, as shown in the following equations, where O_2 represents oxygen and OH^- represents hydroxide[18–20].

$$^{\bullet}O_2^- + {}^{\bullet}O_2^- + 2H^+ \rightarrow H_2O_2 + O_2 \qquad (6)$$

$$H_2O_2 + e^-{}_{CB} \rightarrow {}^{\bullet}OH + OH^- \qquad (7)$$

$$H_2O_2 + {}^{\bullet}O_2^- \rightarrow {}^{\bullet}OH + OH^- + O_2 \qquad (8)$$

$$H_2O_2 + h\nu \rightarrow {}^{\bullet}OH + {}^{\bullet}OH \qquad (9)$$

Once ROS are produced, they can oxidize the organic contaminants present in solution, either forming a degradation by product or, in the case of complete mineralization, carbon dioxide. Specific types of ROS can be detected and quantified through the use of electron spin resonance spectroscopy or through the degradation of fluorescent probes[21].

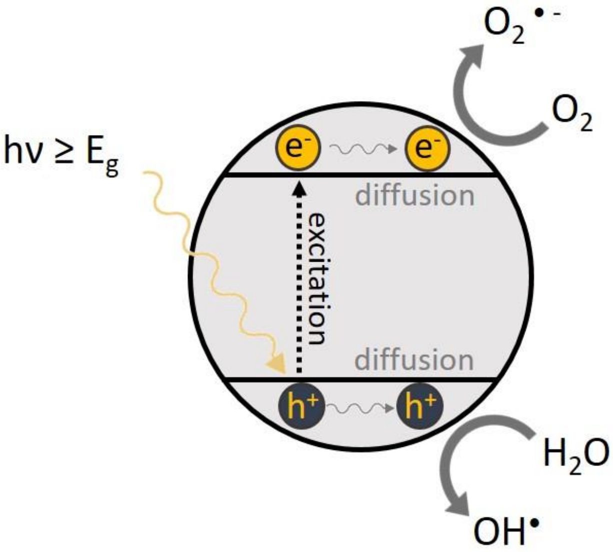

Figure 1.1. Mechanism of TiO_2 photocatalysis.

The photocatalytic generation of ROS, and the interaction of ROS with the surrounding media, drives both the water treatment efficacy and the potential for toxicity of TiO_2 NPs. There are several important characteristics of both the TiO_2 NPs and the water chemistry that affect this behavior. ROS generation by TiO_2 NPs is heavily influenced by the crystal structure of TiO_2, with the anatase form of TiO_2 exhibiting higher levels of photoactivity than the rutile form. Anatase TiO_2 has a larger band gap (3.28 eV) than the rutile form (3.0 eV), which increases the oxidative capacity of the charge carriers created[22]. Anatase TiO_2 also has an indirect band gap not observable in the rutile form, which is expected to increase the lifetimes of the generated electron-hole pairs, allowing the charge carriers to encounter and react with adsorbed molecules before recombination[23]. Charge carriers generated within anatase TiO_2 have also been shown to diffuse to the surface from deeper in the bulk material than charge carriers generated in rutile TiO_2[23]. TiO_2 NPs that contain a mixture of crystalline forms, like the commonly-used P25 mixture of 20% rutile and 80% anatase, exhibit an even greater photocatalytic activity than the sum of the contributions from the pure crystal phases would predict[24,25]. This is due to the transfer of charges between the anatase and rutile phase, limiting charge recombination and promoting ROS generation[24,25].

In solution, primary TiO_2 NPs will aggregate to form larger clusters, limiting the available amount of surface area to participate in photocatalytic reactions[26]. The probability that two particles will attach upon collision is defined as the attachment efficiency, α, and is controlled by the surface chemistry of the particles[27]. When the two particles have a similar charge, electrostatic repulsive forces will increase as the distance between the particles decreases.

However, the van der Waal's attractive forces will increase as the distance between the particles decreases, eventually outweighing the repulsive forces at small distances and allowing aggregation to take place. This net attractive or repulsive force between two particles that changes as a function of distance is described by Derjaguin-Landau-Verwey-Overbeek (DLVO) theory[28,29]. This phenomena is directly affected by water chemistry parameters like the pH and the ionic strength. The pH affects the surface charge of the particles, which can enhance or limit the electrostatic repulsion. Ionic strength affects the size of the electric double layer, which is formed as the particle attracts ions with an opposing charge that form the first fixed (Stern) layer, followed by the attraction of ions with similar charge that form the second diffuse layer. When the ionic strength is increased, the electric double layer compacts, decreasing repulsive forces and increasing the chance of aggregation[27,30]. Aggregation can also be impacted by the presence of natural organic matter, which can adsorb to particle surfaces, affecting the surface charge or participating in interparticle bridging[31,32]. Aggregation state has been directly linked to $^{\bullet}OH$ production by TiO_2, with smaller, less dense aggregates producing more $^{\bullet}OH$ than larger, denser aggregates[26].

Finally, once ROS is generated, the interactions with contaminants or organisms present will determine the overall level of treatment efficacy or toxicity. The potential for a contaminant or organism to interact with ROS is significantly increased when they are in direct contact with the TiO_2 surface[33–36]. This behavior is dominated by electrostatic interactions. For example, cationic organic dyes like methylene blue are more likely to adsorb to a negatively charged TiO_2 surface, so both adsorption and degradation will increase with pH[37–39]. The relative hydrophobic/hydrophilic properties of the TiO_2 surface are also key predictors of NP toxicity[40]. These properties influence both the adsorption of water and oxygen, which is necessary to produce ROS, and the adsorption of contaminants, which brings ROS into the close proximity required for degradation processes[40,41]. Natural organic matter can also affect the likelihood of ROS-contaminant or ROS-organism interactions by scavenging the produced ROS, reducing the photoactivity of TiO_2 NPs[42].

Overall, it is clear that an understanding of the behavior of MONPs like TiO_2, whether in a water treatment scenario or a study of environmental behavior and toxicity, requires that the NPs are thoroughly characterized within the media of interest. This dissertation addresses key challenges in this area, developing and evaluating analytical strategies for the study of both the environmental implications and applications of TiO_2 NPs. Chapter 2 addresses the need for MONP labeling methods that enable studies of the fate and transport of TiO_2 NPs to be performed in complex matrices containing background titanium. A method for producing gold core-labeled TiO_2 NPs is presented, along with examples of quantification within a variety of complex, environmentally-relevant media. Chapter 3 situates the core/shell labeling method detailed in Chapter 2 within the broader context of MONP labeling strategies. Existing procedures for the incorporation of traceable labels within MONPs are evaluated, and recommendations are provided for both the characterization of labeled MONPs and the selection of a labeling method for a specific study. In Chapter 4, TiO_2 NPs are studied in the context of photocatalytic water treatment applications. Two model TiO_2 NPs are characterized across different water chemistry conditions from the dual perspectives of the surface composition on the molecular level, and the broader extrinsic properties like aggregation state, hydrophobicity, and ROS generation. The relationships between these properties and the photocatalytic degradation of methylene blue dye are presented.

2 Gold core-labeled TiO_2 nanoparticles for tracking behavior in complex matrices: synthesis, characterization, and demonstration

Alyssa R. Deline, William M. Young, and Jeffrey A. Nason

Environmental Science: Nano

Royal Society of Chemistry

1050 Connecticut Ave NW, Suite 500

Washington DC 20036

Date: February 2018

2.1 Abstract

Titanium dioxide nanoparticles (TiO_2 NPs) are increasingly entering natural systems due to their widespread production and use. It is critical that TiO_2 NP behavior is studied in real-world systems, but experimental work is complicated by the high levels of background titanium present in every environmental compartment. To assist in distinguishing between engineered NPs and background titanium, labeled particles with gold nanoparticle cores and TiO_2 shells (Au@TiO_2 NPs) were developed and the properties and behavior compared to unlabeled TiO_2 NPs. Both particle types had primary particle diameters of approximately 200 nm and were stable in solutions at ionic strengths up to 500 mM due to a polyvinylpyrrolidone surface coating. To demonstrate utility, the Au@TiO_2 NPs were used in several spike-and-recovery experiments in complex matrices such as activated sludge and a river water-sunscreen mixture. Au@TiO_2 NPs were accurately quantified at using instrumental neutron activation analysis and inductively coupled plasma optical emission spectrometry.

2.2 Introduction

Titanium dioxide nanoparticles (TiO_2 NPs) are produced in quantities on the order of thousands of tons per year for multiple consumer and industrial applications[8]. Once synthesized, TiO_2 NPs are often embedded in a product to act as a pigment, to impart UV protection, or to serve as a photocatalyst[8]. The use and disposal of many of these products ensures that TiO_2 NPs will be directly released into both natural waters and water treatment systems, where TiO_2 NP detection and quantification is difficult.

TiO_2 NPs have been shown to have toxic effects on a variety of aquatic organisms due to the production of reactive oxygen species, raising concern that the increasing quantities being released in the environment could have a negative impact[21]. Exposure to TiO_2 NPs has been shown to decrease algal growth[43,44], inhibit ammonia oxidizing bacteria[45], and induce oxidative stress in rainbow trout[46]. Additionally, TiO_2 is oxidatively stable under a wide range of conditions. TiO_2 NP residues can persist in the environment even as other components of a product like sunscreen degrade[47], and these residues also have the potential to negatively affect organisms[48,49].

Understanding the behavior and environmental effects of TiO_2 NPs in complex systems is critical, but researchers must first overcome the challenge of distinguishing the engineered particles from relatively high concentrations of naturally occurring titanium. In modeling studies focused on European surface waters, the predicted environmental concentration of engineered TiO_2 NPs ranges from 3 ng/L to 1.6 μg/L in river water[50,51], and from 2.5 to 10.8 μg/L in wastewater treatment effluent[51]. In contrast, natural titanium levels in river water have been reported in the range of 2 to 107 µg/L[52]. Background titanium is present in every environmental compartment[53], as well as in plants[54] and organisms[55,56]. Environmental samples will likely contain a mixture of engineered and natural titanium-based materials in both bulk and nano-sized forms, complicating the study of engineered TiO_2 NPs in environmental samples.

As reviewed by von der Kammer et al., several analytical techniques have been developed for the study of nanoparticles in complex matrices: these include techniques for NP extraction/separation, the detection and quantification of engineered NPs, and particle imaging[57]. Field-flow fractionation (FFF) methods can be used to separate nanomaterials of interest from heterogeneous mixtures by exploiting differences in the size or density of the materials in the sample[58]. When FFF is coupled with inductively coupled plasma mass spectrometry (ICP-MS) techniques, nanomaterials can be quantified at environmental concentrations[59]. Additionally, a wide range of particle visualization methods have been applied to the study of engineered NPs, from conventional electron microscopies to more advanced methods like hyperspectral imaging and synchrotron-based techniques[57].

While these are powerful tools, each of these analytical techniques require additional strategies to determine if the detected NPs are naturally-occurring or engineered. For mass-based quantification techniques, comparing elemental or isotopic ratios in samples containing the nanomaterial of interest versus samples with no direct exposure, can assist in making these judgments[57,60,61]. In the case of imaging, the subjective analysis of characteristics like particle morphology can be used. Unfortunately, there are experimental scenarios where no useful isotopic or elemental ratio exists, or the visual characteristics of engineered NPs are not distinctive enough for confidence in identification. To complement these existing analytical techniques, another approach is the application of a traceable label to the nanomaterial of interest. Incorporating a label that is rare in the sample background has the potential to facilitate easier analysis in studies of nanomaterial transport, biouptake, and toxicity.

Four major categories of labels have been applied to enhance studies of the behavior of TiO_2 NPs: fluorescent dyes, dopants, radioisotopes, and stable isotopes. Most commonly, a fluorescent dye is either embedded within the structure or attached to the exterior surface of TiO_2 NPs and detected using fluorescence spectrophotometry or microscopy[62–65]. This is a simple and inexpensive labeling method, but the reported detection limits for fluorescently-labeled metal oxide nanomaterials in environmental samples are in the μg/L-mg/L range, limiting the study of environmentally relevant concentrations of TiO_2 NPs to simpler matrices[66–68]. Another drawback of this method is the potential for the fluorescent dye to alter particle properties and behavior, especially in cases where the dye coats the NP surface and is directly exposed to the surrounding media[69].

TiO_2 NPs have also been doped with rare earth elements, and quantified down to the equivalent of 560 μg/L of Ti using inductively coupled plasma optical emission spectrometry (ICP-OES)[70]. The presence of a rare earth element dopant can alter particle properties like the surface area, ζ-potential, and photocatalytic activity[71]. Furthermore, dopants in the labeled TiO_2 NPs have been shown to preferentially appear on the surface of the nanoparticles where they are most likely to interact with the surrounding environment[70].

TiO_2 NPs have also been labeled with both stable and radioactive isotopes for transport and biouptake experiments at environmentally relevant concentrations. The stable isotope ^{47}Ti was used to study bioaccumulation of TiO_2 NPs in mussels using ICP-MS for quantification down to 8.6 ng/L of Ti[72]. Radiolabeling techniques include the use of a cyclotron to prepare TiO_2 NPs labeled with ^{48}V (half-life=15.97 d), ^{7}Be (half-life=53.29 d), ^{18}F (half-life=109.7 min), and ^{45}Ti [73–75] (half-life=3.08 h), and the use of commercially available radionuclides to prepare TiO_2 NPs labeled with $^{44,45}Ti$ (half-lives=60.4 a, 3.08 h)[74]. Once labeled with a radioisotope, TiO_2 NPs can be detected using positron emission tomography or a radiometric detector like a gamma counter. Isotopic labelling techniques have the benefits of very low detection limits and a much smaller impact on particle properties, but these techniques are expensive and may require specialized equipment.

Choosing the appropriate labeling technique for a given study requires several considerations. The limit of detection must be appropriate for the concentrations used in the study, and the quantification method must be compatible with the study matrix. Study duration must not outlast the stability of the label, especially in the case of radiolabeling methods. Also, particle properties relevant to the behavior being studied must be kept consistent between labeled and unlabeled TiO_2 NPs. In some cases, a detection method that gives information beyond the mass of particles present may be desired (e.g. visualization within an organism).

Core-shell labeling has the potential to provide a powerful complementary technique to these existing methods. Encapsulating a stable metallic label that is rare in the sample matrix with a TiO_2 shell allows more of the labeling element to be incorporated than doping methods permit, enhancing sensitivity without altering particle surface chemistry. The primary disadvantage of this method is that the core-shell particles must be synthesized; the technique cannot be directly applied to commercially available TiO_2 NPs. Additionally, care must be taken to ensure that particle density is unaffected by the presence of the core. However, the method is highly customizable, and can in theory be applied using a variety of core materials and TiO_2 crystal structures. Using gold as the labeling element allows for many different mass quantification and particle visualization techniques to be employed in analysis, such as ICP-MS[76–78], transmission electron microscopy[79–82], and hyperspectral imaging[83,84]. Another notable analytical technique that the Au@TiO_2 system lends itself to is instrumental neutron activation analysis (INAA). INAA is performed by bombarding a sample with neutrons to form radioactive isotopes that can be detected using gamma ray spectroscopy, allowing for quantification at low parts-per-billion levels in complex matrices with very little sample preparation. The technique has been employed to study gold nanoparticle uptake in embryonic zebrafish and biodistribution within the individual organs of mice[85,86].

In this work, gold core-labeled TiO_2 NPs (Au@TiO_2 NPs) were developed as a novel tool for studies of the fate, transport, and bioavailability of TiO_2 NPs. Environmental concentrations of gold are far lower than titanium. The gold nanoparticle core is simple to detect using a variety of analytical methods that allow for quantification of labeled particles, particle visualization, and the study of surface interactions. Au@TiO_2 NPs and unlabeled TiO_2 NPs were synthesized and characterized; the properties and behavior of the two particle types were compared. Spike-and-recovery experiments were performed in both simple and environmentally-relevant media to demonstrate the utility of the labeling technique. ICP-MS, ICP-OES, and INAA techniques were used for quantification.

2.3 Materials and Methods

All glassware used in synthesis was washed thoroughly with freshly made aqua regia solution (3:1 $HCl:HNO_3$) and rinsed with distilled and deionized (DDI) water (18.2 MΩ; Millpore Co. USA). All chemicals met guidelines for purity set by the American Chemical Society (ACS) or the United States Pharmacopeia (USP) unless otherwise noted for ultrapure reagents, and were used without further purification. DDI water was used for all procedures. 100% ACS/USP grade ethanol was used for all procedures. Nanoparticle stock solutions were stored in the dark under refrigeration.

2.3.1 Gold Nanoparticle (AuNP) Core Synthesis

The AuNP cores were synthesized by adapting existing methods developed by Gao et al.[87]. All reagent solutions were prepared directly prior to synthesis. First, 3-5 nm gold seed particles were synthesized as follows. 200 µL of 25 mM trisodium citrate and 1.97 µL of 1 g/mL $HAuCl_4$ (Sigma-Aldrich, ≥49.0 % Au basis) were added sequentially to 19.8 mL DDI water under rapid stirring conditions. A 0.1 M $NaBH_4$ solution was made fresh in water that had previously been chilled for 20 minutes. 600 µL of the $NaBH_4$ solution was added to the $HAuCl_4$/citrate solution, turning the mixture light red. This final solution was allowed to stir for two hours, and then was filtered through a 25 mm syringe filter with a 0.45 µm nylon membrane (VWR International).

The gold seeds were then grown to 30 nm gold core particles. A growth solution was prepared by combining 39.454 mL of DDI water, 8 mL of 5% w/w 40 kDa polyvinylpyrrolidone (PVP) , 3 mL of 0.2 M KI, 4 mL of 0.1 M L-ascorbic acid, and 120 µL of 1 g/mL $HAuCl_4$. 4 mL of the seed solution and 546 µL of 1 M KOH were simultaneously added to the growth solution under rapid stirring, causing the solution to turn dark red. The solution was rapidly mixed for 10 minutes.

To remove unreacted reagents from the AuNP solution, dialysis tubing with a molecular weight cut-off of 14,000 kDa (Sigma-Aldrich) was used. Prior to AuNP synthesis, the dialysis tubing was cut to a length of approximately 40 cm, and cleaned by rinsing thoroughly with DDI water then boiling in 150 mL of DDI water for 15 minutes. This cleaning process was repeated three times, after which the dialysis tubing was stored in 150 mL of DDI water during the AuNP synthetic procedures. After synthesis, the AuNP solution was transferred to the clean dialysis tubing, and the ends sealed. The tubing was then boiled in 500 mL of DDI water for 5 hours, with the water replaced every 45 minutes. The AuNP solution was collected from the tubing and 154 mg of powdered 360 kDa PVP was added. The final AuNP solution was then stirred for 12 hours and stored in the dark under refrigeration. Prior to the TiO_2 coating procedure, the AuNP core solution was centrifuged (Beckman Coulter Allegra 21 Centrifuge) in 50 mL polyethylene centrifuge tubes at 8200 rcf for 45 minutes, and concentrated to a final volume of 25 mL.

2.3.2 TiO_2 Coating Procedure

The AuNPs were coated with TiO_2 by adapting existing methods developed by Goebl et al.[88]. All glassware was rinsed thoroughly with ethanol before use. 40 mL of ethanol, 8 µL of 20 mM

HCl, 190 mg of powdered 360 kDa PVP, and 1.7 mL of concentrated AuNP core solution were combined in a jar and stirred rapidly. In a 20 mL scintillation vial, 5 mL of ethanol and 90 µL of titanium tetraisopropoxide (TTIP) were added and mixed together by inverting the sealed jar. Under rapid stirring, the TTIP solution was pipetted into the Au core solution dropwise, at a rate of 300 µL/min. 100 mg of 360 kDa PVP was then added and the solution was stirred for at least 12 hours at room temperature.

The Au@TiO_2 NPs were then centrifuged at 8200 rcf for one hour. The supernatant was decanted and replaced with 30 mL of ethanol. The mixture was bath sonicated (VWR B1500A-MTH) at high power for 10 minutes to disperse the NP pellet. This process was then repeated three times using 30 mL of DDI water. The Au@TiO_2 NP solution was transferred to Teflon-lined digestion vessels and hydrothermally treated for 12 hours at 120°C in an oven (DX302C, Yamato), forming an anatase TiO_2 shell.

Unlabeled TiO_2 NPs were synthesized using the same TiO_2 coating procedure, but 1.7 mL DDI water was substituted for the concentrated AuNP core solution. All nanoparticle stock solutions were bath-sonicated at high power for 10 minutes prior to use in demonstration experiments.

2.3.3 Nanoparticle Characterization

The primary particle sizes of Au@TiO_2 NPs, unlabeled TiO_2 NPs, and the AuNP cores, along with the number of AuNP cores per TiO_2 shell, were analyzed by transmission electron microscopy (TEM) (FEI Titan). The average NP size and number of cores per shell were determined using ImageJ (N>100 for all TEM analyses). Additionally, a scanning transmission electron microscopy (STEM) tilt series was collected using a high angle annular dark frequency (HAADF) detector. The α tilt angle varied from -50° to +40° in 1° increments for $|\alpha| < 30°$ and 2° increments for $|\alpha| \geq 30°$ (FEI Titan). Inspect 3D software was used to align the data, and a video file of the full tilt series is included in the supplemental data for this manuscript. The hydrodynamic diameters (D_h) and ζ-potentials of particle suspensions in DDI water (Au@TiO_2 NPs, unlabeled TiO_2 NPs, and AuNP cores) were determined using dynamic light scattering (DLS) (90Plus and ZetaPALS, Brookhaven Instruments). For ζ-potential, 20 mL samples of 10 mg/L particle suspensions were prepared in 1 mM KCl. A titration unit (BI-ZTU, Brookhaven Instruments) was used to measure the electrophoretic mobility at 0.5 pH unit increments in the range of pH 3-11, with 3 measurements of 20 cycles collected at each increment. ζ-potential was calculated using the Smoluchowski model. Details are included in the Supporting Information (SI).

Homoaggregation studies were performed on the Au@TiO_2 and unlabeled TiO_2 NPs using time-resolved DLS measurements, as described previously[89–91]. For these experiments, 3.5 mL of a 10 ppm solution of NPs were added to a cuvette, minus the volume of KCl to be added. Three DLS runs of 1 minute each were used to determine the average initial D_h value. After this measurement, KCl was added to the NP solution in the cuvette for a final concentration ranging from 100-500 mM. The cuvette was inverted to mix and immediately analyzed for 120 DLS measurements, each 15 seconds long. The pH of each KCl/NP solution was measured after the experiment; pH values ranged from 5.25 to 5.68.

Single particle ICP-MS (sp-ICP-MS) was used to provide additional measurements of AuNP core size and the number of AuNP cores per shell. Samples of the AuNP cores before and after coating with TiO_2 were each analyzed using a Perkin Elmer NexION 300D ICP-MS equipped with a Meinhard high solids low flow nebulizer (type 0.5 mL/min, type C) and a glass Perkin Elmer cyclonic spray chamber. Each measurement run was 60 seconds with a dwell time of 100 µs. The sample flow rate was 0.3 mL/min. The transport efficiency for each measurement was determined using a mass-based method with a 60 nm AuNP reference standard (U.S. National Institute of Standards and Technology, RM 8013)[92]. Dissolved gold standards were used to produce a calibration curve. Syngistix software in Nano mode was used to identify the particle event peaks in each sample, and to convert each particle event's measured peak area to a mass of Au and an AuNP diameter.

The surface composition of samples of the Au@TiO_2 NPs and unlabeled TiO_2 NPs was analyzed using X-ray photoelectron spectroscopy (XPS) (ThermoScientific ESCALAB 250 spectrometer). Lyophilized Au@TiO_2 nanopowder was pressed onto double-stick carbon tape and mounted on a sample rod. The unlabeled TiO_2 NP sample was prepared by dropcasting the aqueous stock solution onto a clean silicon wafer, which was then mounted on a sample rod. A monochromatic AlKα X-ray source was used at an operating power of 150 W with a nominal spot size of 500 µm. Survey scans were collected at a pass energy of 150 eV, while high-resolution spectra were collected at a pass energy of 20 eV. The binding energy scale for all measurements was calibrated to the C_{1s} peak at 284.6 eV. Two 500 µm areas were analyzed for each sample, and all compositional values reported are the average values. Peak analysis was performed with Avantage software.

Crystal structure of lyophilized nanopowders was analyzed using X-Ray Diffraction (XRD) (Bruker-AXS D8 Discovery). Scans were performed at 2Θ values between 20° and 80° at a rate of 5°/min. UV-Visible spectra were collected for NP suspensions in DDI water at 25 mg Au/L concentrations for wavelengths between 400 and 700 nm. (ThermoScientific Orion AquaMate 8000 UV Vis Spectrophotometer).

The NP stock solution concentrations of Au and Ti were measured using ICP-OES (Prodigy, Teledyne Leeman). Detection limits in DDI water were determined using ICP-MS (X-Series 2, Thermo Fisher Scientific). Prior to analysis, samples were digested using a HNO_3/HF procedure. Details of the acid digestion are included in the SI (Appendix A).

2.3.4 Spike-and-Recovery Demonstrations

A simple spike-and-recovery experiment was performed in DDI water. Au@TiO_2 NPs were added to DDI water to a final concentration of 1 µg/L Au and 1.5 µg/L Ti. For background titanium, unlabeled TiO_2 NPs were added to a final concentration of 1.5 µg/L. Triplicate samples were acid digested using the procedure described in the SI (Appendix A), and concentrations of Au and Ti were measured using ICP-MS (X-Series 2, Thermo Fisher Scientific).

For a more complex spike-and-recovery scenario, Willamette River water was collected from the influent of the Taylor Drinking Water Treatment Plant in Corvallis, OR. Water quality details are included in the SI (Appendix A). A commercially available Ti-containing sunscreen was added to the collected river water to a final concentration of 40 mg/L sunscreen. This corresponded to 285 µg/L of background Ti in the matrix, as measured by ICP-OES. The solution of sunscreen and river water was spiked with Au@TiO_2 NPs at final concentrations of 325 and 650 µg/L Au. Samples were acid digested using the procedure described in the SI (Appendix A), and Au and Ti concentrations were measured using ICP-OES. Each experiment was completed in triplicate.

A third spike-and-recovery experiment was conducted in activated sludge using instrumental neutron activation analysis (INAA) for quantification. Return activated sludge was collected from the Corvallis Wastewater Treatment Plant, stored in the refrigerator, and used within 24 hours. The sludge was analyzed for total dissolved solids and total suspended solids using Standard Methods 2540C and 2540D[93]. For the spike-and-recovery experiments, sludge was inverted several times to mix, and 1 mL samples were added to pre-washed, pre-weighed 1.4 mL polyethylene vials. Au@TiO_2 NPs were added to the sludge at Au masses of 10 ng, 100 ng, and 10 µg, each run in triplicate. Triplicate samples were also prepared with the sludge alone to determine the concentration of background Au. Samples were heated at 60°C in an oven to dewater, re-weighed, and stored in a desiccator prior to INAA conducted at the Oregon State University Radiation Center.

For INAA quantification, five replicates of Au standards were prepared by pipetting liquid standard (SpecPure AAS Au) onto filter paper placed in 1.4 mL polyethylene vials for final masses of 10 µg Au. Vials were weighed, and then DDI water was added to distribute the liquid standard. All standard and sample vials were heat-sealed. Vials were irradiated with a nominal flux of 2.6×10^{12} n/cm^2/s for 14 hours while rotating. Gamma counting was conducted for

10,000 s at a distance of 10 cm using a HPGe detector (Ortect GEM-25185P, 33% efficiency). The gamma spectra were analyzed with Genie2000® software (Canberra Industries) using the standard peak-search algorithm with a focus on the 411 keV ^{198}Au peak. The mass of Au in each sample was calculated with the direct comparison method using the following equation:

$$\frac{Activity_{sample}}{Activity_{standard}} = \frac{Mass_{sample}}{Mass_{standard}}.$$

2.4 Results and Discussion

2.4.1 Nanoparticle Synthesis and Characterization

The Au@TiO_2 core/shell system was chosen as an alternative labeling technique with the potential for enhanced detection capabilities over doping and fluorescent methods while better maintaining the surface chemistry of unlabeled TiO_2 systems. While the crystal structure of the TiO_2 coating can be easily altered with heat treatments, the anatase form was chosen for this study because it has the highest potential for the generation of reactive oxygen species[23,94]. Figure 2.1 shows the Au@TiO_2 NPs at each step of the synthetic process, along with unlabeled TiO_2 NPs. Additional TEM images of the Au@TiO_2 NPs captured at a lower magnification are included in Appendix A as Figures 7.1.1 and 7.1.2. Figure 2.1 shows that the anatase TiO_2 shells and unlabeled TiO_2 NPs are composed of smaller TiO_2 crystallites, resulting in a porous structure. Au@TiO_2 NPs were ellipsoidal in shape both before and after hydrothermal treatment, while the AuNP cores remained spherical. The placement of the AuNP cores within the shell is inconsistent from particle to particle; in some cases the cores protrude from the edges of the shell.

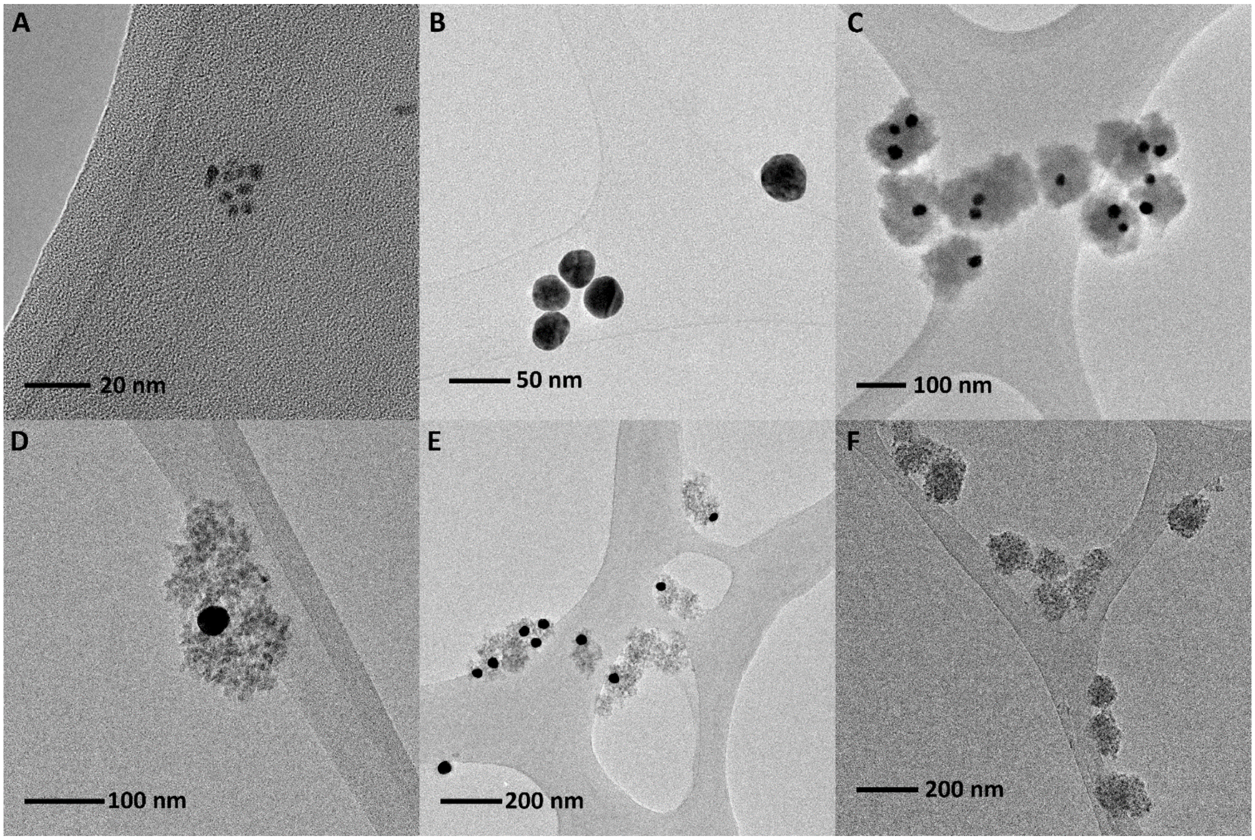

Figure 2.1. TEM images of a) Au seed particles, b) AuNP cores, c) Au@TiO_2 NPs with an amorphous TiO_2 coating, d-e) Au@TiO_2 NPs with an anatase TiO_2 coating after hydrothermal treatment, and f) unlabeled TiO_2 NPs.

To better examine the anatase shell coverage for the Au@TiO_2 NPs, a STEM tilt series was collected. A video of the full tilt series is included as a supplemental file to this manuscript. Figure 2.2 shows representative images of the series at a variety of tilt angles. The majority of the AuNP cores in the image are nearly completed covered by the anatase TiO_2 shell, a feature which is visible even though the large Z contrast between the gold and TiO_2 increases the visibility of the AuNPs in the images relative to the TiO_2 shell. The leftmost AuNP in the images shown in Figure 2.2 has the least amount of coverage, and is likely to interact with the surrounding media. In this core/shell system, the optimal shell coverage is achieved if the lattice mismatch between the AuNP cores and the TiO_2 shells is minimized, decreasing interfacial tension[95]. The lattice mismatch for the Au@TiO_2 system with an anatase shell is 7.4% (calculations included in the SI), while an amorphous shell can more freely orient to the AuNP surface. The shell is therefore more likely to be thinner and more incomplete for the anatase system.

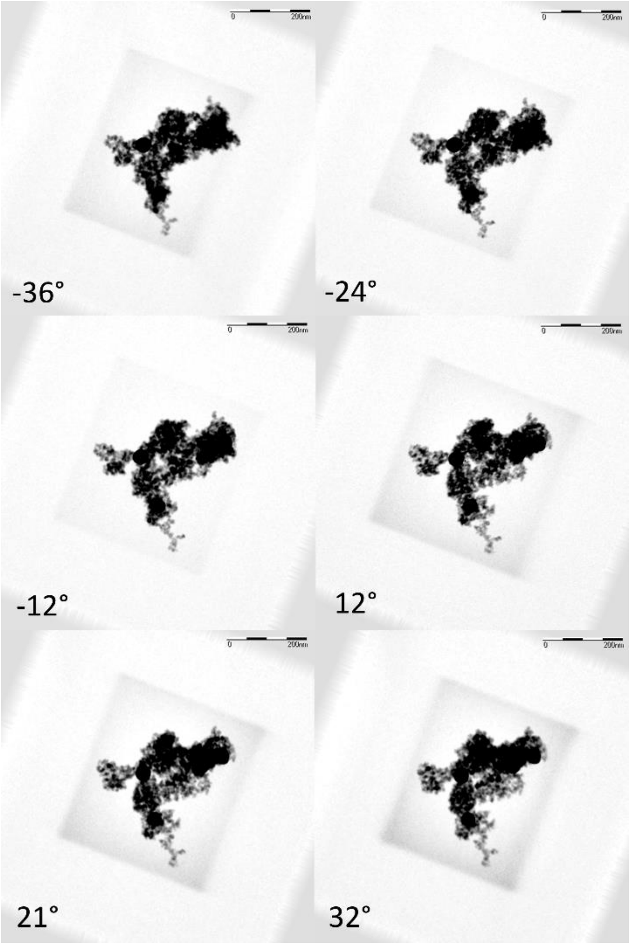

Figure 2.2. Selected images from a HAADF-STEM tilt series collected on an Au@TiO_2 NP, with α tilt angles included in the lower left corner of each frame.

The sizes of the Au@TiO_2 NPs and unlabeled TiO_2 NPs are summarized in Table 2.1, with the TEM-measured diameters representing the largest axis of the ellipsoidal NPs. The Au@TiO_2 NPs prepared for this study are larger than the 100 nm diameter typically used as the cutoff for nanomaterial classification, but both the core and shell sizes can be adjusted using published methods[87,88]. The unlabeled TiO_2 NPs are similar in size to the Au@TiO_2 NPs, making them suitable for comparison. The DLS-measured D_h values for both the Au@TiO_2 and TiO_2 NPs are in good agreement with the TEM-measured diameters, indicating that the NPs in solution remain unaggregated.

Table 2.1. NP sizes measured by TEM and DLS for Au@TiO_2 NPs and unlabeled TiO_2 NPs, reported as the average ± standard deviation for TEM and the average ± standard error for DLS.

	Unlabeled TiO_2 NPs	**Au@TiO_2 NPs**
Diameter (TEM)	169 ± 75 nm	206 ± 85 nm
Hydrodynamic Diameter (DLS)	185 ± 2 nm	176 ± 1 nm

The sizes of the AuNP cores were also measured using a variety of techniques. The results are summarized in Table 2.2. Size distribution plots of the sp-ICP-MS and TEM measurements are included in the SI (Appendix A). The average sp-ICP-MS measurement of the AuNP diameter prior to coating with TiO_2 is in good agreement with the average TEM-measured diameter, despite the large difference in the number of particles analyzed. After coating, the diameter measured by sp-ICP-MS increased, consistent with the appearance of multiple cores per shell. The D_h measured via DLS is nearly two times the primary particle diameter measured via TEM. This indicates that some of the homoaggregation resulting in more than one core appearing in each shell occurred prior to the coating procedure. The average number of AuNP cores per TiO_2 shell as determined by TEM analysis was 2 ± 1, and the number of cores per shell was estimated as 2.1 by comparing the sp-ICP-MS data of the AuNPs before and after coating (Calculations are included in the SI).

Table 2.2. AuNP Core sizes measured by sp-ICP-MS, TEM, and DLS, reported as the average ± standard deviation for sp-ICP-MS and TEM, and the average ± standard error for DLS.

Technique	**Sp-ICP-MS**		**TEM**	**DLS**
NPs measured	**AuNPs within Au@TiO$_2$ NPs**	**AuNP cores prior to coating**	**AuNPs within Au@TiO$_2$ NPs**	**AuNP cores prior to coating**
Diameter, nm	41 ± 10	36 ± 6	35 ± 4	60 ± 1
N$_p$ analyzed	23499	37901	120	--

When choosing the core/shell ratio of the Au@TiO$_2$ NPs for a specific experimental application, a balance must be struck between particle density, photocatalytic activity, and detection sensitivity. A larger AuNP core will enhance detection sensitivity and can allow for more analytical techniques to be used in studies of the labeled NPs. For example, the use of single-particle ICP-MS techniques for quantification requires a minimum particle diameter of 13 nm for AuNPs[96]. The increased sensitivity comes at the cost of producing greater differences in density between labeled and unlabeled TiO$_2$ NPs. The effect of the core/shell ratio on photocatalytic activity is more complicated to predict. Hybridization of TiO$_2$ catalysts with plasmonic materials like gold has been shown to enhance photocatalytic activity in a variety of model redox reactions[97]. In a study of Au@TiO$_2$ systems, the enhancement effect was strongest when the weight percentage of Au was below 1%[88].

For the Au@TiO$_2$ particles produced in this work, the weight percentage of Au determined from TEM analysis was in the range of 10-19%, depending on the assumptions used when estimating the three-dimensional volume of the NPs from a two-dimensional image (all calculations are included in the SI). This corresponds to a deviation in density from an unlabeled TiO$_2$ NP ranging from 5.3-10%. The Ti:Au ratios and Au weight percentages as determined by a variety of analytical techniques are summarized in Table 2.3, with all calculations included in the SI

(Appendix A). The bulk Ti:Au ratio measured by ICP techniques was much lower than the Ti:Au ratios determined through TEM analysis. The difference in the Ti:Au ratio determined by the mass-based ICP methods and the size-based TEM analyses suggests that the TiO_2 shell may be porous, a conclusion that is also supported by the appearance of the TiO_2 shell in TEM images (Figure 2.1). Therefore, the actual Au weight percentage per particle and deviation in density from unlabeled TiO_2 NPs are both likely to be larger than the values presented here, as porosity was not taken into account.

XPS analysis was also performed. Spectra are included in Appendix A (Figures 7.1.3-7.1.5). The top 10 nm of the Au@TiO_2 NP surfaces were found to have a similar ratio of Ti/Au than the bulk solution as measured by ICP techniques, which was unexpected given the core-shell structure of the particles. The XPS results reveal that metallic gold is present in measureable quantities on the surface of the Au@TiO_2 NPs, and can therefore be expected to interact with the surrounding environment to some extent. These results confirm observations of Au@TiO_2 NPs via TEM and STEM (Figures 2.1 and 2.2) where incomplete coating of some AuNP cores was observed. The Ti:Au ratios measured via ICP-OES and ICP-MS are most relevant to the analysis of the experimental data generated in this work, and were used in the spike-and-recovery demonstrations to determine how much titanium was from the labeled NPs versus the background.

Table 2.3. Ti/Au ratio and Au wt % as estimated using TEM, ICP-OES/MS, and XPS analysis. All calculations are included in the SI.

	TEM	**ICP-OES/MS**	**XPS**
	NP (Calculated per individual NP)	**Bulk (Measured across stock solution)**	**Surface (Top 10 nm)**
Ti:Au	2.5 - 5.1	1.5-2.3	1.4
Au wt %	10 - 19 %	21-29 %	30 %

The properties of the Au@TiO_2 NPs and unlabeled TiO_2 NPs were measured and compared. The ζ-potentials of AuNP cores, Au@TiO_2 NPs, and unlabeled TiO_2 NPs are summarized in Figure 2.3. Each particle type has a PVP coating, but there are likely small differences in the surface density of the PVP coating between Au and TiO_2 surfaces, leading to differences in the magnitude of the negative surface charge. For each particle type, the ζ-potential remains negative across the entire pH range tested. At pH 6.2, there is no statistical difference between the ζ-potentials of labeled and unlabeled TiO_2 NPs. Upon coating with TiO_2, the ζ-potential of the AuNP cores shifts to become more negative. Although differences exist between the Au@TiO_2 NPs and unlabeled TiO_2 NPs, both have a highly negative (<−30 mV) surface charge in the environmentally relevant pH range.

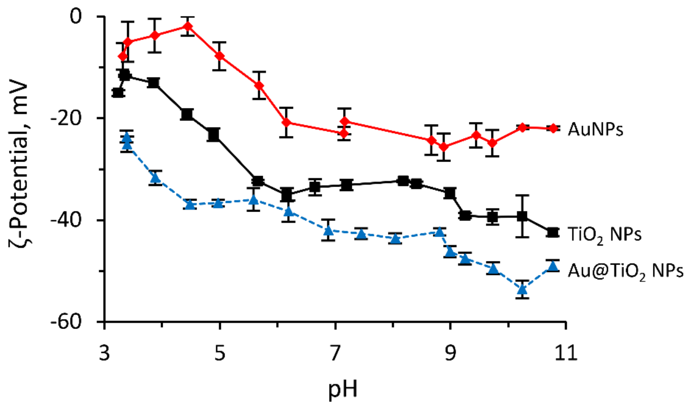

Figure 2.3. Variation of ζ–potential vs. pH for AuNP cores, Au@TiO_2 NPs, and unlabeled TiO_2 NPs.

To further examine the potential impact of the differences in ζ-potentials between unlabeled and labeled TiO_2 NPs, homoaggregation behavior in KCl solutions was studied (Figures 7.1.8 and 7.1.9 in Appendix A). Neither nanoparticle type homoaggregated at KCl concentrations ≤ 200 mM and the Au@TiO_2 NPs aggregated only slightly to 1.37, 1.39, and 1.50 times their initial D_h values for KCl concentrations of 300, 400, and 500 mM, respectively. Both particle types ultimately remained stable in solution, likely due to a combination of steric and electrostatic stabilization due to the TiO_2 surface and the PVP coating.

It was also important to verify that the crystal structures for the labeled and unlabeled particles were similar. The XRD spectra for the Au@TiO_2 and unlabeled TiO_2 NPs confirm that the TiO_2 is in the anatase form for both NP types (Figure 2.4). The Au@TiO_2 spectrum also includes peaks for metallic gold. It should be noted that XRD is not a surface-sensitive characterization technique, and that the presence of these metallic gold peaks does not indicate incomplete coating of the AuNP cores with TiO_2. Metallic gold peaks consistently appear in XRD spectra of Au@TiO_2 NPs, even those with Au wt % values well below 1%[88,98,99]. The XRD spectra was used to compare the primary TiO_2 crystallite sizes of the labeled and unlabeled NPs. The primary crystallite size was 5.8 nm for the unlabeled TiO_2 NPs and 6.0 nm for the Au@TiO_2 NPs, confirming that for both particle types the TiO_2 is comprised of multiple smaller crystals.

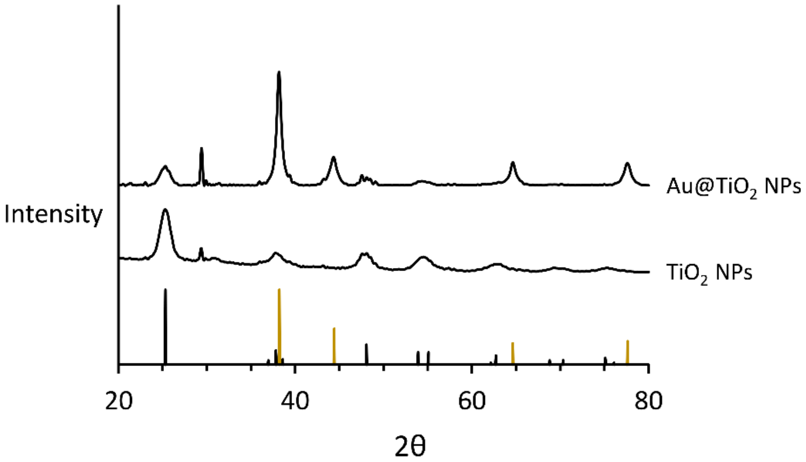

Figure 2.4. XRD spectra of Au@TiO$_2$ and TiO$_2$ NPs. Standard spectra of anatase TiO$_2$ (black) and gold (yellow) are also included below the NP spectra[100].

The UV-Vis spectra of the uncoated AuNP cores and the Au@TiO$_2$ NPs are included in Figure 2.5. The TiO$_2$ coating enhances the absorbance of the surface plasmon resonance (SPR) peak. The SPR peak was also red-shifted by 10 nm for the Au@TiO$_2$ NPs. These observed changes in optical properties after coating with TiO$_2$ are caused by the larger refractive index of TiO$_2$ versus the DDI water that originally surrounded the AuNP cores, and are consistent with other examinations of Au@TiO$_2$ NPs[98,99,101]. The continued presence of the SPR peak suggests that techniques like surface enhanced raman spectroscopy (SERS) could potentially be used in Au@TiO$_2$ experiments. SERS has previously been used to probe the adsorption and photodegradation of dyes on Au@TiO$_2$ surfaces[102].

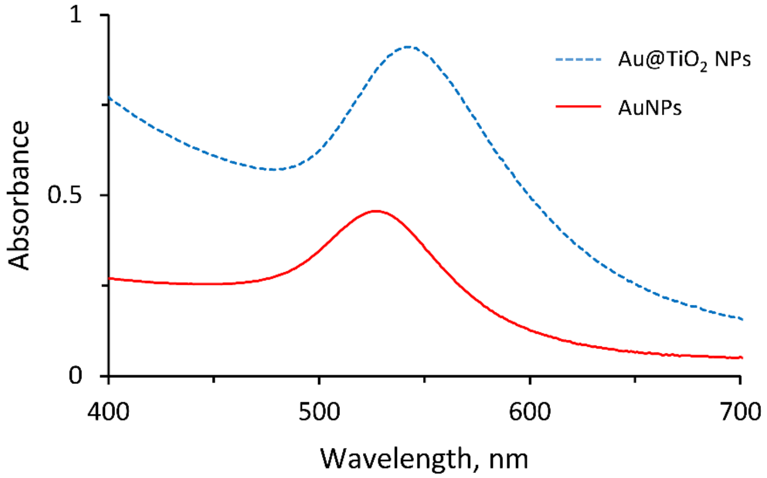

Figure 2.5. UV-Vis spectra for uncoated AuNP cores and Au@TiO$_2$ NPs, both at concentrations of 25 mg/L Au.

The particle characterization studies indicate that Au@TiO$_2$ NPs are generally suitable for use in experiments requiring labeled TiO$_2$ NPs. The size of the AuNP core allows for a variety of techniques to be used in detection and quantification, while also keeping the Au wt % higher than values previously shown to alter photocatalytic activity. The deviation in density from unlabeled TiO$_2$ NPs remained below 20% in all calculations. There was no significant homoaggregation observed for the labeled or unlabeled NPs, indicating that the small differences in surface charge and density will be unlikely to affect behavior in the simple systems studied. Prior to the use of Au@TiO$_2$ NPs in transport and toxicology experiments, the surface charge and aggregation behavior of labeled and unlabeled TiO$_2$ NPs should be compared across the full range of pH, ionic strength, and natural organic matter concentrations that the NPs will be exposed to in the planned experiment.

In many cases, labeled TiO$_2$ NPs are not fully characterized and compared to their unlabeled counterparts, especially in the case of fluorescently-labeled TiO$_2$ NPs[63–65]. Fluorescent dyes attached to the surface of TiO_2 NPs can be expected to alter the properties of the bare mineral surface. Isotopic labeling methods, using both stable and radioactive isotopes, will likely have limited impact on particle properties and behavior, as long as care is taken to prevent thermally-induced structural changes from direct radioactivation[103]. Changes to surface chemistry and agglomeration behavior have not been studied in detail for these methods, but an increase in specific surface area has been reported when stable isotopic methods are employed[72]. For TiO_2 NPs labeled with rare-earth-element dopants, small differences in D_h and ζ-potential were observed between labeled and unlabeled NPs, similar to differences observed in this work[70]. Additionally, the ratio of dopant:Ti was 1.3-2.8 times greater for the surface of the labeled NPs than the ratio used during synthetic procedures, indicating that the dopant preferentially appeared on the NP surfaces[70]. In this work, the ratio of Au:Ti was 1.1-1.6 times greater for the surface than the ratio measured in the bulk Au@TiO_2 NP solution, which TEM images suggest is likely due to incomplete coating of the AuNP cores. Overall, the core/shell labeling method as evaluated in this work has a similar impact on TiO_2 surface properties when compared to dopant labeling techniques, and a lower impact when compared to labeling techniques featuring the surface attachment of fluorescent dyes. Core/shell labeling will have a greater impact on particle density than fluorescent and dopant labeling techniques, but this comes with the benefit of theoretically providing greater detection sensitivity with a wider variety of detection methods. The detection sensitivity was explored in more detail using spike-and-recovery experiments in several complex matrices.

2.4.2 Spike-and-Recovery Demonstrations

The procedures employed in this work to quantify Au@TiO_2 NPs are described and justified here. For experiments that measured the Au@TiO_2 NPs against a background of titanium from other sources, the known Ti:Au ratio of the Au@TiO_2 NPs was used to determine the breakdown of titanium from the engineered NPs versus the sample background. The concentrations of gold and titanium were first measured in the stock solution of Au@TiO_2 NPs using the same quantification method used for sample analysis (e.g. ICP-MS), and converted to a mass ratio of Ti:Au. A bulk measurement of Ti:Au across the stock solution was chosen, as opposed to using estimates of Ti:Au from images or other analyses of individual Au@TiO_2 NPs, to better take into account any particle-to-particle deviations arising from deviation in shell thickness or the number of AuNP cores per shell. The Ti:Au ratio of the Au@TiO_2 NP stock solution was re-measured after the experiment was completed, to ensure that no changes in Ti:Au occurred over time that could have confounded the resulting data.

When analyzing experimental data, the amount of titanium from the Au@TiO_2 NPs in a given sample was determined using the equation:

$$[Ti]_{NPs} = [Au]_{sample} \times (Ti{:}Au)_{stock},$$

where $[Au]_{sample}$ was the measured concentration of gold in the sample and $(Ti{:}Au)_{stock}$ was the ratio of titanium to gold measured across the bulk Au@TiO_2 NP stock solution used in the experiment.

The amount of titanium from the sample background matrix was calculated as follows:

$$[Ti]_{b/g} = [Ti]_{sample} - [Ti]_{NPs},$$

where $[Ti]_{sample}$ was the total amount of titanium measured in the sample.

As a demonstration of the utility of Au@TiO_2 NPs, three spike-and-recovery experiments were performed. First, a simple mixture of Au@TiO_2 NPs (at 1 µg Au/L) and TiO_2 NPs (at 1.5 µg/L) was prepared in DDI water, with the unlabeled TiO_2 NPs representing a “background” of titanium. The Ti:Au ratio in the Au@TiO_2 NP stock was measured as 1.5 using ICP-OES. Figure 2.6 summarizes $[Au]_{sample}$ and $[Ti]_{sample}$, along with the known spiked and experimentally-determined recovered values of $[Ti]_{NP}$ and $[Ti]_{b/g}$. The spiked values, shown with the dotted lines in Figure 2.6, are the known quantities of titanium added to the sample as either Au@TiO_2 NPs ($[Ti]_{NP}$) or TiO_2 NPs ($[Ti]_{b/g}$).

In this experiment, 80.4% of the total added gold and 98.7% of the total added titanium was recovered successfully, with the 95% confidence intervals putting the experimentally-determined breakdown of titanium sources within the range of the known amounts added. The gold recovery was lower than expected once the additional TiO_2 was added to the sample as background. This was likely caused by the volume of acids used being slightly lower than optimal during the digestion procedure, and due to the lack of hydrochloric acid in the final sample matrix. The ICP sample preparation procedures were adjusted to correct for these issues for the remaining spike-and-recovery experiments. More details about acid digestion methods and modifications are included in the SI (Appendix A). Based on these initial results, Au@TiO_2 NPs can be employed to study environmentally-relevant concentrations of TiO_2 NPs, an advantage over labeling methods with higher limits of detection.

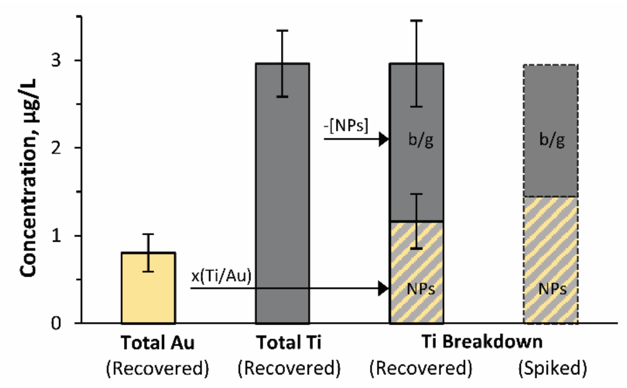

Figure 2.6. Concentrations of Au and Ti measured via ICP-MS, along with the experimentally-determined recovered and known spiked breakdown of Ti from labeled NPs (Ti, NPs) and the background matrix (Ti, b/g).

A second spike-and-recovery experiment was performed in river water mixed with a Ti-containing sunscreen. Water quality information for the collected Willamette river water is included in Appendix A Table 7.1.6. The background titanium in the river water-sunscreen mixture was measured at 285 ± 33 µg/L using ICP-OES. This corresponds to limits of detection and quantification for unlabeled TiO_2 NPs of 394 µg Ti/L and 615 µg Ti/L, respectively (calculations included in SI).

Prior to this experiment, the Ti:Au ratio of the Au@TiO_2 NP stock solution was re-measured as 2.3, higher than the measured value of 1.5 for the previous experiment due to the changes in the acid digestion procedure (described in the SI). The Ti:Au ratio of 2.3 remained constant when measured before and after the experiment. Two concentrations of Au@TiO_2 NPs were tested, 325 µg Au/L (referred to as the low dose) and 650 µg Au/L (referred to as the high dose).

Figure 2.7 shows $[Au]_{sample}$ and $[Ti]_{sample}$ for each spike concentration tested, along with the spiked and recovered values of $[Ti]_{NP}$ and $[Ti]_{b/g}$. Here, bars labeled "spiked", shown with the dotted lines in Figure 2.6, are the known quantities of titanium added to the sample as either Au@TiO_2 NPs ($[Ti]_{NP}$) or TiO_2 NPs ($[Ti]_{b/g}$). Gold recovery was 105.5% for the low dose experiment and 94.3% for the high dose experiment. This provided accurate quantification of Au@TiO_2 NPs against the background at a concentration lower than the limit of quantification possible for unlabeled TiO_2 NPs. This accuracy was possible despite relatively low recoveries of total titanium (80.2% for the low dose and 80.0% for the high dose). These lower Ti recoveries, compared to the simple spike-and-recovery system in DDI water, were likely caused by the presence of the rutile form of TiO_2 in the sunscreen mixture. The titanium recoveries in this work are comparable to the 81% recoveries achieved for P25 TiO_2 NPs (a rutile/anatase mixture) spiked into a food product and prepared for ICP-MS using a microwave acid digestion method more rigorous than the hot-plate methods used in this work[104]. In future work, more adjustments can be made to increase the accuracy of the total titanium recovery, such as using greater volumes of concentrated acid throughout the procedure and allowing trace amounts of hydrofluoric acid to remain in the final sample solutions. Despite these challenges, this experiment illustrates that commonly-used methods of quantification for unlabeled NPs like ICP-OES are able to be applied to Au@TiO_2 NPs in real-world environmental samples. ICP-MS can be employed to provide greater sensitivity for experiments that require a lower Au@TiO_2 concentration than the spike-and-recovery demonstrations discussed in this work.

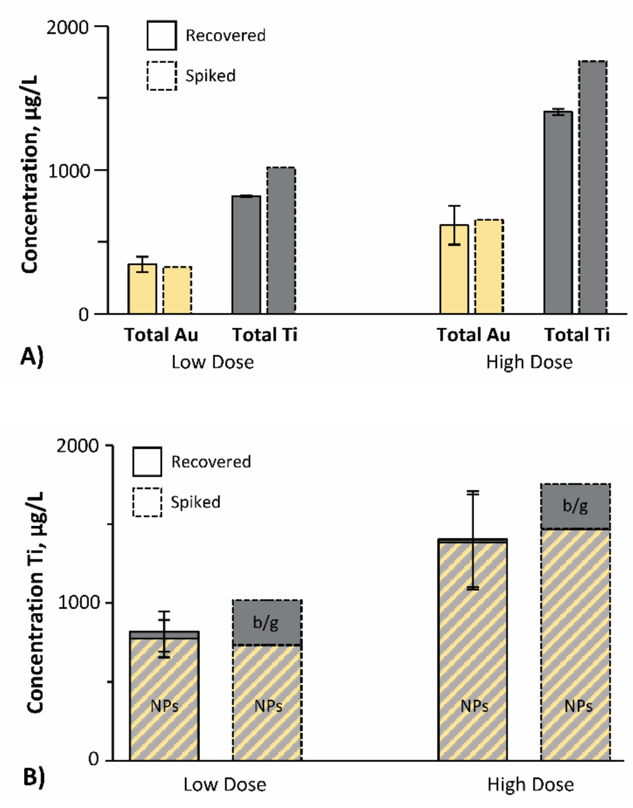

Figure 2.7. A) Spiked and recovered concentrations of Au and Ti measured via ICP-OES for 325 (low) and 650 (high) µg Au/L Au@TiO_2 NP doses in a river water and sunscreen mixture. B) The known (spiked) and experimentally-determined (recovered) breakdown of Ti from labeled NPs (Ti, NPs) and the background (Ti, b/g).

A final spike-and-recovery experiment was performed in activated sludge collected from the Corvallis Wastewater Treatment Plant. INAA was used for quantification to take advantage of facile sample preparation, pg-level detection limits for gold, and high recovery of elements embedded in a mineral lattice[105,106]. The average value of background gold in 1 mL of the activated sludge matrix was 28.7 ± 0.6 ng, which corresponds to an average gold content in dried sludge of 5356 ± 588 µg/kg (calculations included in the SI). While regional variation of sludge composition can be expected, this is a considerably greater amount of background gold than the 177 and 580 µg/kg concentrations measured in activated sludge by Westerhoff et al.[107]. Although unanticipated, the higher gold concentrations were consistently measured across all sludge samples, and allow for the type of analysis necessary to determine the feasibility of using Au@TiO_2 NPs in matrices with elevated concentrations of the labeling element. Due to the short half-life of titanium daughter isotopes, and high background concentrations of titanium in the activated sludge, ICP-OES was used to measure the amount of background titanium in the sludge, and to re-measure the Ti:Au ratio in the Au@TiO_2 NP stock (which remained consistent at 2.3).

Figure 2.8 summarizes the masses of gold measured in each of the three spike-and-recovery experiments, which consisted of Au@TiO_2 NPs added to the sludge in 10 ng, 100 ng, and 10 μg quantities. For the 10 ng experiment, accurate quantification of the Au@TiO_2 NPs was not achieved due to the high concentration of background gold in the sludge matrix relative to the gold added as Au@TiO_2 NPs. A 60 ng experiment would be the minimum Au@TiO_2 spike concentration required to reach the calculated limit of quantification of 11.2 mg Au/kg sludge. While there was still a significant amount of background gold present in the 100 ng Au experiment, it could be subtracted from the total mass of gold measured in the samples to recover the accurate quantity of gold from the added Au@TiO_2 NPs. The background gold was determined to be insignificant in the 10 μg experiment: the Au@TiO_2 NPs could be accurately quantified whether or not the background gold was subtracted from the total amount of gold measured.

The limits of detection and quantification for Au@TiO_2 NPs in dry sludge were determined to be 7.3 mg Au/kg (corresponding to 16.8 mg Ti/kg) and 11.2 mg Au/kg (corresponding to 25.8 mg

Ti/kg), respectively. If unlabeled NPs were used, the limits of detection and quantification for TiO_2 NPs in dry sludge would be much higher at 429 mg Ti/kg and 1160 mg Ti/kg, respectively. Au@TiO_2 NPs allowed for quantification at more than fifty times lower NP concentrations with facile sample preparation, despite the presence of background concentrations of the labeling element in a highly complex matrix. This method also allows for samples to be sent to a facility with INAA capabilities after an experiment is completed.

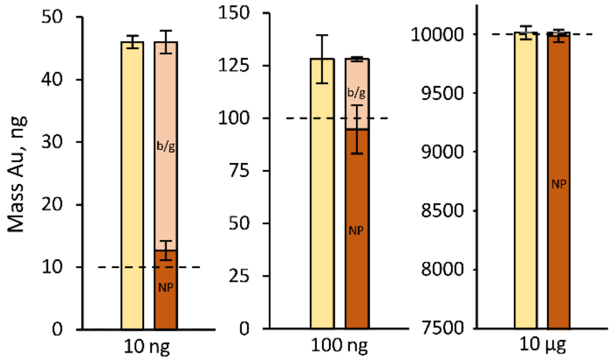

Figure 2.8. Masses of Au measured via INAA for 10 ng, 100 ng, and 10 µg Au@TiO_2 spikes in activated sludge. The total mass Au (shown in yellow), mass Au from the activated sludge background (pale orange), and mass Au experimentally-determined to be from the Au@TiO2 NPs (dark orange), are all shown for each experiment. The dotted lines represent the known spiked values of Au from the added NPs.

Using this core/shell labeling method, the behavior of TiO_2 NPs in complex samples containing background titanium can be studied with a variety of analytical techniques. For simple systems, the presence of the AuNP SPR peak enables the use of UV-Vis spectroscopy for quantification (standard curve included in the SI). In more complex samples, ICP-OES and ICP-MS was employed to quantify the labeled TiO_2 NPs at environmentally-relevant concentrations, using the known Ti:Au ratio of the Au@TiO_2 NPs to determine which portion of the total titanium was attributable to the sample background. Even in systems where full titanium recovery was problematic, gold recoveries remained accurate, allowing for accurate determination of

Au@TiO_2 NP concentrations. Accurate Au@TiO_2 quantification was also achieved in activated sludge, an exceptionally complex matrix containing elevated concentrations of gold, using INAA. When compared to other labeling methods, Au@TiO_2 labeling allowed for detection at lower quantities than those achieved for fluorescent labeling and rare-earth element doping. In contrast, radiolabeling and stable isotopic labeling have been used to achieve lower limits of quantification than those obtained in this work. In systems containing no background gold, limits of quantification rivaling isotopic labeling techniques will be possible using INAA. One additional benefit of the Au@TiO_2 labeling system is that it allows for radioactivation of samples for quantification via INAA to occur after an experiment is complete, which eliminate the temporal stability challenges and the limitations of handling radioactive materials that are inherent in TiO_2 radiolabeling techniques.

2.5 Conclusions

Gold core-labeled TiO_2 NPs were successfully synthesized, characterized, and quantified at environmentally-relevant concentrations in real-world matrices. The labeled particles had properties similar to unlabeled TiO_2 NPs, and were accurately recovered in complex environmental samples using ICP-OES, ICP-MS, and INAA. The synthetic procedures can be adapted to produce Au@TiO_2 NPs with different sizes, crystal structures, and surface coatings. Remaining synthetic challenges to be addressed include deviation in the number of AuNP cores per TiO_2 shell, incomplete coating of some AuNP cores, and small differences in ζ-potential and homoaggregation behavior between labeled and unlabeled particles. Prior to their use in toxicological studies, the photocatalytic activities and organismal toxicities of Au@TiO_2 NPs and TiO_2 NPs should be compared. Additional studies could evaluate the applicability of Au@TiO_2 NPs to analytical techniques that provide more information than the mass of NPs in a fractionated sample, including particle visualization techniques and SERS.

As a labeling technique, Au@TiO_2 NPs are especially appropriate for experiments that require longer time frames than fluorescent labels and short-lived radioisotopes allow, as the metal core-labeling technique is not time-sensitive. This includes studies of trophic transfer or chronic accumulation in organisms. Another suitable application of Au@TiO_2 NPs would be for studies that benefit from the use of single-particle ICP-MS for quantification, as AuNPs have a lower size detection limit (below 20 nm) than TiO_2 NPs (above 100 nm)[96]. The gold core-labeling method has the additional advantage of expanding access to INAA techniques for the quantification of TiO_2 NPs in complex matrices. Overall, the development of Au@TiO_2 NPs represents a useful complement to existing strategies for the detection and quantification of metal oxide nanomaterials in complex matrices.

2.6 Conflicts of Interest

There are no conflicts to declare.

2.7 Acknowledgements

We thank Katie Challis and James Ranville for sp-ICP-MS analysis, Peter Eschbach and Teresa Sawyer for training and assistance with TEM imaging, Leah Minc for INAA quantification, Stephen Golledge for XPS analysis, and Makenna Pennel for assistance with troubleshooting synthetic methods. Electron microscopy facilities at Oregon State University are supported by grants from the M.J. Murdock Charitable Trust, the Oregon Nanoscience and Microtechnologies

Institute (ONAMI), and the National Science Foundation (1040588). XPS work was performed at the Center for Advanced Materials Characterization in Oregon (CAMCOR), which is supported by grants from the W.M. Keck Foundation, the M.J. Murdock Charitable Trust, ONAMI, the Air Force Research Laboratory (FA8650-05-1-5041), the National Science Foundation (0923577 and 0421086), and the University of Oregon. We are grateful to National Science Foundation Awards 1255020 and 1314109-DGE for funding.

3 Evaluation of Labeling Methods Used for Investigating the Environmental Behavior and Toxicity of Metal Oxide Nanoparticles

Alyssa R. Deline and Jeffrey A. Nason

3.1 Abstract

The analysis of the environmental behavior and toxicity of metal oxide nanoparticles (MONPs) is complicated by high metal concentrations in natural matrices. To better detect and quantify MONPs in complex samples, a variety of traceable labels can be incorporated. There are four primary categories of MONP labels: fluorescent dyes, radioisotopes, stable isotopes, and dopant/core-shell labels. This review describes each MONP labeling technique, along with its advantages and drawbacks, and provides strategies for choosing the most appropriate labeling method for a given study design.

3.2 Introduction

Metal oxide nanoparticles (MONPs) are produced and applied at the highest rate of any class of nanomaterial, inspiring a growing body of research on the potential impact of MONPs to the environment and human health[7]. The broad category of "MONP" describes any nanoparticle with an inorganic core composed of a metallic element bonded to oxide (O^{2-}) anions. MONPs are used in a variety of applications, including paints and coatings, sunscreens, chemical mechanical planarization, personal care products, antimicrobial treatments, and catalysis[8,108].

A considerable amount of work has focused on studying the toxicity of MONPs, especially the commonly produced transition metal oxides silicon dioxide (SiO_2 NPs), titanium dioxide (TiO_2 NPs), zinc oxide (ZnO NPs) and copper oxide (CuO NPs). The general trend of reported toxicities to mammalian cell lines and microbes is CuO NPs > ZnO NPs > TiO_2 NPs > SiO_2 NPs[2,13,109–114]. Nanomaterials composed of iron oxides (FeO_x NPs), cerium dioxide (CeO_2), and aluminum oxide (Al_2O_3 NPs) are typically regarded as nontoxic[114–117], but in some cases have been shown to induce inflammatory responses[118–121]. There are several relevant mechanisms of toxicity. In photocatalytically active MONPs like TiO_2, the production of reactive oxygen species (ROS) is the cause of the toxic response, while in soluble MONPs like ZnO and CuO, the response is primarily caused by the release of toxic metal ions[122,123]. MONPs that do not generate ROS or release ions can still cause toxicity through interactions with cell membrane surfaces or uptake into cells[21]. While MONP toxicity is well understood in single organism studies, more work needs to be done to understand MONP toxicity in the complex multi-organism scenarios that would more accurately represent natural systems.

MONPs have a wide range of physicochemical, structural, and electronic properties that contribute to their exposure pathway and toxicity toward organisms. Predictive models for MONP toxicity are difficult to develop, as the relevant particle properties are heavily dependent on the surrounding environment[124]. It is therefore vital that MONP behavior is studied in matrices that reflect real-world complexity; yet, this is uniquely challenging due to natural background concentrations of elements found in MONPs. Metal oxides of interest in nanotoxicology also exist in large quantities as natural minerals in the Earth's crust[125]. Additionally, some of the corresponding metallic elements (e.g., Zn, Cu) are present in organisms as elements essential for nutrition[126]. Table 3.1 summarizes the disparities between the background concentrations of metals in the environment and the expected concentrations and production rates of the most common MONPs. It is clear that MONP concentrations in most samples can be expected to be several orders of magnitude lower than concentrations of naturally occurring metals and metal oxides, complicating detection and quantification.

Table 3.1. Estimated MONP and background metal concentrations.

MONP	Background Metal Concentration	MONP Production Rate	Estimated MONP Concentration
SiO_2	270 g/kg in Earth's crust[127] 2.81 mg/L in oceans[128] 5.42 mg/L in rivers[129] 10 µg/kg in human body[130]	5,500 t/yr[8]	
TiO_2	5.0 g/kg in Earth's crust[127] 0.48 µg/L in oceans[128] 0.489-10 µg/L in rivers[129,131]	3,000 t/yr[8]	3 ng/L - 1.6 µg/L in river water[50]; 1.4 - 10.8 µg/L in WWTP effluent[50,51]
ZnO	79 mg/kg in Earth's crust[127] 0.41 µg/L in oceans[128] 0.60-30 µg/L in rivers[129,131] 2.0 µg/kg in human body[130]	550 t/yr[8]	1 - 55 ng/L in river water[51]; 0.22 – 1.42 µg/L in WWTP effluent[51]
Al_2O_3	83 g/kg in Earth's crust[127] 0.54 µg/L in oceans[128] 50 µg/L in rivers[129] 0.1 µg/kg in human body [130]	55 t/yr[8]	
FeO_x	69 g/kg in Earth's crust[127] 0.06 µg/L in oceans[128] 40-66 µg/L in rivers[129,131] 10 µg/kg in human body[130]	55 t/yr[8]	
CeO_2	32 mg/kg in Earth's crust[127] 0.0028 µg/L in oceans[128] 0.08-0.262 µg/L in rivers[129,131]	55 t/yr[8]	
CuO	79 mg/kg in Earth's crust[127] 0.25 µg/L in oceans[128] 1.48-10 µg/L in rivers[129,131] 0.1 µg/kg in human body[130]	> 150 t/yr[108]	

Background metal concentrations for rivers and oceans represent the estimated world average concentration in the dissolved fraction.

Several analytical techniques have been developed to address the challenge of studying nanomaterials in complex matrices, but limitations remain for each strategy[57,132]. Field-flow fractionation (FFF) techniques have been used to separate particles in solution by size or relative density, providing sensitive sample fractionation for the identification of nano-sized materials in real-world samples[58,59]. When coupled with a detector like inductively coupled plasma-mass spectrometry (ICP-MS), FFF allows researchers to determine the size and mass distribution of MONPs in samples like commercial sunscreens and natural waters[133,134]. Single particle ICP-MS (sp-ICP-MS) methods have been used to provide the MONP number concentration and size distribution in complex samples[135,136]. Both of these techniques are limited by the inability to distinguish engineered MONPs from natural colloids in the nano-size range, and by the confounding effects of particle dissolution[137]. Another drawback for sp-ICP-MS is that the minimum particle size for detection is in the 20-80 nm range for most MONPs, and above 200 nm for SiO_2 NPs[96]. One technique that addresses the challenge of discerning between engineered and natural colloids is the strategy of comparing isotopic ratios within the MONP to those found in the natural environment, or comparing the ratio of the MONP metal to a concomitant element[57,60,138]. However, this method of comparing elemental and isotopic ratios cannot be applied when there is no appropriate ratio to utilize, and the high background concentration of metals in the environment make small fluctuations in ratios difficult to identify with accuracy.

Visualization techniques have also been used to identify MONPs in complex matrices. Both scanning electron microscopy (SEM) and transmission electron microscopy (TEM) have been applied to visualize MONPs in a variety of samples including fibroblast cells, commercial sunscreens, and food products[104,139,140]. One drawback of using SEM/TEM techniques is that there is often a qualitative determination that an observed particle is engineered versus naturally occurring based on particle morphology, even when energy dispersive x-ray (EDX) analysis is used to verify the elemental composition of particles within a sample. In some cases, the presence of a concomitant element may be used to assist in this determination, just as elemental ratios are used in ICP-MS techniques. Another drawback is that statistically-significant particle counts are time consuming and expensive to acquire. An additional visualization technique is atomic force microscopy (AFM), which can be used to characterize the morphology and distribution of MONPs in a sample[139,141]. However, particle size distributions cannot be truly quantitatively determined using AFM alone. For SEM, TEM, and AFM analyses, it is vital that samples are prepared with care to limit the incorporation of experimental artefacts. Overall, the application of each of these quantification and visualization techniques for examining MONPs in natural systems requires considerable improvement in the ability to detect minute MONP concentrations against a complex background containing naturally occurring metals and metal oxides.

To address these limitations in current analytical methods, a traceable label can be incorporated into MONPs to distinguish them from the sample background. This allows for the sensitive detection of engineered nanomaterials in the size range of interest even when natural colloids of the same metallic composition are present within the sample. To be effective, the presence of the label cannot change the relevant properties and behavior of the MONP, and it must enable the quantification and/or visualization of the engineered MONPs at environmentally relevant concentrations. In this critical review we describe existing MONP labeling techniques in detail, analyze the benefits and disadvantages of each, identify gaps in the current body of literature, and provide guidelines for choosing the most appropriate labeling method.

3.3 Summary of Labeling Methods

There are four major classes of MONP labels: fluorescent dyes, radioisotopes, stable isotopes, and dopant/core labels. Here we present relevant synthetic and analytical methods, notable examples of use and detection, potential impacts on MONP properties, and important experimental design considerations for each category of label. This review focuses on MONP labeling applications relevant to toxicological impact and environmental transport. While additional procedures have been developed for applications in biomedical imaging and nanomedicine, they are not included in this review. This is because these MONPs are often functionalized for biocompatibility and targeted transport to a specific organ, making them unsuitable for toxicological studies where the properties need to be similar to manufactured MONPs that do not undergo such functionalization[142].

3.3.1 Fluorescent Dye Labels

The most common MONP labeling technique is the incorporation of a fluorescent dye. There are several synthetic routes that are used to produce fluorescent dye labeled MONPs, as summarized in Figure 3.1. One method is to covalently attach a fluorescent dye to the surface of a previously synthesized or purchased MONP using an aminosilane coupling agent. SiO_2, TiO_2, CeO_2 NPs, and ZnO NPs labeled with fluorescein isothiocyanate (FITC) have each been prepared using this method[114,143]. MONPs can also be doped with fluorescent dyes throughout the particle structure using a modification of existing sol-gel[66,143] or microemulsion[144,145] synthetic processes. Here, the dye is mixed into the synthetic solution that containing the metal-alkyl precursor. Optionally, the dye-doped MONP can then be coated with an undoped metal oxide shell[67,142,143]. Another method of producing core@shell fluorescent MONPs is the amino acid-catalyzed seed regrowth technique (ACSRT), in which amino acids drive the production of densely doped seeds, then additional metal-alkyl precursor is added to form a shell[146–148]. Each of these dye-doping and core@shell methods have been used primarily to label SiO_2 NPs, but could be extended to other MONPs. While the surface attachment approach has the benefit of applicability to commercially available MONPs, it introduces both the silane coupling agent and the fluorescent dye to the surface of the MONP of interest, which could potentially impact particle surface properties or lead to the premature release of dye. Coating fluorescently-doped SiO_2 seeds with an unlabeled SiO_2 shell has been shown to limit the release of dye, as has the employment of an amino acid catalyst in the hydrolysis reaction [147–149]. A combination of these two approaches resulted in fluorescent dye leakages of below 5% after a 72 hour exposure to high ionic strength media[147].

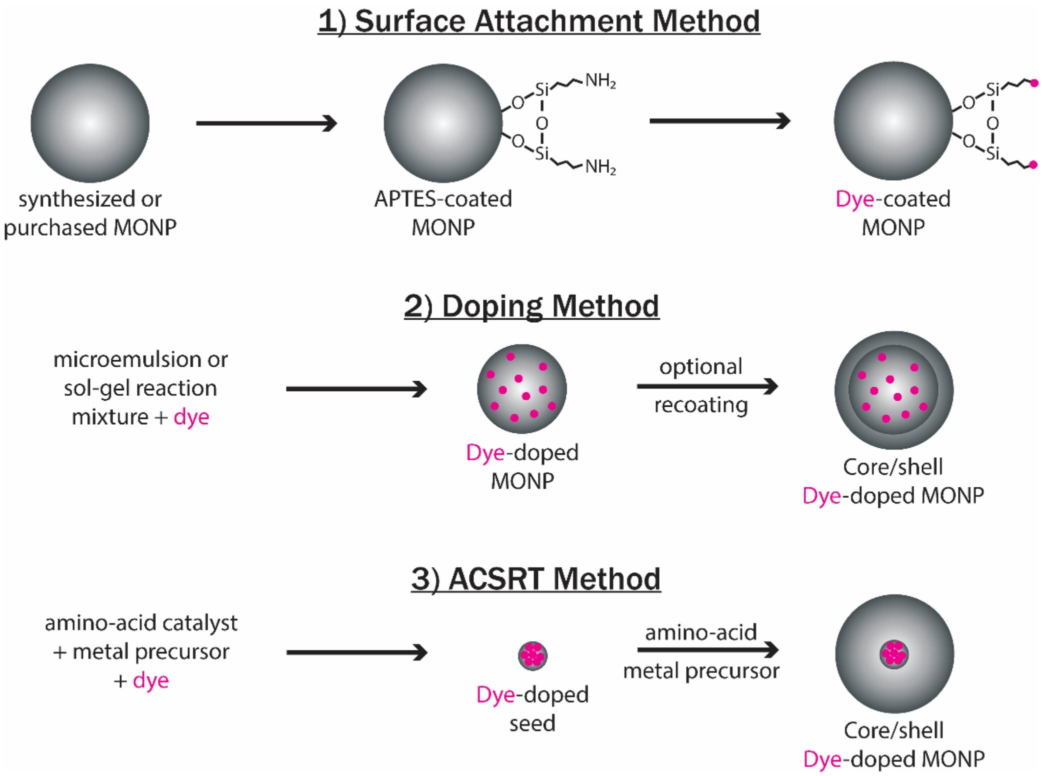

Figure 3.1. Synthetic techniques used to prepare fluorescent dye-labeled MONPs.

In addition to the dye incorporation method, the dye itself can affect MONP properties and detection. Multiple classes of fluorescent dyes have been employed in MONP labeling, most notably fluoresceins[63,114,147,150], rhodamines[67,146,147], and perylenes[142,151,152]. Each dye has a different molecular size, charge, and fluorescence spectrum, all of which hold relevance to the properties and detection of the labeled MONP. The optical properties of several common fluorescent dyes have been summarized by Resch-Genger et al.[153]. Photostability varies between dyes, and the chosen dye must remain stable throughout the duration of a study[142,147]. Temperature stability is also important to consider, as it can limit the MONP crystal structures that are able to be formed after the dye has been incorporated. For example, rutile TiO_2 could not be formed using the embedded dye synthetic strategies while keeping the dye intact, as the heat treatments required to form the rutile structure occur at temperatures much higher than the 200-300°C required to degrade the dye[154,155].

Fluorescently-labeled MONPs have been used to study MONP behavior in a variety of complex systems, including activated sludge biomass[67,145], skin cells and collagens[149,156], and HeLa cells[142,151,157,158]. The most common techniques for visualization and quantification of dye-labeled MONPs are fluorescence spectrophotometry[66,67,159], fluorescence microscopy[63,142,145,152], and confocal microscopy[114,142,146,151]. In one notable study by Xia et al., fluorescent labels were attached to ZnO, CeO_2, and TiO_2 NP surfaces in order to study the subcellular localization of MONPs using confocal microscopy[114]. The FITC-labeled CeO_2 and TiO_2 NPs could be visualized in the caveolae of bronchial epithelial cells and the lysosomes of macrophage cells, despite neither particle type inducing toxic effects to the cells. For ZnO NPs, the FITC-labeled particles could be observed in the caveolae of the bronchial epithelial cells, but not in the lysosomes of macrophage cells, despite inducing toxic effects in both cell types. However, clumping of the macrophage lysosomes was apparent after exposure to ZnO NPs, and Zn^{2+} ions could be visualized in the lysosomes through the use of the Zn^{2+}-sensitive Newport Green indicator, indicating that any ZnO NPs taken up into the lysosomes were likely dissolving and losing the FITC label. Experiments were also performed using Zn^{2+} added as $ZnSO_4$, which showed Zn^{2+} localization within the same compartments as Zn^{2+} added as ZnO NPs. One major drawback of this use of fluorescent dye labeling is that it is impossible to discern the Zn^{2+} that was taken up as ions that had been released into cell media through dissolution, from the Zn^{2+} that was released from the ZnO NPs as they dissolved within the compartment of interest. It is possible that ZnO NPs synthesized using a core/shell synthetic strategy could maintain the fluorescent label long enough to be visible even as they become partially dissolved. Additionally, while this study was rigorous in the inclusion of free FITC controls and $ZnSO_4$ experiments, there was no comparison of the dissolution rates or surface chemistry of the FITC-labeled MONPs to their unlabeled counterparts. This is especially important when considering that the FITC label was attached to the MONP surfaces through silane linkages, introducing new inorganic and organic components to the surface of the particles that could affect interactions with the surrounding media and tissue. Despite these limitations, this study provides a useful example of the potential power of fluorescent dye labeling methods in elucidating complex toxicological mechanisms.

The primary disadvantage of fluorescent labeling is the relatively high limit of detection provided by the method. Reported limits of detection are as low as 26 µg/L in distilled water[66], but as sample complexity increases, autofluorescence of the background can increase the limit of detection to 77 µg/L in seawater[66] and 500 µg/L in synthetic wastewater[67]. Limits have been reported as high as 5 mg/L[150], and in each case the detection limits can be expected to increase with exposure time due to dye release and photobleaching[160]. Light penetration is limited in intact tissues, which may need to be sliced prior to imaging[160]. The fluorescent label also limits the use of other analytical assays to those that do not have an absorption band overlap with the dye. For example, the silicomolybdate titration for dissolved silica species[161] and several colorimetric assays for reactive oxygen species production[21] cannot be used on fluorescently-labeled MONPs. Additionally, some dyes may be degraded *in vivo*, either through exposure to the acidic environments present in some subcellular compartments, or through enzyme-catalyzed degradation processes[114,162].

However, fluorescence labeling has several major benefits. The preparation of dye-labeled MONPs and the corresponding sample analysis have been consistently reported as less expensive when compared to other labeling methods[153,159] Tools for automating data analysis have also been developed, including the Particle_in_Cell-3D tool for confocal microscopy images that allows researchers to make rapid comparisons of cellular uptake[151]. Overall, the wide variety of synthetic methods and characterization described in the literature, as well as the commercial availability of fluorescent dyes and dye-labeled MONPs, make this labeling technique one of the most facile to apply.

3.3.2 Radioactive Isotope Labels

Another MONP labeling technique is the assimilation of a radioactive isotope. A summary of radioisotopes used in the study of MONP transport and toxicity is included in Table 3.2. The three most common methods of producing radiolabeled MONPs are neutron activation, ion bombardment from a cyclotron source, and the use of radioactive precursors. These are summarized in Figure 3.2. It should be noted that silicon and aluminum do not have useable radioisotopes that can be prepared through direct activation from neutron or ion bombardment[163]. These MONPs can instead be labeled through the activation of ^{18}O to form ^{18}F [164], through ^{7}Be-recoil labeling[165], or through the addition of another material through doping or core/shell methods[150,166–168].

Table 3.2. Radioisotopes used in study of MONPs.

Radioisotope	Production Method	Half-Life	Radioactivity of MONPs, MBq/mg	Detection Method	Ref.
SiO_2					
^{7}Be	cyclotron, recoil	53.29 d	1	γ-spectrometry	165
^{14}C	^{14}C precursor	5730 yr	8.5×10^{-6}	accelerator mass spectrometry	166
^{56}Co	^{56}Co precursor	77.26 d	1.28	γ-spectrometry	167
^{110m}Ag	^{110m}Ag precursor	249.8 d	9.48×10^{-4}	γ-spectrometry	150
^{198}Au	neutron activation	2.69 d [169]	16.3	γ-spectrometry	168
TiO_2					
^{7}Be	cyclotron, recoil	53.29 d	0.30	γ-spectrometry	74
^{48}V	ion bombardment	15.97 d	0.071	γ-spectrometry	73
^{48}V	ion bombardment	15.97 d	1	γ-spectrometry	170
^{48}V	ion bombardment	15.97 d	3.70	γ-spectrometry	74
^{48}V	ion bombardment	15.97 d	1.0 - 2.35	γ-spectrometry	171–173
^{48}V	ion bombardment	15.97 d	not reported	liquid scintillation counting	174
^{18}F	ion bombardment	109.8 min	0.700	PET	75
^{44}Ti	^{44}Ti precursor	60.4 yr	0.01	γ-spectrometry	74
^{45}Ti	^{45}Ti precursor	3.08 h	135	dose calibrator	74
ZnO					
^{65}Zn	neutron activation	244 d	not reported	γ-spectrometry	175
^{65}Zn	^{65}Zn precursor	244 d	not reported	γ-spectrometry	176
^{65}Zn	neutron activation	244 d	not reported	γ-spectrometry	177
FeO_x					
^{55}Fe	^{55}Fe precursor	2.74 yr	not reported	liquid scintillation counting	178
^{59}Fe	neutron activation	44.5 d	not reported	γ-spectrometry	179
^{59}Fe	^{59}Fe precursor	44.5 d	not reported	whole body counting	180
^{56}Co	ion bombardment	77.26 d	0.113	γ-spectrometry	181
^{125}I	^{125}I precursor	59.43 d	1.85	γ-spectrometry, DAR	182
CeO_2					
^{139}Ce	diffusion	137.6 d	1.242	γ-spectrometry	183
^{139}Ce	ion bombardment	137.6 d	0.975	γ-spectrometry	183
			0.150		105

^{141}Ce	neutron activation	35.2 d	0.052	γ-spectrometry	184
^{141}Ce	ion bombardment	35.2 d	0.100	γ-spectrometry	185–187
^{141}Ce	^{141}Ce precursor	35.2 d	not reported	γ-spectrometry	177
^{141}Ce	neutron activation	35.2 d	23	γ-spectrometry	188
^{18}F	^{18}F precursor	109.8 min		PET	
Al_2O_3					
^{18}F	ion bombardment	109.8 min	2.31	PET	164
^{13}N	ion bombardment	9.97 min	1.85	PET	189

In the case of neutron activation, post-synthesis MONPs are directly activated through exposure to a neutron flux from a reactor source. This allows the study of many commercially available MONPs, with the exception of TiO_2 NPs due to the lack of appropriate products formed by Ti[190]. Some temperature increase of the materials can be expected during irradiation, causing MONP aggregation or the degradation of some surface coatings, but this can be mitigated by minimizing the neutron flux and amount of material being irradiated[105]. Low increases in the specific radiation activity of the MONPs are unlikely to modify the activities and behavior of the MONPs themselves, but increased radiation exposure could have a confounding effect when determining toxicity in some cases[105].

Direct activation from a cyclotron source can also be applied to commercial or synthesized MONPs. Ion bombardment is more likely than neutron activation to alter material properties through sintering and phase transformations, due to high temperature increases from the Coulomb interaction between the ion flux and the lattice[103,170]. For example, the ratio of the rutile crystalline phase to the anatase phase present in TiO_2 NPs has been shown to increase after irradiation under certain high activity conditions, a structural transformation that typically occurs above 650°C[103,105]. Holzwarth et al. have shown that thin layers of TiO_2 NPs exposed to protons at energies of 23.5 MeV with a beam current of 5-10 µA will achieve a useful level of radioactivity for detection, without undergoing any thermally-caused changes to the NPs[103]. Cyclotron irradiation can be used to produce positron emitting MONPs labeled with ^{18}F for any material that can be enriched with ^{18}O [75,164]. These labeled materials can be imaged in real-time 3D using positron emission tomography (PET). However, the short half-life of ^{18}F (109.8 min) makes this technique inappropriate for long term-studies. Cyclotron sources are also used for recoil labeling, in which MONPs are irradiated in a mixture with ^{7}Be-forming lithium compounds[74,165]. The ^{7}Be produced is at a high enough energy to become implanted in the MONP structure.

If no cyclotron or nuclear reactor is accessible, a radioactive precursor can be used to label MONPs. This can be accomplished through the use of a radioactive precursor in synthetic procedures, giving researchers more control over MONP properties than direct activation. It can also be used in a low-temperature diffusion process to label MONPs post-synthesis, allowing commonly manufactured MONPs like P25 TiO_2 NPs to be radiolabeled without direct activation[74]. Radioactive precursors are highly expensive, and not all radioisotopes are commercially available or easy to produce, limiting the possible applications of these procedures.

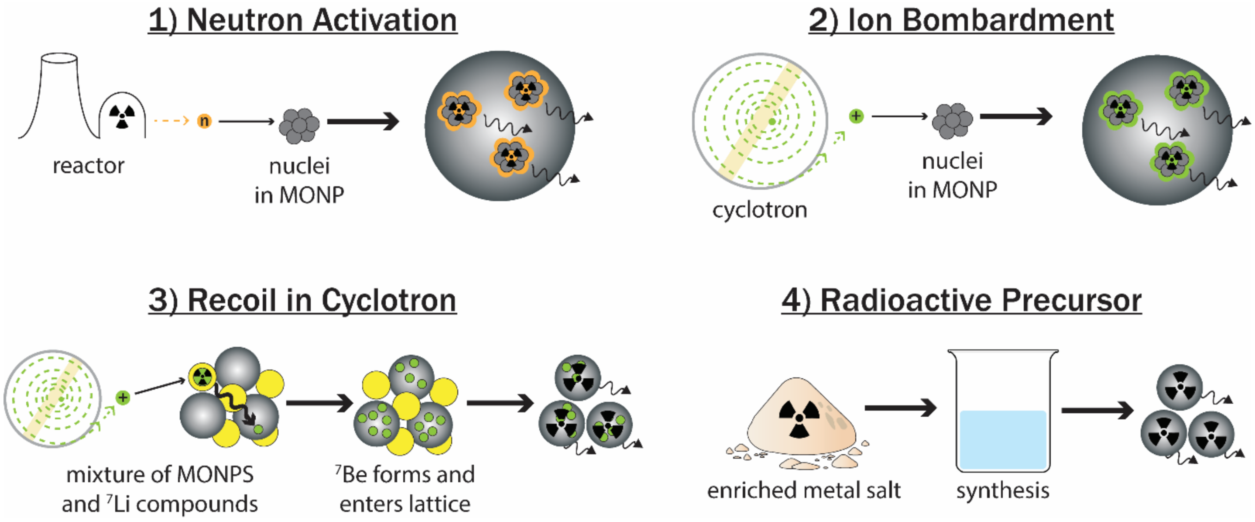

Figure 3.2. Techniques used to prepare radiolabeled MONPs.

Radiolabeling is especially useful for complex samples that require extensive acid digestion procedures for ICP-MS analysis. Radiolabels can be quantified using several techniques that require limited sample preparation. Scintillation counting allows for the radioactivity of multiple isotopes to be quantified within a single sample through the reaction of the emitted radioactive particles with a fluorescent material (the “scintillator”), creating pulses of light at wavelengths specific to the energy of the emitted particle. This is applicable to α-, β-, and γ-emitting radioisotopes. The quantification of γ-emitting radiolabels can also be achieved through γ-spectrometry using either a scintillation counting detector, or a detector composed of a semiconductive material, in which the emitted radiation causes the promotion of electrons to the conduction band. Ultimately, the limit of detection for a radiolabeled MONP will depend on the resolution and detection efficiency of the detector, the potential interferences from the sample matrix interacting with the emitted particles, and the radioactivity of the prepared MONPs[191]. The resulting radioactivities of labeled MONPs prepared for various studies of behavior and toxicity have been included in Table 3.2 to provide a relative comparison of the radioactivity imparted by different radiolabeling strategies.

These advantages related to limited sample preparation have made radiolabeling especially useful for biological studies. Kreyling et al. employed ^{48}V-labeled TiO_2 NPs ([^{48}V]TiO_2 NPs) in a series of three studies to compare the biodistribution and biokinetics of TiO_2 NPs (given to) rats through three different exposure pathways: intravenous, oral, and inhalation[171–173]. Interestingly, the amount of [^{48}V]TiO_2 NPs retained in the syringes used for NP application in each study varied considerably across samples, and up to 50% of the nominal dose was found to be retained in the syringes. The actual applied dose was able to be quantified by directly measuring the amount of [^{48}V]TiO_2 NPs remaining in the syringe using γ-spectrometry, which does not require any rinsing or further treatment of the syringes that could confound the measurement. This determination of the actual applied dose, in addition to the quantification of [^{48}V]TiO_2 NPs across the entire rat body and in excretions, allowed for a complete mass balance to be developed. The resulting values were also corrected for the potential release of the ^{48}V label through the use of complementary studies that identified differences in behavior between ionic and particulate ^{48}V. These studies used a highly quantitative approach made possible through radiolabeling to show that intravenous injection of NPs does not result in the same biological behavior as other routes of exposure, and should not be used as a surrogate experimental method.

Radiolabeling methods have several limitations, including the requirement of access to controlled laboratory space and specialized equipment. The safety precautions that must be taken in handling radioactive materials often limit characterization of labeled MONPs to techniques that require a very small amount of material. In some cases, the specific activity level of labeled materials may be high enough to influence toxicity toward an organism through exposure to radiation; it is therefore recommended that additional toxicological studies are performed in tandem with unlabeled materials when the specific activities and NP doses are high. Finally, radiolabeling techniques are expensive. Synthetic costs using radioactive precursors were reported as fifteen times higher than the cost of fluorescence labeling for SiO_2 NPs[150].

The primary advantage of radiolabeling is that it provides the lowest detection limits of any labeling method with very little sample preparation required for analysis. Detection limits depend on the specific activities of the radiolabeled MONPs and the type of detector used, but these values typically fall in the range of pg/L to ng/L. Radiolabels can be directly applied to commercial NPs, allowing researchers to study the most environmentally relevant materials. Quantification can be achieved along with real-time imaging, providing important information about the mechanisms of MONP uptake, metabolism, and toxicity.

3.3.3 Stable Isotope Labels

In stable isotopic labeling, MONPs are labeled through enrichment with a stable isotope of the relevant metal that occurs at a low abundance in the environment. Many stable isotopes have been successfully employed in the study of MONPs, as summarized in Table 3.3. The preparation of MONPs enriched with a stable isotope is achieved through synthesis with an enriched precursor material. Enriched precursors are commercially available as soluble salt complexes, solid metals, or solid metal oxides. In the cases of enriched metals and metal oxides, the material must be broken down using acid digestion prior to MONP synthesis. Once a soluble metal isotope solution is achieved there is no limit to the customization (e.g. shape, size, crystal structure, surface coating) that can be applied to an isotopically-labeled MONP. The main limitation inherent in the preparation of MONPs labeled with stable isotopes is that commonly manufactured MONPs cannot be effectively labeled with stable isotopes post-synthesis.

MONPs labeled with stable isotopes are most often quantified using ICP-MS, which may also be coupled to FFF or other sample fractionation techniques. The limits of detection for these studies will depend on the relative abundance of the labeling isotope, the presence of any interfering complexes in the sample matrix, and the resolving precision of the instrumentation. To identify the amount of the labeling isotope that corresponds to the MONPs, the concentration of the isotope in the background matrix must be determined and subtracted. This can be achieved by measuring the labeling isotope directly, or by measuring another isotope of the same metal and using the natural ratio of the isotopes to correct in calculations. In cases where the sample matrix is heterogeneous, it may be preferable to measure a non-labeling isotope in each individual sample, as opposed to measuring the labeling isotope in a smaller set of “background” samples. Using labeling isotopes with lower abundance will increase detection sensitivity, but these precursors are more expensive. Isotopic labeling studies also require that attention is paid to potential isobaric and polyatomic interferences that affect the determination of the isotopic ratio within a sample. For example, matrices high in sulfates can interfere with the detection of multiple isotopes of Ti, while Ce measurements are impacted by the presence of neodymium[104,192,193]. Polyatomic interferences for each element have been summarized by May and Wiedmeyer[194].

Quantifying isotopic ratios within a sample requires high instrumental precision in resolving peaks between two adjacent isotopes. Isotopically-labeled MONPs can be quantified at environmentally relevant concentrations using conventional quadrupole ICP-MS instruments alone, but sensitivity can be increased even further through the use of high resolution multi-collector ICP-MS (MC-ICP-MS) instruments[193,195]. MC-ICP-MS instruments are much more expensive than conventional ICP-MS instruments, but may be especially useful in cases where organisms are chronically exposed to very lose doses of MONPs.

In addition to quantification using ICP-MS, isotopically-labeled MONPs can be visualized within a sample using time-of-flight secondary ion mass spectrometry (ToF-SIMS)[196]. In a study of ZnO NP uptake and toxicity in HaCaT cells, the luminescence of ZnO NPs and the use of a stable ^{68}Zn label allowed for both confocal laser scanning microscopy (CLSM) and ToF-SIMS to be used within the same study. ToF-SIMS provided a two dimensional image free from background interference, which was then compared to the three dimensional CLSM images. It was determined that Zn^{2+} ions from ZnO NPs are absorbed and transported into the cytoplasm and nuclei, and that the relative amounts of intracellular Ca^{2+} and K^+ are affected by the ZnO NP dose. Laser ablation ICP-MS (LA-ICP-MS) can also be used for 2D imaging of samples containing isotopically-labeled MONPs. However, this technique offers spatial resolution of only 5-20 μm, while ToF-SIMS can be operated to provide sub 100 nm resolution[160,197].

Stable isotopic tracers are often used in studies of ZnO and CuO NPs, due to the labeling method's effectiveness for MONPs that dissolve throughout the course of the experiment. Ions released directly from the MONPs will still bear the isotopic label and can be quantified using the same methods of analysis used for the MONPs[198]. It is also possible to use more than one stable isotope in the same study to gain a better understanding of the localization of released ions versus the nanomaterial. Laycock et al. used a combination of ^{68}ZnO NPs and ^{64}Zn^{2+} ions incubated in soil from 1-12 months to study uptake in earthworms[199]. As the soil incubation time increased, the amount of Zn from all forms increased in the pore water, resulting in higher bioaccumulation efficiencies. There was no discernable difference between the relative amounts of ^{68}Zn and ^{64}Zn in the different compartments (soil, water, and organism) of the experiment, which supports the hypothesis that the ^{68}Zn was taken up in the ionic form after the ^{68}ZnO NPs dissolved in the soil media. One method to help determine whether this is the case would be to extend an approach developed by Merrifield and Lead, in which multiple isotopic labels were embedded in the same nanoparticle[200]. In this study, a three-layer silver nanoparticle was synthesized with two different stable isotopes labeling the core (^{109}Ag) and the shell (^{107}Ag). These were separated by a layer of gold that was added to prevent core dissolution, ensuring that only the ^{107}Ag from the NP shell would be exposed to organisms in the ionic form. Comparing the concentrations of the two silver isotopes in both the exposed organisms and the media would allow for the determination of the relative contributions of the ionic versus particulate silver. Although this method has only been applied to silver nanoparticles, the same approach could be extended to soluble MONPs like ZnO NPs.

The primary disadvantage of stable isotopic labeling is that the manufactured MONPs that are the most environmentally relevant to study cannot be effectively labeled after purchase. One possible solution to this problem is the use of the “reverse labeling” procedure developed by Croteau et al.[201,202]. In one study, freshwater snails were chronically exposed to ^{65}Cu isotopes until the isotopic ratios within the snail tissues was altered, effectively eliminating the metal background from the experiment[201]. This enabled researchers to measure the uptake of Cu, which naturally primarily contains the isotope ^{63}Cu, from particles that had been collected from a river impacted by acid mine drainage. The naturally aged complex colloids composed of a mixture of Al and Fe oxides with sorbed Cu were able to be tested directly on the organisms. A similar approach was used to study Zn uptake in snails from natural particles collected from two acid mine drainage impacted rivers[202]. The authors were able to show that a higher strength of Zn sorption to the collected particles resulted in lower assimilation within the organisms. This reverse labeling technique is effective for biological studies involving essential elements like Zn, Cu, and Fe, which will be easily assimilated into the organism. It remains to be seen whether this approach can be extended to other MONPs comprised of metals that are not essential elements. Another potential drawback is that the media that the experiment is performed in must be free of the background metal. Thus, the reverse labeling approach would be difficult to apply in experiments requiring the use of complex natural media. This issue could be mitigated through control experiments identifying differences in the fate and uptake of the element of interest from the media alone when compared to the MONPs.

Despite this drawback, there are major advantages to stable isotopic labeling. MONPs can be detected at very low, environmentally relevant concentrations. Stable isotope labels are the most enduring of any technique, are measurable even in ions released from dissolution, and do not have the equipment and safety limitations of radioisotopes. Additionally, there is likely to be no impact on MONP properties, although extra care must be taken not to introduce artefacts during the sample preparation required for quantification.

Table 3.3. Stable isotopes used in study of MONPs.

Stable Isotope (% Rel. Abundance)	**MONP Studies Employing Stable Isotope**	**Reported Limits of Quantification**
TiO_2		
^{47}Ti (7.5)	• Bioaccumulation in mussels[72]	8.6 ng/L in mussels[72]
ZnO		
^{64}Zn (48.6)	• Uptake of Zn^{2+} vs ZnO NPs in earthworms using multi-isotope approach[199]	
^{67}Zn (4.1)	• Uptake in snails[203,204] • Uptake in endobenthic organisms[205]	< 15 µg/g in snails[204]
^{68}Zn (18.6)	• Dermal absorption of ZnO NPs from sunscreens in mice and humans[206–210] • Uptake and cytotoxicity to human skin cells[196] • Bioavailability of ZnO NPs vs. bulk Zno vs. Zn^{2+} ions to aquatic organisms[198] • Uptake and elimination for bulk vs. nano-sized ZnO[211]. • Evaluation of cost-effectiveness for Zn isotopic labels[212] • Up take of Zn^{2+} vs ZnO NPs in earthworms using multi-isotope approach[199]	5 ng/g[212] 175 ng/g in blood[207]
CuO		
^{65}Cu (30.8)	• Synthesis and detection of spherical and rod-shaped ^{65}CuO NPs[213] • Uptake of CuO NPs vs. Cu^{2+} in freshwater worms from aquatic and sediment exposures[214,215] • Toxicity and bioaccumulation in snails[216]	10 ng/g in snails[213]
FeO_x		

^{57}Fe (2.14)	• Exchange of atoms between goethite nanorods and dissolved Fe^{2+} [217,218] • Detection of $^{57}Fe@SiO_2$ NPs in river sediment slurry[219]	7.8 µg/L Fe in river sediment slurry[219]

3.3.4 *Dopant and Core/Shell Labeling*

The final category of MONP labeling techniques is the use of dopants and core/shell labels.

In the case of doping, MONPs are synthesized with another metal that is rare in the samples of interest replacing a fraction of the metal present in the MONP lattice structure. It should be noted that some radiolabels that feature an element not present in the unlabeled MONP, e.g. those prepared through ^{7}Be recoil labeling, are also effectively labeled with a dopant. To prepare dopant-labeled MONPs featuring another nonradioactive label, existing sol-gel synthesis methods can be altered by adding a soluble salt of the labeling metal to the MONP metal-alkyl precursor solution. The amount of dopant present in the final labeled MONP can be adjusted by altering the stoichiometric ratio of the labeling metal to the primary metal in the solution[70,220]. ICP-MS or ICP-optical emission spectrometry (ICP-OES) can be used to quantify the amount of labeled MONPs through the known ratio of the traceable metal to the MONP metal. TiO_2 NPs have been doped with the rare earth elements La and Ce, resulting in limits of detection as low as 16.8 µg Ce/L using ICP-OES[70]. Only a small fraction of Ti atoms needed to be replaced for this degree of sensitivity: the ratio of Ce and La to Ti was varied from 0.005 to 0.03 during synthesis. TiO_2 NPs have also been doped with Nb to examine how bioconcentration factors change as a function of surface chemistry[174]. It is important to consider that the dopant concentration can impact particle properties like the specific surface area and photoreactivity, with the highest enhancements of photoreactivity occurring at dopant concentrations below 1% by weight[71,221]. Dopants have also been shown to preferentially appear on the surface of the MONPs as opposed to the bulk, where they will interact directly with the surrounding media[70]. It is important to monitor the extent to which the electronic and surface properties of the MONPs are altered by dopant labels, as these can affect their behavior and toxicity in experimental studies[221].

In core/shell labeling, a variety of materials have been incorporated as the MONP labels, as summarized by Figure 3.3. The label is typically another metallic nanoparticle, which is then coated with the MONP material. One core material that can be used is quantum dots (QDs), which have the useful luminescent properties of a fluorescent dye label with more long-term stability. The QDs most appropriate for MONP labeling applications are typically composed of CdSe or CdTe NPs that range from 1-6 nm in diameter[153]. QDs can be synthesized or commercially purchased and then coated with MONP materials using microemulsion, sol-gel, or amino acid driven synthetic methods. It is important to ensure the shell prevents the release of QDs or the ions present in them, as they will have different behaviors and toxicities when compared to the MONP-coated QDs[222,223]. In addition to quantification using fluorescence-based techniques, the core materials in QD-labeled MONPs can also be quantified by using ICP-MS. SiO_2-coated CdSe/CdS/ZnS QDs were used to study the potential impacts of oral exposure to SiO_2 NPs in a mouse model, and the known ratio of Cd:Si was used to confirm via ICP-MS that the fluorescent particles imaged in the liver came from the labeled MONPs and not the sample background[146].

Noble metal nanoparticles have also been used for core labeling. SiO_2 NPs have been labeled with an AgNP core, while TiO_2 NPs have been labeled with an AuNP core[159,224]. In the case of AgNP cores, dissolution of the core label can be a concern: Ag^+ ions began to be released from the labeled SiO_2 NPs after 20 days of storage in deionized water[159]. While a variety of synthetic methods for core/shell MONPs featuring noble metal NP cores have been presented, most often these procedures were developed to create MONPs with enhanced catalytic properties and will need to be adjusted to mitigate these effects[88,225–227]. Once the MONP shell is deposited onto the noble metal core, solvothermal treatments may be necessary to achieve the MONP crystal structure desired. Here, it is necessary to take steps to prevent any thermally-induced structural changes to the AuNP or AgNP core, which for rutile TiO_2 can be achieved by adding an additional SiO_2 shell that is later removed through etching[88]. ICP-MS is typically used for quantification, resulting in a reported limit of detection of 24 μg/L for $Ag@SiO_2$ NPs[159]. $Au@TiO_2$ NPs have been accurately quantified at levels of 1.5 μg Ti/L in deionized water using ICP-MS and 750 μg Ti/L in a river water-sunscreen mixture using ICP-OES[224]. Single particle ICP-MS can also be applied as a characterization tool and quantification strategy. In addition, $Au@TiO_2$ NPs have been quantified in activated sludge using instrumental neutron activation analysis (INAA), with reported limits of detection and quantification of 16.8 mg Ti/kg sludge and 25.8 mg Ti/kg sludge, respectively[224]. The core/shell labeling approach allows INAA quantification to be extended beyond facilities with a reactor on-site, as the experiment can be performed prior to irradiation and then samples can be transported for analysis.

Finally, one novel and interesting core-labeling method is the encapsulation of DNA barcodes within a SiO_2 shell. To achieve this, SiO_2 NPs are prepared with positively-charged functional groups on the surface. DNA is then adsorbed onto the positively-charged SiO_2 surface, and encapsulated in an SiO_2 shell using a sol-gel process[228]. The encapsulated DNA has been shown to be stable in the presence of ROS and in temperatures up to 120°C. The DNA can be released using an etching agent, and quantified using quantitative polymerase chain reaction (qPCR) methods at concentrations as low as 100 ng Si/L[229]. This technique has been used to study SiO_2 colloid transport within wastewater treatment systems, and the transfer of SiO_2 colloids between trophic levels[229,230]. When digital particle PCR (dpPCR) is used for quantification, individual SiO_2 NPs can be detected and counted, resulting in a limit of detection of approximately one particle per μL solution[231].

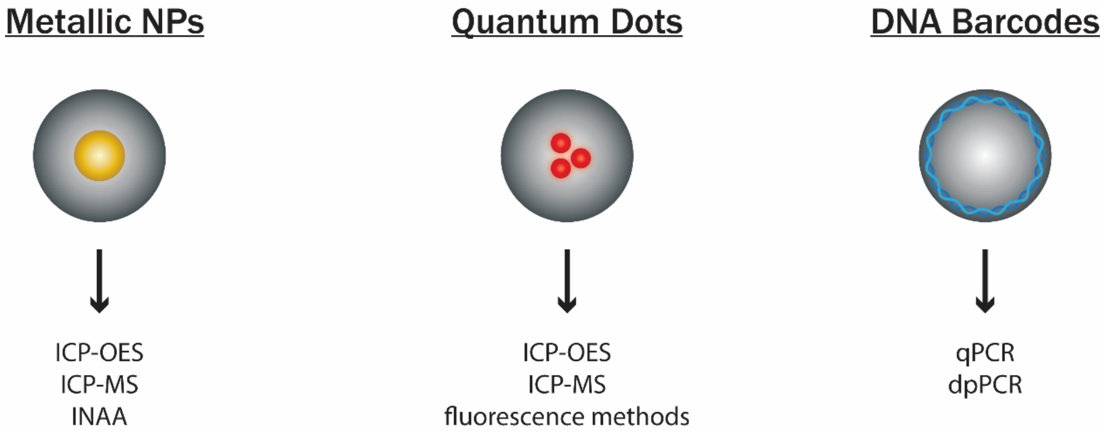

Figure 3.3. Label materials and quantification techniques used for core-labeling strategies.

Doping and core/shell labeling techniques provide unique advantages and disadvantages. Metallic labels are more stable than fluorescent dyes, but can potentially be released as ions in the cases of dopants on the MONP surface, or core labels comprised of materials susceptible to dissolution. With the exception of DNA barcode labels, dopant and core/shell labeling techniques are more inexpensive than isotopic labeling strategies, while some of the same quantification techniques (ICP-MS, INAA) can be employed. Some core/shell systems are also compatible with sp-ICP-MS techniques, which can provide number concentrations and size distributions for the core particle within a complex sample. The primary disadvantages are that these techniques cannot be applied directly to commercially available nanoparticles, and that some properties of the unlabeled MONP may be affected. These include photocatalytic activity for both dopants and core labels, and density for core labels.

3.4 Properties and Characterization of Labeled MONPs

A critical step in employing any labeling method is the proper characterization of the resulting labeled MONPs and comparison to their unlabeled counterparts. Without this characterization, it remains uncertain whether the labeled MONP's behavior determined within a study can be truly representative of the MONP. The MONP properties that could potentially be altered through the incorporation of a label, resulting in changes to behavior, are discussed in detail in this section and summarized in Table 3.4.

The defining property of nanomaterials that has given rise to concern about their potential environmental implications is their size. Nanoparticles of different sizes exhibit differences in cellular uptake and localization, as well as differences in the overall toxicity to a variety of organisms[232–235]. Isotopic labeling featuring the use of an enriched precursor is unlikely to alter MONP size, since identical synthetic procedures can be used for both the labeled and unlabeled MONP. However, synthetic procedures for labeling using dopants, core/shell structures, and fluorescent dyes will need to be optimized to ensure that the size of the labeled MONP corresponds to the size of interest for the unlabeled MONP. In the case of direct radioactivation, exposure to extreme temperatures during irradiation could potentially impact the MONP structure and alter the size. Primary particle size can be measured using electron microscopy techniques. The hydrodynamic diameter, which takes into account MONP agglomeration and solvation, can be determined using dynamic light scattering (DLS) or nanoparticle tracking analysis (NTA).

In some cases, the size of the individual crystallites that compose MONPs may differ from the primary particle size. Crystallite size can be measured using x-ray diffraction (XRD) or TEM analysis. The crystal structure of the MONPs can also be measured using XRD or determined using selected area electron diffraction (SAED) performed within TEM analysis. Differences in the crystallite size or crystal structure between the labeled and unlabeled MONPs will impact the surface area and photocatalytic activity of MONPs[22,23]. Characterizing these differences is especially relevant for doped MONPs, where changes in the elements present in the lattice structure give rise to differences in atomic spacing that can impact crystallite size. Alterations to the crystalline properties are also likely to occur for labeling techniques that expose the MONPs to different temperature treatments than their unlabeled counterparts. This includes labels like fluorescent dyes that may require differences in the synthetic temperatures to prevent dye degradation, and direct radioactivation techniques that may expose MONPs to high temperatures.

Closely related to size is MONP surface area, which can affect toxicity through its relationship to photocatalytic activity, ROS generation, and dissolution kinetics[236,237]. The specific surface area

(SSA) is commonly determined using Brauner-Emmett-Teller (BET) analysis, which uses the measurement of the physical adsorption of small nonreactive gas molecules to a dry nanopowder, allowing for the porosity of the particles to be included. The SSA measured via BET analysis does not take into account the agglomeration state of the MONPs once they are in solution. Changes to this parameter would most likely be brought about by dopant, fluorescent dye, and core/shell labels, which are the most likely to impact the porosity of the MONPs due to the incorporation of labeling compounds that differ in size and properties from the MONP materials. Surface area can also be estimated using size measurements from DLS or electron microscopy and the density of the bulk material[238].

Another group of properties that must be examined when labeling techniques are employed are those that comprise MONP surface chemistry. This includes the functionalization of MONPs with a stabilizing ligand, the surface charge, and the relative hydrophobicity or hydrophilicity of the surface. These surface properties have an important impact on the bioavailability and toxicity of nanomaterials due to the impact on aggregation state, dissolution rate, adsorption of natural organic matter, and interactions with cells and organisms[89,90,235,239,240]. A variety of surface coatings are used on MONPs to impart stability through electrostatic or steric repulsion, to enhance dispersion within an MONP-enabled product, or to control the MONP reactivity. For some MONP labeling strategies, the incorporation of a functionalized surface coating will not be possible. This includes the surface attachment of fluorescent dyes to MONPs, which will prevent another functional ligand from being attached to the surface. Additionally, direct activation techniques for radiolabeling are generally not applied to MONPs with a surface coating, as the coating is likely to be altered and also impact the amount of radioactivity imparted to the metal oxide. Doped MONPs may have differences in the total coverage of a surface coating due to differences in lattice spacing and binding behavior between the metal oxide and the dopant label. The coverage can be probed using thermogravimetric analysis (TGA)[241].

In the current body of literature, ζ-potential (a surrogate for surface charge) is often the primary characterization performed to compare labeled and unlabeled MONPs. Since ζ-potential measurements depend on a combination of the nanomaterial, solution, and instrumentation, information about each of these relevant parameters must also be reported[242]. It is important to recognize that differences in the steric stability or hydrophobic/hydrophilic properties of a labeled MONP can still be present even when the ζ-potential is unchanged by the label. The surface properties of MONPs are most likely to be affected by labels that appear directly on the surface of the MONP, like dopants and surface-attached fluorescent dyes. DLS can be used to determine the critical coagulation concentrations and aggregation behavior of MONPs in different aqueous media as a way to identify differences in electrostatic and steric stability between labeled and unlabeled MONPs. The adsorption of dyes like Rose Bengal and Nile Blue can be used to characterize the hydrophobic/hydrophilic surface properties of MONPs[243–245]. Additionally, the likelihood of the label to interact directly with the surrounding media should be evaluated. For metal labels used as dopants or in core labels, XPS analysis can be used to determine the elemental composition of the surface of the labeled MONP, which can then be compared to the bulk composition measured by ICP-OES or ICP-MS. Determining the effects of changing solvents on the optical or fluorescent properties of the label within the MONP is another useful indicator of label impact: a greater solvatochromic shift indicates more exposure of the fluorescent dye to the outside medium, and a greater probability that the dye could influence behavior[142,147].

There are several additional MONP characteristics that provide further information about the potential for toxicity. First, the overlap of the band gap energy of an MONP with the energy potentials of key cellular redox processes has been shown to be a strong predictor of toxicity for low solubility MONPs[246]. Band gap energies can be determined using diffuse reflectance UV-Vis spectroscopy[246]. For ZnO and CuO NPs, particle dissolution and release of ions is the primary mechanism of toxicity, making the label impact on dissolution behavior important to consider. Dissolution can be quantified by exposing MONPs to the media of interest, separating MONPs from released ions through filtration or centrifugation, and measuring the concentration of the metal ions using ICP-OES or ICP-MS techniques. Surface redox reactivity can be measured using a colorimetric assay for methylene blue reduction developed by Corredor et al.[247], and has been shown to correlate to antimicrobial activity for CuO NPs[248]. Finally, a variety of colorimetric assays exist for the determination of ROS production by NPs, as summarized in reports by Djurišić et al. and Crandon[21,245]. Most notably, 2′7′-dichlorofluorescein diacetate (DCFH-DA) is a commonly used nonspecific probe that applies to both intracellular and acellular ROS generation[21,245,249]. Here, exposure to ROS causes the oxidative conversion of DCFH to the fluorescent product DCF, which can be easily measured using fluorescence spectrometry and converted to equivalents of hydrogen peroxide using a standard curve. To study ROS generation under irradiation for photocatalytically active materials like TiO_2, a procedure has been developed that measures the conversion of fluorescein to non-fluorescent products[250]. Electronic properties like the band gap energy or the potential to generate ROS are most likely to be affected by metallic dopant and core/shell labels, which can increase the formation of oxygen vacancies on the MONP surface or participate directly in charge transfer and subsequent band gap narrowing with the MONP material [97,251–253]. Core labels composed of plasmonic NPs can also affect the electronic properties by creating intense electric field "hot spots" on the MONP surface, with a much greater potential to generate electron-hole pairs in photocatalysis than the rest of the MONP surface[97,254].

Proper characterization of a label's impact to MONP properties helps ensure that the overall transport or toxicity is not affected. Additionally, if differences in the studied behavior for labeled versus unlabeled MONPs are discovered, rigorous characterization of the individual properties of the MONP could assist in revealing mechanistic insights into the behavior.

Table 3.4. MONP Properties and Characterization Techniques

MONP Property	**Suitable Characterization Methods**
Size	SEM/TEM, DLS, NTA, sp-ICPMS
Crystallite Size	XRD, TEM
Crystal Structure	XRD, SAED
Surface Area	BET, Calculations from size
Ligand Density	TGA
Surface Charge	ζ-potential, Surface charge titration
CCC, Aggregation Behavior	DLS, NTA
Deposition Behavior	Quartz Crystal Microbalance
Density	Differential sedimentation
Hydrophobicity/Hydrophilicity	Adsorption of rose bengal and nile blue dyes
Band Gap Energy	Diffuse reflectance UV-Vis
Dissolution	ICP-OES, ICP-MS
Photocatalytic Activity	Methylene blue dye degradation under UV exposure
Surface Redox Reactivity	Methylene blue reduction assay
ROS Generation	Colorimetric assays using dye indicators (e.g. DCFH-DA)

In addition to characterization techniques that determine whether the label has impacted particle properties, characterization should also include factors related to the detection sensitivity and stability of the labeled MONPs. For MONPs labeled with a stable isotope or another metal, detection sensitivity is controlled by the elemental or isotopic ratios of the labeled MONPs, which can be measured using ICP-MS. For fluorescent MONPs with dyes or QDs incorporated as labels, the fluorescence quantum yield should be determined using fluorescence spectrometry. The radioactivity of MONPs labeled with radioisotopes can be measured using scintillation counting or γ-spectrometry. The stability of the label should be evaluated for the relevant media, temperatures, and time-scales of the experiment, to ensure that the label will not be released. Along with this information, the limit of detection (LOD) and limit of quantification (LOQ) should be determined and reported for the media of interest. Numerous efforts have been made within the nanotoxicology community for more complete characterization of all NPs used in studies evaluating toxicity and exposure[255,256]. In the case of labeled MONPs, it is especially vital that the property-activity relationships determined through experimental work are inferred based on the true properties of the material, and not confounded by the impact of the label.

3.5 Evaluation of Labeling Strategies

Each labeling technique has several advantages and limitations. The decision of which labeling strategy to use will be based on balancing the detection sensitivity, label stability, cost and equipment requirements, label effects on MONP properties, and ease of labeling and quantification. Table 3.5 provides a summary of these qualities for each labeling approach.

In terms of detection sensitivity, radiolabeling methods are the most sensitive of any technique, offering detection limits as low as pg/L even in complex matrices like mouse tissues. Fluorescent dyes offer the lowest amount of detection sensitivity, often with detection limits higher than environmentally relevant doses. Sensitivity can be decreased even further in matrices that prevent the luminescence of the particles from reaching a detector. Stable isotopes, dopants, and core/shell labeling techniques fall into the detection limit range of ng/L-μg/L, allowing for sensitive detection with a variety of quantification techniques.

Also relevant to detection sensitivity is the stability of the label, both over time and in a variety of matrices. Here, stable isotope labels offer superior stability. They do not degrade over time, and are released from the labeled MONP only as the free ions that would be released through dissolution in an unlabeled particle. These ions can still be detected against a background. For radioisotopes, there exists a wide range of half-lives, and it is important to ensure that the radioactive decay will still allow for the required detection limits to be achieved at the end of the experiment. In addition, small amounts of the radiolabel may diffuse to the surface and be released from the MONP[171–173]. For fluorescent dye labels, the label has been consistently shown to leach from particles over time. Some core labels like AgNPs and QDs may also leach toxic ions that impact study results. The stability of dopant labels under biological conditions has not been adequately investigated. Coating the doped MONPs with a layer of the undoped metal oxide may assist in preserving the dopant labels. In each case, it is necessary to perform experiments testing label stability in the matrix of interest. To adjust for label release, controls should be performed to determine differences in behavior between the free label and labeled

MONP. In terms of temperature stability, organic materials like fluorescent dyes and DNA barcodes are the most likely to degrade. It is unlikely that these types of labeled particles can be heat treated to form all MONP crystalline structures without damaging the integrity of the label. If these materials are not adequately protected within the MONP shell, enzymes and ROS produced by organisms may also degrade the labels.

Cost and equipment requirements can be a limiting factor in choosing a labeling strategy. Isotopic labeling techniques are the most expensive, as isotopically-enriched reagents and direct radioactivation techniques are costly. The cost of the enriched reagent material necessary to produce 100 mg of ZnO NPs ranges from $4000 to $35000 for the stable isotopes summarized in Table 3.3[212]. In the case of radiolabeling, there is not only specialized equipment required for the production and quantification of the MONPs; there are also equipment requirements and costs associated with the safe use and disposal of radioactive materials. Fluorescent dyes are by far the most inexpensive label to incorporate and quantify. In one comparative study, fluorescently-labeled SiO_2 NPs cost 2.7 times less to synthesize than AgNP core-labeled NPs, and 15 times less than radioactive AgNP core-labeled NPs[159]. Quantification of the fluorescent NPs cost 7 times less than the AgNP core-labeled NPs, and 5.2 times less than the radioactive AgNP core-labeled NPs[159].

The applicability of the label to a specific type of MONP is one aspect that may be the deciding factor in choosing a specific labeling method for a given study. Some labels, such as NP cores or dopants, cannot be applied to pre-synthesized, commercially-available MONPs. These commercial MONPs are utilized in large quantities, and as such the potential environmental impact is of interest to researchers. Direct radio-activation is the best labeling option for pre-synthesized MONPs that do not contain organic stabilizing ligands that could degrade during neutron or ion bombardment. While diffusion labeling using isotopes and the surface attachment of fluorescent dyes also apply to commercial MONPs, the stability and detection sensitivity offered by these labels is much lower. Other MONP labeling techniques are not appropriate for labeling highly soluble MONPs. These include core/shell, dopant, and fluorescent dye labels.

The potential effects of labels on key MONP properties have been discussed in detail in the previous section. To summarize, MONPs labeled with stable isotopes are the least likely to have properties impacted due to being elementally and structurally identical to the unlabeled MONP. MONP surface properties are most likely to be affected by dopant labels and by fluorescent dyes that have been attached to the MONP post-synthesis. Surface chemistry will affect aggregation behavior, the formation of protein coronas, and interactions with biomass. Photocatalytic activity and other electronic properties are most likely to be impacted by the incorporation of other metals, especially plasmonic metals like gold and silver, into the MONP as cores or dopants. The electronic properties of the MONP control the potential to generate ROS and impart toxicity for MONPs where dissolution is not the primary mechanism of toxicity. The dopant concentration or core size should be optimized to limit these effects.

To provide guidance on how to choose and employ a specific labeling technique for a given study, two case studies will now be explored. First, we consider the example of a month-long study examining TiO_2 NP distribution and toxicity within a 60 L mesocosm containing multiple trophic levels of organisms, similar to a study performed by Bour et al. using CeO_2 NPs[257].

Background levels of CeO_2 were present in both the water and sediment in the previous study, and mesocosm studies open to the atomosphere could also be affected by atmospheric deposition. With TiO_2, the background concentration is likely to be even greater (Table 3.1). The use of a label could enhance sensitivity while also limiting the impact of heterogeneity in the levels of background TiO_2 within different samples of the same mesocosm compartment. This type of study requires a label that can be produced and used in large quantities, is highly stable over time, and can be easily quantified down to low µg/L concentrations. The limitations on the quantities of radioactive materials that can be handled, as well as the short half-life of many radioisotopes, prohibit the use of radiolabels in this type of study. While stable isotopes offer the stability and detection sensitivity required, the high expense of producing the quantity necessary to evaluate their behavior in multiple mesocosm experiments is undesirable. Fluorescent dyes typically do not provide the detection sensitivity required, and may also be released from the MONP or degraded by photobleaching over the course of the study. A metallic label, used as either a dopant or a core label, is highly stable over time and provides low limits of quantification even in complex media. The cost of producing the labeled MONP is not as high as for isotopic labeling, and multiple TiO_2 crystal structures can be formed. A variety of quantification techniques can also be used, including ICP-OES, ICP-MS, and even INAA. This provides flexibility that allows samples from compartments that are difficult to prepare for ICP-MS analysis to be quantified by INAA, while samples from compartments with higher concentrations of MONPs can be easily quantified by ICP-OES. The size, surface charge, and aggregation behavior should be compared between the labeled and unlabeled MONPs, as these parameters are especially relevant for transport and uptake. Additionally, the impact of the core label on the photocatalytic activity should be determined, as this is a property that drives TiO_2 toxicity. The ratio of the metal label to the Ti within the labeled NPs should be reported, as well as the limits of detection and quantification.

Another case study we consider is the monitoring of ZnO NP uptake and translocation within an organism. Zn is an essential element for many organisms, and as such it is likely to be present prior to NP exposure. The use of a label allows for sensitive detection of the ZnO NPs against background levels of Zn, and can also provide the ability to visualize the ZnO NPs within the organism. As ZnO is a soluble MONP with ion-driven toxicity, it is important to be able to distinguish not only the ZnO NPs from the background Zn, but the Zn^{2+} ions after they are released through dissolution. Isotopic labeling techniques are ideal for these experiments because the Zn itself is specifically labeled and can be traced whether in ionic or particulate form. Radiolabeling is especially effective for examining MONP distribution among specific tissues and organs, as the sensitivity and ease of analysis offered by γ-spectrometry allows for the measurement of the small MONP quantities that may be present within a single biological compartment. ^{65}Zn also has the benefit of having an extremely long half-life for a radiolabel (244 days), sufficient even for long-term studies of chronic toxicity. If visualization is also desired, positron-emitting radiolabels like ^{18}F can be used to enable PET imaging, though these labels lack temporal stability due to the short half-life. Fluorescent dyes and QD labels can also be used along with fluorescence microscopy. In the case of fluorescent dyes and QD labels, the solubility of ZnO NPs may make the label release and degrade in some compartments, limiting the capacity for imaging. For gavage, intravenous, or intratracheal doses of MONPs, the true administered dose must be determined by measuring the amount of MONPs remaining within the syringe, a task easily accomplished when a radiolabel is present. Characterization of radiolabeled MONPs used in this type of study should include a comparison of dissolution kinetics for the labeled and unlabeled ZnO NPs, tested in media with relevant pH and ionic strength values. It is also important to determine that no structural impact occurred during radiolabeling if direct activation was used to prepare the NPs. Size and crystal structure are two properties that could potentially be affected. The radioactivity of the produced MONPs should be reported, along with the limits of detection and quantification.

Table 3.5. Summary of labeling strategies.

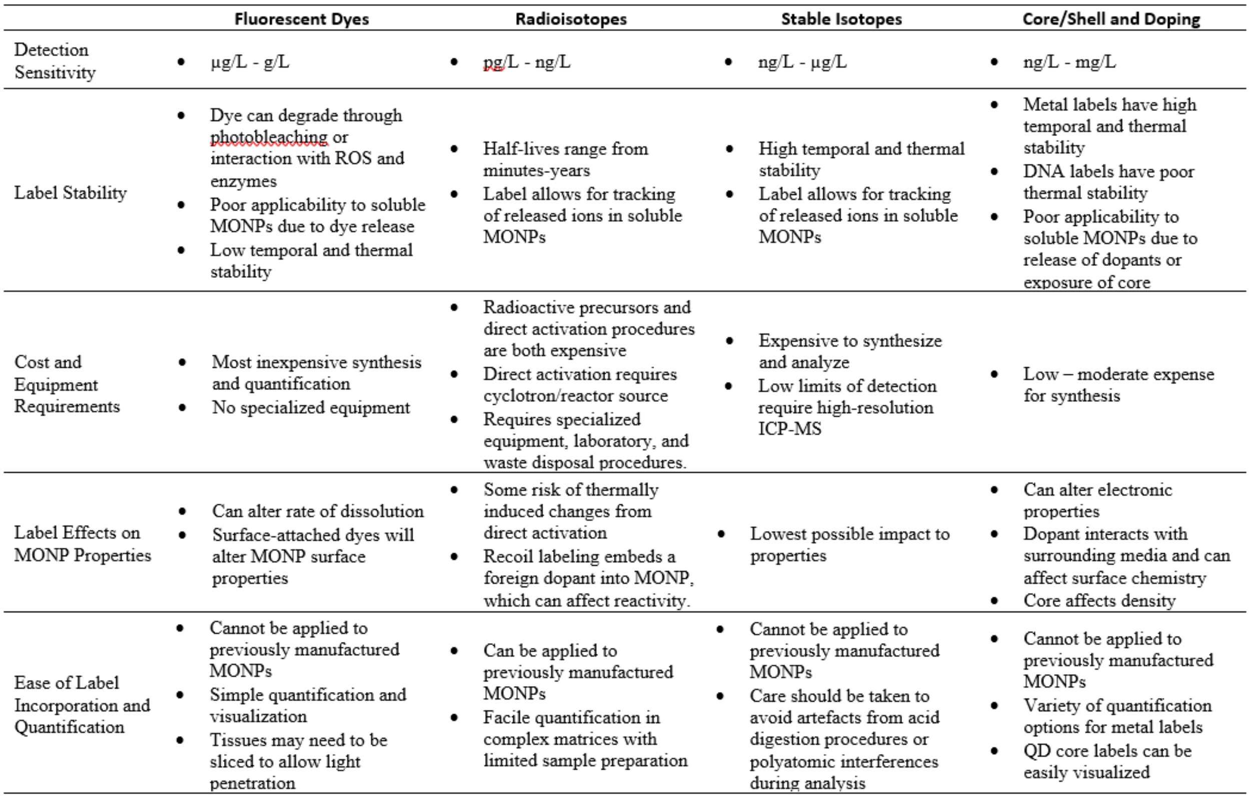

	Fluorescent Dyes	**Radioisotopes**	**Stable Isotopes**	**Core/Shell and Doping**
Detection Sensitivity	• μg/L - g/L	• pg/L - ng/L	• ng/L - μg/L	• ng/L - mg/L
Label Stability	• Dye can degrade through photobleaching or interaction with ROS and enzymes • Poor applicability to soluble MONPs due to dye release • Low temporal and thermal stability	• Half-lives range from minutes-years • Label allows for tracking of released ions in soluble MONPs	• High temporal and thermal stability • Label allows for tracking of released ions in soluble MONPs	• Metal labels have high temporal and thermal stability • DNA labels have poor thermal stability • Poor applicability to soluble MONPs due to release of dopants or exposure of core
Cost and Equipment Requirements	• Most inexpensive synthesis and quantification • No specialized equipment	• Radioactive precursors and direct activation procedures are both expensive • Direct activation requires cyclotron/reactor source • Requires specialized equipment, laboratory, and waste disposal procedures.	• Expensive to synthesize and analyze • Low limits of detection require high-resolution ICP-MS	• Low – moderate expense for synthesis
Label Effects on MONP Properties	• Can alter rate of dissolution • Surface-attached dyes will alter MONP surface properties	• Some risk of thermally induced changes from direct activation • Recoil labeling embeds a foreign dopant into MONP, which can affect reactivity.	• Lowest possible impact to properties	• Can alter electronic properties • Dopant interacts with surrounding media and can affect surface chemistry • Core affects density
Ease of Label Incorporation and Quantification	• Cannot be applied to previously manufactured MONPs • Simple quantification and visualization • Tissues may need to be sliced to allow light penetration	• Can be applied to previously manufactured MONPs • Facile quantification in complex matrices with limited sample preparation	• Cannot be applied to previously manufactured MONPs • Care should be taken to avoid artefacts from acid digestion procedures or polyatomic interferences during analysis	• Cannot be applied to previously manufactured MONPs • Variety of quantification options for metal labels • QD core labels can be easily visualized

3.6 Conclusion

A variety of MONP labeling techniques have been developed for the purpose of studying MONPs in complex systems. When any of these labeling strategies is employed, characterization is critical to ensuring that the properties and behavior of the labeled MONP are representative of the unlabeled form. The decision of which technique to use will depend on the label stability and detection sensitivity requirements of the study, limitations imposed by equipment and cost, and the preservation of MONP properties that are critical to understanding the mechanism of behavior. Rigorous characterization and comparison of key properties to unlabeled MONPs is necessary for meaningful conclusions to be drawn from experiments that employ a labeling strategy. Currently, there are limited comparisons of key characteristics affecting MONP transport and toxicity. Improved reporting of label parameters, like the amount of the label incorporated into the MONPs, and the limits of detection and quantification, will help ensure that progress can continue to be made optimizing the preparation and utility of labeled MONPs. Ultimately, no one labeling technique will meet all research needs. The successful development and application of a variety of MONP labeling strategies enables experimental designs that reflect the complexity of the natural environment, better allowing for the determination of the mechanisms driving transport and toxicity.

4 Effect of nanomaterial surface properties and water chemistry on contaminant degradation by titanium dioxide nanoparticles

Alyssa R. Deline and Jeffrey A. Nason

4.1 Abstract

Titanium dioxide nanoparticles (TiO_2 NPs) are used in a variety of commercial and industrial applications, which has inspired interest in their potential environmental implications. These materials also have great potential for use in the treatment of emerging organic pollutants, and the photodegradation of several model contaminants by TiO_2 NPs have been studied under a variety of conditions. While TiO_2 photocatalysis has been studied extensively in simple systems, there exists limited mechanistic insight linking the surface properties and transformations of the NPs to their larger scale behavior in a complex system. This study examines two model TiO_2 NPs in the real-world treatment scenario of a UV-irradiated slurry used for treating organic contaminants at three different levels of focus.The molecular-level properties of the TiO_2 surface were examined using XPS analysis. The extrinsic properties of the TiO_2 NPs in well-controlled aquatic systems were examined through characterization and colorimetric assays. These properties were compared to the performance of the TiO_2 NPs in the degradation of methylene blue dye. No direct correlations between the XPS-determined surface composition and the overall treatment efficacy of the TiO_2 NPs were observed. The most important properties determining the extent of MB dye degradation were 1) crystal structure and ROS generation, 2) pH stability, and 3) aggregation state.

4.2 Introduction

Titanium dioxide nanoparticles (TiO_2 NPs) have great potential for use in the treatment of emerging organic pollutants, including those that cannot be efficiently biodedgraded[18]. In photocatalytic water treatment processes using TiO_2 NPs, the NPs are irradiated with light, which excites electrons from the valence band to the conduction band, creating electron-hole pairs. These charge carriers can then participate in redox reactions with water and oxygen to form reactive oxygen species (ROS). The primary species of ROS generated by TiO_2 NPs are hydroxyl radicals ($^{\bullet}OH$), which have an oxidation potential of 2.80 V, greater than the potential for common oxidizing agents like ozone or hydrogen peroxide[18]. The generated ROS oxidize the organic contaminants in the solution, in some cases facilitating complete mineralization of the compounds to carbon dioxide[258,259]. Organic dyes like methylene blue (MB) are often used as a model contaminant to compare the degradation efficiencies of different pure and hybridized TiO_2 NPs, primarily due to the ability to make facile measurements of degradation using ultraviolet-visible (UV-Vis) spectrophotometry[260]. The overall efficacy of an advanced oxidation treatment system featuring TiO_2 NP photocatalysis is dependent on key parameters of the TiO_2 NPs, water chemistry, and treatment operation (e.g. light wavelength and intensity used).

One aspect of photocatalytic efficiency is the potential for a specific type of TiO_2 surface to generate ROS. For example, differences in this potential arise for TiO_2 NPs with different crystal structures. The anatase form of TiO_2 consistently exhibits greater photocatalytic activity than the rutile form, while mixed-phase TiO_2 NPs that are 20-30% rutile are more effective than pure anatase NPs[23–25]. This variation in photocatalytic activity is caused by differences in the band gap energy required to excite electrons to the valance band, and in the ability of free charges to diffuse to the surface without recombining[22–25]. The intensity of the light used for irradiation can also affect the rate of $^{\bullet}OH$ production, with more $^{\bullet}OH$ produced as the light intensity is increased[261]. The characteristics of the water also factor into ROS generation potential: TiO_2 thin films irradiated in solutions with greater levels of dissolved oxygen present will produce more ROS than TiO_2 irradiated in solutions with lower levels of dissolved oxygen[262].

Another key component of photocatalytic activity is the relative amount of TiO_2 surface available to absorb light and generate ROS. The specific surface area of TiO_2 nanopowders determined using Brunaeuer-Emmett-Teller (BET) analysis has been shown to be important to the production of ROS, with more $^{\bullet}OH$ produced by NPs with a higher specific surface area[263]. However, the specific surface area is unlikely to reflect the amount of surface area available once the TiO_2 NPs are dispersed in solution. Other studies have indicated that aggregation behavior will dictate $^{\bullet}OH$ production: smaller, less dense aggregates of TiO_2 NPs have higher rates of $^{\bullet}OH$ production than TiO_2 aggregates that are larger and more dense[26]. The aggregate density and size are directly affected by water quality parameters like the pH and ionic strength, as predicted by Derjaguin-Landau-Verwey-Overbeek (DLVO) theory[264,265]. Therefore, it is important to consider the available TiO_2 NP surface area that will be present in the media of interest.

Finally, interactions between the TiO_2 and the organic contaminant of interest affect the degradation rate by bringing the contaminant to the TiO_2 surface where the contaminant is most likely to be oxidized by the very short lived ROS species (half-lives on the order of nanoseconds) that are produced[17]. This is directly related to the pH of the solution, which controls the protonation state of the TiO_2 surface as well as that of the organic contaminant[266]. For MB dye, adsorption to TiO_2 NPs increases with pH due to the positive charge of the dye molecule and the increasingly negative charge of the TiO_2 NPs, resulting in a greater rate of degradation[37,38]. The hydrophobicity of the TiO_2 NP surfaces is also relevant. Many organic contaminants have hydrophobic characteristics, which will be more likely to adsorb to a hydrophobic TiO_2 surface[267,268].

The surfaces of photocatalysts are often characterized using x-ray photoelectron spectroscopy (XPS), which provides molecular-level insights into the oxidation state, elemental composition, and local binding environment of material surfaces. In clean, well-controlled systems, the relationship between the XPS-analyzed surface properties of TiO_2 and extrinsic properties like the hydrophobic/hydrophilic character or the generation rate of $^{\bullet}OH$ are well understood[269,270]. However, there exists limited mechanistic insight linking the molecular-level surface properties of TiO_2 NPs to key extrinsic properties and overall photocatalytic activity within a more complex water treatment scenario.

In this study, two model TiO_2 NPs with different crystal structures were examined at three different levels of focus. First, the molecular-level properties of the TiO_2 NP surfaces were analyzed using XPS in three different water chemistry conditions, both before and after exposure to simulated solar irradiation. Next, key NP properties like the specific surface area, aggregation state, surface charge, hydrophobicity, and $^{\bullet}OH$ generation were explored under the same conditions. Surface area was characterized using both BET analysis and DLS to determine if one method holds more relevance to the photocatalytic activity of TiO_2 NPs. Colorimetric assays performed in the media of interest were used to examine particle hydrophobicity and $^{\bullet}OH$ generation. Finally, the photocatalytic degradation of MB dye by the two NP types was studied. The relationships between the molecular-level surface properties and the broader properties of the NPs were compared to contaminant degradation performance, allowing for a better understanding of the role that surface structure plays in controlling nanoparticle behavior and treatment efficacy in aquatic systems.

4.3 Materials and Methods

All glassware used was washed thoroughly with 10% nitric acid solution, and rinsed with distilled and deionized (DDI) water (18.2 MΩ; Millipore Co. USA). Unless otherwise noted, all chemicals were purchased from Sigma Aldrich and used without further purification.

4.3.1 Nanoparticle Stock Preparation

Two TiO_2 NP types were chosen for this study, AEROXIDE® TiO_2 P25 (Evonik Degussa Corp.) and pure anatase TiO_2 NPs (Sigma Aldrich). For each NP stock, the TiO_2 NPs were transferred to a pre-weighed glass beaker, which was then covered with a watch glass and re-weighed. The NPs were then transferred from the beaker to a clean 500 mL amber glass bottle by repeated rinsing of the beaker with DDI water until 460 mL total of DDI water was added. The stocks were bath sonicated (VWR B1500A-MTH) for 30 minutes at high power, as recommended by Chowdhury et al.[271]. Each stock solution was covered in aluminum foil and stored under refrigeration. The concentrations of the two stock solutions were calculated to be 10.91 g/L for the P25 TiO_2 NPs and 12.30 g/L for the anatase TiO_2 NPs. Prior to use in experiments or characterization, NP stock solutions were removed from refrigeration and brought to room temperature, and then bath sonicated for 15 minutes at high power. All stock aliquots were removed after the sonication process, while stirring on a magnetic stir plate.

4.3.2 Simulated Solar Irradiation

Simulated solar irradiation for all experiments and characterization other than XPS analysis was performed using a 4000 Watt Atlas Materials Testing Solutions’ Gentex SolarConstant 4000 Single Control set to one sun output. 70 mL samples were prepared and exposed to the UV light in 120 mL glass jars with diameters of 60 mm (VWR International), with the sides of the jars covered by aluminum foil. Simulated solar irradiation of NPs for XPS samples was performed using an Abet Technologies model 10500 solar simulator set to one sun output. 25 mL samples were prepared and exposed to the UV light in 60 mL glass jars with diameters of 53.3 mm (VWR International), with the sides of the jars covered by aluminum foil. The solar irradiance spectra of the two solar simulators were collected using a portable spectrometer with a cosine corrector (AvaSpec-ULS2048CL-EVO, Avantes). Spectra are presented in the supporting information (SI). All exposures to simulated solar light were performed for 1 h under continuous stirring using a magnetic stir plate, and then stirred in the dark at room temperature for 15 minutes before use in experiments or characterization. Control tests were performed to evaluate the potential evaporation of solutions during irradiation. Evaporation was found to be less than 2% by weight for all experimental conditions.

4.3.3 Nanoparticle Characterization

The hydrodynamic diameter (D_h) and ζ-potential values of the two TiO_2 NP types were determined in three different aqueous media: DDI water adjusted to pH 5.8, DDI water adjusted to pH 7.4, and 1x phosphate buffered saline (PBS) solution diluted from a 10x concentrated stock. 10 mg/L solutions of each NP type were prepared. KCl was added at a final concentration of 1 mM to the pH-adjusted DDI water samples to provide ions for the ζ-potential analysis. The pH was adjusted for the DDI water samples using 1 and 10 mM solutions of potassium hydroxide (KOH) and hydrochloric acid (HCl). For the ambient samples (no exposure to irradiation), a 3.5 mL aliquot was removed from a continuously stirring solution and immediately analyzed using dynamic light scattering (DLS) followed by ζ-potential analysis (90Plus and ZetaPALS, Brookhaven Instruments). For the irradiated samples, the pH adjusted 10 mg/L solutions were exposed to simulated solar light for 1 h, stirred in the dark for 15 minutes, and then pH adjusted again if necessary. A 3.5 mL aliquot was then removed from a continuously stirring solution and immediately analyzed using DLS followed by ζ-potential analysis. For DLS analysis, 3 runs of 1 minute each were collected. For ζ-potential, 3 runs of 20 cycles were collected. ζ-potential was calculated using the Smoluchowski model. Details are included in the SI (Appendix B). BET analysis of surface area was performed on the as-received nanopowders using N_2 physisorption measurements collected with a Micromeritics ASAP 2020 after 3 hours of degassing at 200°C.

4.3.4 Rose bengal dye adsorption

Procedures for the hydrophobicity assay using RB dye adsorption were modified from Xiao et al.[243]. A 40 mg/L stock of rose bengal dye was prepared in either DDI water or 1x PBS. The DDI water samples were then pH-adjusted to 5.8 or 7.4 using 1 and 10 mM solutions of KOH and HCl. TiO_2 NP solutions were prepared in the same media at concentrations of 20 mg/L, 200 mg/L, and 2 g/L. NP solutions either remained ambient or were exposed to simulated solar light for 1 h, stirred in the dark for 15 minutes, and then pH-adjusted if necessary. 750 μL of the dye solution and 750 µL of a NP solution in a specific media (e.g. PBS) were added to 2 mL centrifuge tubes and mixed by inverting. Samples were placed on a shaker table for 3 h at 25°C. The TiO_2 NPs were removed from the solution by centrifuging at 14,000 rpm for 15 minutes (Eppendorf Centrifuge 5415 C). The absorbance at 542 nm was measured using a Thermo Scientific Orion AquaMate 800 UV Vis spectrophotometer. All samples were run in triplicate, and controls were also run containing only the rose bengal dye in the media of interest. The partitioning quotient (PQ) of each sample was calculated using the following equation (Eq. 1):

$$\mathrm{PQ} = \frac{\text{Mass of rose bengal dye adsorbed by } \mathrm{TiO_2} \text{ NPs}}{\text{Mass of rose bengal dye remaining in solution}} \quad (1)$$

The PQ was plotted against the surface areas determined by both BET and DLS analysis. The slopes of the resulting lines were determined using linear regression analysis, and reported as the relative hydrophobicity for the specific NP-media combination. Surface area calculations and plots of PQ vs. surface area are included in the SI (Appendix B).

4.3.5 Fluorescein dye degradation

Methods for the evaluation of photocatalytic $^{\bullet}OH$ generation by TiO_2 NPs were adapted from Wormington et al.[250]. 70 mL samples containing final concentrations of 10 µM fluorescein sodium salt and 500 mg/L TiO_2 NPs were prepared in either DDI water or PBS media, and the DDI water solutions were pH adjusted to 5.8 or 7.4. The samples were exposed to 1 h of simulated solar irradiation under constant stirring. All samples were run in triplicate, and controls were also run containing only the fluorescein dye in the media of interest. Fluorescence intensity was measured using a fluorescence spectrophotometer (Varian Cary Eclipse) at excitation/emission 460/530 nm.

4.3.6 XPS analysis

The surface composition of the TiO_2 NPs before and after irradiation with simulated solar light was analyzed using XPS (ThermoScientific ESCALAB 250 spectrometer). 25 mL samples of 10 g/L TiO_2 NPs were prepared in the media of interest, which was then pH adjusted if necessary. A 50 μL aliquot of the ambient solution was removed from the solution while stirring and dropcast onto a clean Si wafer. The sample on the wafer was transferred to a small polyethylene glove bag (VWR International) filled with purified dry nitrogen gas, and allowed to dry for 30 minutes. The Si wafer was then mounted on a sample stub using carbon tape. The sample was then transferred to the loading chamber of the instrument and vacuum pumped for 10 minutes, then transferred to the analysis chamber and analyzed via XPS. After the aliquot was taken of the ambient solution, the solution was exposed to simulated solar light for 1 h under continuous stirring. Another 50 μL aliquot was removed from the solution while stirring and dropcast onto a clean Si wafer, then the same steps were followed as for the ambient sample. For the TiO_2 NP samples in PBS media, a 1.8 mL aliquot was removed and transferred to a 2 mL centrifuge tube. The sample was centrifuged for 8 minutes at 18000 rpm (Allegra X-30 B06322, Beckman Coulter), and then the supernatant was decanted and replaced with 1.8 mL DDI water. The centrifuge washing process was repeated once more. This washing step was performed due to the presence of a thick salt layer from the PBS that formed on sample surfaces during drying, preventing the observation of TiO_2 NPs during XPS analysis.

A monochromatic AlKα X-ray source was used at an operating power of 150 W with a nominal spot size of 500 μm. Survey scans were collected at a pass energy of 150 eV, while high-resolution spectra were collected at a pass energy of 20 eV. The binding energy scale for all measurements was calibrated to the C1s peak at 284.8 eV. Peak analysis was performed with Avantage software. Survey and high-resolution scans are included in the SI (Appendix B), along with more detail of peak analysis procedures.

4.3.7 Photocatalytic degradation of MB dye

70 mL samples of TiO_2 NPs (0-100 mg/L) and MB dye (10 μM) were prepared in PBS media or DDI water, in 120 mL glass jars charged with a stir bar. For the samples prepared in DDI water, the pH was adjusted to 5.8 or 7.4 using 1 and 10 mM solutions of KOH and HCl. The intial pH, temperature, and dissolved oxygen value was recorded, and then the samples were exposed to simulated solar light for 1 h. At each time point of interest (time= 0, 15, 30, 45, 60 mins) a 1.8 mL sample from each jar was removed and centrifuged for 15 minutes at 16000g to remove NPs. The UV-Vis absorbance at 665 nm was measured and recorded for each supernatant. MB dye concentrations were calculated using a standard curve (provided in the SI, Appendix B). Tables of average temperature, pH, and dissolved oxygen content before and after irradiation are included in the SI (Appendix B).

4.4 Results and Discussion

4.4.1 Commercial nanopowders

P25 TiO_2 NPs from Evonik Degussa Corp. and anatase TiO_2 NPs from Sigma-Aldrich were chosen for this study based on their extensive use in scientific literature regarding both the applications and implications of TiO_2 nanomaterials. Each of the two nanomaterial types have been rigorously characterized in a variety of aqueous media[250,264,272,273]. For example, the University of California Center for Environmental Implications on Nanotechnology (UC CEIN) has employed P25 TiO_2 as a standard reference material for studies of the environmental behavior of TiO_2 NPs[274]. The P25 NPs are composed of mixed crystalline phases, approximately 80% anatase and 20% rutile, while the anatase NPs are composed purely of the anatase form[264,272,273]. The primary particle sizes of both NP types are consistently reported in the range of 20-30 nm[264,272,273], with manufacturer-reported primary particle sizes of 21 nm for the P25 and <25 nm for the anatase NPs.

4.4.2 TiO_2 NP agglomeration state and surface charge

The D_h and ζ-potential values of 10 mg/L NP suspensions at each water chemistry condition (pH 5.8, pH 7.4, and pH 7.4 with the presence of PBS buffer) both before and after a 1 h exposure to simulated solar light are summarized in Table 4.1, and also shown in Figure 3.1. The ambient D_h at each water chemistry condition was much greater than the primary particle size due to particle aggregation, even in the non-buffered solutions with very low ionic strength. This behavior is consistently observed for TiO_2 NPs that have not been stabilized with polymer coatings[250,264,271,272]. The D_h values of the anatase TiO_2 NP suspensions prior to irradiation were larger than that of the P25 NPs in each condition. For the P25 NPs, the ambient D_h changed with water chemistry, following the trend of pH 7.4 < PBS media < pH 5.8. TiO_2 aggregation is known to increase as pH decreases toward the isoelectric point, and also in solutions like the PBS media, which have a higher ionic strength than the pH adjusted DDI water solutions[275]. The isoelectric point has previously been reported in the range of pH 6-7 for the NPs studied here, but in this work it was found to be <5.8 for both NP types[31,276,277]. For the anatase NPs, there was no significant difference in the D_h values of the NPs in different media, which correlates to the smaller differences observed in ζ-potential compared to the P25 NP suspensions.

Table 4.1. D_h and ζ-potential of 10 mg/L NP solutions, before and after the solutions were irradiated by simulated solar UV light for 1 h. Values are reported as the mean ± the standard error.

		D_h, nm		**ζ-potential, mV**	
		Ambient	**Irradiated**	**Ambient**	**Irradiated**
P25 NPs	pH 5.8	1118.1 ± 87.1	1048.6 ± 38.1	-21.36 ± 0.77	-20.56 ± 4.2
	pH 7.4	291.3 ± 3.4	17178 ± 5752	-28.30 ± 0.73	-29.69 ± 0.61
	pH 7.4 + PBS	686.2 ± 16.1	320.2 ± 6.7	-24.07 ± 4.08	-23.14 ± 2.61
Anatase NPs	pH 5.8	1600.3 ± 152.5	18249 ± 4664	-22.92 ± 1.41	-18.29 ± 3.48
	pH 7.4	1302.8 ± 232.2	12065 ± 404	-23.34 ± 1.5	-30.44 ± 0.7
	pH 7.4 + PBS	1493.5 ± 152.7	820.7 ± 141.4	-25.30 ± 0.74	-24.78 ± 1.8

After 1 h irradiation, the suspensions were allowed to cool from the 35°C reached during exposure back to room temperature while stirring, pH-adjusted for minor changes that occurred during irradiation if necessary, and then the sizes and ζ-potentials were re-measured without sonication. Irradiation caused significant impact on the agglomeration states of both nanoparticle types. Figure 4.1 illustrates the effect of the solar irradiation on the aggregation state and ζ-potentials of the TiO_2 NPs at each condition. In each case, the ζ-potentials were highly negative both before and after irradiation. The only significant difference in ζ-potential caused by irradiation was the decrease in the anatase NPs at pH 7.4 from -23.3 ± 1.5 mV to -30.4 ± 0.7 mV, which was determined using a Student's *t* test with a 95% probability level ($p = 0.013$). In all other cases, any differences in NP behavior that occur after irradiation cannot be explained by the effects of changes in surface charge.

Significant increases in the D_h after irradiation were observed for the anatase NPs at pH 5.8 and pH 7.4 with no buffer added, and for the P25 NPs at pH 7.4 with no buffer added. A cycle of temperature increase followed by cooling to room temperature has been shown to cause an initial disagglomeration of TiO_2 NPs at the higher temperature, which is followed by the reagglomeration of NPs in a more diffuse, non-optimal configuration during cooling, resulting in an increase in the measured D_h of the suspension[278]. This is consistent with the increases in D_h observed in this study, where a similar temperature cycle was applied. For both NP types, the size of the NPs prepared in the PBS media decreased after irradiation. While exposure to UV light has previously been shown to disaggregate TiO_2 NPs[279], this decrease in D_h could also be caused by larger NP aggregates settling out of solution[278]. It is more likely that larger particles are settling out of solution, as no irradiation-induced disagglomeration was observed for the pH 5.8 or pH 7.4 conditions, and the large size of the initial agglomerates in PBS media increases the likelihood that further agglomeration would cause settling. There was visible settling of nanopowder in the sample cuvettes. After irradiation, the D_h values for P25 NPs in different media follow the trend of PBS media < pH 5.8 < pH 7.4, potentially as a result of sedimentation in PBS media, while the differences in D_h were not statistically significant for the anatase NPs in different media. Anatase NP aggregates were larger in size than P25 NP aggregates for conditions other than pH 7.4, where there was no significant difference in size as determined using a Student's *t* test with a 95% probability level ($p = 0.425$).

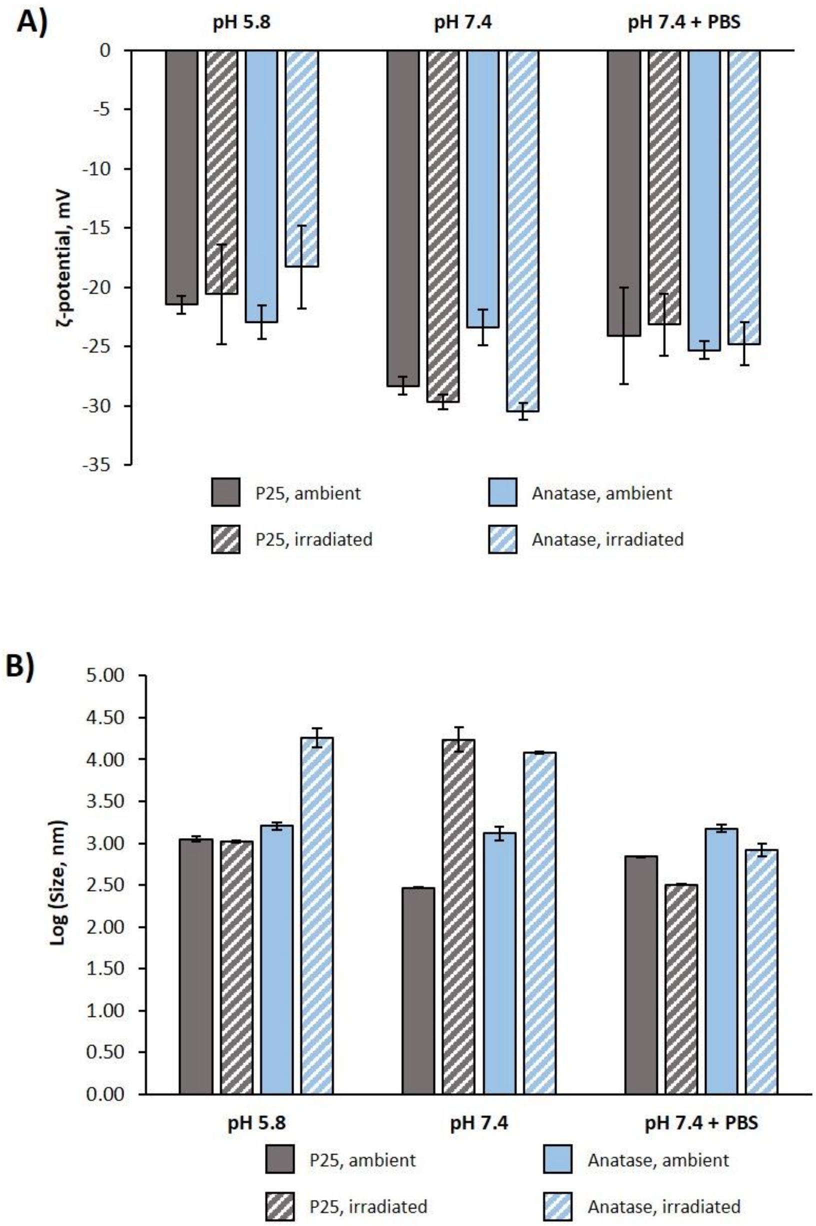

Figure 4.1. A) ζ–potential and B) Log(D_h) of 10 mg/L NP solutions, before and after NP stock solutions were irradiated by simulated solar UV light for 1 h. Error bars represent the standard error between measurements.

4.4.3 Surface area of TiO2 NPs

Surface area has been identified as an important driver of the photogeneration of hydroxyl radicals by TiO_2 NPs[263]. There is currently no consensus on the best method for determining NP surface area, but BET and DLS analysis are both consistently used to characterize this property. Surface areas derived from BET analysis have the advantage of including the porosity of the NPs, which includes both the pore spaces present in the primary particles, and the spaces that form between particle aggregates. However, there are several disadvantages. BET analysis can only be performed on the dry nanopowder. This can be a limitation to the practicality of the measurement, which necessitates lyophilization or drying to be performed prior to analysis. Additionally, several hundred milligrams of material are required per measurement. The use of nanopowder is also a limitation to the potential relevance of the measurement when the values are applied to describe behavior of NPs in aqueous media, as the aggregation state will differ when compared to the nanopowder form. Surface areas calculated from the DLS-measured D_h have the advantage of being informed by the aggregation state of the NPs in the aquatic media of interest. The measurement is also rapid and facile to perform, and requires only minute amounts of the NPs. However, this method of estimating surface area has the disadvantage of requiring the simplifying assumption that aggregates are perfect spheres. In addition, DLS analysis is not ideal for highly polydisperse samples, as measurements are intensity-weighted and can be heavily impacted by the presence of a few large aggregates. The TiO_2 NP surface areas determined using both approaches are summarized in Table 4.2. Calculations for the D_h-derived values are provided in the SI (Appendix B).

The BET-derived surface area for P25 NPs was in good agreement with the manufacturer reported value of 50 m^2/g. The anatase NPs were reported by the manufacturer to have a surface area of 45-55 m^2/g, but were found to have a much greater surface area of 83.7 m^2/g. As expected due to the effects of aggregation, the DLS-derived surface areas are much lower, ranging from 0.083 – 4.87 m^2/g for the P25 NPs, and from 0.085 to 1.88 m^2/g for the anatase NPs. The fact that the anatase TiO_2 has a greater surface area when measured by BET, but typically a lower surface area when measured by DLS, allows for the evaluation of which surface area method holds the most relevance to other properties and behavior examined in this study.

Table 4.2. Surface area of P25 and SA NPs, as determined using B.E.T. analysis and estimated from DLS-measured D_h values. For DLS values, the range represents the values calculated from both the unexposed NP stock and the NP stock exposed to simulated solar UV light. Sample calculations are included in the SI.

TiO_2 NP Type	**pH**	**Surface Area, m^2/g**		
		DLS, Ambient	**DLS, Irradiated**	**BET**
P25	5.8	1.27	1.35	48.9 ± 0.3
	7.4	4.87	0.083	
	7.4 (w/ PBS)	2.07	4.43	
Anatase	5.8	0.964	0.085	83.7 ± 0.4
	7.4	1.18	0.128	
	7.4 (w/ PBS)	1.03	1.88	

4.4.4 Hydrophobicity

The hydrophobicity of nanomaterials, which describes their relative aversion to water, is an important property in the study of nanomaterial behavior. Hydrophobicity affects particle stability and interactions with environmentally relevant materials like proteins and biomass[243,280–282], and nanoparticles or colloids that are hydrophobic are more likely to aggregate when in water[280]. The hydrophobicity of different NPs can be compared between samples using an assay measuring the adsorption of rose bengal dye[243,245]. These dye interactions have been shown to follow the same trends as the water contact angle for NPs[243]. The relative hydrophobicity is defined as the slope of the line between the partitioning quotient and the surface area dose of the nanoparticle; a higher slope indicates a more hydrophobic surface. The relative hydrophobicities of P25 and anatase TiO_2 NPs were determined for each water chemistry condition before and after irradiation, using both the BET- and DLS-derived surface area values. This data is summarized in Figure 4.2. There was no measurable adsorption of rose bengal dye to either TiO_2 NP type at pH 7.4, with or without the presence of PBS buffer, indicating the materials have hydrophilic character at this pH.

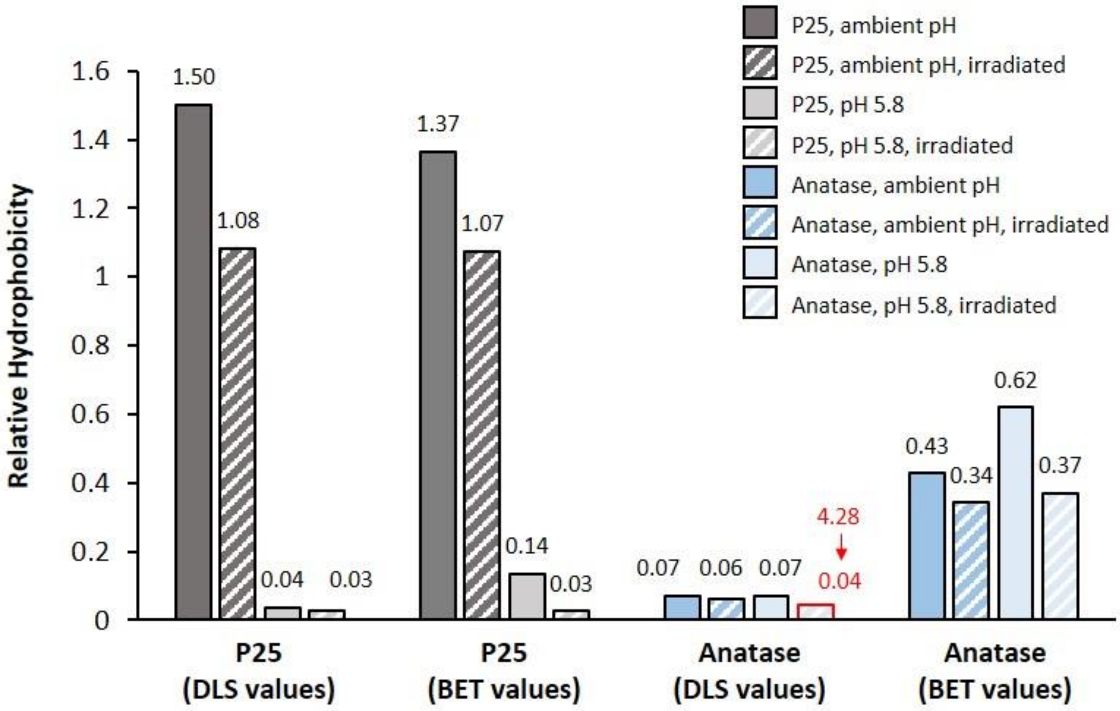

Figure 4.2. Relative hydrophobicity values for P25 and anatase TiO_2 NPs in different aquatic media, using BET- and DLS-derived surface area dose values. For anatase NPs at pH 5.8 after irradiation (identified in red), the slope calculated using the pre-irradiation D_h is shown due to the likely impact of intensity-weighting on the post-irradiation D_h value. Ambient pH is defined as the pH of the nanoparticles and dye in unadjusted DDI water (pH 4.68 for P25 and pH 5.74 for anatase).

P25 NPs were much more hydrophobic than the anatase NPs at the ambient pH (4.68 for P25 and pH 5.74 for anatase). There was no measurable hydrophobicity for either TiO_2 NP type at the pH 7.4 conditions. For the relative hydrophobicity of anatase TiO_2 NPs at pH 5.8 after irradiation using the DLS-derived surface area, an extremely large value of 4.28 was determined. This was likely due to the D_h measurement being impacted heavily by the presence of several large aggregates, resulting in a high D_h value. This causes the appearance that the rose bengal dye adsorbed to an artificially lowered surface area dose. To facilitate a more relevant comparison, the calculation is presented here using the D_h value measured prior to irradiation, which results in a relative hydrophobicity value of 0.04. This approach is supported by the ambient pH differing from the pH 5.8 condition by only 0.06 pH units, which is unlikely to result in such a dramatic difference in rose bengal adsorption behavior. In the ambient pH experiments the hydrophobicity decreased very slightly from 0.07 to 0.06 after irradiation.

Exposure to UV light is known to increase the hydrophilicity of both anatase and rutile TiO_2 surfaces[283–286]. This has been shown to be caused by the UV-induced oxidation of the TiO_2 surface that allows for the photodegradation of the hydrophobic carbon impurities on the TiO_2 surface that arise from exposure to the ambient atmosphere[41,286]. Figure 4.2 illustrates that 1 h of exposure to simulated solar light containing UV rays results in a measurable decrease in hydrophobicity determined by rose bengal adsorption for both NP types at both the ambient pH and pH 5.8. Due to the differences in surface area measurements between BET and DLS methods, there are differences in the relative hydrophobicity trend at pH 5.8 between the two NP types. When BET analysis is used, anatase NPs are much more hydrophobic, and when DLS analysis is used, the hydrophobicity is nearly equivalent between the two particle types.

A previous study found that the hydrophilicity measured by H_2O water vapor adsorption enthalpy was greater for anatase TiO_2 than for rutile TiO_2, and that the P25 mixture had a hydrophilicity nearly identical to pure anatase[287]. Similarly, superhydrophilicity under UV irradiation was achieved within 120 minutes for polycrystalline anatase and rutile (110) surfaces, but 300 minutes of exposure was required for rutile (001) surfaces to achieve superhydrophilicity[288]. These previous findings indicate that the relative hydrophobicity of the P25 NPs should be equal to or slightly greater than the anatase NPs, which was reflected in the DLS-analyzed results in this study. The results here suggest that the DLS-derived surface area is more relevant than the BET-derived surface area in the determination of hydrophobicity in aquatic media through rose bengal dye adsorption.

4.4.5 ROS Generation

The generation of ROS, specifically hydroxyl and superoxide radicals, is the driver of the photocatalytic treatment of organic and microbial contaminants by TiO_2[21,123,250,289–291]. ROS generation can be determined by electron spin resonance spectroscopy (ESR) or by the use of fluorescent probes, most commonly 2′,7′-dichlorodihydrofluorescein diacetate (DCFH-DA)[21,249]. However, many probes are not appropriate for the measurement of ROS generation under irradiation. For example, DCFH changes from its nonfluorescent form to the fluorescent molecule dichlorofluorescein (DCF) when oxidized by ROS, specifically hydroxyl radicals ($^{\bullet}OH$). However, the dye also degrades in the presence of UV light, decreasing the measured fluorescence and confounding data interpretation[21]. Fluorescein (FL) has been used by Wormington et al. to determine the impact of natural organic matter and UV intensity on photocatalytic $^{\bullet}OH$ generation by anatase TiO_2 NPs[250]. Higher concentrations of produced $^{\bullet}OH$ were found to correlate to increased mortality to *Daphnia magna* in standard toxicity assays[250,292]. FL is a fluorescent compound that is nonfluorescent once oxidized by $^{\bullet}OH$ produced by TiO_2 or by peroxide formed by the FL dye itself under irradiation[293]; irradiation controls with no NPs present can be used to determine the difference. FL has over ten times the chemiluminescence intensity of DCF, and provides the most sensitive (but not the most specific) detection of the $^{\bullet}OH$ out of the xanthene dye family[294].

The measured decrease in fluorescence intensity after irradiation alone and irradiation with the TiO_2 NPs present is summarized in Figure 4.3 for each water chemistry condition. The control samples, which were not exposed to irradiation or TiO_2 NPs, exhibited increases in fluorescence intensity that followed the trend of pH 5.8 < pH 7.4 = PBS media, consistent with earlier reports that the fluorescence intensity of FL decreases with decreasing pH and is unaffected by moderate changes to salinity[295]. A greater decrease in fluorescence proportional to the control samples indicates greater generation of ROS within a sample. For all three TiO_2 NP conditions (P25, anatase, and irradiation control), the greatest percent decrease in fluorescence was observed in the PBS media, followed by the pH 7.4 water, and then the pH 5.8 water. Without a standard curve of $^{\bullet}OH$ production, quantitative comparisons between the three media types are not possible. However, within each water chemistry condition, the P25 NPs caused a greater fluorescence decrease than the anatase NPs, indicating greater ROS production by the P25 NPs.

This was confirmed using a Student's *t* test with 95% confidence intervals (p-values were 0.0057, 0.0031, and 0.0051 for the pH 5.8, pH 7.4, and PBS media, respectfully).

This result is consistent with previous examinations of P25 and anatase TiO_2. One previous study used ESR to measure the relative production of $^{\bullet}OH$ by different TiO_2 NPs under UVA irradiation, and determined that P25 produced more $^{\bullet}OH$ than two different types of pure anatase NPs[296]. ESR was also used to probe the mechanism for this increase in ROS production. It was found that the electron-hole pairs produced by the rutile TiO_2 at the crystal phase interface are transferred to the anatase phase instead of recombining, increasing total ROS production[297]. Greater $^{\bullet}OH$ production by P25 versus anatase TiO_2 under irradiation has also measured using the fluorescent probe terephthalic acid[298]. One benefit of using fluorescent probes over ESR is that they can be employed under the same simulated treatment conditions (e.g. mixing within a reactor) as the contaminant degradation or microbial inactivation experiments that they are being compared to, as long as the probe is stable in the thermal and chemical conditions tested. This allowed for the validation of the previous ESR studies in relevant aquatic media.

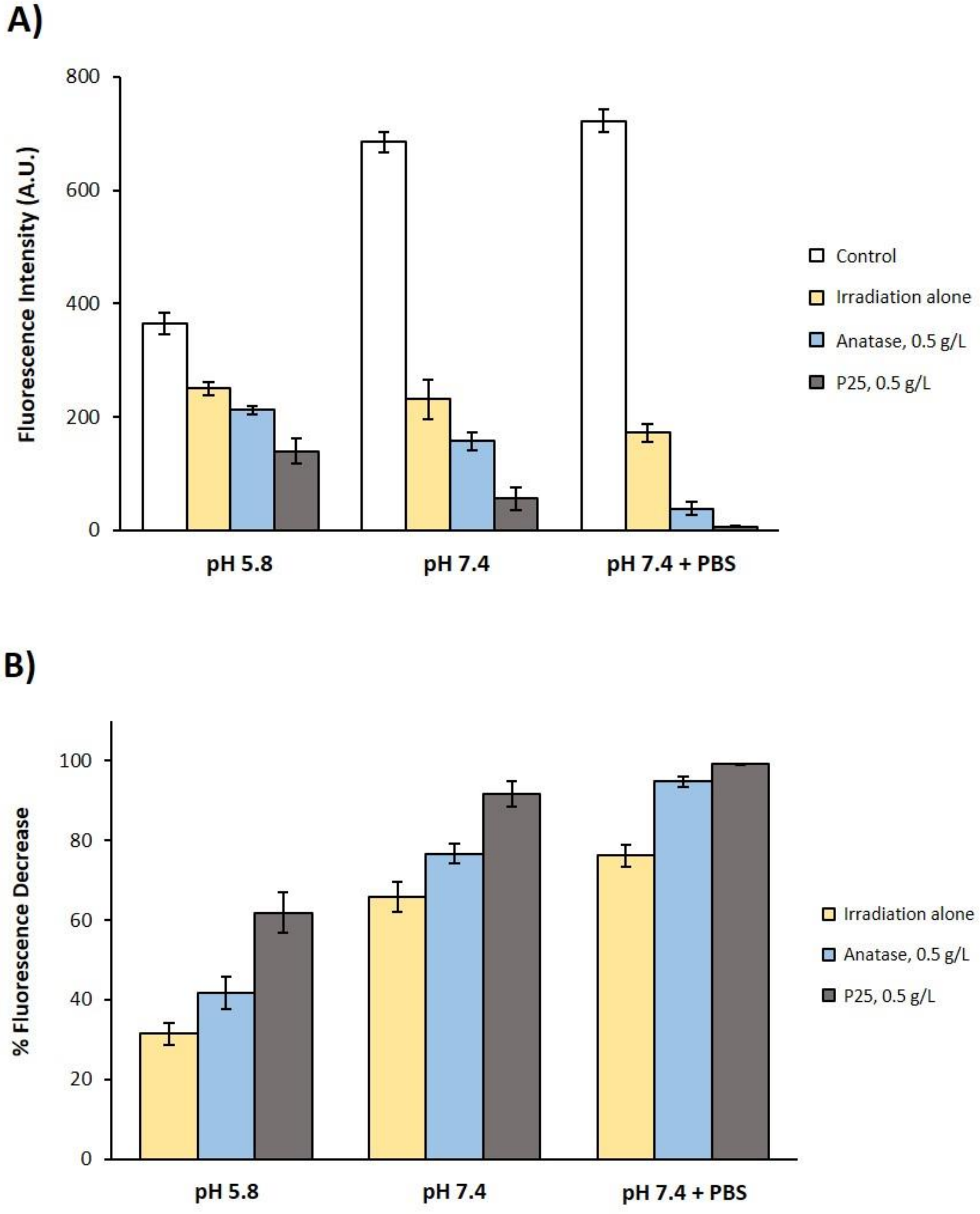

Figure 4.3. A) The measured total fluorescence of samples with fluorescein dye in each water chemistry and NP exposure condition. B) The % decrease in fluorescence compared to the control at each exposure condition. A greater decrease in fluorescence indicates that more ROS has been generated. Error bars represent standard deviations of triplicate measurements.

4.4.6 XPS Analysis

To identify the oxidative and compositional changes taking place on the TiO_2 NP surfaces, XPS analysis was performed on NP samples collected from each aqueous media before and after 1 h of simulated solar irradiation. Changes in the oxidation state of Ti on the TiO_2 NP surfaces due to the formation of coordinatively unsaturated Ti sites would cause an additional peak shoulder to form in the Ti2p spectrum at 455.3 eV to represent the Ti^{3+} oxidation state[299]. No changes were observed to the sharp Ti^{4+} (Ti $2p_{3/2}$) peaks at the binding energy of 458.6 eV in any of the irradiation or water chemistry conditions tested. Representative spectra of the anatase TiO_2 NPs in pH 7.4 water before and after irradiation are presented in Figure 4.4. All other spectra are included in the SI (Appendix B). The lack of irradiation-induced changes to the Ti2p spectrum was also observed in previous studies by Simonsen et al. and Krishnan et al.[269,300,301].

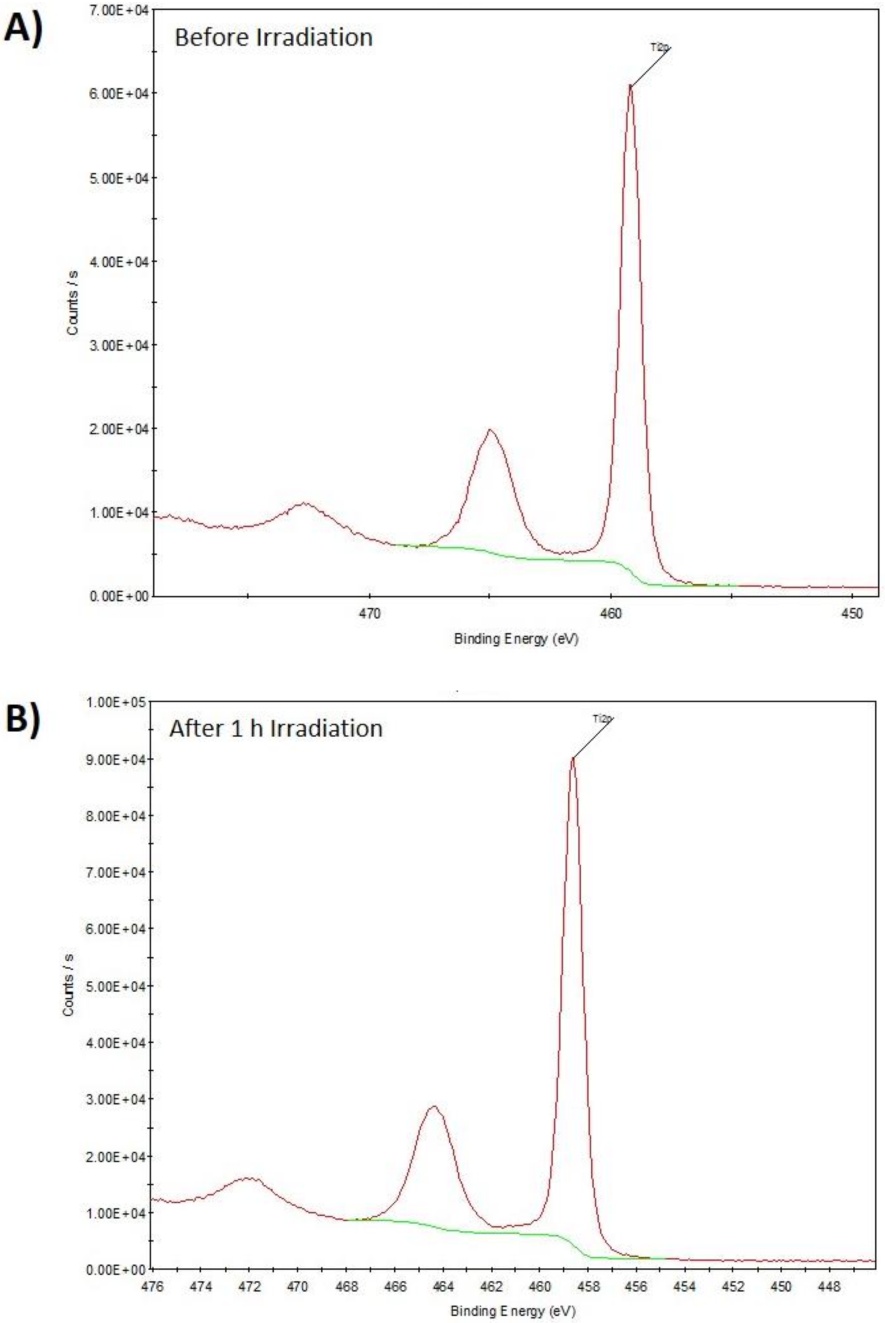

Figure 4.4. The Ti2p spectra of anatase NPs in pH 7.4 water A) before irradiation, and B) after 1 h of irradiation with simulated solar light.

The O1s spectra of the P25 TiO_2 NPs in PBS media before irradiation is presented in Figure 4.5 as a representative example (all O1s spectra and peak fitting is included in the SI). Each O1s spectra was fitted with two Gaussian functions. The first peak, with a binding energy of approximately 530 eV, was assigned to the Ti-O from the TiO_2 lattice. The second peak, with a binding energy of approximately 531 eV, is assigned to oxygen present on the TiO_2 surface as bound hydroxyl groups and in carbonyl species. These O1s peak assignments have been previously utilized in the literature, usually without the deconvolution of the carbonyl oxygen peak from the hydroxyl oxygen peak[269,300–302].

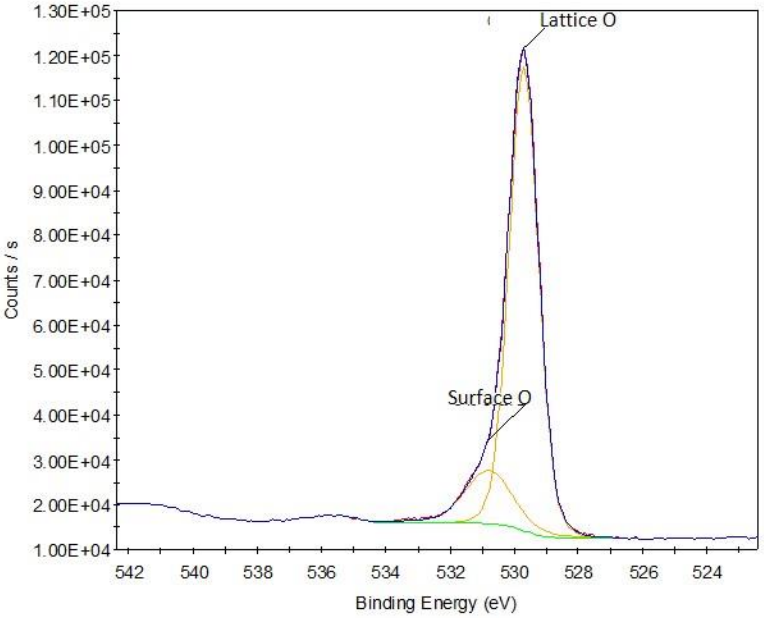

Figure 4.5. The O1s spectra of P25 NPs in PBS media before irradiation.

The modeled O1s peak data for P25 and anatase TiO_2 NPs in each water chemistry and irradiation condition is summarized in Table 4.3. For two of the NP samples in PBS media, SiO_2 was present from the sample substrate. These samples were the P25 NPs after irradiation and the anatase NPs prior to irradiation, and they are shown in red in Table 4.3. The Si content was 1.54% for the irradiated P25 sample and 4.51% for the ambient anatase sample. The O1s binding energy for SiO_2 has been reported to be 533.1 eV, so this is likely to artificially increase the amount of surface oxygen measured in these samples even though no additional shoulder was visible in the spectra[303].

The amount of oxygen present on the NP surfaces changes as the aquatic media is varied. For both NP types, before and after UV irradiation, the amount of surface oxygen follows the trend of pH 5.8 < pH 7.4 < PBS media. The trends in the effect of irradiation differed between the two NP types. For the P25 NPs, the relative amount of surface oxygen decreased in the pH 5.8 media and increased in the pH 7.4 media. For the anatase NPs, the relative amount of surface oxygen increased in both the pH 5.8 and pH 7.4 media. The PBS media samples were impacted by the presence of SiO_2 and as such are excluded from this comparison.

Previous XPS studies of irradiation on TiO_2 surfaces have focused on TiO_2 thin films exposed to both UV and visible light[300,301]. It was observed that light exposure increased both the surface oxygen and the total oxygen, which the authors attributed to the increased presence of hydroxyl oxygen bound to the surface[300,301]. An increase in the hydroxyl content on the TiO_2 surface has been shown to enhance both hydrophilicity and photocatalytic activity[304], with the rate of contaminant degradation having a linear relationship to the amount of surface adsorbed hydroxyl groups[301]. A comparison of thin films composed of P25 TiO_2 NPs versus anatase NPs showed that the P25 samples had a greater total amount of hydroxyl groups both before and after UV irradiation, but that the anatase sample had a greater increase in hydroxyl groups after irradiation (32.1% versus 23.9%)[301]. In this study, the surface oxygen content of the anatase NPs was greater than that of the P25 NPs before irradiation in all media tested. After irradiation, the surface oxygen content of the anatase NPs was greater than the P25 NPs in the pH 5.8 media, and slightly lower than the P25 NPs in the pH 7.4 media. This difference from previous results likely arose from the contribution of carbon-bound oxygen to the surface oxygen peak. In previous studies, the % carbon was very low compared to this study, and the fact that the surface bound oxygen does not always increase after UV irradiation also indicates that the contribution of the carbon-bound oxygen to the surface oxygen peak is greater in this study than in the previous studies. Therefore, the surface oxygen peak cannot be assumed to be representative of hydroxyl oxygen alone. Despite this limitation, the total ratio of oxygen to titanium increased in all samples after irradiation, and could potentially be the more relevant predictor of behavior in more complex aquatic media.

Table 4.3. Fitted parameters for the O1s XPS spectra for TiO_2 NP samples before and after 1 h irradiation with simulated solar light. The presence of SiO_2 was found in two samples, which could potentially impact the O1s parameters. The values that could be impacted by the SiO_2 are highlighted in red.

	P25			**Anatase**		
	pH 5.8	pH 7.4	PBS	pH 5.8	pH 7.4	PBS
O 1s Peak Data						
O surface %	6.0	8.9	16.5	8.0	12.3	22.7
O lattice %	94.0	91.1	83.5	92.0	87.7	77.3
O surface / Ti	0.12	0.19	0.32	0.16	0.26	0.44
O lattice / Ti	1.87	2.16	2.10	1.87	2.04	2.04
O total / Ti	1.88	2.05	2.06	1.83	2.06	2.01
O 1s Peak Data After Irradiation						
O surface %	4.8	15.1	19.0	8.1	14.6	19.0
O lattice %	95.2	84.9	81.0	91.9	85.4	81.0

O surface / Ti	0.10	0.32	0.35	0.16	0.30	0.36
O lattice / Ti	1.99	2.37	2.51	2.03	2.33	2.63
O total / Ti	1.98	2.41	2.55	2.00	2.41	2.48
% Relative Change in O Surface / Ti After Irradiation	-20.72	66.97	9.61	2.79	14.76	-17.78
% Relative Change in O Lattice / Ti After Irradiation	6.42	9.75	19.70	8.68	13.97	29.36
% Relative Change in O Total / Ti After Irradiation	5.07	17.78	23.49	8.84	17.11	23.46

The C1s spectra of the P25 TiO_2 NPs in PBS media before and after irradiation are presented in Figure 4.6. The C1s spectra were modeled with four gaussian functions, representing aliphatic C (284.8 eV), hydroxyl C (~286 eV), epoxy C (~287.5 eV), and carbonyl C (~289 eV). For each sample, the aliphatic carbon was the dominant carbon species, ranging from 62-72% of the total carbon.

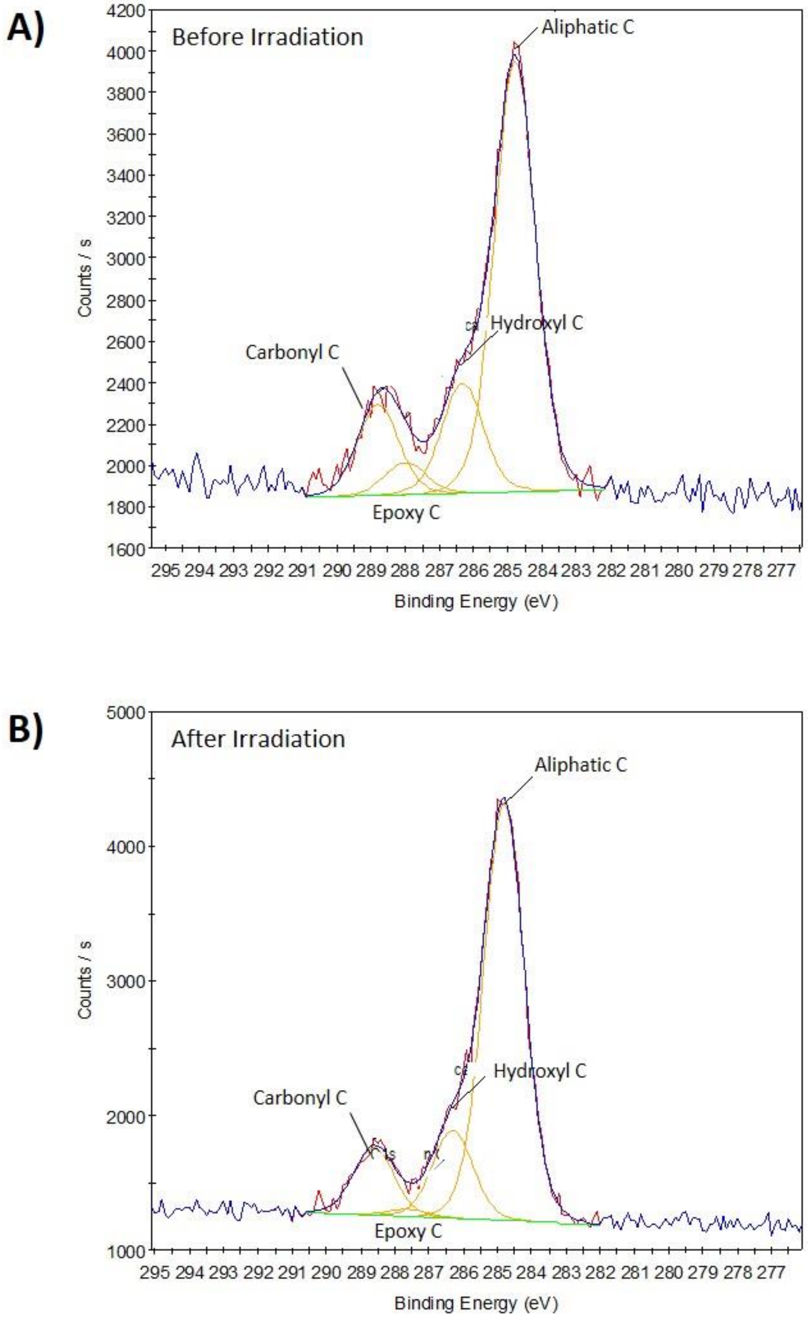

Figure 4.5. The C1s spectra of P25 NPs in PBS media A) before irradiation, and B) after 1 h of irradiation with simulated solar light. The for modeled Gaussian peaks are assigned to aliphatic, hydroxyl, epoxy, and carbonyl C as labeled.

The modeled C1s data is summarized in Table 4.4. The changes in aliphatic and total carbon after irradiation followed the same trends for both TiO_2 NP types. The aliphatic and total carbon both decreased for the pH 5.8 condition and increased for both the pH 7.4 and PBS media conditions, with the greatest increase occurring in the PBS media. The P25 sample in PBS media had a much greater increase in aliphatic and total carbon after irradiation than the anatase sample. The anatase NPs had a greater decrease after irradiation for the pH 5.8 condition, and a greater increase for the pH 7.4 conditions.

Previous studies have shown a pronounced decrease in both the total and aliphatic carbon present when TiO_2 powders and thin films are exposed to UV light in the presence of oxygen[41,269,305]. In these studies, the TiO_2 was never exposed to the ambient atmosphere during the irradiation, using either atmospheric controlled chambers or *in situ* studies with ambient pressure XPS to avoid this complication. In this work, the goal was to identify if these changes can still be observed for TiO_2 NPs exposed to normal atmospheric impurities and different water chemistries, so no such controls were performed. The carbon content of the sample has been linked to hydrophilicity, which increases as the C/Ti ratio decreases, and to catalytic activity, which has been shown to increase with the ratio of aliphatic C to Ti[41,306]. The ratios of C/Ti are greater than what would be expected from atmospheric impurities, so there is likely some contamination within the solutions. Since increases in C/Ti were observed in the pH 7.4 media and very large increases were observed in PBS media, it is possible that the pH adjustment solutions and the 10X PBS media concentrate contained some amount of carbon contamination.

Future work will need to determine and eliminate the source of carbon contamination before mechanistic relationships can be truly quantified.

Table 4.4. Fitted parameters for the C1s XPS spectra for TiO_2 NP samples before and after 1 h irradiation with simulated solar light.

	P25			**Anatase**		
	pH 5.8	pH 7.4	PBS	pH 5.8	pH 7.4	PBS
C 1s Peak Data						
% $C_{aliphatic}$	62.7	63.1	64.8	64.9	64.0	64.6
$C_{aliphatic}$ / Ti	0.16	0.14	0.16	0.19	0.15	0.19
C_{total} /Ti	0.26	0.20	0.24	0.30	0.24	0.29
C 1s Peak Data After Irradiation						
Aliphatic C %	69.2	64.4	71.9	62.3	65.9	68.6
$C_{aliphatic}$ / Ti	0.14	0.15	0.40	0.11	0.23	0.30
C_{total} /Ti	0.23	0.23	0.55	0.17	0.34	0.43
% Relative Change in $C_{aliphatic}$ / Ti After Irradiation	-13.4	4.5	151.8	-45.3	46.4	58.9
% Relative Change in C_{total} /Ti After Irradiation	-11.6	15.3	127.0	-43.0	42.2	49.7

It is also important to consider that additional ions were present on the TiO_2 NP surfaces that were exposed to the PBS media. Phosphorus, sodium, and chloride remained on the surface even after the washing steps that were taken prior to XPS analysis. The content of these species before and after irradiation is summarized in Table 4.5. The Na content is significant in each sample, and in the P25 sample it is greater than the total C content prior to irradiation. After irradiation, the Na content is reduced for both NP types, with a greater reduction taking place for the P25. The P content is smaller than the aliphatic C content on the two NP surfaces, and also decreases slightly after irradiation. The Cl content is negligible.

Some effects of the presence of these common anions and cations to TiO_2 photocatalytic activity have been studied. Studies of Na have primarily focused on substitution within the lattice structure taking placing during the crystallization process, which does not apply here[307]. However, Ti-O-Na bonds on the surface have also been observed[307,308]. It has been proposed that these bonds decrease the photocatalytic activity of TiO_2 by promoting the recombination of electron-hole pairs, which would decrease hydroxyl radical formation[308,309]. TiO_2 NPs modified to have a surface P/Ti ratio of 0.09 (very comparable to the ratios observed in this study) were more efficient at the photocatalytic degradation of organic contaminants when compared to the unmodified TiO_2 NPs that contained no surface phosphates, even though the adsorption of the organic substrates decreased[310]. The proposed mechanism of the photocatalytic enhancement was an increase in the charge separation of electron-hole pairs caused by the formation of a negative electrostatic field, which resulted in increased production of hydroxyl radicals[310]. A recent study of humic acids also confirmed that TiO_2 interactions with phosphate decrease the adsorption of organic materials[311].

Table 4.5. XPS elemental ratios for additional ions present in TiO_2 NP samples in PBS media before and after 1 h irradiation with simulated solar light.

	P25	Anatase
PBS Media Data		
Na/Ti	0.31	0.23
P/Ti	0.10	0.09
Cl/Ti	0.04	0.00
PBS Media Data, After Irradiation		
Na/Ti	0.15	0.15
P/Ti	0.08	0.07
Cl/Ti	0.00	0.00
% Relative Change in Na / Ti After Irradiation	-52.1	-35.0

Overall, XPS analysis revealed that both water chemistry and UV irradiation impacted the composition of TiO_2 NP surfaces, specifically the surface content of oxygen, total and aliphatic carbon, and the PBS media components Na and P. The relationships between the surface composition of the TiO_2 NPs and other relevant properties like hydrophobicity, aggregation state, and $^{\bullet}OH$ generation were further examined.

4.4.7 Relationships between XPS and other properties

Previous studies have linked the surface content of both oxygen and carbon to the hydrophobic/hydrophilic character of TiO_2[41,304]. An increase in surface oxygen has been shown to decrease hydrophobicity, while increased levels of surface carbon increase hydrophobicity[41,304]. Using the method of comparing rose bengal dye adsorption, this work found that the relative hydrophobicity of P25 and anatase NPs at pH 5.8 was comparable, and that irradiation with simulated solar light caused a slight decrease in hydrophobicity (Figure 4.2). The XPS analysis showed that the P25 and anatase NPs in pH 5.8 media had similar levels of both surface and total oxygen, and that the levels of total oxygen slightly increased after irradiation. The aliphatic and total carbon both decreased after irradiation for the pH 5.8 condition of both NP samples. When the data for the pH 5.8 condition is examined alone, the conclusions drawn from previous studies are supported. In addition, an increase in pH from 5.8 to 7.4 resulted in lower rose bengal adsorption (assumed to be a result of lower hydrophobicity) and greater total and surface oxygen content for both NP types, which is also supported by the previous data. However, some inconsistencies remain.

The surface oxygen decreased after irradiation for the sample of P25 NPs in pH 5.8 media, but slightly increased for the anatase NPs (Table 4.3). This could be a result of the surface oxygen being the lowest in this sample, and therefore being the most affected by the contributions from carbon-bound oxygen. Both the total and aliphatic carbon content increased as the pH increased, the opposite of the hydrophobicity trend. The total and aliphatic carbon also increased after irradiation for both NP types in the pH 7.4 and PBS media, while the surface oxygen decreased after irradiation for the anatase NPs in the PBS media. These results indicate that total oxygen is the best predictor of hydrophobicity for TiO_2 NPs in aquatic media, as opposed to surface oxygen or carbon species. This is likely the case because the total oxygen is less affected by the difference between carbon-bound versus hydroxyl oxygen in the samples, which were not separated within the surface oxygen peak. The carbon data in this study is unreliable for the prediction of NP properties due to contamination. Furthermore, the conclusions of previous XPS studies performed on clean solid surfaces in the absence of atmospheric exposure or aquatic media, in which the C/Ti ratios decreased after irradiation and created hydrophilic surfaces, could not be directly applied to this study of TiO_2 NPs due to the presence of carbon from an undetermined source, likely impurities within the test media.

The relationship between $^{\bullet}OH$ production and XPS results was also considered. Previously, photocatalytic activity, assumed to be the result of increased $^{\bullet}OH$ production, was shown to increase with the amount of surface adsorbed oxygen and initial aliphatic carbon content[301,306]. In this study the P25 NPs were shown to produce more $^{\bullet}OH$ (Figure 4.3), but conclusions could not be drawn about the impact of water chemistry. The previous conclusions about relationships between XPS data and $^{\bullet}OH$ production could not be confirmed by this work. P25 NPs had lower or equivalent surface oxygen compared the anatase samples. With regard to aliphatic carbon, P25 NPs had a lower content than anatase NPs in all samples prior to irradiation, and also had a lower content in the pH 7.4 media after irradiation.

These experiments were performed in aquatic media with different water chemistry conditions to determine if previous conclusions on the mechanisms behind TiO_2 NPs could be confirmed in more environmentally-relevant systems, quantified, and connected to larger scale properties and behavior. The added complexity resulted in changes to the expected relationships between the surface composition and the relative hydrophobicity and $^{\bullet}OH$ generation, primarily due to the impact of carbon contamination. In future work, some of the mechanistic insight may be able to be recovered through the purging of the aquatic samples with clean O_2, followed by irradiation in a completely sealed container for longer periods of time. No relationships were observed between the XPS data and $^{\bullet}OH$ generation; however, the ratio of total oxygen to titanium did follow the same trends as the NP hydrophobicity.

The impact of these surface and extrinsic properties on the overall photocatalytic degradation of organic contaminants was explored using MB dye as a model contaminant.

4.4.8 MB Dye Degradation

The photocatalytic degradation of MB dye is commonly utilized in protocols for evaluating the efficacy of photocatalysts like TiO_2 NPs[260,312]. MB dye photodegradation by anatase and P25 TiO_2 NPs in different aqueous media is summarized in Figure 4.6. P25 NPs were more effective than anatase NPs in every medium tested, requiring much lower doses to reach complete degradation. Figure 4.6B illustrates that this difference cannot be ascribed to differences in the BET surface area between the two particle types. MB dye removal by adsorption and thermal degradation was also tested, using TiO_2 NP doses of 5000 mg/L, and these removal rates remained below 3% for all conditions tested (results included in SI).

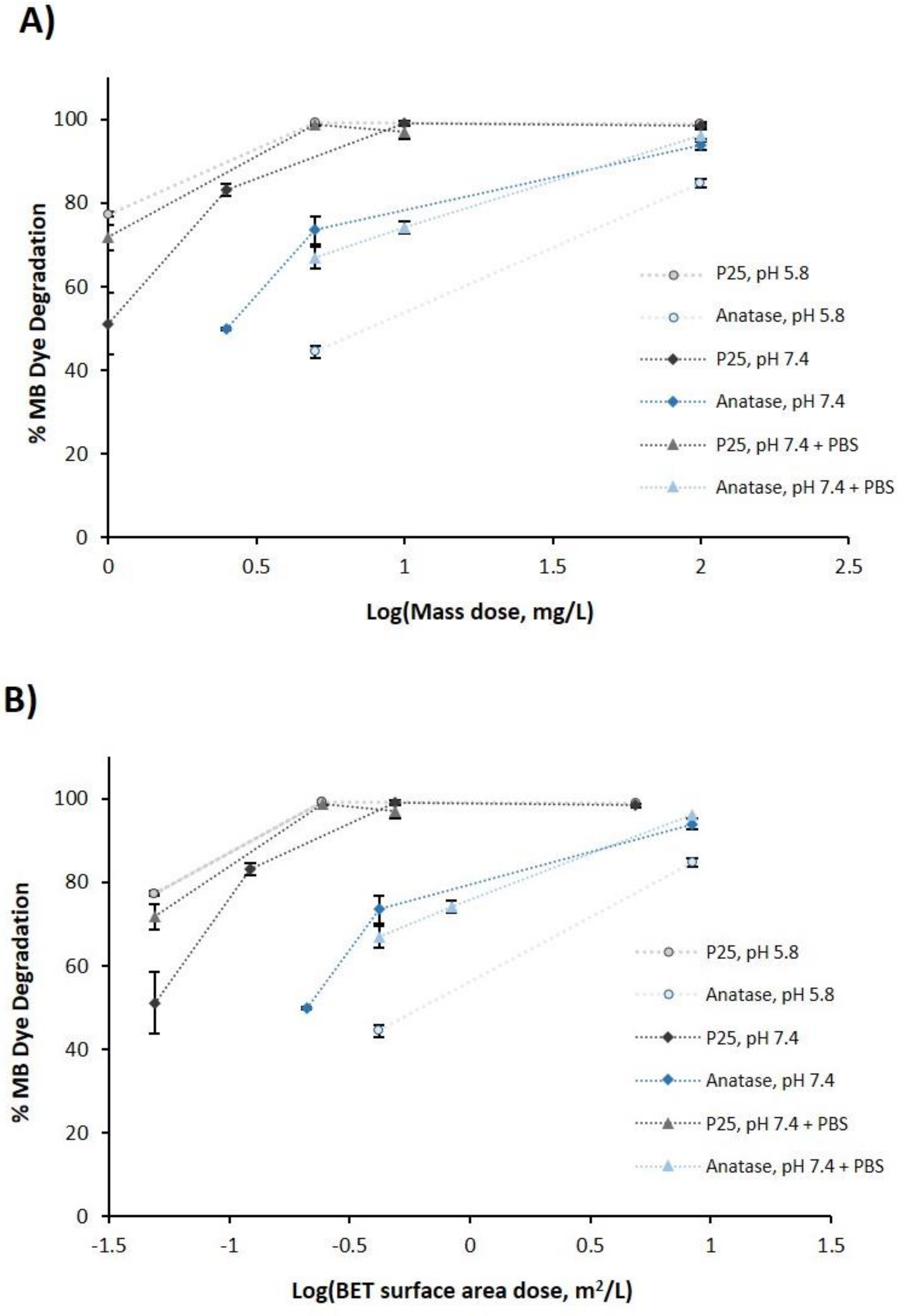

Figure 4.6. The photocatalytic degradation of methylene blue dye after 1 h of exposure to simulated solar light as a function of the A) mass dose of TiO_2 NPs, and B) BET-derived surface area dose of TiO_2 NPs. Error bars represent standard deviations of triplicate samples.

Figure 4.7 summarizes the impact of water chemistry on the degradation of MB dye by P25 NPs, anatase NPs, and irradiation alone. Opposite trends can be observed for the two NP types. For P25 NPs, the % MB dye degradation increases from pH 7.4 < PBS media < pH 5.8, while for the anatase NPs the % MB dye degradation increases from pH 5.8 < PBS media < pH 7.4. MB dye degradation by irradiation alone increases slightly as the pH increases from 5.8 to 7.4, with no differences observed from the presence of the PBS media. The DLS-derived surface area was also shown to be affected by the aqueous media (Table 4.2). To determine if these trends in surface area relate to the differences observed in MB dye degradation, the mass dose of TiO_2 NPs was converted to a surface area dose for the two NP types. Figure 4.8 shows that these changes in surface area do not fully account for the differences in the effects of water chemistry.

Previous studies have also found that mixed phase TiO_2 like Degussa P25 is a more effective photocatalyst than pure anatase TiO_2, and have attributed this effect to the increased production of hydroxyl radicals caused by charge transfer between the two crystal phases[24,313–315]. The effects of the aqueous media on MB dye degradation have also been explored. In one study, MB dye photodegradation by TiO_2 increased as the pH was increased from 3, to the range of 6-7, to 9, which was attributed to enhanced adsorption of the positively charged MB dye molecule onto the increasingly negative TiO_2 surface[37,38]. While an increase in MB dye degradation by P25 NPs with increases in pH was not observed in this work, the previous studies did not examine smaller increases in pH or consider the potential effects of aggregation. The enhanced MB dye degradation rates of mixed-phase TiO_2 NPs like P25 have also been shown to be heavily affected by pH. In one study, 90% rutile TiO_2 NPs were more efficient than 15% rutile NPs at pH 4, less efficient at pH 10, and had equivalent rates of degradation at pH 7[313]. The synergistic effect of pH and crystal phase composition was attributed to the promotion of electron transfer from anatase to rutile in acidic media and the promotion of hole transfer from rutile to anatase at neutral and basic media[313]. The results of this study may also indicate that pH has a unique effect on mixed-phase TiO_2 NPs, but it is important to take into account the other properties examined here (i.e. aggregation state).

The effect of ionic strength has also been studied, and the presence of NaCl has been shown to decrease the degradation of MB dye by P25 NPs[290], the opposite of what was observed in this study for P25 photoactivity in pH 7.4 media versus PBS media. In this study, the PBS media imparts not only ionic strength but also buffering capacity, which is typically not present in studies of MB photodegradation by TiO_2. As the MB dye is degraded in the unbuffered pH 5.8 and pH 7.4 samples, the pH decreases to the range of pH 5.3-5.6 and pH 6.0-6.7, respectively (see SI for details). There is a greater decrease in pH with greater amounts of MB degradation, consistent with the proposed pathway of MB dye degradation that releases several acidic components throughout the process[38]. Due to the increased degradation of MB dye by P25 when compared to anatase, the pH changes are more prominent and the presence of the buffer is more likely to positively impact the degradation process.

The process of MB dye degradation by TiO_2 NPs involves a balance of the effects of aggregation, the interactions between the dye and TiO_2 surface, and the potential for the TiO_2 surface to generate ROS. These relationships were explored in more detail.

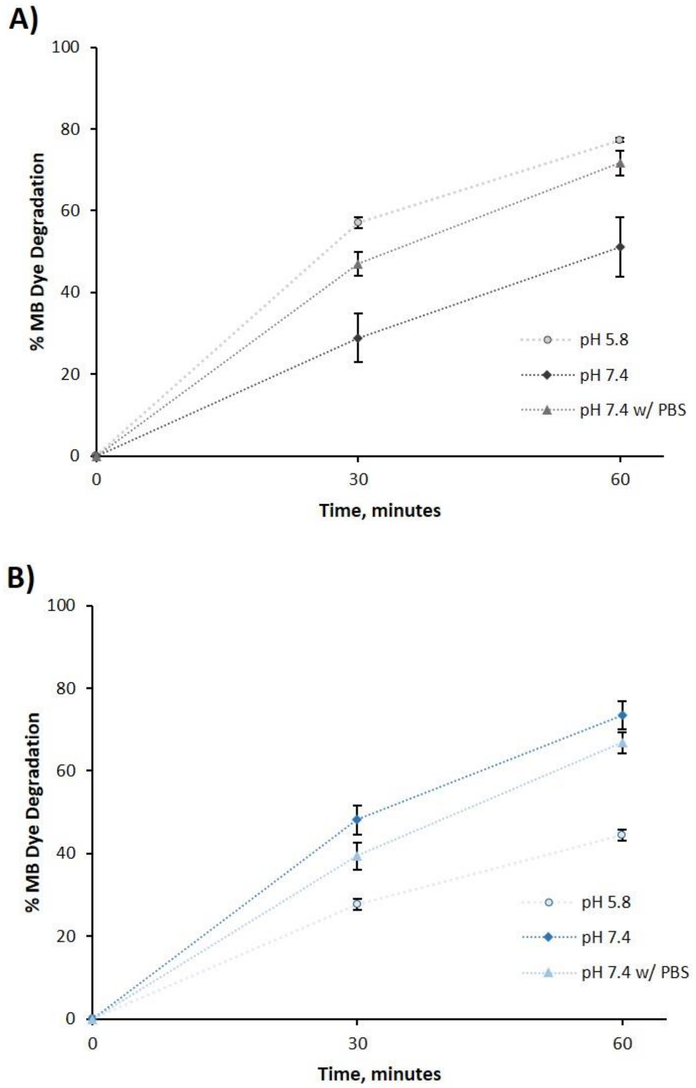
A)
100
80
60
40
20
0
% MB Dye Degradation
0
30
60
Time, minutes
pH 5.8
pH 7.4
pH 7.4 w/ PBS
B)
100
80
60
40
20
0
% MB Dye Degradation
0
30
60
Time, minutes
pH 5.8
pH 7.4
pH 7.4 w/ PBS

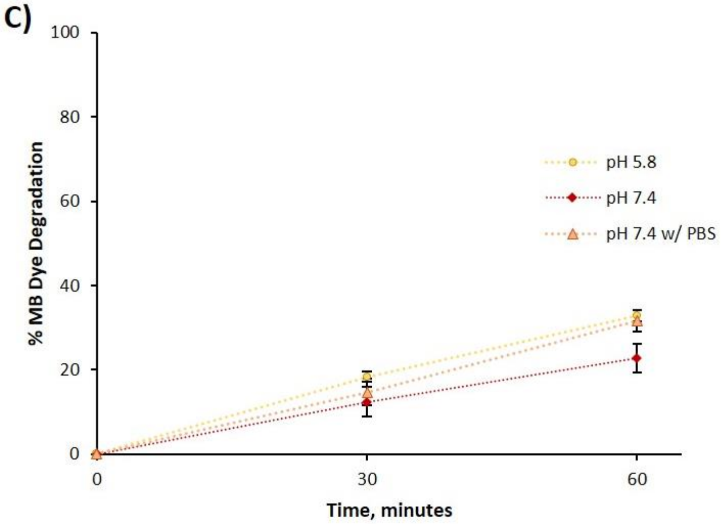

Figure 4.7. The effect of water chemistry on the photocatalytic degradation of methylene blue dye during exposure to simulated solar light by A) 1 mg/L P25 NPs, B) 5 mg/L anatase NPs, and C) irradiation alone. Error bars represent standard deviations of triplicate samples.

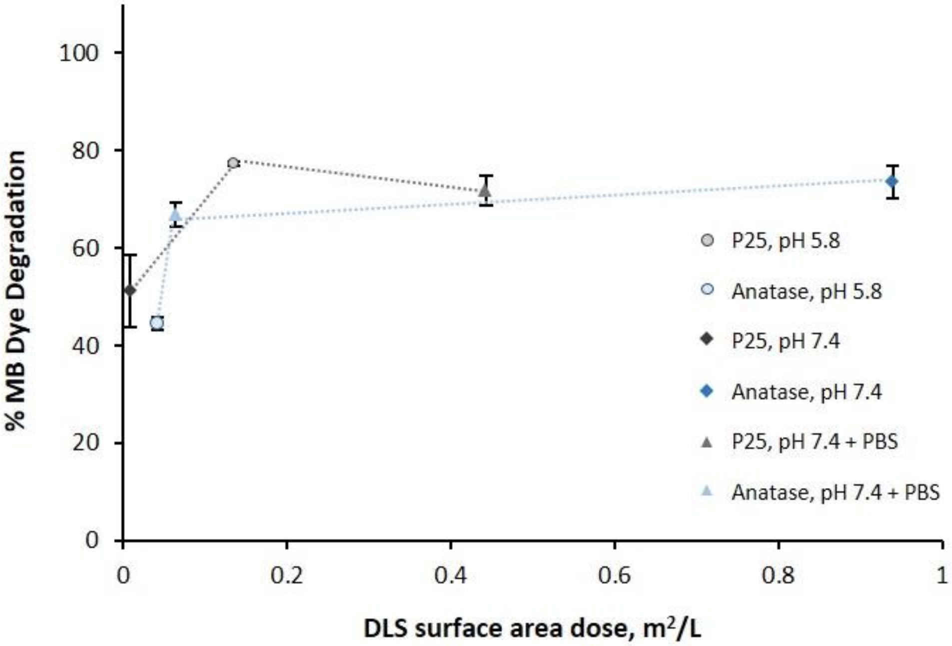

Figure 4.8. The photocatalytic degradation of methylene blue dye after 1 h exposure to simulated solar light by P25 and anatase Nps in pH 5.8, pH 7.4, and PBS media, presented as a function of the DLS-derived surface area dose. Error bars represent standard deviations of triplicate samples.

4.4.9 Relationships between properties and dye degradation

No direct correlations were observed between trends in XPS-derived surface composition and MB dye degradation. However, there were some relationships between the NP properties examined and overall MB degradation that can be organized into a hierarchy of 1) crystal structure and ROS generation, 2) decrease in pH during MB degradation, and 3) aggregation state. P25 outperformed anatase NPs in all media tested, and also produced the most $^{\bullet}OH$. This difference could not be described by surface area or aggregation state, indicating that the crystal structure is more relevant than these properties. For both the P25 and anatase NPs, the difference in activity between the pH 5.8 and pH 7.4 samples directly follows the trends in the DLS-determined surface area (Figure 4.8). When comparing the pH 7.4 samples with and without the presence of PBS, the extent of the pH decrease in the unbuffered sample was the predictor of whether the PBS would enhance or decrease MB degradation. For the P25 NPs, greater MB degradation led to more of a decrease in pH when compared to the anatase NPs. Therefore, the addition of PBS enhanced MB degradation for the P25 TiO_2 NPs at pH 7.4. For the anatase NPs, the decrease in pH was less pronounced, and the impact of the enhanced aggregation and sedimentation outweighed the benefits of the added buffering capacity. The hydrophobicity was not directly related to the MB dye degradation efficiency, likely because the cationic properties of the dye dictate that electrostatic interactions will drive adsorption to the TiO_2 surface. In the case of a nonpolar, hydrophobic organic contaminant, hydrophobicity may have more impact.

Overall, this study provides a method for exploring changes in surface properties likely to occur during treatment applications of TiO_2 NPs in complex waters, and for comparing the properties and efficacy of multiple NP types in a realistic treatment scenario. In addition to discovering that the most important properties predicting TiO_2 treatment efficacy were NP crystal structure, pH stability, and aggregation state, it was found that the DLS-derived surface area was more relevant than BET-derived surface area despite the latter being the more commonly reported value. Previous ESR observations of the impact of crystal structure on $^{\bullet}OH$ generation were also validated across multiple aquatic media. Unfortunately, previously determined relationships between the surface composition of TiO_2 NPs and their photocatalytic efficiency were not observable due to complications from an unknown source of carbon within the sample. Future work in the surface analysis aspect of this work should include determining the source of the carbon contamination, and using Fourier transform infrared spectroscopy as an orthogonal method to more specifically probe the relative contributions of surface bound hydroxyl groups versus carbon bound oxygen, providing additional information beyond what was acquired via XPS[316]. Contaminant degradation by TiO_2 involves complex relationship between the amount of available surface area, potential for surface to generate ROS, and contaminant-surface interactions, and thorough characterization in environmentally-relevant media is necessary for accurate mechanistic understanding.

5 Conclusion

This dissertation addresses the study of MONPs in environmentally-relevant systems, with a special emphasis on TiO_2 NPs. The importance of rigorous characterization to our understanding of nanomaterial behavior is highlighted throughout each of the presented studies.

Chapter 2 discussed the development and utility of gold core-labeled TiO_2 NPs (Au@TiO_2 NPs). To enable the detection and quantification of TiO_2 NPs within complex matrices, Au@TiO_2 NPs were prepared and quantified in complex media containing background titanium. The gold core enabled facile quantification in real environmental samples like activated sludge and a river water-sunscreen mixture. Multiple quantification techniques can be used, including both bulk and single-particle inductively-coupled plasma mass spectrometry (sp-ICP-MS), and instrumental neutron activation analysis (INAA). One unique benefit of this labeling approach is that INAA techniques can be used to quantify the labeled TiO_2 NPs present in a sample after the completion of the experiment, potentially allowing for the expansion of this technique to research facilities that do not have INAA facilities on site. Small differences in the ζ-potential and homoaggregation state were observed between the labeled and unlabeled particles. This core/shell labeling technique is recommended for experiments that require enhanced detection sensitivity and label stability over fluorescent dye labels, or would benefit from the application of sp-ICP-MS or INAA quantification strategies. Future research directions can include extending this approach to other core and shell materials. This work provides the field of environmental nanotechnology with a useful labeling tool that can be applied to the study of MONPs in complex samples.

Chapter 3 provided a detailed analysis of the existing MONP labeling strategies, contextualizing the Au@TiO_2 NPs within the current state of the literature. Fluorescent dyes, radioisotopes, stable isotopes, and dopant and core/shell labels were each discussed in detail. In general, fluorescent dyes provide the benefit of facile visualization and quantification at an inexpensive cost, but are the least resilient and sensitive label. Isotopic labeling techniques are the most expensive, but offer the greatest sensitivity. Core/shell and dopant labels provide flexibility in quantification, at a cost and sensitivity in between that of fluorescent dyes and isotopic labels, but an increased probability of affecting the electronic properties of MONPs. Recommendations for rigorous characterization of labeled MONPs were made, as the current literature contains relatively limited comparisons of the properties of labeled versus unlabeled MONPs. The choice of which labeling technique to use for a given study will depend on the requirements for detection sensitivity, label stability, cost and equipment, impact to MONP properties, and quantification. This work provides the field of environmental nanotechnology with useful guidance on choosing and executing a labeling strategy, and also has the potential to improve the reporting of key MONP properties for labeled versus unlabeled NPs.

Chapter 4 examined the behavior of two model TiO_2 NPs in a water treatment scenario, comparing the relative impact of surface elemental composition with other extrinsic properties. A balance was observed where the inherent ROS generation potential of the particles due to crystal structure outweighed all other properties, followed by the competing effects of the pH stability of the solution and the aggregation state of the media. No relationship between the fundamental surface properties identified by XPS and the degradation of the model organic contaminant methylene blue could be observed, but analyses were complicated by the presence of carbon contamination. This approach of characterizing the ROS generation potential, aggregation state, hydrophobicity, and elemental surface composition across multiple aquatic matrices can be used as a model to compare the treatment efficacy of different pure and hybridized photocatalytic NPs in increasingly complex media. Providing rigorous characterization of how the extrinsic properties of the NPs are likely to change in real-world treatment scenarios will inform better treatment design. The results of Chapter 4 confirm that the behavior of MONPs in complex matrices does not always line up with what is mechanistically expected in more simple systems, due to the variety of competing property transformations. This chapter provides the field of environmental nanotechnology with methodologies for the rigorous characterization of MONPs in water treatment scenarios.

This work as a whole has contributed to shifting the study of MONPs toward more relevant and complex matrices. This is vital to the determination of the potential environmental impacts, both positive and negative, of the increased production and use of these materials in the real world.

6 Bibliography

(1) Marambio-Jones, Catalina Hoek, E. A review of the antibacterial effects of silver nanomaterials and potential implications for human health and the environment. *J. Nanoparticle Res.* **2010**, *12*, 21.

(2) Dizaj, S. M.; Lotfipour, F.; Barzegar-Jalali, M.; Zarrintan, M. H.; Adibkia, K. Antimicrobial activity of the metals and metal oxide nanoparticles. *Mater. Sci. Eng. C* **2014**, *44*, 278–284.

(3) Thostenson, E. T.; Ren, Z.; Chou, T.-W. Advances in the science and technology of carbon nanotubes and their composites: a review. *Compos. Sci. Technol.* **2001**.

(4) Hardman, R. A toxicologic review of quantum dots: Toxicity depends on physicochemical and environmental factors. *Environmental Health Perspectives*. 2006.

(5) Bera, D.; Qian, L.; Tseng, T. K.; Holloway, P. H. Quantum dots and their multimodal applications: A review. *Materials*. 2010.

(6) National Nanotechnology Institute. *NNI Supplement to the President's 2018 Budget*; 2018.

(7) Aitken, R. J.; Chaudhry, M. Q.; Boxall, A. B. A.; Hull, M. Manufacture and use of nanomaterials: Current status in the UK and global trends. *Occup. Med. (Chic. Ill).* **2006**, *56* (5), 300–306.

(8) Piccinno, F.; Gottschalk, F.; Seeger, S.; Nowack, B. Industrial production quantities and uses of ten engineered nanomaterials in Europe and the world. *J. Nanoparticle Res.* **2012**, *14* (9), 1109.

(9) Peralta-Videa, J. R.; Zhao, L.; Lopez-Moreno, M. L.; de la Rosa, G.; Hong, J.; Gardea-Torresdey, J. L. Nanomaterials and the environment: A review for the biennium 2008-2010. *Journal of Hazardous Materials*. 2011.

(10) Gottschalk, F.; Kost, E.; Nowack, B. Engineered nanomaterials in water and soils: A risk quantification based on probabilistic exposure and effect modeling. *Environ. Toxicol. Chem.* **2013**.

(11) Adams, L. K.; Lyon, D. Y.; McIntosh, A.; Alvarez, P. J. J. Comparative toxicity of nano-scale TiO2, SiO2 and ZnO water suspensions. In *Water Science and Technology*; 2006; Vol. 54, pp 327–334.

(12) Kaweeteerawat, C.; Ivask, A.; Liu, R.; Zhang, H.; Chang, C. H.; Low-Kam, C.; Fischer, H.; Ji, Z.; Pokhrel, S.; Cohen, Y.; et al. Toxicity of metal oxide nanoparticles in

Escherichia coli correlates with conduction band and hydration energies. *Environ. Sci. Technol.* **2015**, *49* (2), 1105–1112.

(13) Huang, Y.-W.; Wu, C.; Aronstam, R. S. Toxicity of Transition Metal Oxide Nanoparticles: Recent Insights from in vitro Studies. *Materials (Basel).* **2010**, *3* (10), 4842–4859.

(14) Sharma, V. K. Aggregation and toxicity of titanium dioxide nanoparticles in aquatic environment--a review. *J. Environ. Sci. Health. A. Tox. Hazard. Subst. Environ. Eng.* **2009**, *44* (14), 1485–1495.

(15) Kamat, P. V.; Meisel, D. Nanoscience opportunities in environmental remediation. *Comptes Rendus Chimie*. 2003.

(16) Khin, M. M.; Nair, a. S.; Babu, V. J.; Murugan, R.; Ramakrishna, S. A review on nanomaterials for environmental remediation. *Energy Environ. Sci.* **2012**, *5* (8), 8075.

(17) Fujishima, A.; Zhang, X.; Tryk, D. A. TiO2 photocatalysis and related surface phenomena. *Surf. Sci. Rep.* **2008**, *63* (12), 515–582.

(18) Lee, S.-Y.; Park, S.-J. TiO2 photocatalyst for water treatment applications. *J. Ind. Eng. Chem.* **2013**, *19* (6), 1761–1769.

(19) Chong, M. N.; Jin, B.; Chow, C. W. K.; Saint, C. Recent developments in photocatalytic water treatment technology: A review. *Water Res.* **2010**, *44* (10), 2997–3027.

(20) Buxton, G. V; Greenstock, C. L.; Helman, W. P.; Ross, A. B. Critical Review of rate constants for reactions of hydrated electrons, hydrogen atoms and hydroxyl radicals (?OH/?O ? in Aqueous Solution. *J. Phys. Chem. Ref. Data* **1988**.

(21) Djurišić, A. B.; Leung, Y. H.; Ng, A. M. C.; Xu, X. Y.; Lee, P. K. H.; Degger, N.; Wu, R. S. S. Toxicity of Metal Oxide Nanoparticles: Mechanisms, Characterization, and Avoiding Experimental Artefacts. *Small* **2015**, *11* (1), 26–44.

(22) Batzill, M. Fundamental aspects of surface engineering of transition metal oxide photocatalysts. *Energy Environ. Sci.* **2011**, *4* (9), 3275.

(23) Luttrell, T.; Halpegamage, S.; Tao, J.; Kramer, A.; Sutter, E.; Batzill, M. Why is anatase a better photocatalyst than rutile?--Model studies on epitaxial TiO2 films. *Sci. Rep.* **2014**, *4*, 4043.

(24) Shi, L.; Weng, D. Highly active mixed-phase TiO2 photocatalysts fabricated at low temperatureand the correlation between phase compositionand photocatalytic activity. *J. Environ. Sci.* **2008**, *20* (10), 1263–1267.

(25) Cong, S.; Xu, Y. Explaining the High Photocatalytic Activity of a Mixed Phase TiO 2 : A Combined Effect of O 2 and Crystallinity. **2011**, 21161–21168.

(26) Jassby, D.; Farner Budarz, J.; Wiesner, M. Impact of aggregate size and structure on the photocatalytic properties of TiO2 and ZnO nanoparticles. *Environ. Sci. Technol.* **2012**, *46* (13), 6934–6941.

(27) Zhang, W. Nanoparticle Aggregation: Principles and Modeling; 2014; Vol. 811, pp 19–43.

(28) Derjaguin, B.; Landau, L. Theory of the stability of strongly charged lyophobic sols and of the adhesion of strongly charged particles in solutions of electrolytes. *Prog. Surf. Sci.* **1993**.

(29) Verwey, E. J. W.; Overbeek, J. T. G. Long distance forces acting between colloidal particles. *Trans. Faraday Soc.* **1946**, *42* (0), B117–B123.

(30) Loosli, F.; Stoll, S. Effect of surfactants, pH and water hardness on the surface properties and agglomeration behavior of engineered TiO 2 nanoparticles. *Environ. Sci. Nano* **2017**, *4* (1), 203–211.

(31) Wang, P.; Qi, N.; Ao, Y.; Hou, J.; Wang, C.; Qian, J. Effect of UV irradiation on the aggregation of TiO2in an aquatic environment: Influence of humic acid and pH. *Environ. Pollut.* **2016**, *212*, 178–187.

(32) Loosli, F.; Le Coustumer, P.; Stoll, S. Effect of natural organic matter on the disagglomeration of manufactured TiO2 nanoparticles. *Environ. Sci. Nano* **2014**, *1*, 154.

(33) Lin, D.; Ji, J.; Long, Z.; Yang, K.; Wu, F. The influence of dissolved and surface-bound humic acid on the toxicity of TiO 2 nanoparticles to Chlorella sp. *Water Res.* **2012**.

(34) von Moos, N.; Slaveykova, V. I. Oxidative stress induced by inorganic nanoparticles in bacteria and aquatic microalgae--state of the art and knowledge gaps. *Nanotoxicology* **2014**, *8* (6), 605–630.

(35) Friedmann, D.; Mendive, C.; Bahnemann, D. TiO2 for water treatment: Parameters affecting the kinetics and mechanisms of photocatalysis. *Appl. Catal. B Environ.* **2010**, *99* (3–4), 398–406.

(36) Gogniat, G.; Thyssen, M.; Denis, M.; Pulgarin, C.; Dukan, S. The bactericidal effect of TiO2 photocatalysis involves adsorption onto catalyst and the loss of membrane integrity. *FEMS Microbiol. Lett.* **2006**, *258* (1), 18–24.

(37) Id, C. R. E. F.; Ore, E.; Library, M. Influence of operational parameters on the TiO 2 photocatalytic degradation of Methylene blue. **2017**.

(38) Houas, A. Photocatalytic degradation pathway of methylene blue in water. *Appl. Catal. B Environ.* **2001**, *31* (2), 145–157.

(39) Feng, J.; Zhu, J.; Lv, W.; Li, J.; Yan, W. Effect of hydroxyl group of carboxylic acids on the adsorption of Acid Red G and Methylene Blue on TiO2. *Chem. Eng. J.* **2015**, *269*, 316–322.

(40) Fan, W.; Liu, L.; Peng, R.; Wang, W.-X. High bioconcentration of titanium dioxide nanoparticles in Daphnia magna determined by kinetic approach. *Sci. Total Environ.* **2016**, *569–570*, 1224–1231.

(41) Ohtsu, N.; Masahashi, N.; Mizukoshi, Y.; Wagatsuma, K. Hydrocarbon decomposition on a hydrophilic TiO2 surface by UV irradiation: Spectral and quantitative analysis using in-situ XPS technique. *Langmuir* **2009**, *25* (19), 11586–11591.

(42) Alrousan, D. M. A.; Dunlop, P. S. M.; McMurray, T. A.; Byrne, J. A. Photocatalytic inactivation of E. coli in surface water using immobilised nanoparticle TiO2films. *Water Res.* **2009**.

(43) Hall, S.; Bradley, T.; Moore, J. T.; Kuykindall, T.; Minella, L. Acute and chronic toxicity of nano-scale TiO2 particles to freshwater fish, cladocerans, and green algae, and effects of organic and inorganic substrate on TiO2 toxicity. *Nanotoxicology* **2009**, *3* (2), 91–97.

(44) Fu, L.; Hamzeh, M.; Dodard, S.; Zhao, Y. H.; Sunahara, G. I. Effects of TiO2 nanoparticles on ROS production and growth inhibition using freshwater green algae pre-exposed to UV irradiation. *Environ. Toxicol. Pharmacol.* **2015**, *39* (3), 1074–1080.

(45) Luo, Z. X.; Qiu, Z. Z.; Chen, Z.; Du Laing, G.; Liu, A. F.; Yan, C. Z. Impact of TiO2 and ZnO nanoparticles at predicted environmentally relevant concentrations on ammonia-oxidizing bacteria cultures under ammonia oxidation. *Environ. Sci. Pollut. Res.* **2015**, *22* (4), 2891–2899.

(46) Federici, G.; Shaw, B. J.; Handy, R. D. Toxicity of titanium dioxide nanoparticles to rainbow trout (Oncorhynchus mykiss): Gill injury, oxidative stress, and other physiological effects. *Aquat. Toxicol.* **2007**, *84* (4), 415–430.

(47) Labille, J.; Feng, J.; Botta, C.; Borschneck, D.; Sammut, M.; Cabie, M.; Auffan, M.; Rose, J.; Bottero, J. Y. Aging of TiO2 nanocomposites used in sunscreen. Dispersion and fate of the degradation products in aqueous environment. *Environ. Pollut.* **2010**, *158* (12), 3482–3489.

(48) Fouqueray, M.; Noury, P.; Dherret, L.; Chaurand, P.; Abbaci, K.; Labille, J.; Rose, J.; Garric, J. Exposure of juvenile Danio rerio to aged TiO2 nanomaterial from sunscreen. *Environ. Sci. Pollut. Res.* **2013**, *20* (5), 3340–3350.

(49) Santaella, C.; Allainmat, B.; Simonet, F.; Chanéac, C.; Labille, J.; Auffan, M.; Rose, J.; Achouak, W. Aged TiO 2 -Based Nanocomposite Used in Sunscreens Produces Singlet Oxygen under Long-Wave UV and Sensitizes Escherichia coli to Cadmium. *Environ. Sci. Technol.* **2014**, *48* (9), 5245–5253.

(50) Gottschalk, F.; Sun, T.; Nowack, B. Environmental concentrations of engineered nanomaterials: Review of modeling and analytical studies. *Environ. Pollut.* **2013**, *181*, 287–300.

(51) Gottschalk, F.; Sonderer, T.; Scholz, R. W.; Nowack, B. Modeled environmental concentrations of engineered nanomaterials (TiO2, ZnO, Ag, CNT, fullerenes) for different regions. *Environ. Sci. Technol.* **2009**, *43* (24), 9216–9222.

(52) Durum, W. .; Haffty, J. Occurrence of Minor Elements in Water. *Geol. Surv. Circ.* **1961**, *445*, 1–11.

(53) Safety, I. P. on C.; Titanium, W. T. G. on E. H. C. for. *Titanium*; World Health Organization: Geneva, 1982.

(54) Shkol’nik, M. I. *Trace Elements in Plants*; Elsevier Science: Burlington, 1984.

(55) Wang, J.; Hou, Y.; Ma, J. Titanium in Cells, Tissues, Organs, and Organisms. In *Encyclopedia of Metalloproteins*; Kretsinger, R. H., Uversky, V. N., Permyakov, E. A., Eds.; Springer New York: New York, NY, 2013; pp 2247–2248.

(56) Zierden, M. R.; Valentine, A. M. Contemplating a role for titanium in organisms. *Metallomics* **2016**, *8* (1), 9–16.

(57) von der Kammer, F.; Ferguson, P. L.; Holden, P. A.; Masion, A.; Rogers, K. R.; Klaine, S. J.; Koelmans, A. A.; Horne, N.; Unrine, J. M. Analysis of engineered nanomaterials in complex matrices (environment and biota): General considerations and conceptual case studies. *Environ. Toxicol. Chem.* **2012**, *31* (1), 32–49.

(58) Baalousha, M.; Stolpe, B.; Lead, J. R. Flow field-flow fractionation for the analysis and characterization of natural colloids and manufactured nanoparticles in environmental systems: A critical review. *J. Chromatogr. A* **2011**, *1218* (27), 4078–4103.

(59) Meermann, B. Field-flow fractionation coupled to ICP-MS: separation at the nanoscale, previous and recent application trends. *Anal. Bioanal. Chem.* **2015**, *407* (10), 2665–2674.

(60) Makishima, A.; Zhu, X.-K.; Belshaw, N. S.; O’Nions, R. K. Separation of titanium from silicates for isotopic ratio determination using multiple collector ICP-MS. *J. Anal. At. Spectrom.* **2002**, *17* (10), 1290–1294.

(61) Praetorius, A.; Gundlach-Graham, A.; Goldberg, E.; Fabienke, W.; Navratilova, J.; Gondikas, A.; Kaegi, R.; Günther, D.; Hofmann, T.; von der Kammer, F.; et al. Single-particle multi-element fingerprinting (spMEF) using inductively-coupled plasma time-of-flight mass spectrometry (ICP-TOFMS) to identify engineered nanoparticles against the elevated natural background in soils. *Environ. Sci. Nano* **2017**, *4* (2), 307–314.

(62) Thurn, K. T.; Paunesku, T.; Wu, A.; Brown, E. M. B.; Lai, B.; Vogt, S.; Maser, J.; Aslam, M.; Dravid, V.; Bergan, R.; et al. Labeling TiO2 nanoparticles with dyes for optical fluorescence microscopy and determination of TiO2-DNA nanoconjugate stability. *Small* **2009**, *5* (11), 1318–1325.

(63) Chowdhury, I.; Cwiertny, D. M.; Walker, S. L. Combined Factors Influencing the Aggregation and Deposition of nano-TiO 2 in the Presence of Humic Acid and Bacteria. *Environ. Sci. Technol.* **2012**, *46* (13), 6968–6976.

(64) Chowdhury, I.; Walker, S. L. Deposition mechanisms of TiO2 nanoparticles in a parallel plate system. *J. Colloid Interface Sci.* **2012**, *369* (1), 16–22.

(65) Xia, T.; Kovochich, M.; Liong, M.; Mädler, L.; Gilbert, B.; Shi, H.; Yeh, J. I.; Zink, J. I.; Nel, A. E. Comparison of the Mechanism of Toxicity of Zinc Oxide and Cerium Oxide Nanoparticles Based on Dissolution and Oxidative Stress Properties. *ACS Nano* **2008**, *2* (10), 2121–2134.

(66) Clemente, A.; Moreno, N.; Lobera, M. P.; Balas, F.; Santamaria, J. Fluorescently labelled SiO2 nanoparticles as tracers in natural waters: dependence of detection limits on environmental conditions. *Environ. Sci. Nano* **2016**, *3* (3), 631–637.

(67) Otero-González, L.; Field, J. A.; Calderon, I. A. C.; Aspinwall, C. A.; Shadman, F.; Zeng, C.; Sierra-Alvarez, R. Fate of fluorescent core-shell silica nanoparticles during simulated secondary wastewater treatment. *Water Res.* **2015**, *77*, 170–178.

(68) Vitorge, E.; Szenknect, S.; Martins, J. M. F.; Barthès, V.; Gaudet, J.-P. Comparison of three labeled silica nanoparticles used as tracers in transport experiments in porous media. Part II: Transport experiments and modeling. *Environ. Pollut.* **2014**, *184*, 613–619.

(69) Alvarez Lemus, M. A.; Monroy, H.; López, T.; De la Cruz Hernández, E. N.; López-González, R. Effect of surface modification on the bioactivity of sol-gel TiO 2 -based nanomaterials. *J. Chem. Technol. Biotechnol.* **2016**, *91* (8), 2148–2155.

(70) Gomez, V.; Clemente, A.; Irusta, S.; Balas, F.; Santamaria, J. Identification of TiO 2 nanoparticles using La and Ce as labels: application to the evaluation of surface contamination during the handling of nanosized matter. *Environ. Sci. Nano* **2014**, *1* (5), 496–503.

(71) Štengl, V.; Bakardjieva, S.; Murafa, N. Preparation and photocatalytic activity of rare earth doped TiO2 nanoparticles. *Mater. Chem. Phys.* **2009**, *114* (1), 217–226.

(72) Bourgeault, A.; Cousin, C.; Geertsen, V.; Cassier-Chauvat, C.; Chauvat, F.; Durupthy, O.; Chanéac, C.; Spalla, O. The challenge of studying TiO2 nanoparticle bioaccumulation at environmental concentrations: Crucial use of a stable isotope tracer. *Environ. Sci. Technol.* **2015**, *49* (4), 2451–2459.

(73) Abbas, K.; Cydzik, I.; Del Torchio, R.; Farina, M.; Forti, E.; Gibson, N.; Holzwarth, U.; Simonelli, F.; Kreyling, W. Radiolabelling of TiO2 nanoparticles for radiotracer studies. *J. Nanoparticle Res.* **2010**, *12* (7), 2435–2443.

(74) Hildebrand, H.; Schymura, S.; Holzwarth, U.; Gibson, N.; Dalmiglio, M.; Franke, K. Strategies for radiolabeling of commercial TiO2 nanopowder as a tool for sensitive nanoparticle detection in complex matrices. *J. Nanoparticle Res.* **2015**, *17* (6), 278.

(75) Pérez-Campaña, C.; Sansaloni, F.; Gómez-Vallejo, V.; Baz, Z.; Martin, A.; Moya, S. E.; Lagares, J. I.; Ziolo, R. F.; Llop, J. Production of 18 F-Labeled Titanium Dioxide Nanoparticles by Proton Irradiation for Biodistribution and Biological Fate Studies in Rats. *Part. Part. Syst. Charact.* **2014**, *31* (1), 134–142.

(76) Balasubramanian, S. K.; Jittiwat, J.; Manikandan, J.; Ong, C.-N.; Yu, L. E.; Ong, W.-Y. Biodistribution of gold nanoparticles and gene expression changes in the liver and spleen after intravenous administration in rats. *Biomaterials* **2010**, *31* (8), 2034–2042.

(77) Sonavane, G.; Tomoda, K.; Makino, K. Biodistribution of colloidal gold nanoparticles after intravenous administration: Effect of particle size. *Colloids Surfaces B Biointerfaces* **2008**, *66* (2), 274–280.

(78) De Jong, W. H.; Hagens, W. I.; Krystek, P.; Burger, M. C.; Sips, A. J. A. M.; Geertsma, R. E. Particle size-dependent organ distribution of gold nanoparticles after intravenous administration. *Biomaterials* **2008**, *29* (12), 1912–1919.

(79) Sadauskas, E.; Wallin, H.; Stoltenberg, M.; Vogel, U.; Doering, P.; Larsen, A.; Danscher, G. Kupffer cells are central in the removal of nanoparticles from the organism. *Part. Fibre Toxicol.* **2007**, *4* (1), 10.

(80) Bartneck, M.; Keul, H. A.; Zwadlo-Klarwasser, G.; Groll, J. Phagocytosis Independent Extracellular Nanoparticle Clearance by Human Immune Cells. *Nano Lett.* **2010**, *10* (1), 59–63.

(81) Mayhew, T. M.; Mühlfeld, C.; Vanhecke, D.; Ochs, M. A review of recent methods for efficiently quantifying immunogold and other nanoparticles using TEM sections through cells, tissues and organs. *Ann. Anat. - Anat. Anzeiger* **2009**, *191* (2), 153–170.

(82) Jong, W. H. De; Burger, M. C.; Verheijen, M. A.; Geertsma, R. E. Detection of the Presence of Gold Nanoparticles in Organs by Transmission Electron Microscopy. *Materials (Basel).* **2010**, *3* (12), 4681–4694.

(83) Avellan, A.; Schwab, F.; Masion, A.; Chaurand, P.; Borschneck, D.; Vidal, V.; Rose, J.; Santaella, C.; Levard, C. Nanoparticle Uptake in Plants: Gold Nanomaterial Localized in Roots of Arabidopsis thaliana by X-ray Computed Nanotomography and Hyperspectral Imaging. *Environ. Sci. Technol.* **2017**, *51* (15), 8682–8691.

(84) Mortimer, M.; Gogos, A.; Bartolomé, N.; Kahru, A.; Bucheli, T. D.; Slaveykova, V. I. Potential of Hyperspectral Imaging Microscopy for Semi-quantitative Analysis of Nanoparticle Uptake by Protozoa. *Environ. Sci. Technol.* **2014**, *48* (15), 8760–8767.

(85) Harper, S. L.; Carriere, J. L.; Miller, J. M.; Hutchison, J. E.; Maddux, B. L. S.; Tanguay, R. L. Systematic evaluation of nanomaterial toxicity: Utility of standardized materials and rapid assays. *ACS Nano* **2011**, *5* (6), 4688–4697.

(86) Balogh, L.; Nigavekar, S. S.; Nair, B. M.; Lesniak, W.; Zhang, C.; Sung, L. Y.; Kariapper, M. S. T.; El-Jawahri, A.; Llanes, M.; Bolton, B.; et al. Significant effect of size on the in vivo biodistribution of gold composite nanodevices in mouse tumor models. *Nanomedicine Nanotechnology, Biol. Med.* **2007**, *3* (4), 281–296.

(87) Gao, C.; Vuong, J.; Zhang, Q.; Liu, Y.; Yin, Y. One-step seeded growth of Au nanoparticles with widely tunable sizes. *Nanoscale* **2012**, *4*, 2875.

(88) Goebl, J.; Joo, J. B.; Dahl, M.; Yin, Y. Synthesis of tailored Au@TiO2 core-shell nanoparticles for photocatalytic reforming of ethanol. *Catal. Today* **2014**, *225*, 90–95.

(89) Stankus, D. P.; Lohse, S. E.; Hutchison, J. E.; Nason, J. a. Interactions between natural organic matter and gold nanoparticles stabilized with different organic capping agents. *Environ. Sci. Technol.* **2011**, *45* (8), 3238–3244.

(90) Surette, M. C.; Nason, J. A. Effects of surface coating character and interactions with natural organic matter on the colloidal stability of gold nanoparticles. *Environ. Sci. Nano* **2016**, *3* (5), 1144–1152.

(91) Nason, J. A.; McDowell, S. A.; Callahan, T. W. Effects of natural organic matter type and concentration on the aggregation of citrate-stabilized gold nanoparticles. *J. Environ. Monit.* **2012**, *14* (7), 1885.

(92) Pace, H. E.; Rogers, N. J.; Jarolimek, C.; Coleman, V. A.; Higgins, C. P.; Ranville, J. F. Determining Transport Efficiency for the Purpose of Counting and Sizing Nanoparticles via Single Particle Inductively Coupled Plasma Mass Spectrometry (vol 83, pg 9361, 2011). *Anal. Chem.* **2012**, *84* (10), 4633.

(93) Standard Method 2540 D: Total Suspended Solids Dried at 103-105 C. In *Standard methods for the examination of water & wastewater*; Eaton, A. D., Clesceri, L. S., Rice, E. W., Greenberg, A. E., Eds.; American Public Health Association: Washington D.C., 2005.

(94) Jin, C.; Tang, Y.; Yang, F. G.; Li, X. L.; Xu, S.; Fan, X. Y.; Huang, Y. Y.; Yang, Y. J. Cellular toxicity of TiO2 nanoparticles in anatase and rutile crystal phase. *Biol. Trace Elem. Res.* **2011**, *141* (1–3), 3–15.

(95) Gupta, R. K.; Misra, M. *Metal Semiconductor Core-shell Nanostructures for Energy and Environmental Applications*; Micro and Nano Technologies; Elsevier Science, 2017.

(96) Lee, S.; Bi, X.; Reed, R. B.; Ranville, J. F.; Herckes, P.; Westerhoff, P. Nanoparticle size detection limits by single particle ICP-MS for 40 elements. *Environ. Sci. Technol.* **2014**, *48* (17), 10291–10300.

(97) Hou, W.; Cronin, S. B. A review of surface plasmon resonance-enhanced photocatalysis. *Adv. Funct. Mater.* **2013**, *23* (13), 1612–1619.

(98) Kim, Y.-S.; Rai, P.; Yu, Y.-T. Microwave assisted hydrothermal synthesis of Au@TiO2 core–shell nanoparticles for high temperature CO sensing applications. *Sensors Actuators B Chem.* **2013**, *186*, 633–639.

(99) Chen, Y.; Zhu, B.; Yao, M.; Wang, S.; Zhang, S. The preparation and characterization of Au@TiO2 nanoparticles and their catalytic activity for CO oxidation. *Catal. Commun.* **2010**, *11* (12), 1003–1007.

(100) Wyckoff, R. W. G. *Crystal Structures - Volume 1.*; Interscience Publishers: New York, 1963.

(101) Tom, R. T.; Nair, A. S.; Singh, N.; Aslam, M.; Nagendra, C. L.; Philip, R.; Vijayamohanan, K.; Pradeep, T. Freely Dispersible Au@TiO 2 , Au@ZrO 2 , Ag@TiO 2 , and Ag@ZrO 2 Core−Shell Nanoparticles: One-Step Synthesis, Characterization, Spectroscopy, and Optical Limiting Properties. *Langmuir* **2003**, *19* (8), 3439–3445.

(102) Liu, W.; Guo, Q.-H.; Qin, W.; Yao, J.-L.; Gu, R.-A. In-Situ Surface Enhanced Raman Spectroscopic Investigation of Photocatalysis at Au@ TiO2 Surface. *Chem. J. Chinese Univ.* **2011**, *8*, 39.

(103) Holzwarth, U.; Bulgheroni, A.; Gibson, N.; Kozempel, J.; Cotogno, G.; Abbas, K.; Simonelli, F.; Cydzik, I. Radiolabelling of nanoparticles by proton irradiation: temperature control in nanoparticulate powder targets. *J. Nanoparticle Res.* **2012**, *14* (6), 880.

(104) Weir, A.; Westerhoff, P.; Fabricius, L.; Hristovski, K.; von Goetz, N. Titanium dioxide nanoparticles in food and personal care products. *Environ. Sci. Technol.* **2012**, *46* (4),

2242–2250.

(105) Oughton, D. H.; Hertel-Aas, T.; Pellicer, E.; Mendoza, E.; Joner, E. J. Neutron Activation of Engineered Nanoparticles As a Tool for Tracing Their Environmental Fate and Uptake in Organisms. *Environ. Toxicol. Chem.* **2008**, *27* (9), 1883.

(106) McBride, M. B.; Richards, B. K.; Steenhuis, T.; Russo, J. J.; Sauvé, S. MOBILITY AND SOLUBILITY OF TOXIC METALS AND NUTRIENTS IN SOIL FIFTEEN YEARS AFTER SLUDGE APPLICATION. *Soil Sci.* **1997**, *162* (7), 487–500.

(107) Mulchandani, A.; Westerhoff, P. Recovery Opportunities for Metals and Energy from Sewage Sludges. *Bioresour. Technol.* **2016**, *215* (March).

(108) Holden, P. A.; Klaessig, F.; Turco, R. F.; Priester, J. H.; Rico, C. M.; Avila-Arias, H.; Mortimer, M.; Pacpaco, K.; Gardea-Torresdey, J. L. Evaluation of Exposure Concentrations Used in Assessing Manufactured Nanomaterial Environmental Hazards: Are They Relevant? *Environ. Sci. Technol.* **2014**, *48* (18), 10541–10551.

(109) Jeng, H. A.; Swanson, J. Toxicity of metal oxide nanoparticles in mammalian cells. *J Env. Sci Heal. A Tox Hazard Subst Env. Eng* **2006**, *41* (12), 2699–2711.

(110) Horie, M.; Nishio, K.; Fujita, K.; Endoh, S.; Miyauchi, A.; Saito, Y.; Iwahashi, H.; Yamamoto, K.; Murayama, H.; Nakano, H.; et al. Protein adsorption of ultrafine metal oxide and its influence on cytotoxicity toward cultured cells. *Chem. Res. Toxicol.* **2009**, *22* (3), 543–553.

(111) Kasemets, K.; Ivask, A.; Dubourguier, H. C.; Kahru, A. Toxicity of nanoparticles of ZnO, CuO and TiO2 to yeast Saccharomyces cerevisiae. *Toxicol. Vitr.* **2009**, *23* (6), 1116–1122.

(112) Karlsson, H. L.; Cronholm, P.; Gustafsson, J.; Möller, L. Copper oxide nanoparticles are highly toxic: A comparison between metal oxide nanoparticles and carbon nanotubes. *Chem. Res. Toxicol.* **2008**, *21* (9), 1726–1732.

(113) Wu, Q.; Nouara, A.; Li, Y.; Zhang, M.; Wang, W.; Tang, M.; Ye, B.; Ding, J.; Wang, D. Comparison of toxicities from three metal oxide nanoparticles at environmental relevant concentrations in nematode Caenorhabditis elegans. *Chemosphere* **2013**, *90* (3), 1123–1131.

(114) Xia, T.; Kovochich, M.; Liong, M.; Mädler, L.; Gilbert, B.; Shi, H.; Yeh, J. I.; Zink, J. I.; Nel, A. E.; Ma, L.; et al. Comparison of the Mechanism of Toxicity of Zinc Oxide and Cerium Oxide Nanoparticles Based on Dissolution and Oxidative Stress Properties. *ACS Nano* **2008**, *2* (10), 2121–2134.

(115) Ng, A. M. C.; Guo, M. Y.; Leung, Y. H.; Chan, C. M. N.; Wong, S. W. Y.; Yung, M. M.

N.; Ma, A. P. Y.; Djurišić, A. B.; Leung, F. C. C.; Leung, K. M. Y.; et al. Metal oxide nanoparticles with low toxicity. *J. Photochem. Photobiol. B Biol.* **2015**, *151*, 17–24.

(116) Li, K.; Chen, Y.; Zhang, W.; Pu, Z.; Jiang, L.; Chen, Y. Surface Interactions Affect the Toxicity of Engineered Metal Oxide Nanoparticles toward Paramecium. *Chem. Res. Toxicol.* **2012**, *25* (8), 1675–1681.

(117) Hoecke, K. Van; Quik, J. T. K.; Mankiewicz-Boczek, J.; Schamphelaere, K. A. C. De; Elsaesser, A.; Meeren, P. Van der; Barnes, C.; McKerr, G.; Howard, C. V.; Meent, D. Van De; et al. Fate and Effects of CeO 2 Nanoparticles in Aquatic Ecotoxicity Tests. *Environ. Sci. Technol.* **2009**, *43* (12), 4537–4546.

(118) Braydich-Stolle, L. K.; Speshock, J. L.; Castle, A.; Smith, M.; Murdock, R. C.; Hussain, S. M. Nanosized aluminum altered immune function. *ACS Nano* **2010**, *4* (7), 3661–3670.

(119) Kahn, E.; Baarine, M.; Pelloux, S.; Riedinger, J. M.; Frouin, F.; Tourneur, Y.; Lizard, G. Iron nanoparticles increase 7-ketocholesterol-induced cell death, inflammation, and oxidation on murine cardiac HL1-NB cells. *Int. J. Nanomedicine* **2010**, *5* (1), 185–195.

(120) Park, E. J.; Kim, H.; Kim, Y.; Yi, J.; Choi, K.; Park, K. Inflammatory responses may be induced by a single intratracheal instillation of iron nanoparticles in mice. *Toxicology* **2010**, *275* (1–3), 65–71.

(121) Zeyons, O.; Thill, A.; Chauvat, F.; Menguy, N.; Cassier-Chauvat, C.; Orear, C.; Daraspe, J.; Auffan, M.; Rose, J.; Spalla, O. Direct and indirect CeO2 nanoparticles toxicity for Escherichia coli and Synechocystis. *Nanotoxicology* **2009**, *3* (4), 284–295.

(122) Gajewicz, A.; Schaeublin, N.; Rasulev, B.; Hussain, S.; Leszczynska, D.; Puzyn, T.; Leszczynski, J. Towards understanding mechanisms governing cytotoxicity of metal oxides nanoparticles: Hints from nano-QSAR studies. *Nanotoxicology* **2015**, *9* (3), 313–325.

(123) Li, Y.; Zhang, W.; Niu, J.; Chen, Y. Mechanism of photogenerated reactive oxygen species and correlation with the antibacterial properties of engineered metal-oxide nanoparticles. *ACS Nano* **2012**, *6* (6), 5164–5173.

(124) Fernández-garcia, M.; Rodriguez, J. A. Metal Oxide Nanoparticles. **2007**, No. October.

(125) Cox, P. A. *The elements: their origin, abundance, and distribution*; Oxford University Press: New York, NY, 1989.

(126) Adriano, D. C. *Trace elements in terrestrial environments: biogeochemistry, bioavailability and risk of metals*; 2001.

(127) Taylor, S. R.; McLennan, S. *The continental crust: Its composition and evolution*; Blackwells Scientific Publications: Palo Alto, CA, 1985.

(128) Bruland, K. W. Trace elements in sea-water. In *Chemical Oceanography*; Riley, J. P., Chester, R., Eds.; Academic Press, 1983; pp 157–220.

(129) Martin, J. M.; Meybeck, M. Elemental mass-balance of material carried by major world rivers. *Mar. Chem.* **1979**, *7* (3), 173–206.

(130) Bowen, H. J. M. *Environmental chemistry of the elements*; 1979.

(131) Gaillardet, J.; Viers, J.; Dupré, B. *Trace Elements in River Waters*; 2013; Vol. 7.

(132) Leopold, K.; Philippe, A.; Wörle, K.; Schaumann, G. E. Analytical strategies to the determination of metal-containing nanoparticles in environmental waters. *TrAC Trends Anal. Chem.* **2016**, *84*, 107–120.

(133) Samontha, A.; Shiowatana, J.; Siripinyanond, A. Particle size characterization of titanium dioxide in sunscreen products using sedimentation field-flow fractionation-inductively coupled plasma-mass spectrometry. *Anal. Bioanal. Chem.* **2011**, *399* (2), 973–978.

(134) Soto-Alvaredo, J.; Dutschke, F.; Bettmer, J.; Montes-Bayón, M.; Pröfrock, D.; Prange, A. Initial results on the coupling of sedimentation field-flow fractionation (SdFFF) to inductively coupled plasma-tandem mass spectrometry (ICP-MS/MS) for the detection and characterization of TiO 2 nanoparticles. *J. Anal. At. Spectrom.* **2016**, *31* (7), 1549–1555.

(135) Donovan, A. R.; Adams, C. D.; Ma, Y.; Stephan, C.; Eichholz, T.; Shi, H. Detection of zinc oxide and cerium dioxide nanoparticles during drinking water treatment by rapid single particle ICP-MS methods. *Anal. Bioanal. Chem.* **2016**, *408* (19), 5137–5145.

(136) Dan, Y.; Shi, H.; Stephan, C.; Liang, X. Rapid analysis of titanium dioxide nanoparticles in sunscreens using single particle inductively coupled plasma-mass spectrometry. *Microchem. J.* **2015**, *122*, 119–126.

(137) Fréchette-Viens, L.; Hadioui, M.; Wilkinson, K. J. Practical limitations of single particle ICP-MS in the determination of nanoparticle size distributions and dissolution: case of rare earth oxides. *Talanta* **2017**, *163* (October 2016), 121–126.

(138) Praetorius, A.; Gundlach-Graham, A.; Goldberg, E.; Fabienke, W.; Navratilova, J.; Gondikas, A.; Kaegi, R.; Günther, D.; Hofmann, T.; von der Kammer, F. Single-particle multi-element fingerprinting (spMEF) using inductively-coupled plasma time-of-flight mass spectrometry (ICP-TOFMS) to identify engineered nanoparticles against the elevated natural background in soils. *Environ. Sci. Nano* **2017**.

(139) Lu, P. J.; Huang, S. C.; Chen, Y. P.; Chiueh, L. C.; Shih, D. Y. C. Analysis of titanium dioxide and zinc oxide nanoparticles in cosmetics. *J. Food Drug Anal.* **2015**, *23* (3), 587–594.

(140) Jin, C.-Y.; Zhu, B.-S.; Wang, X.-F.; Lu, Q.-H. Cytotoxicity of Titanium Dioxide Nanoparticles in Mouse Fibroblast Cells. *Chem. Res. Toxicol.* **2008**, *21* (9), 1871–1877.

(141) Baer, D. R.; Gaspar, D. J.; Nachimuthu, P.; Techane, S. D.; Castner, D. G. Application of surface chemical analysis tools for characterization of nanoparticles. *Anal. Bioanal. Chem.* **2010**, *396* (3), 983–1002.

(142) Blechinger, J.; Herrmann, R.; Kiener, D.; García-García, F. J.; Scheu, C.; Reller, A.; Bräuchle, C. Perylene-Labeled Silica Nanoparticles: Synthesis and Characterization of Three Novel Silica Nanoparticle Species for Live-Cell Imaging. *Small* **2010**, *6* (21), 2427–2435.

(143) van Blaaderen, A.; Vrij, A. Synthesis and Characterization of Colloidal Dispersions of Fluorescent, Monodisperse Silica Spheres. *Langmuir* **1992**, *8* (12), 2921–2931.

(144) Bagwe, R. P.; Yang, C.; Hilliard, L. R.; Tan, W. Optimization of Dye-Doped Silica Nanoparticles Prepared Using a Reverse Microemulsion Method. **2004**, No. 6, 8336–8342.

(145) Kiser, M. A.; Ryu, H.; Jang, H.; Hristovski, K.; Westerhoff, P. Biosorption of nanoparticles to heterotrophic wastewater biomass. *Water Res.* **2010**, *44* (14), 4105–4114.

(146) Zane, A.; McCracken, C.; Knight, D. A.; Young, T.; Lutton, A. D.; Olesik, J. W.; Waldman, W. J.; Dutta, P. K. Uptake of bright fluorophore core-silica shell nanoparticles by biological systems. *Int. J. Nanomedicine* **2015**, *10*, 1547–1567.

(147) Shahabi, S.; Treccani, L.; Rezwan, K. A comparative study of three different synthesis routes for hydrophilic fluorophore-doped silica nanoparticles. *J. Nanoparticle Res.* **2016**, *18* (1), 1–13.

(148) Mahon, E.; Hristov, D. R.; Dawson, K. a. Stabilising fluorescent silica nanoparticles against dissolution effects for biological studies. *Chem. Commun.* **2012**, *48* (64), 7970–4972.

(149) Quignard, S.; Mosser, G.; Boissière, M.; Coradin, T. Long-term fate of silica nanoparticles interacting with human dermal fibroblasts. *Biomaterials* **2012**, *33* (17), 4431–4442.

(150) Vitorge, E.; Szenknect, S.; Martins, J. M. F.; Barthès, V.; Auger, A.; Renard, O.; Gaudet, J.-P. Comparison of three labeled silica nanoparticles used as tracers in transport experiments in porous media. Part I: Syntheses and characterizations. *Environ. Pollut.*

2014, *184*, 605–612.

(151) Torrano, A. A.; Bräuchle, C. Precise quantification of silica and ceria nanoparticle uptake revealed by 3D fluorescence microscopy. *Beilstein J. Nanotechnol.* **2014**, *5* (1), 1616–1624.

(152) Strobl, F. G.; Seitz, F.; Westerhausen, C.; Reller, A.; Torrano, A. A.; Br??uchle, C.; Wixforth, A.; Schneider, M. F. Intake of silica nanoparticles by giant lipid vesicles: Influence of particle size and thermodynamic membrane state. *Beilstein J. Nanotechnol.* **2014**, *5* (1), 2468–2478.

(153) Resch-Genger, U.; Grabolle, M.; Cavaliere-Jaricot, S.; Nitschke, R.; Nann, T. Quantum dots versus organic dyes as fluorescent labels. *Nat. Methods* **2008**, *5* (9), 763–775.

(154) Ovenstone, J.; Yanagisawa, K. Effect of Hydrothermal Treatment of Amorphous Titania on the Phase Change from Anatase to Rutile during Calcination. *Chem. Mater.* **1999**, *11* (10), 2770–2774.

(155) Wang, C.-C.; Ying, J. Y. Sol−Gel Synthesis and Hydrothermal Processing of Anatase and Rutile Titania Nanocrystals. *Chem. Mater.* **1999**, *11* (11), 3113–3120.

(156) Quignard, S. Behaviour of silica nanoparticles in dermis-like cellularized collagen hydrogels. *Biomater. Sci.* **2014**, *2*, 484–492.

(157) Al-Rawi, M.; Diabaté, S.; Weiss, C. Uptake and intracellular localization of submicron and nano-sized SiO 2 particles in HeLa cells. *Arch. Toxicol.* **2011**, *85* (7), 813–826.

(158) Chen, J.; Zhou, H.; Santulli, A. C.; Wong, S. S. Evaluating Cytotoxicity and Cellular Uptake from the Presence of Variously Processed TiO 2 Nanostructured Morphologies. **2010**, 871–879.

(159) Vitorge, E.; Szenknect, S.; Martins, J. M. F.; Barthès, V.; Gaudet, J.-P.; Auger, A.; Renard, O.; Gaudet, J.-P. Comparison of three labeled silica nanoparticles used as tracers in transport experiments in porous media. Part I: Syntheses and characterizations. *Environ. Pollut.* **2014**, *184*, 605–612.

(160) He, X.; Ma, Y.; Li, M.; Zhang, P.; Li, Y.; Zhang, Z. Quantifying and imaging engineered nanomaterials in vivo: Challenges and techniques. *Small* **2013**, *9* (9–10), 1482–1491.

(161) Coradin, T.; Eglin, D.; Livage, J. The silicomolybdic acid spectrophotometric method and its application to silicate/biopolymer interaction studies. *Spectroscopy* **2004**, *18*, 567–576.

(162) Rauf, M. A.; Salman Ashraf, S. Survey of recent trends in biochemically assisted degradation of dyes. *Chem. Eng. J.* **2012**, *209*, 520–530.

(163) Zhang, Z. Radiolabeling of Nanoparticles. In *Toxicology of Nanomaterials*; Wiley-VCH Verlag GmbH & Co. KGaA: Weinheim, Germany, 2016; pp 69–94.

(164) Pérez-Campaña, C.; Gómez-Vallejo, V.; Martin, A.; San Sebastián, E.; Moya, S. E.; Reese, T.; Ziolo, R. F.; Llop, J. Tracing nanoparticles in vivo: a new general synthesis of positron emitting metal oxide nanoparticles by proton beam activation. *Analyst* **2012**, *137* (21), 4902.

(165) Holzwarth, U.; Bellido, E.; Dalmiglio, M.; Kozempel, J.; Cotogno, G.; Gibson, N. 7Be-recoil radiolabelling of industrially manufactured silica nanoparticles. *J. Nanoparticle Res.* **2014**, *16* (9), 2574.

(166) Malfatti, M. A.; Palko, H. A.; Kuhn, E. A.; Turteltaub, K. W. Determining the Pharmacokinetics and Long-Term Biodistribution of SiO2 Nanoparticles In Vivo Using Accelerator Mass Spectrometry. *Nano Lett.* **2012**, *12* (11), 5532–5538.

(167) Cydzik, I.; Bilewicz, A.; Abbas, K.; Simonelli, F.; Bulgheroni, A.; Holzwarth, U.; Gibson, N. A novel method for synthesis of 56Co-radiolabelled silica nanoparticles. *J. Nanoparticle Res.* **2012**, *14* (10), 1185.

(168) Jung, S. H.; Kim, K. Il; Ryu, J. H.; Choi, S. H.; Kim, J. B.; Moon, J. H.; Jin, J. H. Preparation of radioactive core-shell type 198Au@SiO2 nanoparticles as a radiotracer for industrial process applications. *Appl. Radiat. Isot.* **2010**, *68* (6), 1025–1029.

(169) Chen, J.; Geraedts, S. D.; Ouellet, C.; Singh, B. Evaluation of half-life of 198Au. *Appl. Radiat. Isot.* **2011**, *69* (7), 1064–1069.

(170) Gibson, N.; Holzwarth, U.; Abbas, K.; Simonelli, F.; Kozempel, J.; Cydzik, I.; Cotogno, G.; Bulgheroni, A.; Gilliland, D.; Ponti, J.; et al. Radiolabelling of engineered nanoparticles for in vitro and in vivo tracing applications using cyclotron accelerators. *Arch. Toxicol.* **2011**, *85* (7), 751–773.

(171) Kreyling, W. G.; Holzwarth, U.; Haberl, N.; Kozempel, J.; Wenk, A.; Hirn, S.; Schleh, C.; Schäffler, M.; Lipka, J.; Semmler-Behnke, M.; et al. Quantitative biokinetics of titanium dioxide nanoparticles after intratracheal instillation in rats: Part 3. *Nanotoxicology* **2017**, *11* (4), 454–464.

(172) Kreyling, W. G.; Holzwarth, U.; Schleh, C.; Kozempel, J.; Wenk, A.; Haberl, N.; Hirn, S.; Schäffler, M.; Lipka, J.; Semmler-Behnke, M.; et al. Quantitative biokinetics of titanium dioxide nanoparticles after oral application in rats: Part 2. *Nanotoxicology* **2017**, *11* (4), 443–453.

(173) Kreyling, W. G.; Holzwarth, U.; Haberl, N.; Kozempel, J.; Hirn, S.; Wenk, A.; Schleh, C.; Schäffler, M.; Lipka, J.; Semmler-Behnke, M.; et al. Quantitative biokinetics of titanium

dioxide nanoparticles after intravenous injection in rats: Part 1. *Nanotoxicology* **2017**, *11* (4), 434–442.

(174) Isaacson, C. W.; Sigg, L.; Ammann, A. A.; Stadnicka-Michalak, J.; Schirmer, K. Interactions of TiO 2 nanoparticles and the freshwater nematode Plectus aquatilis: particle properties, kinetic parameters and bioconcentration factors. *Environ. Sci. Nano* **2017**, *4* (3), 712–719.

(175) Yeh, T.-K.; Chen, J.-K.; Lin, C.-H.; Yang, M.-H.; Yang, C. S.; Chou, F.-I.; Peir, J.-J.; Wang, M.-Y.; Chang, W.-H.; Tsai, M.-H.; et al. Kinetics and tissue distribution of neutron-activated zinc oxide nanoparticles and zinc nitrate in mice: effects of size and particulate nature. *Nanotechnology* **2012**, *23* (8), 085102.

(176) Li, W. M.; Wang, W. X. Distinct biokinetic behavior of ZnO nanoparticles in Daphnia magna quantified by synthesizing 65Zn tracer. *Water Res.* **2013**, *47* (2), 895–902.

(177) Cohen, J. M.; Derk, R.; Wang, L.; Godleski, J.; Kobzik, L.; Brain, J.; Demokritou, P. Tracking translocation of industrially relevant engineered nanomaterials (ENMs) across alveolar epithelial monolayers in vitro. *Nanotoxicology* **2014**, *8* (sup1), 216–225.

(178) Huang, B.; Xiao, L.; Yang, L. Y.; Ji, R.; Miao, A. J. Facile synthesis of 55Fe-labeled well-dispersible hematite nanoparticles for bioaccumulation studies in nanotoxicology. *Environ. Pollut.* **2016**, *213*, 801–808.

(179) Zhu, M. T.; Feng, W. Y.; Wang, Y.; Wang, B.; Wang, M.; Ouyang, H.; Zhao, Y. L.; Chai, Z. F. Particokinetics and extrapulmonary translocation of intratracheally instilled ferric oxide nanoparticles in rats and the potential health risk assessment. *Toxicol. Sci.* **2009**, *107* (2), 342–351.

(180) Freund, B.; Tromsdorf, U. I.; Bruns, O. T.; Heine, M.; Giemsa, A.; Bartelt, A.; Salmen, S. C.; Raabe, N.; Heeren, J.; Ittrich, H.; et al. A Simple and Widely Applicable Method to ^{59}Fe-Radiolabel Monodisperse Superparamagnetic Iron Oxide Nanoparticles for *In Vivo* Quantification Studies. *ACS Nano* **2012**, *6* (8), 7318–7325.

(181) Marmorato, P.; Simonelli, F.; Abbas, K.; Kozempel, J.; Holzwarth, U.; Franchini, F.; Ponti, J.; Gibson, N.; Rossi, F. 56Co-labelled radioactive Fe 3O 4 nanoparticles for in vitro uptake studies on Balb/3T3 and Caco-2 cell lines. *J. Nanoparticle Res.* **2011**, *13* (12), 6707–6716.

(182) de Barros, A. L. B.; Chacko, A.-M.; Mikitsh, J. L.; Al Zaki, A.; Salavati, A.; Saboury, B.; Tsourkas, A.; Alavi, A. Assessment of Global Cardiac Uptake of Radiolabeled Iron Oxide Nanoparticles in Apolipoprotein-E-Deficient Mice: Implications for Imaging Cardiovascular Inflammation. *Mol. Imaging Biol.* **2013**, *16* (3), 330–339.

(183) Schymura, S.; Fricke, T.; Hildebrand, H.; Franke, K. Elucidating the Role of Dissolution in CeO2 Nanoparticle Plant Uptake by Smart Radiolabeling. *Angew. Chemie Int. Ed.* **2017**, *56* (26), 7411–7414.

(184) Simonelli, F.; Marmorato, P.; Abbas, K.; Ponti, J.; Kozempel, J.; Holzwarth, U.; Franchini, F.; Rossi, F. Cyclotron Production of Radioactive CeO2 Nanoparticles and Their Application for In Vitro Uptake Studies. *IEEE Trans. Nanobioscience* **2011**, *10* (1), 44–50.

(185) Zhang, Z.; He, X.; Zhang, H.; Ma, Y.; Zhang, P.; Ding, Y.; Zhao, Y. Uptake and distribution of ceria nanoparticles in cucumber plants. *Metallomics* **2011**, *3* (8), 816.

(186) Zhang, P.; He, X.; Ma, Y.; Lu, K.; Zhao, Y.; Zhang, Z. Distribution and bioavailability of ceria nanoparticles in an aquatic ecosystem model. *Chemosphere* **2012**, *89* (5), 530–535.

(187) He, X.; Zhang, H.; Ma, Y.; Bai, W.; Zhang, Z.; Lu, K.; Ding, Y.; Zhao, Y.; Chai, Z. Lung deposition and extrapulmonary translocation of nano-ceria after intratracheal instillation. *Nanotechnology* **2010**, *21* (28), 285103.

(188) Rojas, S.; Gispert, J. D.; Abad, S.; Buaki-Sogo, M.; Victor, V. M.; Garcia, H.; Herance, J. R. In vivo biodistribution of amino-functionalized ceria nanoparticles in rats using positron emission tomography. *Mol. Pharm.* **2012**, *9* (12), 3543–3550.

(189) Pérez-Campaña, C.; Gómez-Vallejo, V.; Puigivila, M.; Martín, A.; Calvo-Fernández, T.; Moya, S. E.; Ziolo, R. F.; Reese, T.; Llop, J. Biodistribution of Different Sized Nanoparticles Assessed by Positron Emission Tomography: A General Strategy for Direct Activation of Metal Oxide Particles. *ACS Nano* **2013**, *7* (4), 3498–3505.

(190) Weise, H. P.; Görner, W.; Hedrich, M. Determination of elements by nuclear analytical methods. *Fresenius' Journal of Analytical Chemistry*. 2001, pp 8–14.

(191) Crouthamel, C. E.; Adams, F.; Dams, R. Intrinsic Variables. In *Applied Gamma-Ray Spectrometry*; Elsevier, 1970; pp 1–29.

(192) Faucher, S.; Lespes, G. Quantification of titanium from TiO2 particles in biological tissue. *J. Trace Elem. Med. Biol.* **2015**, *32*, 40–44.

(193) Laycock, A.; Coles, B.; Kreissig, K.; Rehkämper, M. High precision 142 Ce/ 140 Ce stable isotope measurements of purified materials with a focus on CeO 2 nanoparticles. *J. Anal. At. Spectrom.* **2016**, *31* (1), 297–302.

(194) May, T. W.; Wiedmeyer, R. H. A Table of Polyatomic Interferences in ICP-MS. *At. Spectrosc.* **1998**.

(195) Laycock, A.; Stolpe, B.; Römer, I.; Dybowska, A.; Valsami-Jones, E.; Lead, J. R.; Rehkämper, M. Synthesis and characterization of isotopically labeled silver nanoparticles for tracing studies. *Environ. Sci. Nano* **2014**, *1*, 271.

(196) Lee, P. L.; Chen, B. C.; Gollavelli, G.; Shen, S. Y.; Yin, Y. S.; Lei, S. L.; Jhang, C. L.; Lee, W. R.; Ling, Y. C. Development and validation of TOF-SIMS and CLSM imaging method for cytotoxicity study of ZnO nanoparticles in HaCaT cells. *J. Hazard. Mater.* **2014**, *277*, 3–12.

(197) Kubicek, M.; Holzlechner, G.; Opitz, A. K.; Larisegger, S.; Hutter, H.; Fleig, J. A novel ToF-SIMS operation mode for sub 100nm lateral resolution: Application and performance. *Appl. Surf. Sci.* **2014**, *289* (100), 407–416.

(198) Larner, F.; Dogra, Y.; Dybowska, A.; Fabrega, J.; Stolpe, B.; Bridgestock, L. J.; Goodhead, R.; Weiss, D. J.; Moger, J.; Lead, J. R.; et al. Tracing bioavailability of ZnO nanoparticles using stable isotope labeling. *Environ. Sci. Technol.* **2012**, *46* (21), 12137–12145.

(199) Laycock, A.; Romero-freire, A.; Najorka, J.; Svendsen, C.; Gestel, C. A. M. Van; Rehka, M. Novel Multi-isotope Tracer Approach To Test ZnO Nanoparticle and Soluble Zn Bioavailability in Joint Soil Exposures. **2017**.

(200) Merrifield, R. C.; Lead, J. R. Preparation and characterization of three-layer, isotopically labelled core-shell nanoparticles; a tool for understanding mechanisms of bioavailability. *NanoImpact* **2016**, *2*, 54–60.

(201) Croteau, M.; Cain, D. J.; Fuller, C. C. Novel and Nontraditional Use of Stable Isotope Tracers To Study Metal Bioavailability from Natural Particles. *Environ. Sci. Technol.* **2013**, 130318083554006.

(202) Croteau, M.-N.; Cain, D. J.; Fuller, C. C. Assessing the Dietary Bioavailability of Metals Associated with Natural Particles: Extending the Use of the Reverse Labeling Approach to Zinc. *Environ. Sci. Technol.* **2017**, *51* (5), 2803–2810.

(203) Croteau, M.-N.; Dybowska, A. D.; Luoma, S. N.; Valsami-Jones, E. A novel approach reveals that zinc oxide nanoparticles are bioavailable and toxic after dietary exposures. *Nanotoxicology* **2011**, *5* (1), 79–90.

(204) Dybowska, A. D.; Croteau, M.; Misra, S. K.; Berhanu, D.; Luoma, S. N.; Christian, P.; O'Brien, P.; Valsami-Jones, E. Synthesis of isotopically modified ZnO nanoparticles and their potential as nanotoxicity tracers. *Environ. Pollut.* **2011**, *159* (1), 266–273.

(205) Buffet, P. E.; Amiard-Triquet, C.; Dybowska, A.; Risso-de Faverney, C.; Guibbolini, M.; Valsami-Jones, E.; Mouneyrac, C. Fate of isotopically labeled zinc oxide nanoparticles in

sediment and effects on two endobenthic species, the clam Scrobicularia plana and the ragworm Hediste diversicolor. *Ecotoxicol. Environ. Saf.* **2012**, *84*, 191–198.

(206) Gulson, B.; Wong, H.; Korsch, M.; Gomez, L.; Casey, P.; McCall, M.; McCulloch, M.; Trotter, J.; Stauber, J.; Greenoak, G. Comparison of dermal absorption of zinc from different sunscreen formulations and differing UV exposure based on stable isotope tracing. *Sci. Total Environ.* **2012**, *420*, 313–318.

(207) Larner, F.; Gulson, B.; McCall, M.; Oytam, Y.; Rehkämper, M. An inter-laboratory comparison of high precision stable isotope ratio measurements for nanoparticle tracing in biological samples. *J. Anal. At. Spectrom.* **2014**, *29* (3), 471–477.

(208) Gulson, B.; McCall, M.; Larner, F.; Oytam, Y.; Gomez, L.; Baxter, B. Dermal absorption of Zn from ZnO particles in sunscreens applied to humans. *Toxicol. Lett.* **2014**, *229* (2014), S191.

(209) Gulson, B.; McCall, M.; Korsch, M.; Gomez, L.; Casey, P.; Oytam, Y.; Taylor, A.; McCulloch, M.; Trotter, J.; Kinsley, L.; et al. Small Amounts of Zinc from Zinc Oxide Particles in Sunscreens Applied Outdoors Are Absorbed through Human Skin. *Toxicol. Sci.* **2010**, *118* (1), 140–149.

(210) Osmond-McLeod, M. J.; Oytam, Y.; Kirby, J. K.; Gomez-Fernandez, L.; Baxter, B.; McCall, M. J. Dermal absorption and short-term biological impact in hairless mice from sunscreens containing zinc oxide nano- or larger particles. *Nanotoxicology* **2014**, *8* (sup1), 72–84.

(211) Khan, F. R.; Laycock, A.; Dybowska, A.; Larner, F.; Smith, B. D.; Rainbow, P. S.; Luoma, S. N.; Rehkämper, M.; Valsami-Jones, E. Stable isotope tracer to determine uptake and efflux dynamics of ZnO nano- and bulk particles and dissolved Zn to an estuarine snail. *Environ. Sci. Technol.* **2013**, *47* (15), 8532–8539.

(212) Larner, F.; Rehkämper, M. Evaluation of stable isotope tracing for ZnO nanomaterials-new constraints from high precision isotope analyses and modeling. *Environ. Sci. Technol.* **2012**, *46* (7), 4149–4158.

(213) Misra, S. K.; Dybowska, A.; Berhanu, D.; Croteau, M. N.; Luoma, S. N.; Boccaccini, A. R.; Valsami-Jones, E. Isotopically modified nanoparticles for enhanced detection in bioaccumulation studies. *Environ. Sci. Technol.* **2012**, *46* (2), 1216–1222.

(214) Thit, A.; Ramskov, T.; Croteau, M.-N. N.; Selck, H. Biodynamics of copper oxide nanoparticles and copper ions in an oligochaete - Part II: Subcellular distribution following sediment exposure. *Aquat. Toxicol.* **2016**, *180*, 25–35.

(215) Ramskov, T.; Thit, A.; Croteau, M. N.; Selck, H. Biodynamics of copper oxide

nanoparticles and copper ions in an oligochaete - Part I: Relative importance of water and sediment as exposure routes. *Aquat. Toxicol.* **2015**, *164*, 81–91.

(216) Croteau, M.-N.; Misra, S. K.; Luoma, S. N.; Valsami-Jones, E. Bioaccumulation and Toxicity of CuO Nanoparticles by a Freshwater Invertebrate after Waterborne and Dietborne Exposures. *Environ. Sci. Technol.* **2014**, *48* (18), 10929–10937.

(217) Beard, B. L.; Johnson, C. M. Atom Exchange between Aqueous Fe(II) and Goethite: An Fe Isotope Tracer Study. *Environ. Sci. Technol.* **2009**, *43* (4), 1102–1107.

(218) Reddy, T. R.; Frierdich, A. J.; Beard, B. L.; Johnson, C. M. The effect of pH on stable iron isotope exchange and fractionation between aqueous Fe(II) and goethite. *Chem. Geol.* **2015**, *397*, 118–127.

(219) Meermann, B.; Wichmann, K.; Lauer, F.; Vanhaecke, F.; Ternes, T. A. Application of stable isotopes and AF4/ICP-SFMS for simultaneous tracing and quantification of iron oxide nanoparticles in a sediment–slurry matrix. *J. Anal. At. Spectrom.* **2016**, *31* (4), 890–901.

(220) Gomez, V.; Balu, A. M.; Serrano-Ruiz, J. C.; Irusta, S.; Dionysiou, D. D.; Luque, R.; Santamaría, J. Microwave-assisted mild-temperature preparation of neodymium-doped titania for the improved photodegradation of water contaminants. *Appl. Catal. A Gen.* **2012**, *441–442*, 47–53.

(221) Saleh, N. B.; Milliron, D. J.; Aich, N.; Katz, L. E.; Liljestrand, H. M.; Kirisits, M. J. Importance of doping, dopant distribution, and defects on electronic band structure alteration of metal oxide nanoparticles: Implications for reactive oxygen species. *Sci. Total Environ.* **2016**, *568*, 926–932.

(222) Veeranarayanan, S.; Poulose, A. C.; Sheikh Mohamed, M.; Nagaoka, Y.; Iwai, S.; Nakagame, Y.; Kashiwada, S.; Yoshida, Y.; Maekawa, T.; Sakthi Kumar, D. Synthesis and application of luminescent single CdS quantum dot encapsulated silica nanoparticles directed for precision optical bioimaging. *Int. J. Nanomedicine* **2012**.

(223) Ma, N.; Marshall, A. F.; Gambhir, S. S.; Rao, J. Facile synthesis, silanization, and biodistribution of biocompatible quantum dots. *Small* **2010**.

(224) Deline, A. R.; Young, W. M.; Nason, J. A. Gold core-labeled TiO 2 nanoparticles for tracking behavior in complex matrices: synthesis, characterization, and demonstration. *Environ. Sci. Nano* **2018**, *5* (4), 956–968.

(225) Fan, X. M.; Zou, W. J.; Gu, R. A.; Yao, J. L. Preparation of Au@SiO2 core-shell nanoparticles and their surface-enhanced Raman spectra. *Chem. J. Chinese Univ.* **2008**, *29* (1), 130–134.

(226) Chen, C.; Shi, M.; Cargnello, M.; Fornasiero, P.; Murray, C. B.; Gorte, R. J. Au@TiO2 core-shell nanostructures with high thermal stability. *Catal. Letters* **2014**, *144* (11), 1939–1945.

(227) Lee, J. E.; Bera, S.; Choi, Y. S.; Lee, W. I. Size-dependent plasmonic effects of M and M@SiO 2 (M = Au or Ag) deposited on TiO 2 in photocatalytic oxidation reactions. *Appl. Catal. B Environ.* **2017**, *214*, 15–22.

(228) Paunescu, D.; Puddu, M.; Soellner, J. O. B.; Stoessel, P. R.; Grass, R. N. Reversible DNA encapsulation in silica to produce ROS-resistant and heat-resistant synthetic DNA "fossils." *Nat. Protoc.* **2013**, *8* (12), 2440–2448.

(229) Grass, R. N.; Schälchli, J.; Paunescu, D.; Soellner, J. O. B.; Kaegi, R.; Stark, W. J. Tracking Trace Amounts of Submicrometer Silica Particles in Wastewaters and Activated Sludge Using Silica-Encapsulated DNA Barcodes. *Environ. Sci. Technol. Lett.* **2014**, *1* (12), 484–489.

(230) Mora, C. A.; Paunescu, D.; Grass, R. N.; Stark, W. J. Silica particles with encapsulated DNA as trophic tracers. *Mol. Ecol. Resour.* **2015**, *15* (2), 231–241.

(231) Paunescu, D.; Mora, C. A.; Querci, L.; Heckel, R.; Puddu, M.; Hattendorf, B.; Günther, D.; Grass, R. N. Detecting and Number Counting of Single Engineered Nanoparticles by Digital Particle Polymerase Chain Reaction. *ACS Nano* **2015**, *9* (10), 9564–9572.

(232) Kim, K. T.; Klaine, S. J.; Cho, J.; Kim, S. H.; Kim, S. D. Oxidative stress responses of Daphnia magna exposed to TiO2 nanoparticles according to size fraction. *Sci. Total Environ.* **2010**, *408* (10), 2268–2272.

(233) Roh, J. Y.; Park, Y. K.; Park, K.; Choi, J. Ecotoxicological investigation of CeO2 and TiO2 nanoparticles on the soil nematode Caenorhabditis elegans using gene expression, growth, fertility, and survival as endpoints. *Environ. Toxicol. Pharmacol.* **2010**.

(234) Simon-Deckers, A.; Loo, S.; Mayne-L'hermite, M.; Herlin-Boime, N.; Menguy, N.; Reynaud, C.; Gouget, B.; Carrière, M. Size-, composition- and shape-dependent toxicological impact of metal oxide nanoparticles and carbon nanotubes toward bacteria. *Environ. Sci. Technol.* **2009**.

(235) Zhu, M.; Nie, G.; Meng, H.; Xia, T.; Nel, A.; Zhao, Y. Physicochemical properties determine nanomaterial cellular uptake, transport, and fate. *Acc. Chem. Res.* **2013**, *46* (3), 622–631.

(236) Oberdörster, G.; Oberdörster, E.; Oberdörster, J. Nanotoxicology: An emerging discipline evolving from studies of ultrafine particles. *Environmental Health Perspectives*. 2005.

(237) Kennedy, A. J.; Hull, M. S.; Diamond, S.; Chappell, M.; Bednar, A. J.; Laird, J. G.; Melby, N. L.; Steevens, J. A. Gaining a critical mass: A dose metric conversion case study using silver nanoparticles. *Environ. Sci. Technol.* **2015**, *49* (20), 12490–12499.

(238) Hull, M.; Kennedy, A. J.; Detzel, C.; Vikesland, P.; Chappell, M. A. Moving beyond mass: The unmet need to consider dose metrics in environmental nanotoxicology studies. *Environ. Sci. Technol.* **2012**, *46* (20), 10881–10882.

(239) Sharma, V. K. Aggregation and toxicity of titanium dioxide nanoparticles in aquatic environment—A Review. *J. Environ. Sci. J. J. Environ. Sci. Heal. Part A J. Environ. Sci. Heal. Part A* **2009**, *4414* (44), 1093–4529.

(240) Louie, S. M.; Tilton, R. D.; Lowry, G. V. Critical review: impacts of macromolecular coatings on critical physicochemical processes controlling environmental fate of nanomaterials. *Environ. Sci. Nano* **2016**, *3* (2), 283–310.

(241) Sung, H. J.; Al-Abed, S. R.; Luxton, T. Influence of carboxymethyl cellulose for the transport of titanium dioxide nanoparticles in clean silica and mineral-coated sands. *Environ. Sci. Technol.* **2009**.

(242) Lowry, G. V.; Hill, R. J.; Harper, S.; Rawle, A. F.; Hendren, C. O.; Klaessig, F.; Nobbmann, U.; Sayre, P.; Rumble, J. Guidance to improve the scientific value of zeta-potential measurements in nanoEHS. *Environ. Sci. Nano* **2016**, *3* (5), 953–965.

(243) Xiao, Y.; Wiesner, M. R. Characterization of surface hydrophobicity of engineered nanoparticles. *J. Hazard. Mater.* **2012**, *215–216*, 146–151.

(244) Xiao, Y.; Wiesner, M. R. Transport and retention of selected engineered nanoparticles by porous media in the presence of a biofilm. *Environ. Sci. Technol.* **2013**, *47* (5), 2246–2253.

(245) Crandon, L. Addressing persistent challenges in nanotoxicology exposures: techniques for in situ characterization, Oregon State University, 2018.

(246) Zhang, H.; Ji, Z.; Xia, T.; Meng, H.; Low-Kam, C.; Liu, R.; Pokhrel, S.; Lin, S.; Wang, X.; Liao, Y. P.; et al. Use of metal oxide nanoparticle band gap to develop a predictive paradigm for oxidative stress and acute pulmonary inflammation. *ACS Nano* **2012**, *6* (5), 4349–4368.

(247) Corredor, C.; Borysiak, M. D.; Wolfer, J.; Westerhoff, P.; Posner, J. D. Colorimetric Detection of Catalytic Reactivity of Nanoparticles in Complex Matrices. *Environ. Sci. Technol.* **2015**, *49* (6), 3611–3618.

(248) Gilbertson, L. M.; Albalghiti, E. M.; Fishman, Z. S.; Perreault, F.; Corredor, C.; Posner, J.

D.; Elimelech, M.; Pfefferle, L. D.; Zimmerman, J. B. Shape-Dependent Surface Reactivity and Antimicrobial Activity of Nano-Cupric Oxide. *Environ. Sci. Technol.* **2016**, *50* (7), 3975–3984.

(249) Zhao, J.; Riediker, M. Detecting the oxidative reactivity of nanoparticles: a new protocol for reducing artifacts. *J. Nanoparticle Res.* **2014**, *16* (7), 2493.

(250) Wormington, A. M.; Coral, J.; Alloy, M. M.; Delmarï¿½, C. L.; Mansfield, C. M.; Klaine, S. J.; Bisesi, J. H.; Roberts, A. P. Effect of natural organic matter on the photo-induced toxicity of titanium dioxide nanoparticles. *Environ. Toxicol. Chem.* **2017**, *36* (6), 1661–1666.

(251) Tian, Y.; Tatsuma, T. Plasmon-induced photoelectrochemistry at metal nanoparticles supported on nanoporous TiO2. *Chem. Commun.* **2004**.

(252) Choi, H.; Chen, W. T.; Kamat, P. V. Know thy nano neighbor. Plasmonic versus electron charging effects of metal nanoparticles in dye-sensitized solar cells. *ACS Nano* **2012**, *6* (5), 4418–4427.

(253) Zaleska, A. Doped-TiO2 : a review Doped-TiO 2 : A Review. **2014**, No. November 2008.

(254) Linic, S.; Christopher, P.; Ingram, D. B. Plasmonic-metal nanostructures for efficient conversion of solar to chemical energy. *Nat. Mater.* **2011**, *10* (12), 911–921.

(255) Pettitt, M. E.; Lead, J. R. Minimum physicochemical characterisation requirements for nanomaterial regulation. *Environ. Int.* **2013**, *52*, 41–50.

(256) Thomas, D. G.; Gaheen, S.; Harper, S. L.; Fritts, M.; Klaessig, F.; Hahn-Dantona, E.; Paik, D.; Pan, S.; Stafford, G. A.; Freund, E. T.; et al. ISA-TAB-Nano: A Specification for Sharing Nanomaterial Research Data in Spreadsheet-based Format. *BMC Biotechnology*. 2013.

(257) Bour, A.; Mouchet, F.; Cadarsi, S.; Silvestre, J.; Verneuil, L.; Baqué, D.; Chauvet, E.; Bonzom, J.-M.; Pagnout, C.; Clivot, H.; et al. Toxicity of CeO 2 nanoparticles on a freshwater experimental trophic chain: A study in environmentally relevant conditions through the use of mesocosms. *Nanotoxicology* **2015**, *10* (2), 1–11.

(258) Irawaty, W.; Soetaredjo, F. E.; Ayucitra, A. Understanding the Relationship between Organic Structure and Mineralization Rate of TiO2-mediated Photocatalysis. *Procedia Chem.* **2014**.

(259) Yang, L.; Yu, L. E.; Ray, M. B. Degradation of paracetamol in aqueous solutions by TiO2 photocatalysis. *Water Res.* **2008**.

(260) Tschirch, J.; Dillert, R.; Bahnemann, D.; Proft, B.; Biedermann, A.; Goer, B. Photodegradation of methylene blue in water , a standard method to determine the activity of photocatalytic coatings ? **2008**, *34* (4), 381–392.

(261) Ma, H.; Brennan, A.; Diamond, S. A. Photocatalytic reactive oxygen species production and phototoxicity of titanium dioxide nanoparticles are dependent on the solar ultraviolet radiation spectrum. *Environ. Toxicol. Chem.* **2012**, *31* (9), 2099–2107.

(262) Liang, H. chao; Li, X. zhong; Yang, Y. hua; Sze, K. hung. Effects of dissolved oxygen, pH, and anions on the 2,3-dichlorophenol degradation by photocatalytic reaction with anodic TiO2nanotube films. *Chemosphere* **2008**.

(263) Xiong, S.; Tang, Y.; Ng, H. S.; Zhao, X.; Jiang, Z.; Chen, Z.; Ng, K. W.; Loo, S. C. J. Specific surface area of titanium dioxide (TiO2) particles influences cyto- and photo-toxicity. *Toxicology* **2013**.

(264) Keller, A. A.; Wang, H.; Zhou, D.; Lenihan, H. S.; Cherr, G.; Cardinale, B. J.; Miller, R.; Zhaoxia, J. I. Stability and aggregation of metal oxide nanoparticles in natural aqueous matrices. *Environ. Sci. Technol.* **2010**, *44* (6), 1962–1967.

(265) Shih, Y. H.; Liu, W. S.; Su, Y. F. Aggregation of stabilized TiO2nanoparticle suspensions in the presence of inorganic ions. *Environ. Toxicol. Chem.* **2012**.

(266) Akpan, U. G.; Hameed, B. H. Parameters affecting the photocatalytic degradation of dyes using TiO2-based photocatalysts: A review. *J. Hazard. Mater.* **2009**, *170* (2–3), 520–529.

(267) Dong, H.; Zeng, G.; Tang, L.; Fan, C.; Zhang, C.; He, X.; He, Y. An overview on limitations of TiO2-based particles for photocatalytic degradation of organic pollutants and the corresponding countermeasures. *Water Res.* **2015**.

(268) Kuwahara, Y.; Yamashita, H. Efficient photocatalytic degradation of organics diluted in water and air using TiO2 designed with zeolites and mesoporous silica materials. *J. Mater. Chem.* **2011**.

(269) Krishnan, P.; Liu, M.; Itty, P. A.; Liu, Z.; Rheinheimer, V.; Zhang, M.-H.; Monteiro, P. J. M.; Yu, L. E. Characterization of photocatalytic TiO2 powder under varied environments using near ambient pressure X-ray photoelectron spectroscopy. *Sci. Rep.* **2017**.

(270) Henderson, M. A. A surface science perspective on TiO2 photocatalysis. *Surf. Sci. Rep.* **2011**, *66* (6–7), 185–297.

(271) Chowdhury, I.; Hong, Y.; Walker, S. L. Container to characterization: Impacts of metal oxide handling, preparation, and solution chemistry on particle stability. *Colloids Surfaces A Physicochem. Eng. Asp.* **2010**, *368* (1–3), 91–95.

(272) Miller, R. J.; Bennett, S.; Keller, A. A.; Pease, S.; Lenihan, H. S. TiO2 nanoparticles are phototoxic to marine phytoplankton. *PLoS One* **2012**, *7* (1), e30321.

(273) Wu, L.; Buchholz, D.; Bresser, D.; Gomes Chagas, L.; Passerini, S. Anatase TiO2 nanoparticles for high power sodium-ion anodes. *J. Power Sources* **2014**, *251*, 379–385.

(274) Godwin, H. A.; Chopra, K.; Bradley, K. A.; Cohen, Y.; Harthorn, B. H.; Hoek, E. M. V.; Holden, P.; Keller, A. A.; Lenihan, H. S.; Nisbet, R. M.; et al. The University of California Center for the environmental implications of nanotechnology. *Environmental Science and Technology*. 2009.

(275) Chowdhury, I.; Walker, S. L.; Mylon, S. E. Aggregate morphology of nano-TiO2: role of primary particle size, solution chemistry, and organic matter. *Environ. Sci. Process. Impacts* **2013**, *15*, 275.

(276) Pagnout, C.; Jomini, S.; Dadhwal, M.; Caillet, C.; Thomas, F.; Bauda, P. Role of electrostatic interactions in the toxicity of titanium dioxide nanoparticles toward Escherichia coli. *Colloids Surfaces B Biointerfaces* **2012**, *92* (2012), 315–321.

(277) Gerrity, D.; Ryu, H.; Crittenden, J.; Abbaszadegan, M. Photocatalytic inactivation of viruses using titanium dioxide nanoparticles and low-pressure UV light. *J. Environ. Sci. Health. A. Tox. Hazard. Subst. Environ. Eng.* **2008**.

(278) Zhou, D.; Bennett, S. W.; Keller, A. A. Increased mobility of metal oxide nanoparticles due to photo and thermal induced disagglomeration. *PLoS One* **2012**, *7* (5), 1–8.

(279) Bennett, S. W.; Zhou, D.; Mielke, R.; Keller, A. A. Photoinduced Disaggregation of TiO2 Nanoparticles Enables Transdermal Penetration. *PLoS One* **2012**.

(280) Grasso, D.; Subramaniam, K.; Butkus, M.; Strevett, K.; Bergendahl, J. A review of non-DLVO interactions in environmental colloidal systems. *Rev. Environ. Sci. Biotechnol.* **2002**, *1* (1), 17–38.

(281) Staufenbiel, S.; Keck, C. M.; Müller, R. H. The “real environment” quantification of surface hydrophobicity of differently stabilized nanocrystals as key parameter for organ distribution. In *Macromolecular Symposia*; 2014.

(282) Lin, D.; Tian, X.; Wu, F.; Xing, B. Fate and Transport of Engineered Nanomaterials in the Environment. *J. Environ. Qual.* **2010**.

(283) Wang, R.; Hashimoto, K.; Fujishima, A.; Chikuni, M.; Kojima, E.; Kitamura, A.; Shimohigoshi, M.; Watanabe, T. Light-induced amphiphilic surfaces. *Nature* **1997**, *388*, 431–432.

(284) Wang, C. Y.; Groenzin, H.; Shultz, M. J. Molecular species on nanoparticulate anatase TiO2 film detected by sum frequency generation: Trace hydrocarbons and hydroxyl groups. *Langmuir* **2003**.

(285) Foran, P. S.; Boxall, C.; Denison, K. R. Photoinduced superhydrophilicity: A kinetic study of time dependent photoinduced contact angle changes on TiO2 surfaces. *Langmuir* **2012**.

(286) Zubkoy, T.; Stahl, D.; Thompson, T. L.; Panayotov, D.; Diwald, O.; Yates, J. T. Ultraviolet light-induced hydrophilicity effect on TiO2(110) (1×1). Dominant role of the photooxidation of adsorbed hydrocarbons causing wetting by water droplets. *J. Phys. Chem. B* **2005**.

(287) Bolis, V.; Busco, C.; Ciarletta, M.; Distasi, C.; Erriquez, J.; Fenoglio, I.; Livraghi, S.; Morel, S. Hydrophilic/hydrophobic features of TiO2 nanoparticles as a function of crystal phase, surface area and coating, in relation to their potential toxicity in peripheral nervous system. *J. Colloid Interface Sci.* **2012**, *369* (1), 28–39.

(288) Watanabe, T.; Nakajima, A.; Wang, R.; Minabe, M.; Koizumi, S.; Fujishima, A.; Hashimoto, K. Photocatalytic activity and photoinduced hydrophilicity of titanium dioxide coated glass. *Thin Solid Films* **1999**, *351* (1–2), 260–263.

(289) Wang, D.; Zhao, L.; Ma, H.; Zhang, H.; Guo, L.-H. Quantitative Analysis of Reactive Oxygen Species Photogenerated on Metal Oxide Nanoparticles and Their Bacteria Toxicity: The Role of Superoxide Radicals. *Environ. Sci. Technol.* **2017**, acs.est.7b00473.

(290) Marugán, J.; van Grieken, R.; Pablos, C.; Sordo, C. Analogies and differences between photocatalytic oxidation of chemicals and photocatalytic inactivation of microorganisms. *Water Res.* **2010**, *44* (3), 789–796.

(291) Cho, M.; Chung, H.; Choi, W.; Yoon, J. Linear correlation between inactivation of E. coli and OH radical concentration in TiO2 photocatalytic disinfection. *Water Res.* **2004**, *38* (4), 1069–1077.

(292) Coral, J. A. Measuring and Predicting Hydroxyl Radical Generation From Irradiated TiO2 Nanoparticles Under Simulated Environmental Conditions and Correlations to Daphnia magna Toxicity, Clemson University, 2018.

(293) Blum, H. F.; Spealman, C. R. Photochemistry of fluorescein. *J. Phys. Chem.* **1933**, *37* (9), 1123–1133.

(294) Kamidate, T.; Ishida, Y.; Tani, H.; Ishida, A. Determination of hydrogen peroxide by fluorescein chemiluminescence catalyzed with horseradish peroxidase encapsulated in liposome. *Bunseki Kagaku* **2005**, *54* (6), 569–572.

(295) Smart, P. L.; Laidlaw, I. M. S. An evaluation of some fluorescent dyes for water tracing. *Water Resour. Res.* **1977**, *13* (1), 15–33.

(296) Yin, J. J.; Liu, J.; Ehrenshaft, M.; Roberts, J. E.; Fu, P. P.; Mason, R. P.; Zhao, B. Phototoxicity of nano titanium dioxides in HaCaT keratinocytes-Generation of reactive oxygen species and cell damage. *Toxicol. Appl. Pharmacol.* **2012**, *263* (1), 81–88.

(297) Hurum, D. C.; Agrios, A. G.; Gray, K. A.; Rajh, T.; Thurnauer, M. C. Explaining the Enhanced Photocatalytic Activity of Degussa P25 Mixed-Phase TiO $_2$ Using EPR. *J. Phys. Chem. B* **2003**, *107* (19), 4545–4549.

(298) Farner Budarz, J. Lights, Camera, Reaction! The Influence of Interfacial Chemistry on Nanoparticle Photoreactivity, Duke University, 2016.

(299) Carley, A. F.; Chalker, P. R.; Riviere, J. C.; Roberts, M. W. The identification and characterisation of mixed oxidation states at oxidised titanium surfaces by analysis of X-ray photoelectron spectra. *J. Chem. Soc. Faraday Trans. 1* **1987**, *83* (2), 351.

(300) Simonsen, M. E.; Li, Z.; Søgaard, E. G. Influence of the OH groups on the photocatalytic activity and photoinduced hydrophilicity of microwave assisted sol-gel TiO2film. *Appl. Surf. Sci.* **2009**.

(301) Simonsen, M. E.; Jensen, H.; Li, Z.; Søgaard, E. G. Surface properties and photocatalytic activity of nanocrystalline titania films. *J. Photochem. Photobiol. A Chem.* **2008**, *200* (2–3), 192–200.

(302) Naganuma, Y.; Tanaka, S.; Kato, C. Preparation of Sol-Gel Derived Titanium Oxide Thin Films Using Vacuum Ultraviolet Irradiation With a Xenon Excimer Lamp. *Japanese J. Appl. Phys. Part 1-Regular Pap. Short Notes Rev. Pap.* **2004**.

(303) Hollinger, G.; Jugnet, Y.; Pertosa, P.; Minh Duc, T. X-ray photoelectron spectroscopy of thermally grown silicon dioxide films on silicon. *Chem. Phys. Lett.* **1975**, *36* (4), 441–445.

(304) Yu, J.; Yu, J. C.; Ho, W.; Jiang, Z. Effects of calcination temperature on the photocatalytic activity and photo-induced super-hydrophilicity of mesoporous TiO2 thin films. *New J. Chem.* **2002**.

(305) Jribi, R.; Barthel, E.; Bluhm, H.; Grunze, M.; Koelsch, P.; Verreault, D.; Søndergard, E. Ultraviolet irradiation suppresses adhesion on TiO2. *J. Phys. Chem. C* **2009**.

(306) Górska, P.; Zaleska, A.; Kowalska, E.; Klimczuk, T.; Sobczak, J. W.; Skwarek, E.; Janusz, W.; Hupka, J. TiO2 photoactivity in vis and UV light: The influence of calcination temperature and surface properties. *Appl. Catal. B Environ.* **2008**, *84* (3–4), 440–447.

(307) Xie, H.; Li, N.; Liu, B.; Yang, J.; Zhao, X. Role of sodium ion on TiO2photocatalyst: Influencing crystallographic properties or serving as the recombination center of charge carriers? *J. Phys. Chem. C* **2016**.

(308) Yaghoubi, H.; Taghavinia, N.; Alamdari, E. K.; Volinsky, A. A. Nanomechanical properties of TiO2 granular thin films. *ACS Appl. Mater. Interfaces* **2010**.

(309) Sieland, F.; Duong, N. A.; Schneider, J.; Bahnemann, D. W. D. W. Influence of Inorganic Additives on the Photocatalytic Removal of Nitric Oxide and on the Charge Carrier Dynamics of TiO_2 Powders. *J. Photochem. Photobiol. A Chem.* **2018**.

(310) Zhao, D.; Chen, C.; Wang, Y.; Ji, H.; Ma, W.; Zang, L.; Zhao, J. Surface Modification of TiO 2 by Phosphate: Effect on Photocatalytic Activity and Mechanism Implication. *J. Phys. Chem. C* **2008**.

(311) Long, M.; Brame, J.; Qin, F.; Bao, J.; Li, Q.; Alvarez, P. J. J. Phosphate Changes Effect of Humic Acids on TiO_2 Photocatalysis: From Inhibition to Mitigation of Electron–Hole Recombination. *Environ. Sci. Technol.* **2017**.

(312) Mills, A. An overview of the methylene blue ISO test for assessing the activities of photocatalytic films. *Appl. Catal. B Environ.* **2012**, *128*, 144–149.

(313) Kinsinger, N. M.; Dudchenko, A.; Wong, A.; Kisailus, D. Synergistic Effect of pH and Phase in a Nanocrystalline Titania Photocatalyst. *ACS Appl. Mater. Interfaces* **2013**, *5* (13), 6247–6254.

(314) Ohno, T.; Tokieda, K.; Higashida, S.; Matsumura, M. Synergism between rutile and anatase TiO2 particles in photocatalytic oxidation of naphthalene. *Appl. Catal. A Gen.* **2003**, *244* (2), 383–391.

(315) Kaplan, R.; Erjavec, B.; Pintar, A. Enhanced photocatalytic activity of single-phase, nanocomposite and physically mixed TiO2polymorphs. *Appl. Catal. A Gen.* **2015**, *489*, 51–60.

(316) Deiana, C.; Minella, M.; Tabacchi, G.; Maurino, V.; Fois, E.; Martra, G. Shape-controlled TiO2 nanoparticles and TiO2 P25 interacting with CO and H2O2 molecular probes: a synergic approach for surface structure recognition and physico-chemical understanding. *Phys. Chem. Chem. Phys.* **2013**, *15* (1), 307–315.

(317) Russell, L. L. Chemical aspects of groundwater recharge with wastewaters, University of California, Berkeley, 1976.

(318) Silvertooth, J. Evaluation of copper removal from stormwater runoff using compost and Apatite II, Oregon State University, 2014.

(319) *IUPAC Compendium of Chemical Terminology*; Nič, M., Jirát, J., Košata, B., Jenkins, A., McNaught, A., Eds.; IUPAC: Research Triagle Park, NC, 2009.

(320) Shrivastava, A.; Gupta, V.; Article, R. Methods for the determination of limit of detection and limit of quantitation of the analytical methods. *Chronicles Young Sci.* **2011**, *2* (1), 21–25.

7 Appendices

7.1 Appendix A: Supporting Information for Chapter 2

Conversion of electrophoretic mobility values to ζ-potentials

Table 7.1.1. Information used for calculating ζ-potentials from electrophoretic mobility values.

	AuNP Cores		Au@TiO$_2$ NPs		TiO$_2$ NPs	
Surface functionalization	360 kDa polyvinylpyrrolidone					
Shape	Spherical		Ellipsoidal		Ellipsoidal	
D$_h$, nm	60		176		185	
pH and Average electrophoretic mobility (EPM), µm·cm/V·s	pH	EPM	pH	EPM	pH	EPM
	3.31	-0.61	3.38	-1.84	3.24	-1.18
	3.40	-0.39	3.39	-1.97	3.35	-0.92
	3.87	-0.30	3.88	-2.48	3.85	-1.02
	4.44	-0.15	4.48	-2.88	4.43	-1.51
	4.99	-0.61	4.97	-2.87	4.89	-1.82
	5.68	-1.06	5.58	-2.81	5.66	-2.53
	6.15	-1.63	6.19	-2.99	6.16	-2.74
	7.15	-1.80	6.88	-3.28	6.65	-2.62
	7.16	-1.61	7.45	-3.34	7.20	-2.59
	8.67	-1.90	8.04	-3.40	8.18	-2.53
	8.88	-2.01	8.81	-3.31	8.41	-2.57
	9.44	-1.82	8.99	-3.61	8.99	-2.71
	9.72	-1.94	9.25	-3.72	9.25	-3.06
	10.25	-1.70	9.74	-3.86	9.73	-3.08
	10.78	-1.72	10.24	-4.19	10.24	-3.07
			10.77	-3.83	10.77	-3.32
Model used to compute ζ-potential	Smoluchowski					
Sample composition	10 mg/L NPs, 1 mM KCl, KOH or HCl for pH adjustment as applicable					
Viscosity	0.887 mPa					
Measurement details	3 replicates performed at 20 cycles each for each data point					

Acid digestion of samples for ICP analysis

For the spike-and-recovery experiment performed in distilled deionized (DDI) water, and the accompanying measurements of NP stock concentrations, the following procedure was used for acid digestion prior to ICP-MS analysis:

1. Samples were all digested and analyzed in triplicate, and a method blank sample of DDI water was also digested and analyzed during each experiment.
2. Each sample was transferred to a teflon beaker and heated on a hot plate set to 225°C until less than 0.5 mL of solution remained.
3. 8 mL of concentrated (70% w/w) HNO_3 and 2 mL of concentrated (49% w/w) HF was added to each beaker. Each beaker was heated on a hot plate set to 225°C until a single viscous drop of solution remained.
4. 5 mL of concentrated (37% w/w) HCl was added to each beaker, and heated on a hot plate set to 225°C until a single viscous drop of solution remained.
5. 5 mL of concentrated HNO_3 was added to each beaker, and heated on a hot plate set to 225°C until a single viscous drop of solution remained.
6. 8 mL of 2N HNO_3 was added to each beaker. Each beaker was covered with a watch glass, heated on a hot plate until boiling, and then removed from heat. The 2N HNO_3 solution was permitted to remain in the beakers overnight.
7. For each beaker, the solution was diluted to 10 mL using 2N HNO_3, and stored in a polypropylene centrifuge tube. Prior to analysis, each sample was diluted to a 2% HNO_3 concentration using DDI water.

This resulted in a Ti:Au ratio of the Au@TiO_2 NP stock of 1.45. In the spike-and-recovery experiment, 80.4% of the total added gold and 98.7% of the total added titanium was recovered. Adjustments were made to the acid digestion procedure to increase gold recovery and address the organic components of more complex environmental samples.

For the spike-and-recovery experiment performed in a sunscreen-river water mixture, and the accompanying measurements of NP stock concentrations, the following procedure was used for acid digestion prior to ICP-OES analysis:

1. Samples were all digested and analyzed in triplicate, and a method blank sample of DDI water was also digested and analyzed during each experiment.
2. Each sample was transferred to a teflon beaker and heated on a hot plate set to 225°C until less than 0.5 mL of solution remained.
3. 1 mL of concentrated (70% w/w) HNO_3 and 2 mL of 30% H_2O_2 was added to each beaker. Each beaker was heated on a hot plate set to 225°C until a single viscous drop of solution remained.
4. 6 mL of concentrated (70% w/w) HNO_3 and 4 mL of concentrated (49% w/w) HF was added to each beaker. Each beaker was heated on a hot plate set to 225°C until a single viscous drop of solution remained.
5. 4.5 mL of concentrated (37% w/w) HCl and 1.5 mL of concentrated HNO_3 was added to each beaker. Each beaker was heated on a hot plate set to 225°C until a single viscous drop of solution remained.
6. 5 mL of concentrated HNO_3 was added to each beaker along with one drop of concentrated HCl, and heated on a hot plate set to 225°C until a single viscous drop of solution remained.
7. 8 mL of 2N HNO_3 was added to each beaker along with one drop of concentrated HCl. Each beaker was covered with a watch glass, heated on a hot plate until boiling, and then removed from heat. The 2N HNO_3 solution was permitted to remain in the beakers overnight.
8. For each beaker, the solution was diluted to 10 mL using 2N HNO_3, and stored in a polypropylene centrifuge tube. Prior to analysis, each sample was diluted to a 2% HNO_3 concentration using DDI water.

This resulted in a Ti:Au ratio of the Au@TiO_2 NP stock of 2.25. In the spike-and-recovery experiment, 94-105% of the total added gold and 80% of the total added titanium was recovered. As discussed in the main text, the lower titanium recovery in this experiment was likely due to the presence of the rutile phase of titanium from the sunscreen mixture.

Additional TEM images of Au@TiO$_2$ NPs

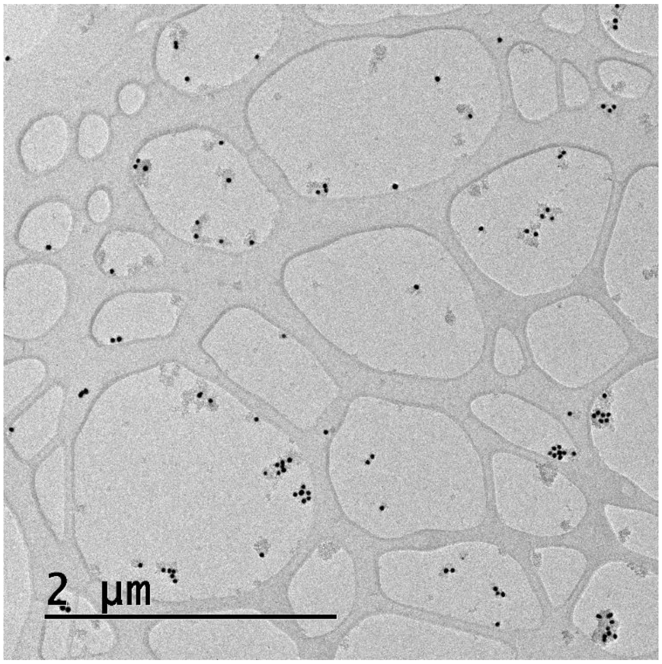

Figure 7.1.1. TEM image of Au@TiO$_2$ NPs.

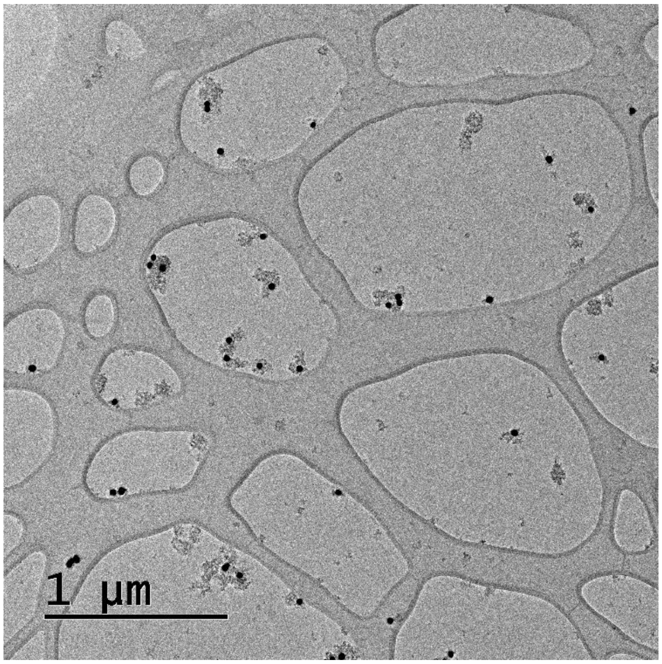

Figure 7.1.2. TEM image of $Au@TiO_2$ NPs.

Estimation of Lattice Mismatch

The lattice mismatch between the AuNP core and the anatase TiO_2 shell was estimated using the following values[100] and calculation.

Lattice constant for Au (as reported for bulk Au surfaces at room temperature): 0.408 nm

Lattice constants for anatase TiO_2 (as reported for bulk surface at room temperature):

a = 0.378 nm, c = 0.951 nm

Lattice mismatch = $\frac{|a_{Au}-a_{Ti}|}{a_{Au}} \times 100\% = \frac{|\ 0.408\ nm-0.378\ nm|}{0.408\ nm} \times 100\% =\ 7.4\%$

Calculation of number of AuNP cores per TiO_2 shell

TEM analysis

For each of the Au@TiO_2 nanoparticles imaged, the number of AuNP cores contained was recorded. This number was averaged over N=120 particles and found to be 2 ± 1 AuNP core per Au@TiO_2 NP.

Sp-ICP-MS analysis

AuNPs were analyzed before and after coating with TiO_2 NPs. After coating, the mass Au per particle increased, which was attributed to multiple AuNPs within one TiO_2 shell appearing as a single peak with larger intensity. The mean and mode values of peak intensity and AuNP size are summarized below in Table 7.1.2.

Table 7.1.2. Summary of results of sp-ICP-MS analysis of AuNP cores before and after coating.

	AuNPs (no coating)	AuNPs (after coating with TiO_2)
Mean Peak Intensity	11.26	17.80
Mode Peak Intensity	8.67	9.67
Mean NP Size, nm	35.6	40.8
Mode NP Size, nm	33.7	35.4

The mass of Au is directly related to the intensity peak signal, allowing for the intensity values to be used directly in the calculation of AuNP cores per shell. The calculation is performed below:

$$Np = \frac{Mean\ intensity_{coated\ AuNPs}}{Mode\ intensity_{uncoated\ AuNPs}} = \frac{17.80}{8.67} = 2.05$$

Calculation of Ti:Au ratio

TEM Analysis

For each of the TiO_2 and Au@TiO_2 nanoparticles imaged, the long and short axes were measured using ImageJ. The long axis average ± standard deviation was reported as the primary particle diameter for each NP type in the main text. For the Au@TiO_2 NPs, the number of AuNP cores in each particle was also recorded.

To estimate a possible range of 3-dimensional ellipsoidal volumes from the 2-dimensional TEM images, two calculations were performed on each Au@TiO_2 and TiO_2 NP:

For the lower limit,

$$\cancel{V}, Au@TiO_2\ NP = \frac{4}{3}\pi\left(\frac{long\ axis}{2}\right)\left(\frac{short\ axis}{2}\right)^2$$

For the upper limit,

$$\cancel{V}, Au@TiO_2\ NP = \frac{4}{3}\pi\left(\frac{long\ axis}{2}\right)^2\left(\frac{short\ axis}{2}\right)$$

The diameter of each of the AuNP cores (as imaged inside of Au@TiO_2 NPs) was measured using ImageJ. The diameter average ± standard deviation was reported as the primary particle diameter in the main text. The volume of each AuNP core was calculated by assuming a spherical shape:

$$\cancel{V}, AuNP = \frac{4}{3}\pi\left(\frac{diameter}{2}\right)^3$$

The results of these analyses are summarized below in Table 7.1.3.

Table 7.1.3. Particle size and volume data, reported as average ± standard deviation, from TEM analyses of NP stocks.

	TiO_2 NPs	Au@TiO_2 NPs	AuNP Cores
Primary Size, nm	169 ± 75	206 ± 85	35 ± 4
Spherical Volume, nm^3	--	--	2.4E+4 ± 1.0E+4
Ellipsoidal Volume (upper limit), nm^3	2.32E+6 ± 2.66E+6	3.23E+6 ± 2.86E+6	--
Ellipsoidal Volume (lower limit), nm^3	1.42E+6 ± 1.50E+6	1.65E+6 ± 1.37E+6	--
Number of cores/shell	--	2 ± 1	--
N_p analyzed	120	100	120

To estimate the average mass of gold present in each AuNP core, the following equation was used:

$$Average\ Mass\ AuNP = (\bar{V}, AuNP)(\rho_{Au})\ ,$$

where $\bar{V}, AuNP$ is the average volume of the AuNP cores and ρ_{Au} is the bulk density of gold.

$$Average\ Mass\ AuNP = (2.4 \times 10^{4}\ nm^{3})\left(1 \times 10^{-21}\frac{cm^{3}}{nm^{3}}\right)\left(19.3\frac{g}{cm^{3}}\right) = 4.6 \times 10^{-16} g\ Au$$

$$Average\ Mass\ AuNP = 4.6 \times 10^{-16} g\ Au$$

To estimate the mass of gold present in each Au@TiO_2 NP, the following calculation was performed on each imaged Au@TiO_2 NP:

$$Mass\ Au\ in\ Au@TiO_2\ NP = (\#_{cores})(Average\ Mass\ AuNP),$$

where $\#_{cores}$ is the number of cores in the Au@TiO$_2$ NP being analyzed.

To estimate a possible range of the mass of titanium present in each Au@TiO$_2$ and TiO$_2$ NP, the following calculations were performed on each imaged Au@TiO$_2$ NP, using both the upper and lower limits for the elliptical Au@TiO$_2$ volume:

$$\bar{V}, TiO_2 = \ (Volume, Au@TiO_2\ NP) - (\bar{V}, AuNP \times \ \#_{cores})$$

$$Mass\ Ti\ in\ Au@TiO_2\ NP = \ (Volume, TiO_2\ )\left(\rho_{TiO_2}\right)\left(\frac{g\ Ti}{g\ TiO_2}\right),$$

where $\rho_{TiO_2}$is the bulk density of anatase TiO$_2$ and $\frac{g\ Ti}{g\ TiO_2}$ is the mass fraction of titanium in TiO$_2$.

An example calculation is included below using the average upper limit for the Au@TiO$_2$ volume and a value of 2 cores per Au@TiO$_2$ NP:

$$\bar{V}, TiO_2 = \ (3.23 \times 10^6\ nm^3) - (2.4 \times 10^4\ nm^3 \times 2) = \ 3.\bar{1}8 \times 10^6\ nm^3$$

$$Mass\ Ti\ in\ Au@TiO_2\ NP = \ (3.\bar{1}8 \times 10^6\ nm^3\ )\left(1 \times 10^{-21}\frac{cm^3}{nm^3}\right)\left(3.78\frac{g}{cm^3}\right)\left(\frac{0.595\ g\ Ti}{g\ TiO_2}\right)$$

$$Mass\ Ti\ in\ Au@TiO_2\ NP = \ 7.2 \times 10^{-15} g\ Ti$$

The Ti:Au ratio was calculated for each Au@TiO$_2$ particle and averaged.

ICP Analysis

The Ti:Au ratio for all ICP analyses was determined using the averages of the gold and titanium concentrations measured in 3 replicate Au@TiO$_2$ NP stock samples (each digested separately).

XPS Analysis

Avantage software was used to perform peak analysis and determine atomic ratios within each sample. Table 7.1.4 summarizes the atomic ratios determined for the Au@TiO_2 NPs.

Table 7.1.4. Atomic ratios and peak binding energies determined using XPS for Au@TiO_2 NP stock. Two 500 µm areas were analyzed on one sample, with identical results.

Peak Name	Binding Energy	Atomic %
Au 4f	83.2 eV	3.6
C 1s	284.8 eV	30
I 3d	618.1 eV	0.4
N 1s	399.4 eV	2.7
O 1s	529.7 eV	43.2
Ti 2p	458.4 eV	20.1

The atomic % was converted to a Ti:Au ratio using the following calculations:

$$Atomic/Molar\ ratio, Ti{:}Au = \frac{Atomic\ \%, Ti}{Atomic\ \%, Au} = \frac{20.1}{3.6} = 5.58\,\frac{mols\ Ti}{mols\ Au}$$

$$Mass\ ratio, Ti{:}Au = (Molar\ ratio, Ti{:}Au)\left(\frac{MW_{Ti}}{MW_{Au}}\right)$$

$$Mass\ ratio, Ti{:}Au = \left(5.58\,\frac{mols\ Ti}{mols\ Au}\right)\left(\frac{47.867\ g\ Ti}{mols\ Ti}\right)\left(\frac{mols\ Au}{196.967\ g\ Au}\right) = 1.4\ \frac{g\ Ti}{g\ Au}$$

XPS Spectra

XPS analysis was performed on a sample of Au@TiO_2 NP stock that was dropcast onto a silicon wafer. The XPS spectra for the Ti2p, O1s, and Au4f regions are included below.

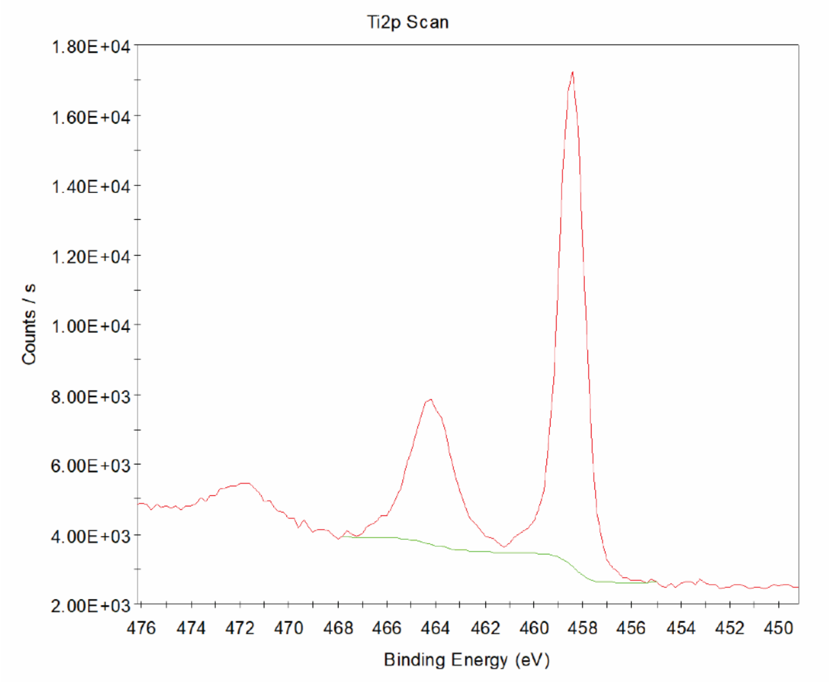

Figure 7.1.3. XPS spectrum of Ti2p region for Au@TiO_2 NPs.

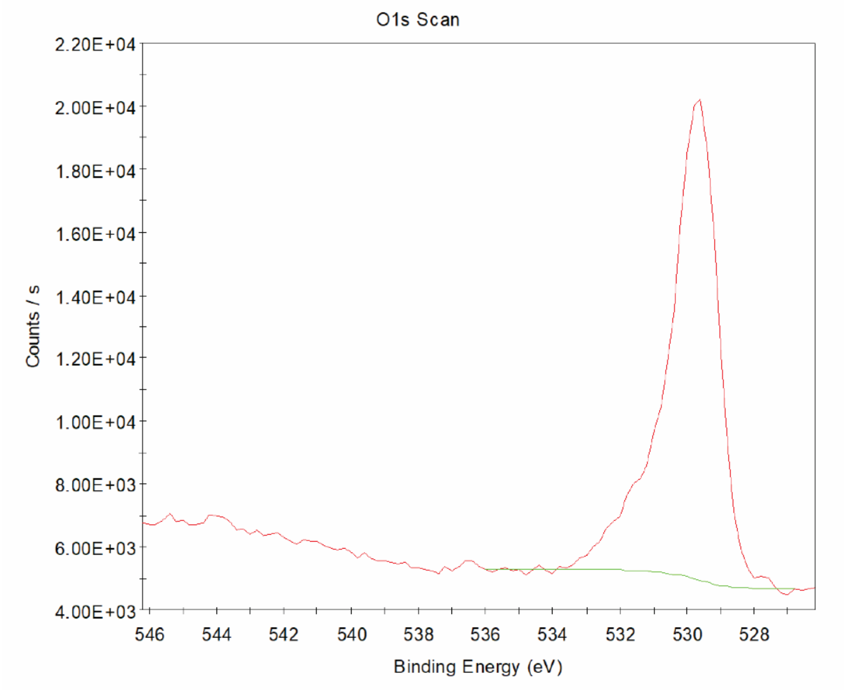

Figure 7.1.4. XPS spectrum of O1s region for Au@TiO$_2$ NPs.

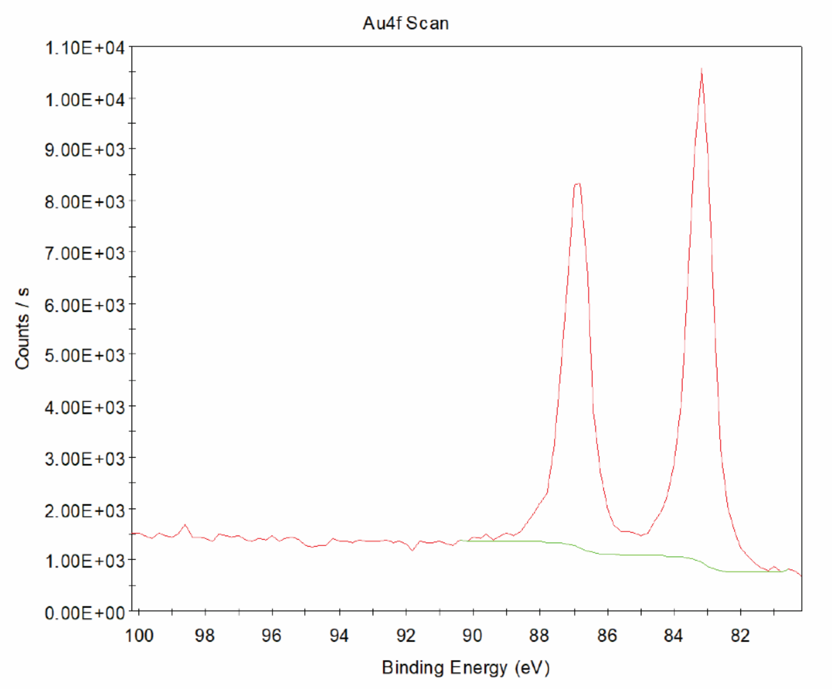

Figure 7.1.5. XPS spectrum of Au4f region for Au@TiO_2 NPs.

Calculation of Au wt %

The Ti:Au ratios were converted to Au wt % using the following equations:

$$Au{:}Ti = \frac{1}{Ti{:}Au}$$

$$Au\ wt\ \% = \left(\frac{wt\ Au}{wt\ Au + wt\ TiO_2}\right) \times 100\%$$

Note that for each (Au:Ti) g of Au there is 1 g of Ti.

$$Au\ wt\ \% = \left(\frac{Au{:}Ti\,\frac{g\ Au}{g\ Ti} \times 1\ g\ Ti}{Au{:}Ti\,\frac{g\ Au}{g\ Ti} \times 1\ g\ Ti + 1\ g\ Ti \times 1.679\,\frac{g\ TiO_2}{g\ Ti}}\right) \times 100\%$$

Both the upper and lower limits of Ti:Au were used for TEM calculations to provide a range of Au wt %.

Calculation of deviation of density from unlabeled TiO$_2$ NPs

TEM analysis

A possible range of particle densities was calculated using the upper and lower limits for elliptical volumes in the equation below:

$$\rho_{Au@TiO_2} = \frac{Average\ Mass\ Au\ in\ Au@TiO_2\ NP + \left(Average\ \bar{V}_{TiO_2} \times \rho_{TiO_2}\right)}{Average\ \bar{V}_{Au@TiO_2}}$$

$$\rho_{Au@TiO_{2,lower}} = \frac{7.\bar{9}7 \times 10^{-16} g\ Au + \left(3.\bar{1}9 \times 10^{6}\ nm^3 \times 1 \times 10^{-21} \frac{cm^3}{nm^3} \times 3.78 \frac{g}{cm^3}\right)}{3.\bar{2}3 \times 10^{6}\ nm^3 \times 1 \times 10^{-21} \frac{cm^3}{nm^3}}$$

$$= 3.\bar{9}8 \frac{g}{cm^3}$$

$$\rho_{Au@TiO_{2,upper}} = \frac{7.\bar{9}7 \times 10^{-16} g\ Au + \left(1.\bar{6}0 \times 10^{6}\ nm^3 \times 1 \times 10^{-21} \frac{cm^3}{nm^3} \times 3.78 \frac{g}{cm^3}\right)}{1.\bar{6}5 \times 10^{6}\ nm^3 \times 1 \times 10^{-21} \frac{cm^3}{nm^3}}$$

$$= 4.\bar{1}6 \frac{g}{cm^3}$$

The range of deviation in density compared to unlabeled anatase TiO$_2$ was found to be 5.3-10% using the equation below:

$$\%\ Deviation = \frac{\rho_{Au@TiO_2} - \rho_{TiO_2}}{\rho_{TiO_2}} \times 100\%$$

Size distribution histograms for AuNP cores

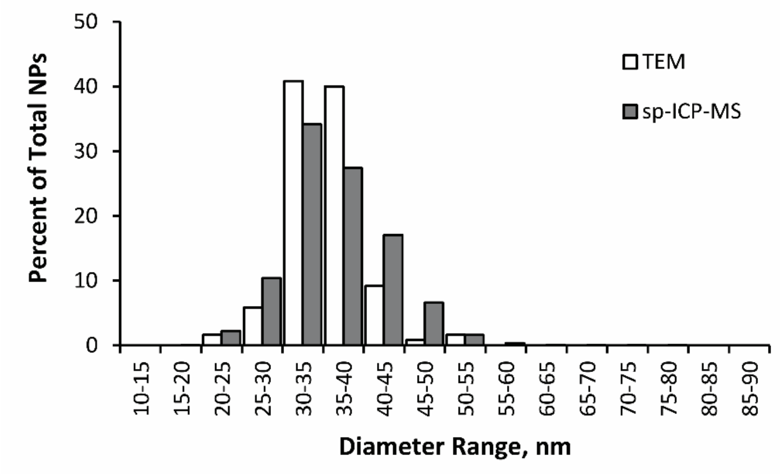

Figure 7.1.6. Comparison of AuNP core size as measured via TEM and sp-ICP-MS analyses. The sp-ICP-MS data represents samples of the AuNP cores measured prior to the coating procedure.

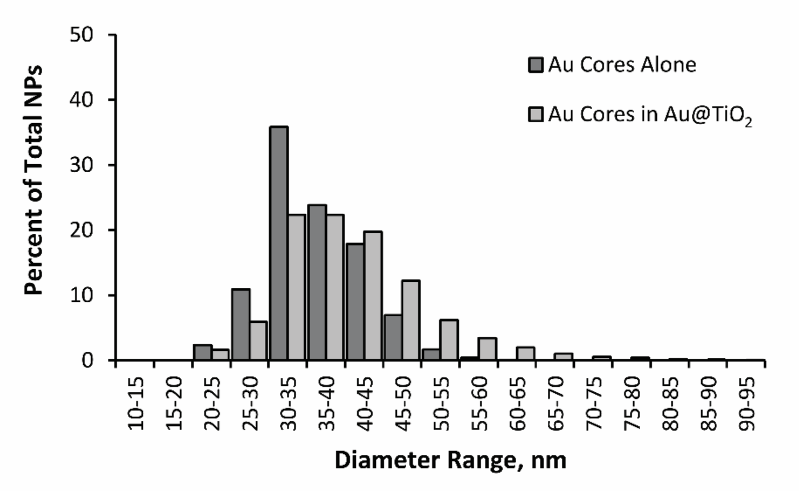

Figure 7.1.7. Comparison of AuNP core size determined via sp-ICP-MS analyses before and after coating with TiO_2.

Homoaggregation studies for Au@TiO_2 and TiO_2 NPs

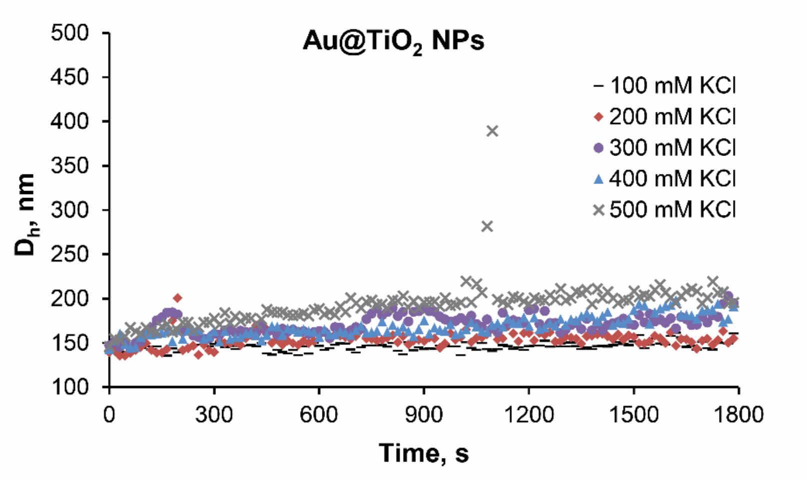

Figure 7.1.8. Hydrodynamic diameter measured over time for Au@TiO_2 NPs in KCl solutions varying from 100-500 mM.

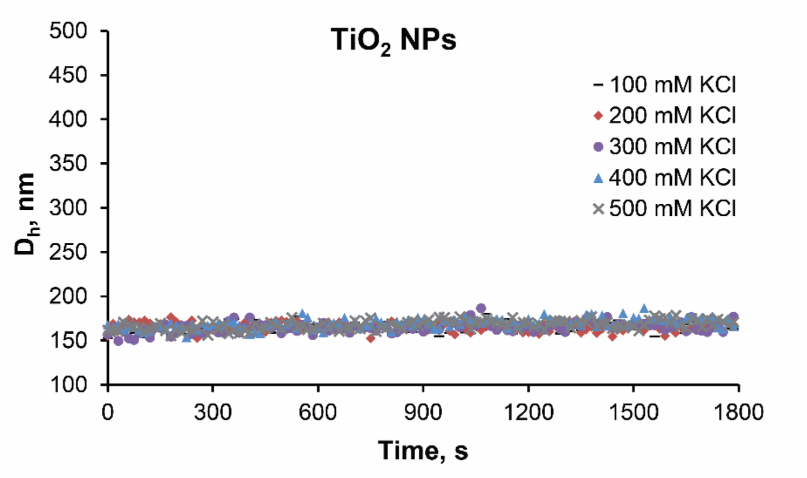

Figure 7.1.9. Hydrodynamic diameter measured over time for TiO_2 NPs in KCl solutions varying from 100-500 mM.

Calculation of primary TiO_2 crystallite size from XRD spectra

The anatase TiO_2 peaks at $2\theta \approx 25°$ were to calculate the average TiO_2 crystallite size using the Scherrer equation, which is included below.

$$Crystallite\ size = \frac{K \cdot \lambda}{\beta \cdot cos\theta},$$

where K is a dimensionless shape factor (assumed here to be 0.9), λ is the wavelength of the CuKα radiation source used (0.15405 nm), β is the full width of the peak at half maximum intensity (determined using EVA software), and θ is the Bragg angle of the peak.

The crystallite size was determined to be 5.8 nm for the unlabeled TiO_2 NPs and 6.0 nm for the Au@TiO_2 NPs.

River water characterization

Samples of Willamette River water were collected from the Taylor Drinking Water Treatment Plant in Corvallis, OR. The pH and turbidity of the water was measured at the facility. Total suspended solids were measured using Standard Method 2540 D. Conductivity was measured using a conductivity probe. The alkalinity was calculated using a gran function plot. The characteristics of the collected water samples are summarized in Table 7.1.6. The ionic strength was estimated by the measured conductivity using the following equation:

$I\,(M) = 1.6 \times 10^{-5} \times EC\ (\frac{\mu S}{cm})$, where I is the ionic strength and EC is the electrical conductivity[317].

The total natural organic matter content of the Willamette River was measured on a different batch of river water than the batch used for experiments and is provided in Table 7.1.6 as a recent measurement of the scale of the organic matter content in Willamette River water. The organic matter content for the Willamette River has been consistently measured by our within the range of 1-2 mg C/L in our lab[318].

Table 7.1.6. Characteristics of Willamette River water used in spike-and-recovery experiments.

pH	7.41
Turbidity	3.55 NTU
Total Suspended Solids	7.1 ± 2.6 mg/L
Conductivity	90.5 µS/cm
Alkalinity	25.5 ± 0.9 mg $CaCO_3$/L
Ionic Strength	1.4 mM
Natural Organic Matter	1.13 ± 0.05 mg C/L

Activated sludge characterization

Return activated sludge was collected from the Corvallis Wastewater Treatment Plant, stored in the refrigerator, and used within 24 hours. The sludge was analyzed for total dissolved solids and total suspended solids using Standard Methods 2540C and 2540D. Triplicate samples were analyzed and the average ± standard deviation is reported here. The total dissolved solids concentration was 371 ± 68 mg/L. The total suspended solids concentration was 8811 ± 233.3 mg/L.

Calculation of limits of detection and quantification

The limit of detection (LOD) and limit of quantification (LOQ) were determined for Ti in the river water-sunscreen mixture, and for both Au and Ti in the return activated sludge matrix. The LODs and LOQs for each matrix were estimated based on a conservative blank determination method using the equations below:

$$LOD = \bar{X}_{blank} + 3.3 \times S_{blank}$$

$$LOQ = \bar{X}_{blank} + 10 \times S_{blank} ,$$

where $\bar{X}_{blank}$ represents the mean concentration measured in triplicate samples of the matrix with no NPs added, and S_{blank} represents the standard deviation measured in triplicate samples of the matrix with no NPs added[319,320].

Spike-and-recovery in river water-sunscreen mixture

For the samples of river water mixed with sunscreen, no background Au was detected. The values of $\bar{X}_{blank}$ and S_{blank} for Ti were 285 µg/L and 33 µg/L, respectively. The LOD and LOQ are calculated below:

$$LOD = 285\ \frac{\mu g}{L} + 3.3 \times 33\ \frac{\mu g}{L} = 394\ \frac{\mu g}{L}$$

$$LOQ = 285\ \frac{\mu g}{L} + 10 \times 33\ \frac{\mu g}{L} = 615\ \frac{\mu g}{L}$$

Spike-and-recovery in return activated sludge

Return activated sludge samples contained both Au and Ti in the background. The values of $\bar{X}_{blank}$ and S_{blank} for Au and Ti are calculated below based on INAA and TSS analyses.

Mass of Au per mL of sludge = 28.7 ± 0.6 ng

Mass of Ti per mL of sludge = 370 ± 580 ng

TSS concentration of sludge = 5358 ± 577 mg/L

$$\bar{X}_{blank,Au} = \frac{(28.7\ ng\ Au)\left(\frac{1\ \mu g}{1000\ ng}\right)}{\left(5358\ \frac{mg}{L}\right)(0.001\ L)\left(\frac{1\ kg}{10^6\ mg}\right)} = 5356\ \frac{\mu g\ Au}{kg\ RAS}$$

$$S_{blank,Au} = 5356\frac{\mu g\ Au}{kg\ RAS}\sqrt{\left(\frac{577}{5358}\right)^2 + \left(\frac{0.6}{28.7}\right)^2} = 588\frac{\mu g\ Au}{kg\ RAS}$$

$$\bar{X}_{blank,Ti} = \frac{(370\ ng\ Ti)\left(\frac{1\ mg}{10^6\ ng}\right)}{\left(5358\ \frac{mg}{L}\right)(0.001\ L)\left(\frac{1\ kg}{10^6\ mg}\right)} = 69.1\ \frac{mg\ Ti}{kg\ RAS}$$

$$S_{blank,Ti} = 69.1\frac{mg\ Ti}{kg\ RAS}\sqrt{\left(\frac{577}{5358}\right)^2 + \left(\frac{580}{370}\right)^2} = 109\frac{mg\ Ti}{kg\ RAS}$$

The LODs and LOQs for both Au and Ti are calculated below:

$$LOD_{Au} = 5356\ \frac{\mu g}{kg} + 3.3 \times 588\ \frac{\mu g}{kg} = 72\bar{9}6\ \frac{\mu g}{kg} = 7.30\ \frac{mg\ Au}{kg\ sludge}$$

$$LOQ_{Au} = 5356\ \frac{\mu g}{kg} + 10 \times 588\ \frac{\mu g}{kg} = 11\bar{2}40\ \frac{\mu g}{kg} = 11.2\ \frac{mg\ Au}{kg\ sludge}$$

$$LOD_{Ti} = 69.1\ \frac{mg}{kg} + 3.3 \times 109\ \frac{\mu g}{kg} = 42\bar{8}.8\ \frac{mg}{kg} = 429\ \frac{mg\ Ti}{kg\ sludge}$$

$$LOQ_{Ti} = 69.1\ \frac{mg}{kg} + 10 \times 109\ \frac{\mu g}{kg} = 11\bar{5}9\ \frac{mg}{kg} = 1160\ \frac{mg\ Ti}{kg\ sludge}$$

UV-Vis standard curve for Au@TiO_2 NPs

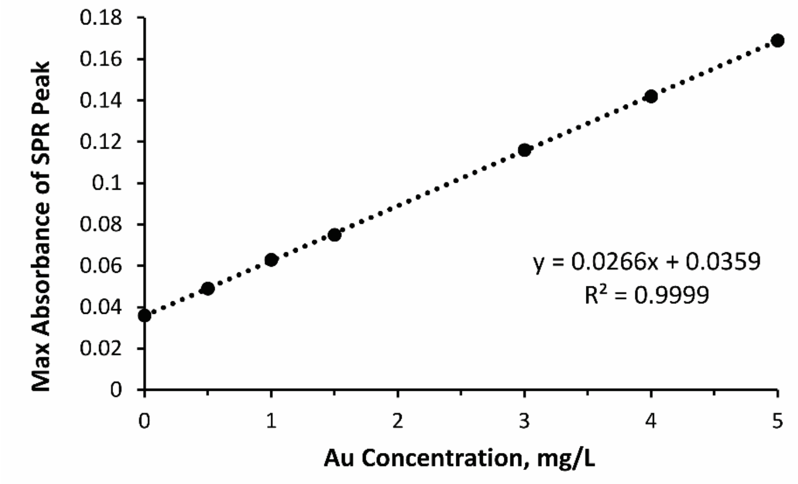

Figure 7.1.10. Standard curve for UV-Vis measurements of Au@TiO_2 NPs in DDI water ranging in concentration from 0.5-5 mg/L.

7.2 Appendix B: Supporting Information for Chapter 4

Solar Irradiance Spectra

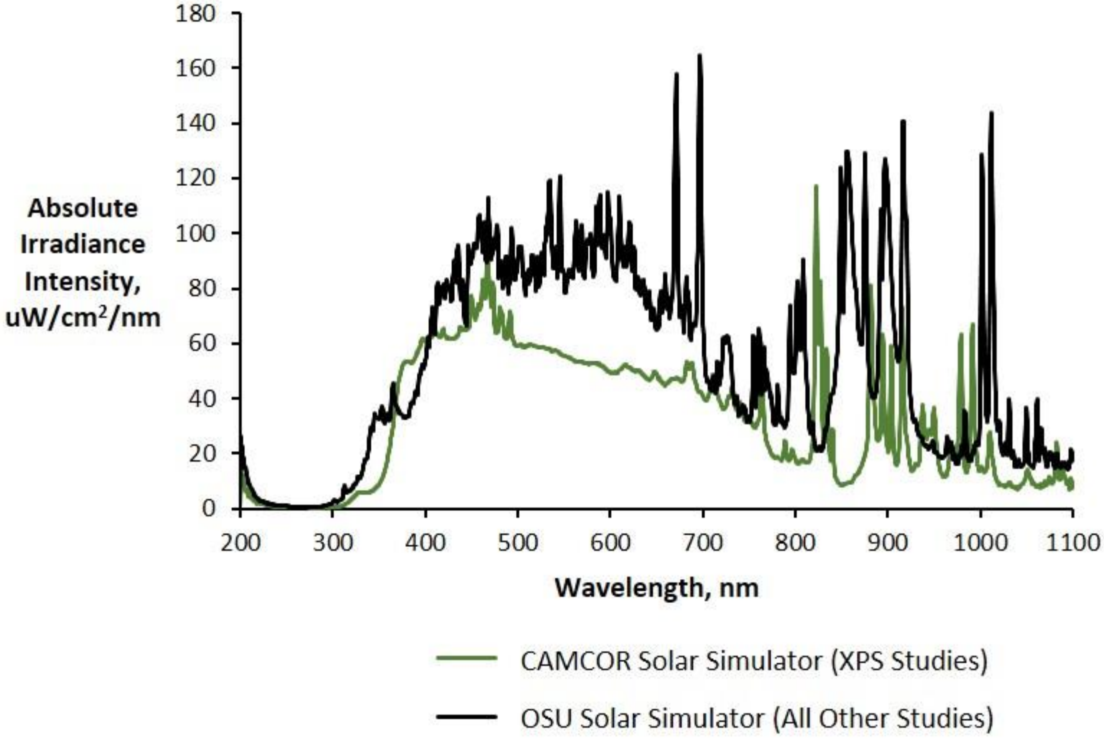

Figure 7.2.1. The solar irradiance spectra of the two solar simulators used in this work.

Surface Area Calculations from DLS Measurements

The surface area in m^2/g was calculated using the hydrodynamic diameter and the manufacturer reported densities (4.23 g/cm^3 for P25 NPs, 3.89 g/cm^3 for anatase NPs) using the equation below:

$$Surface\ Area = \left(\frac{1}{\rho}\frac{cm^3}{g}\right) \times \left(\frac{1 \times 10^{21}\ nm^3}{cm^3}\right) \times \frac{4\pi\left(\frac{D_h}{2}\right)^2\ nm^2}{\frac{4}{3}\pi\left(\frac{D_h}{2}\right)^3\ nm^3} \times \frac{1 \times 10^{-18} m^2}{nm^2}$$

Plots of Partitioning Coefficient vs. Surface Area

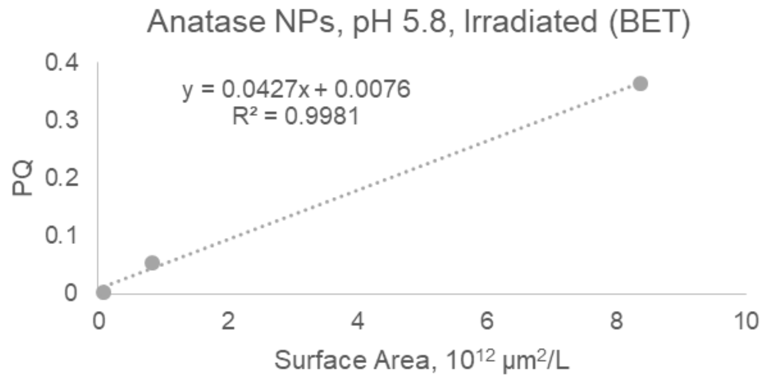

Figure 7.2.2. PQ vs. SA for Anatase NPs in pH 5.8 media after irradiation. SA was determined using BET.

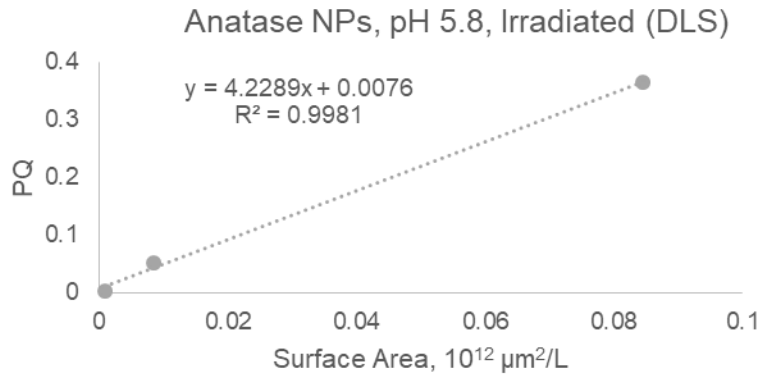

Figure 7.2.3. PQ vs. SA for Anatase NPs in pH 5.8 media after irradiation. SA was determined using DLS.

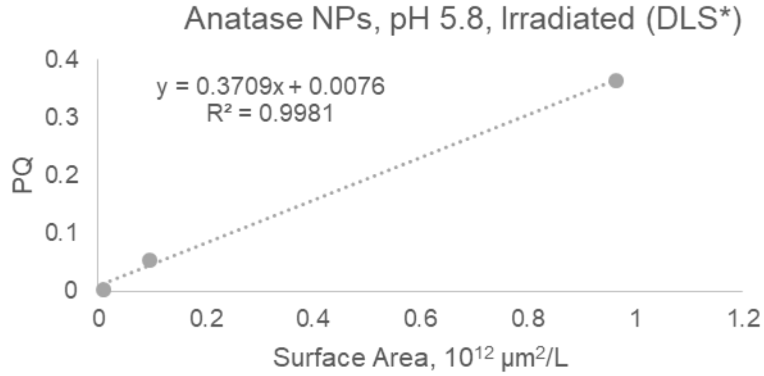

Figure 7.2.4. PQ vs. SA for Anatase NPs in pH 5.8 media after irradiation. SA was determined using DLS. The pre-irradiation D_h was used.

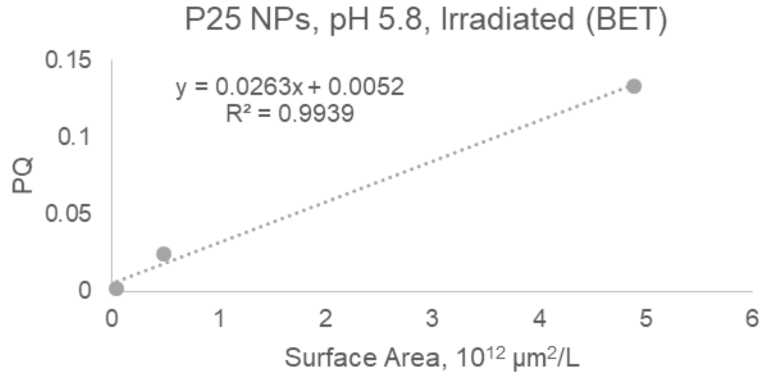

Figure 7.2.5. PQ vs. SA for P25 NPs in pH 5.8 media after irradiation. SA was determined using BET.

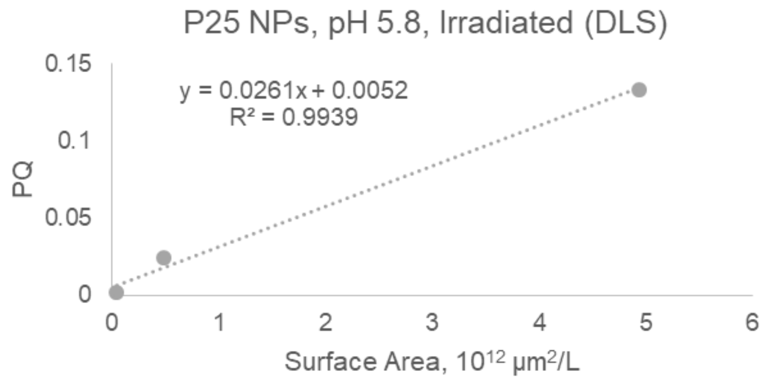

Figure 7.2.6. PQ vs. SA for P25 NPs in pH 5.8 media after irradiation. SA was determined using DLS.

XPS Survey Scans and Atomic Composition

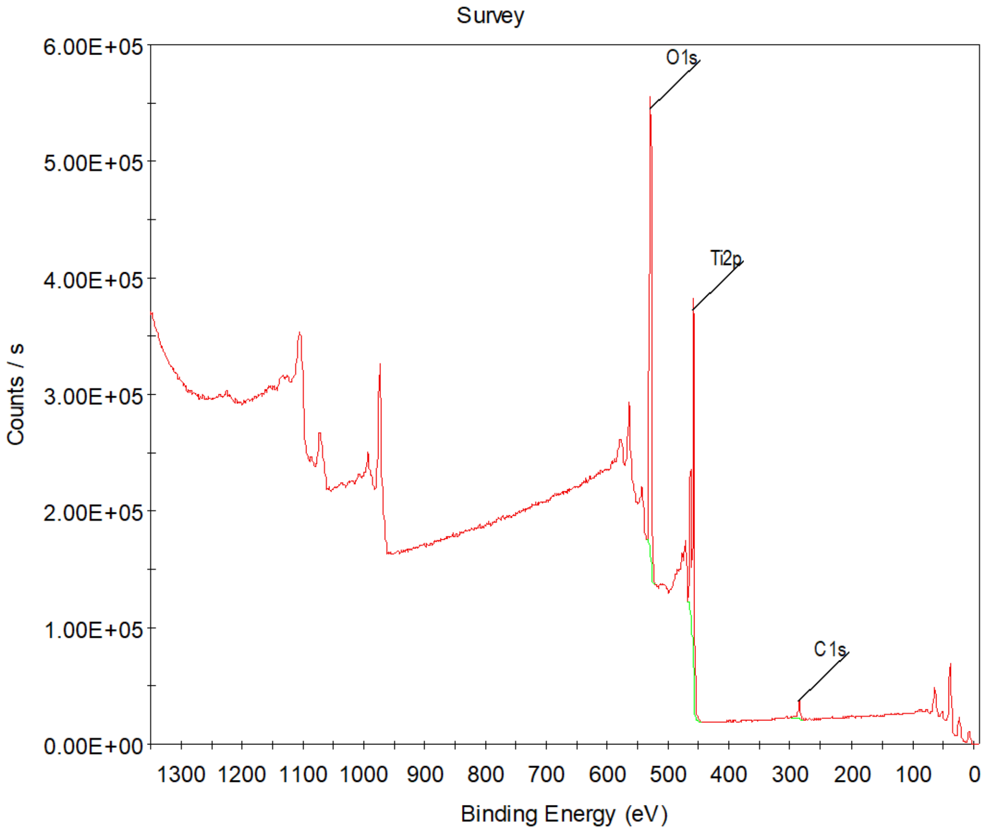

Figure 7.2.7. Survey spectra for P25 NPs in pH 5.8 water, prior to irradiation.

Table 7.2.1. Summary of XPS analysis of P25 NPs in pH 5.8 water, prior to irradiation.

Name	Peak BE	FWHM eV	Atomic %

C1s Scan A	284.77	1.46	4.98
C1s Scan B	286.21	1.46	1.72
C1s Scan C	287.67	1.46	0.06
C1s Scan D	288.67	1.46	1.18
O1s Scan A	529.42	1.06	57.6
O1s Scan B	530.63	1.88	3.7
Ti2p	458.35	0.99	30.76

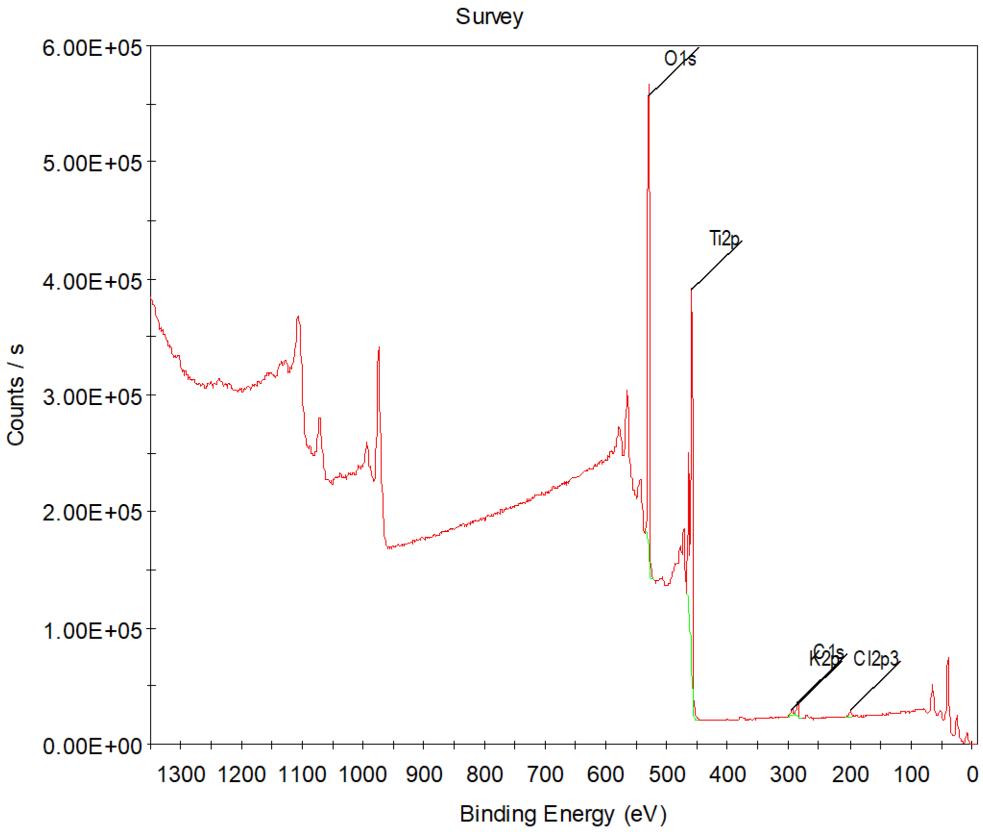

Figure 7.2.8. Survey spectra for P25 NPs in pH 5.8 water, after 1 h irradiation with simulated solar light.

Table 7.2.2. Summary of XPS analysis of P25 NPs in pH 5.8 water, after 1 h irradiation with simulated solar light.

Name	Peak BE	FWHM eV	Atomic %

C1s Scan A	284.82	1.51	4.41
C1s Scan B	286.32	1.51	1.06
C1s Scan C	287.72	1.52	0
C1s Scan D	288.78	1.51	0.9
O1s Scan A	529.57	1.05	59.18
O1s Scan B	530.52	1.28	3
Ti2p	458.5	0.98	31.46

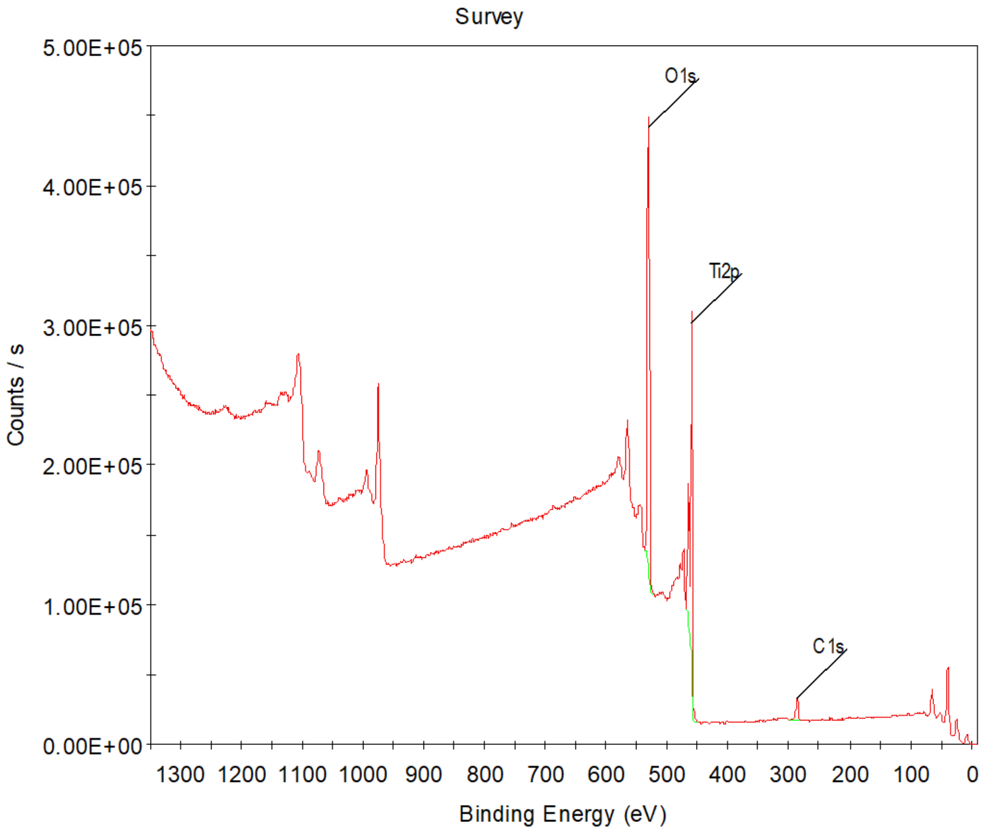

Figure 7.2.9. Survey spectra for Anatase NPs in pH 5.8 water, prior to irradiation.

Table 7.2.3. Summary of XPS analysis of Anatase NPs in pH 5.8 water, prior to irradiation.

Name	Peak BE	FWHM eV	Atomic %

C1s Scan A	284.77	1.42	5.81
C1s Scan B	286.17	1.42	1.8
C1s Scan C	287.67	1.42	0.1
C1s Scan D	288.73	1.42	1.24
O1s Scan A	529.66	1.07	56.11
O1s Scan B	531.02	1.96	4.87
Ti2p	458.56	0.99	30.07

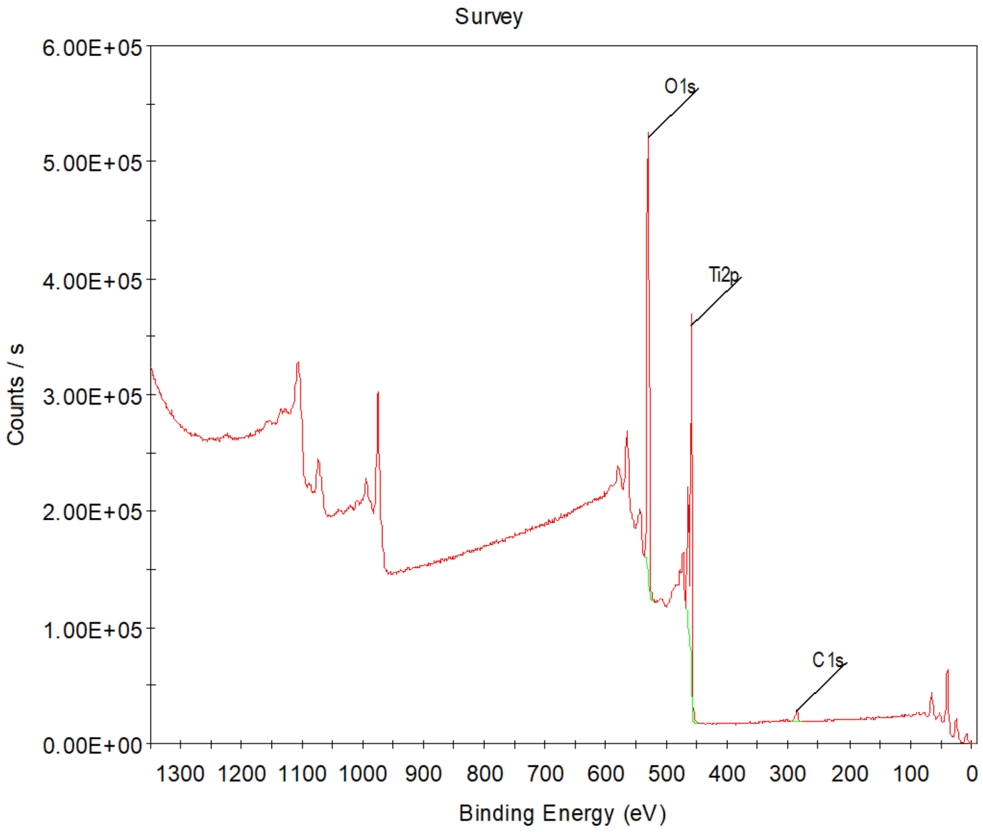

Figure 7.2.10. Survey spectra for Anatase NPs in pH 5.8 water, after 1 h irradiation with simulated solar light.

Table 7.2.4. Summary of XPS analysis of Anatase NPs in pH 5.8 water, after 1 h irradiation with simulated solar light.

Name	Peak BE	FWHM eV	Atomic %

C1s Scan A	284.73	1.54	3.34
C1s Scan B	286.25	1.54	1.06
C1s Scan C	287.63	1.56	0
C1s Scan D	288.74	1.54	0.96
O1s Scan A	529.8	1.05	57.94
O1s Scan B	530.67	1.52	5.12
Ti2p	458.64	0.99	31.58

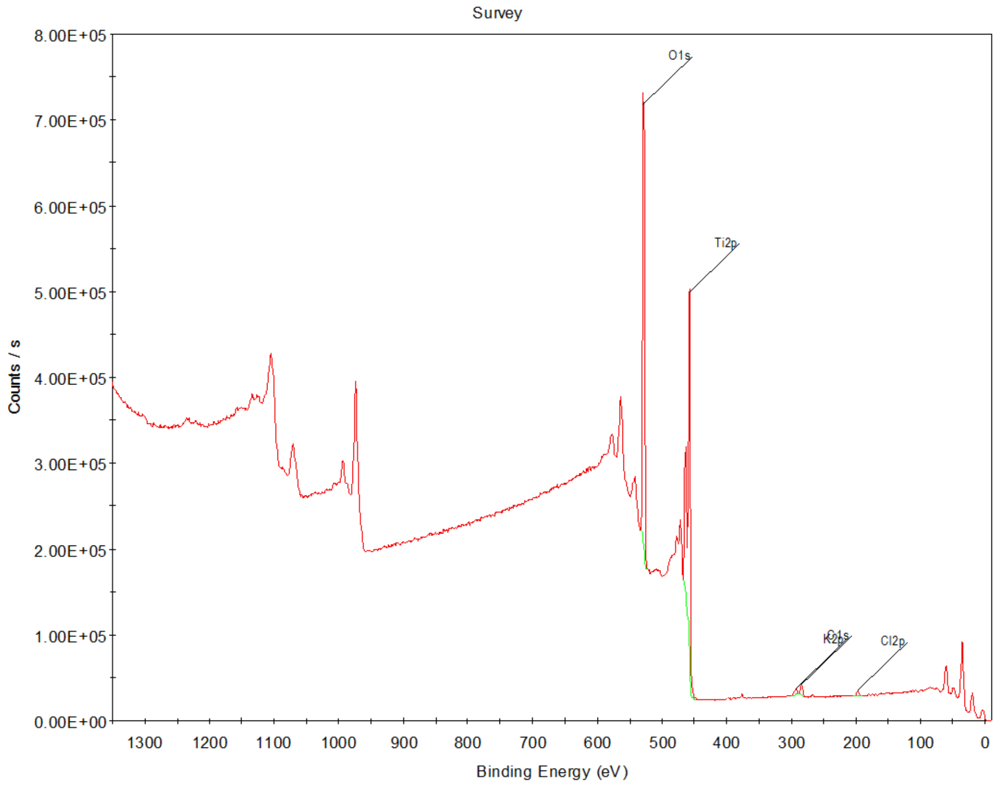

Figure 7.2.11. Survey spectra for P25 NPs in pH 7.4 water, prior to irradiation.

Table 7.2.5. Summary of XPS analysis of P25 NPs in pH 7.4 water, prior to irradiation.

Name	Peak BE	FWHM eV	Atomic %
C1s Scan A	284.81	1.49	3.9

C1s Scan B	286.11	1.49	0.95
C1s Scan C	287.61	1.49	0
C1s Scan D	288.8	1.49	1.33
Cl2p	197.94	1.14	1.14
K2p	293.01	1.53	1.32
O1s Scan A	529.96	1.1	58.54
O1s Scan B	531.27	1.88	5.7
Ti2p	458.67	0.97	27.11

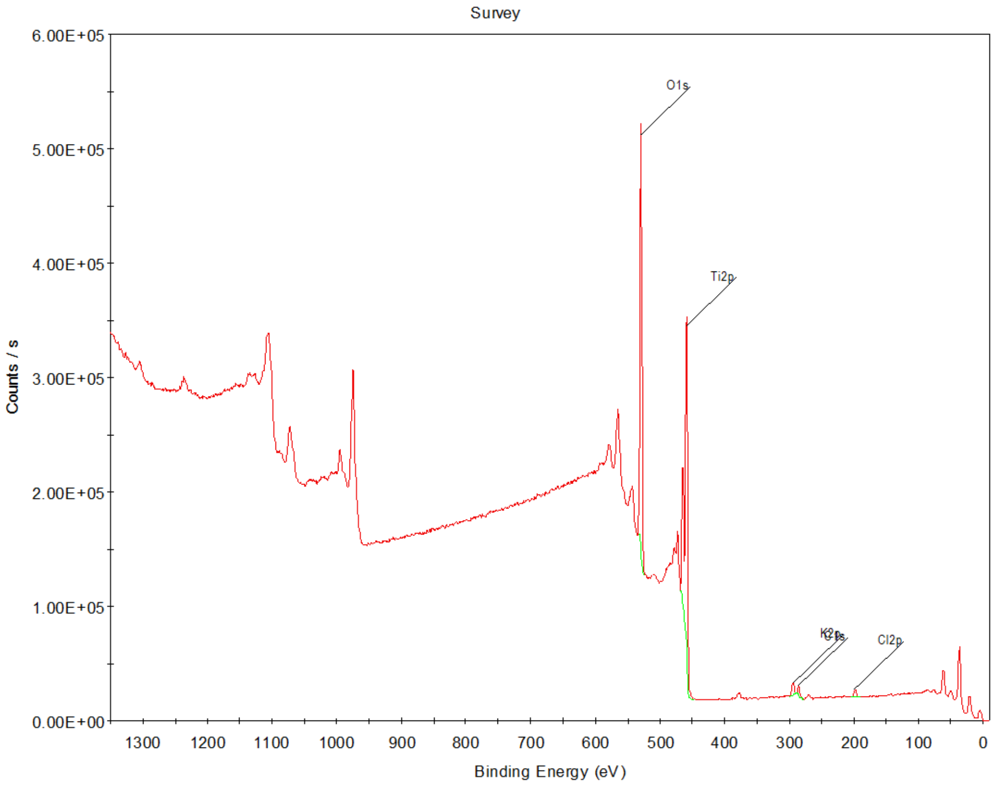

Figure 7.2.12. Survey spectra for P25 NPs in pH 7.4 water, after 1 h irradiation with simulated solar light.

Table 7.2.6. Summary of XPS analysis of P25 NPs in pH 7.4 water, after 1 h irradiation with simulated solar light.

Name	Peak BE	FWHM eV	Atomic %

C1s Scan A	284.77	1.42	3.97
C1s Scan B	286.22	1.42	1.02
C1s Scan C	287.97	1.42	0.33
C1s Scan D	288.84	1.42	0.84
Cl2p	197.94	1.39	2.04
K2p	292.95	1.32	1.73
O1s Scan A	529.74	1.05	54.07
O1s Scan B	530.37	2.22	9.62

Ti2p	458.49	0.95	26.38

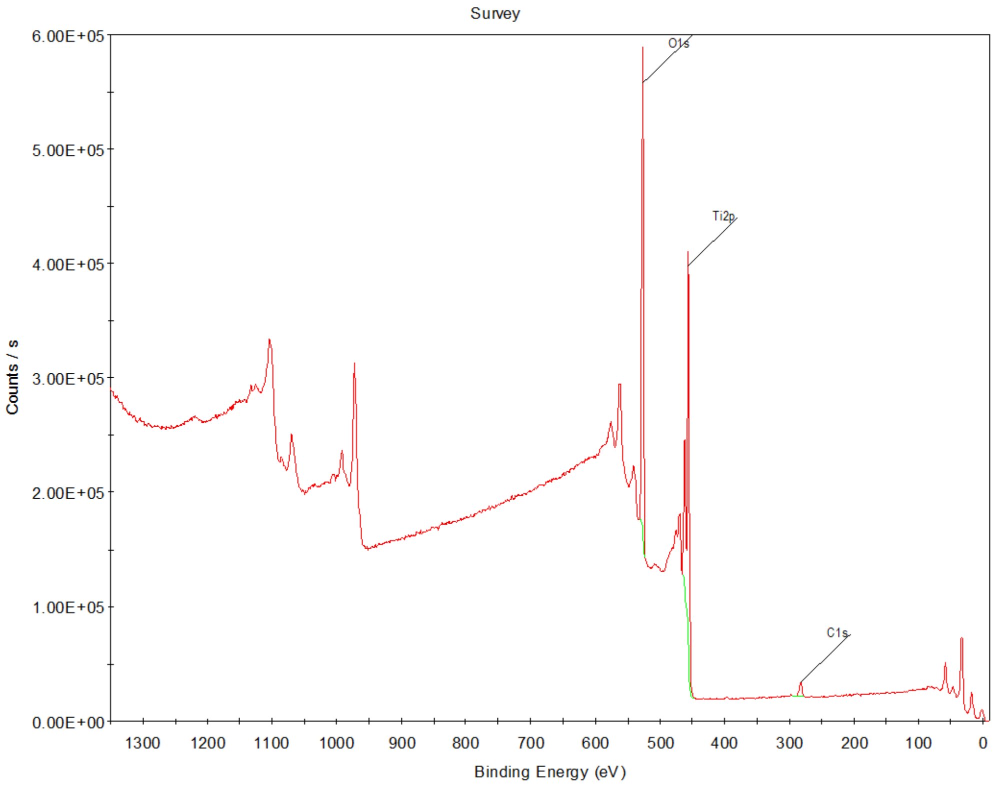

Figure 7.2.13. Survey spectra for anatase NPs in pH 7.4 water, prior to irradiation.

Table 7.2.7. Summary of XPS analysis of anatase NPs in pH 7.4 water, prior to irradiation.

Name	Peak BE	FWHM eV	Atomic %
C1s Scan A	284.76	1.47	4.31
C1s Scan B	286.24	1.47	1.15
C1s Scan C	287.56	1.47	0
C1s Scan D	288.79	1.47	1.27
O1s Scan A	530.66	1.1	57.25
O1s Scan B	531.86	2.3	8
Ti2p	459.17	0.99	28.01

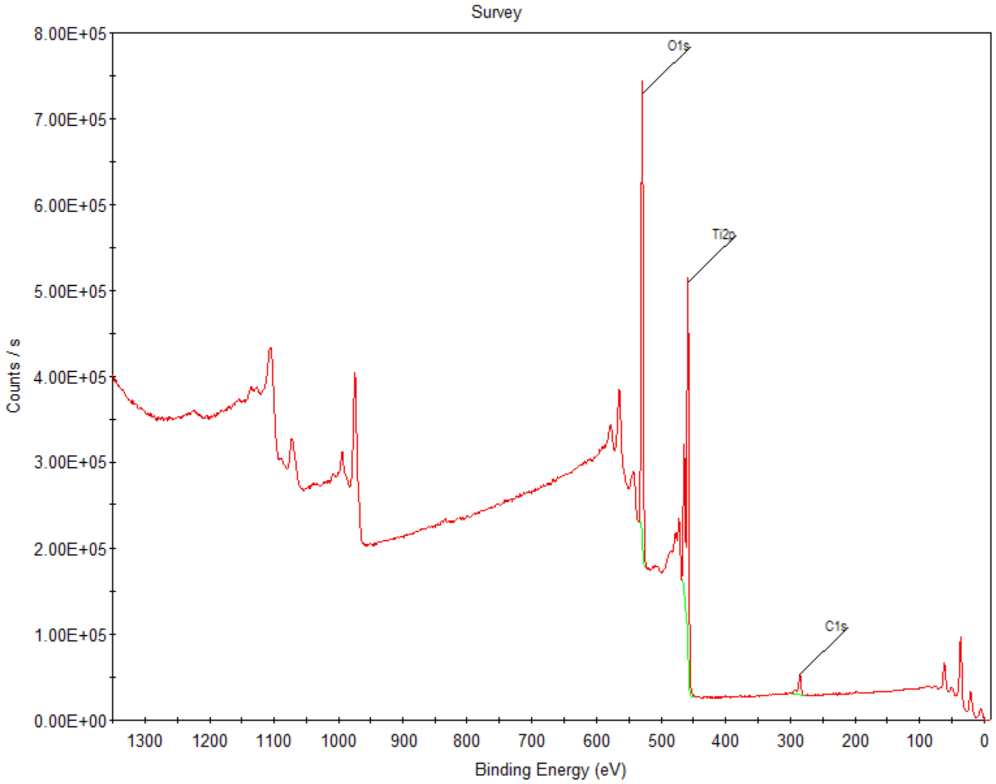

Figure 7.2.14. Survey spectra for anatase NPs in pH 7.4 water, after 1 h irradiation with simulated solar light.

Table 7.2.8. Summary of XPS analysis of anatase NPs in pH 7.4 water, after 1 h irradiation with simulated solar light.

Name	Peak BE	FWHM eV	Atomic %
C1s Scan A	284.8	1.45	6
C1s Scan B	286.26	1.45	1.66
C1s Scan C	288	1.45	0
C1s Scan D	288.67	1.45	1.44
O1s Scan A	529.89	1.09	54.88
O1s Scan B	531.04	2.28	9.39
Ti2p	458.62	0.97	26.63

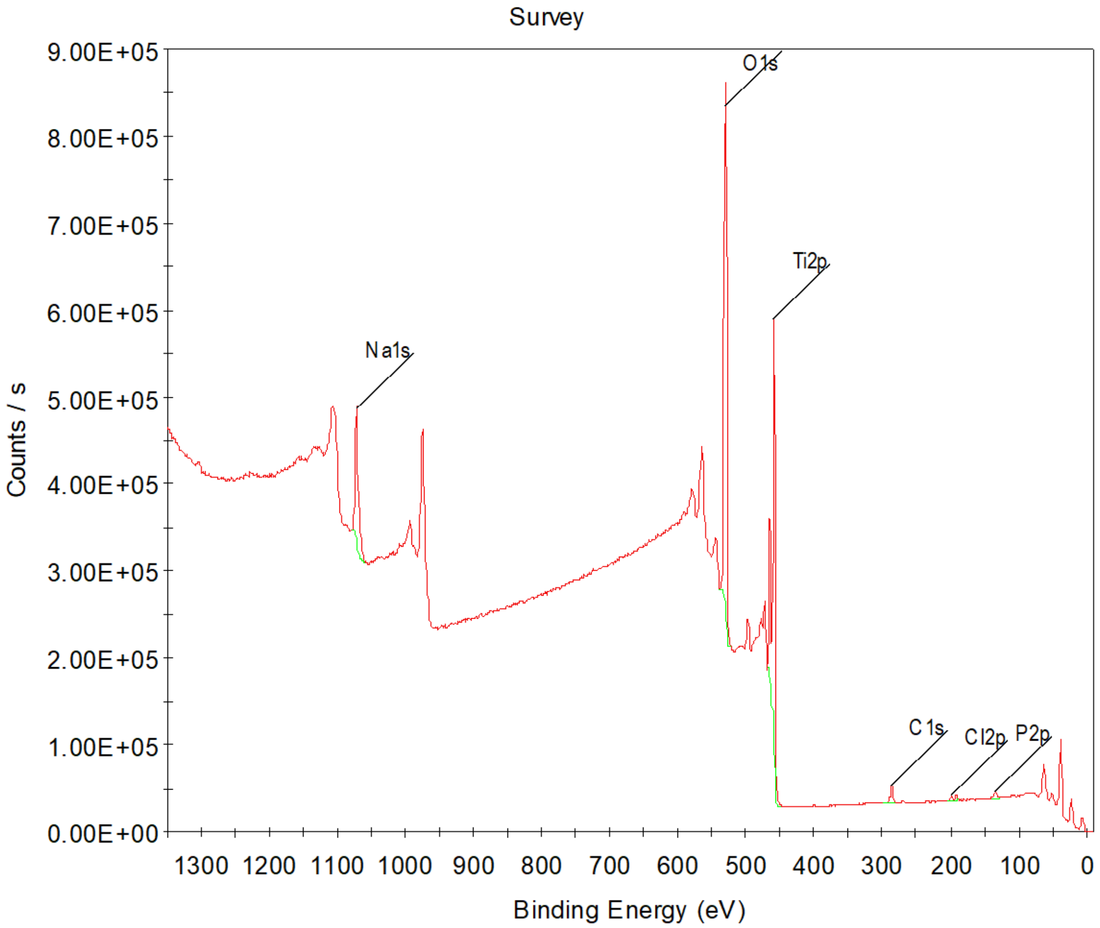

Figure 7.2.15. Survey spectra for P25 NPs in 1X PBS media, prior to irradiation. Samples were centrifuged washed in DDI water twice prior to XPS sample preparation.

Table 7.2.9. Summary of XPS analysis of P25 NPs in 1X PBS media, prior to irradiation. Samples were centrifuged washed in DDI water twice prior to XPS sample preparation.

Name	Peak BE	FWHM eV	Atomic %
C1s Scan A	284.79	1.41	3.75
C1s Scan B	286.32	1.41	0.96
C1s Scan C	287.99	1.41	0.28
C1s Scan D	288.78	1.41	0.79
Cl2p	198.01	1.14	0.97
Na1s	1071.48	1.67	7.29

O1s Scan A	529.7	1.06	50
O1s Scan B	530.8	1.72	9.85
P2p	133.31	1.99	2.28
Ti2p	458.51	0.95	23.84

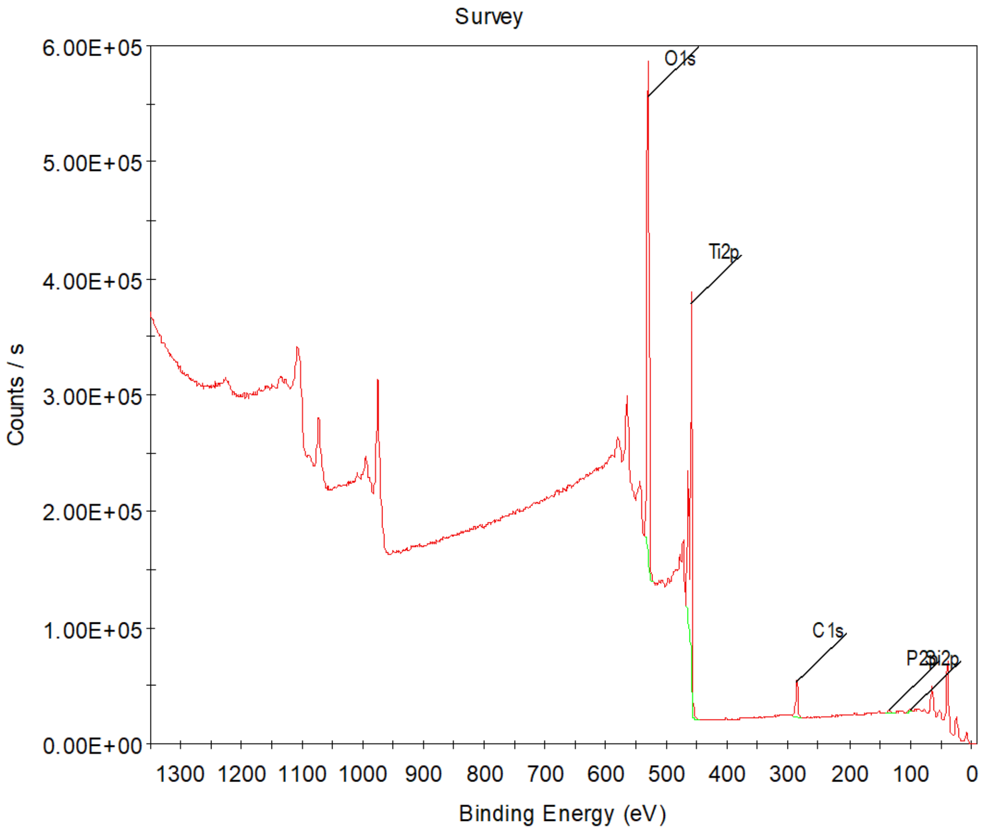

Figure 7.2.16. Survey spectra for P25 NPs in 1X PBS media, after 1 h irradiation with simulated solar light. Samples were centrifuged washed in DDI water twice prior to XPS sample preparation.

Table 7.2.10. Summary of XPS analysis of P25 NPs in 1X PBS media, after 1 h irradiation with simulated solar light. Samples were centrifuged washed in DDI water twice prior to XPS sample preparation. Note that SiO_2 from the wafer substrate was present in this sample.

Name	Peak BE	FWHM eV	Atomic %
C1s Scan A	284.81	1.4	9
C1s Scan B	286.31	1.4	1.9
C1s Scan C	287.61	1.4	0.16
C1s Scan D	288.61	1.4	1.46
Cl2p	199.32	0.07	0
Na1s	1071.55	1.92	3.33
O1s Scan A	529.87	1.08	46.92

O1s Scan B	531.05	2.48	11.02
P2p	133.11	1.55	1.92
Si2p	98.51	0.41	1.54
Ti2p	458.64	0.96	22.74

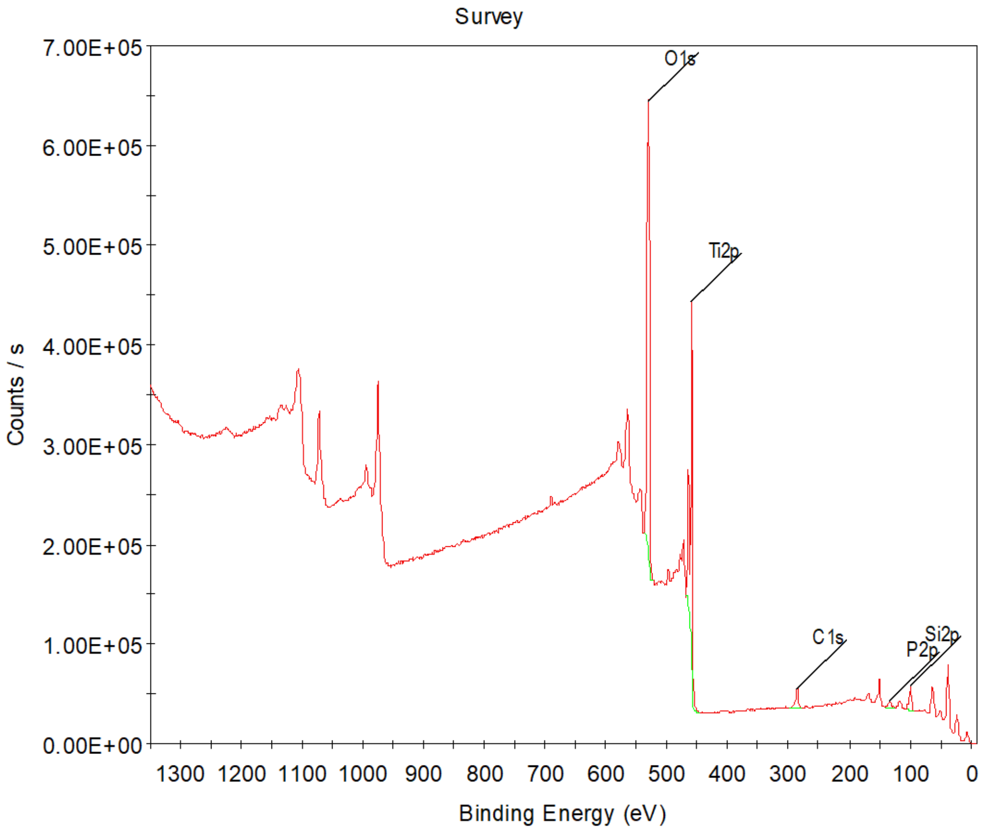

Figure 7.2.17. Survey spectra for anatase NPs in 1X PBS media, prior to irradiation. Samples were centrifuged washed in DDI water twice prior to XPS sample preparation.

Table 7.2.11. Summary of XPS analysis of anatase NPs in 1X PBS media, prior to irradiation. Samples were centrifuged washed in DDI water twice prior to XPS sample preparation. Note that SiO_2 from the wafer substrate was present in this sample.

Name	Peak BE	FWHM eV	Atomic %
C1s Scan A	284.77	1.35	4.18
C1s Scan B	286.26	1.35	1.29
C1s Scan C	287.97	1.35	0.19
C1s Scan D	288.67	1.35	0.81
Cl2p	197.8	0.17	0
Na1s	1071.68	1.85	5.18
O1s Scan A	529.84	1.07	45.81

O1s Scan B	531.27	2.47	13.45
P2p	133.39	1.95	2.08
Si2p	98.33	1.09	4.51
Ti2p	458.62	0.96	22.51

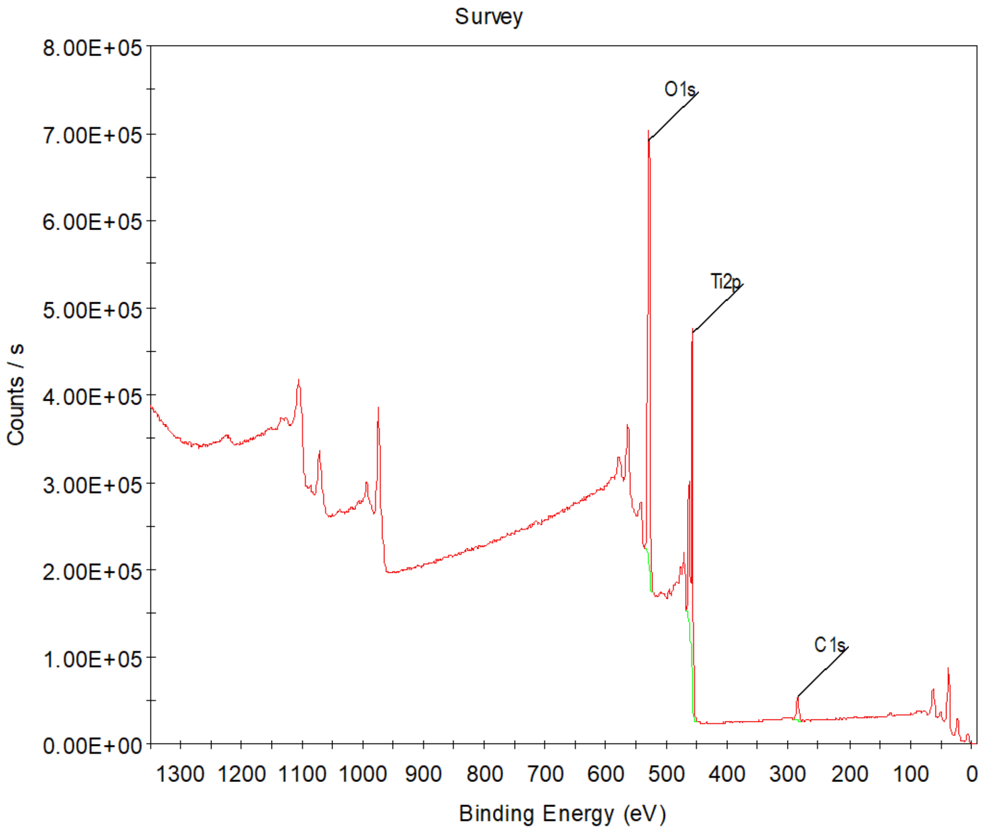

Figure 7.2.18. Survey spectra for anatase NPs in 1X PBS media, after 1 h irradiation with simulated solar light. Samples were centrifuged washed in DDI water twice prior to XPS sample preparation.

Table 7.2.12. Summary of XPS analysis of anatase NPs in 1X PBS media, after 1 h irradiation with simulated solar light. Samples were centrifuged washed in DDI water twice prior to XPS sample preparation.

Name	Peak BE	FWHM eV	Atomic %
C1s Scan A	284.74	1.39	7.15
C1s Scan B	286.25	1.39	1.76
C1s Scan C	287.94	1.39	0.22
C1s Scan D	288.54	1.39	1.3
Na1s	1071.74	2.87	3.63
O1s Scan A	529.88	1.07	48.7
O1s Scan B	530.97	2.19	11.43

P2p	133.32	1.35	1.58
Ti2p	458.63	0.96	24.23

XPS High Resolution Scans

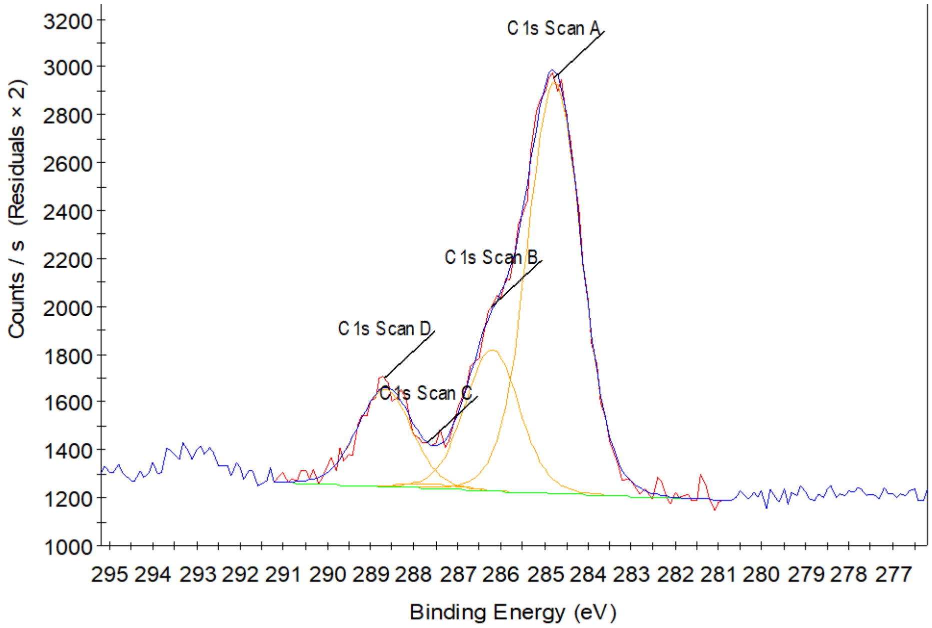

Figure 7.2.19. C1s scan for P25 NPs in pH 5.8 water, prior to irradiation.

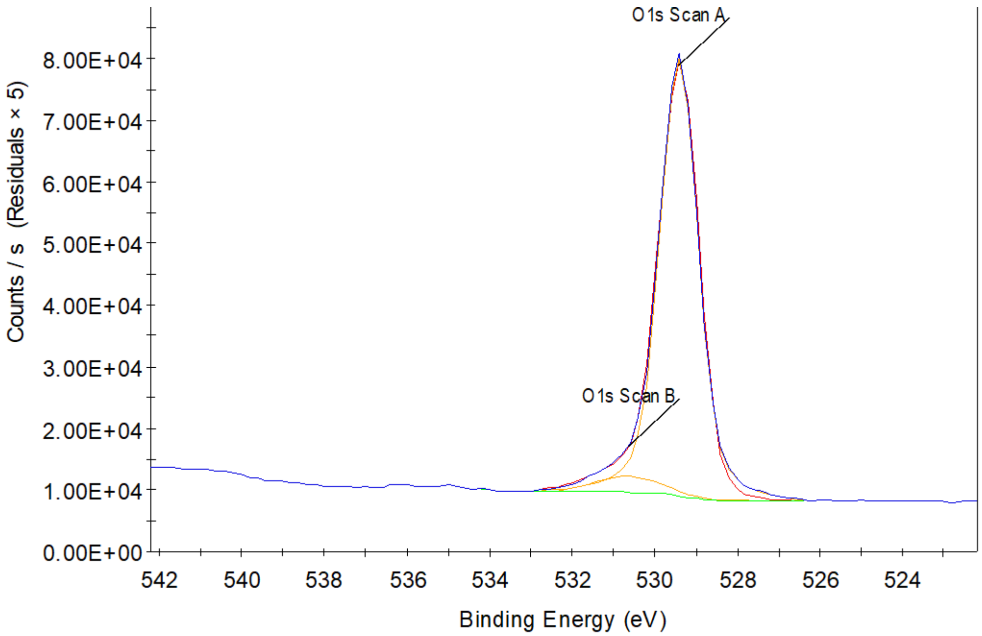

Figure 7.2.20. O1s scan for P25 NPs in pH 5.8 water, prior to irradiation.

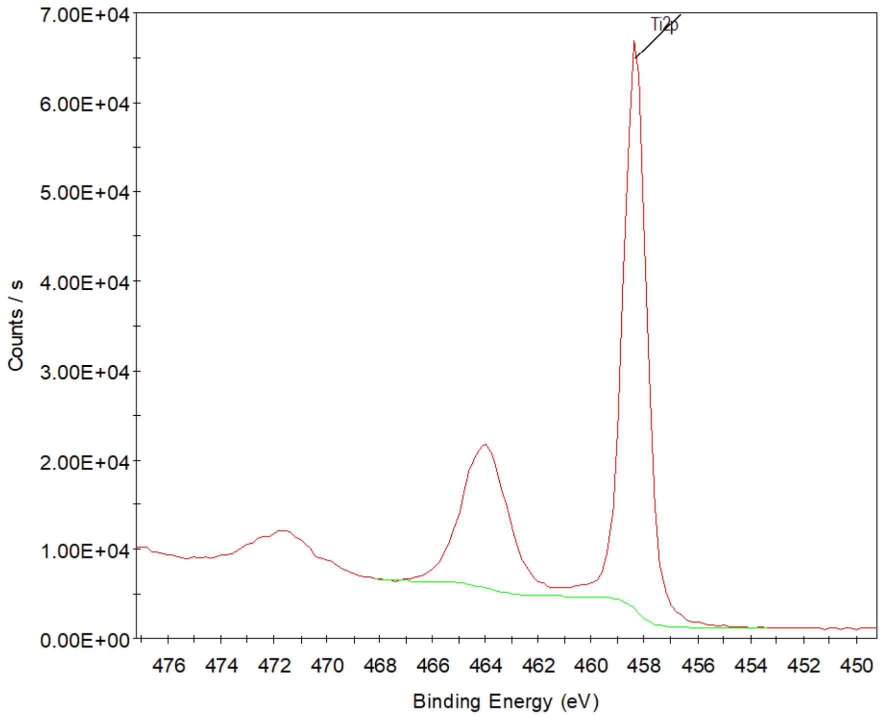

Figure 7.2.21. Ti2p scan for P25 NPs in pH 5.8 water, prior to irradiation.

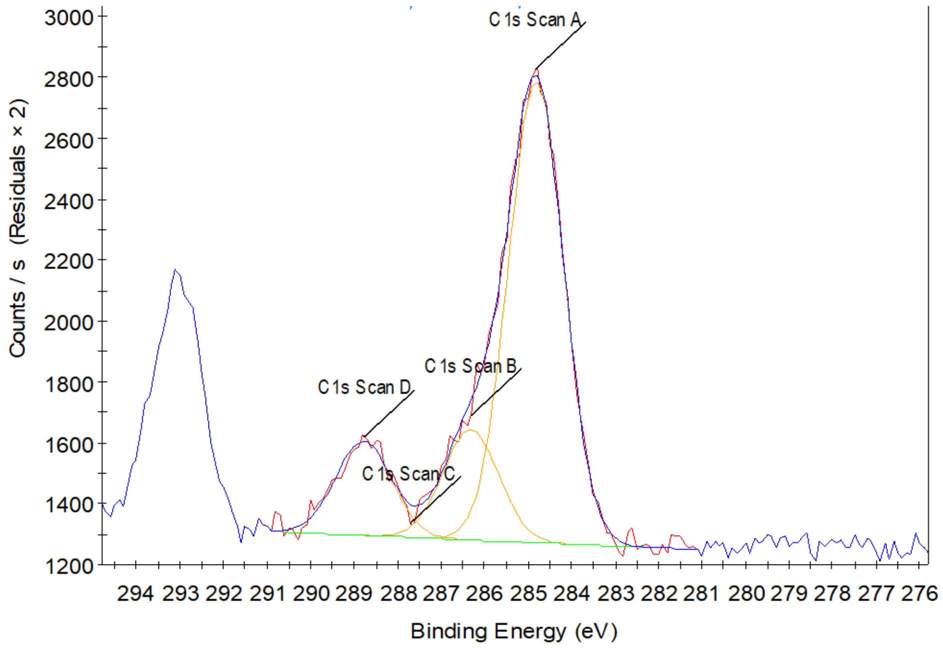

Figure 7.2.22. C1s scan for P25 NPs in pH 5.8 water, after 1 h of irradiation with simulated solar light.

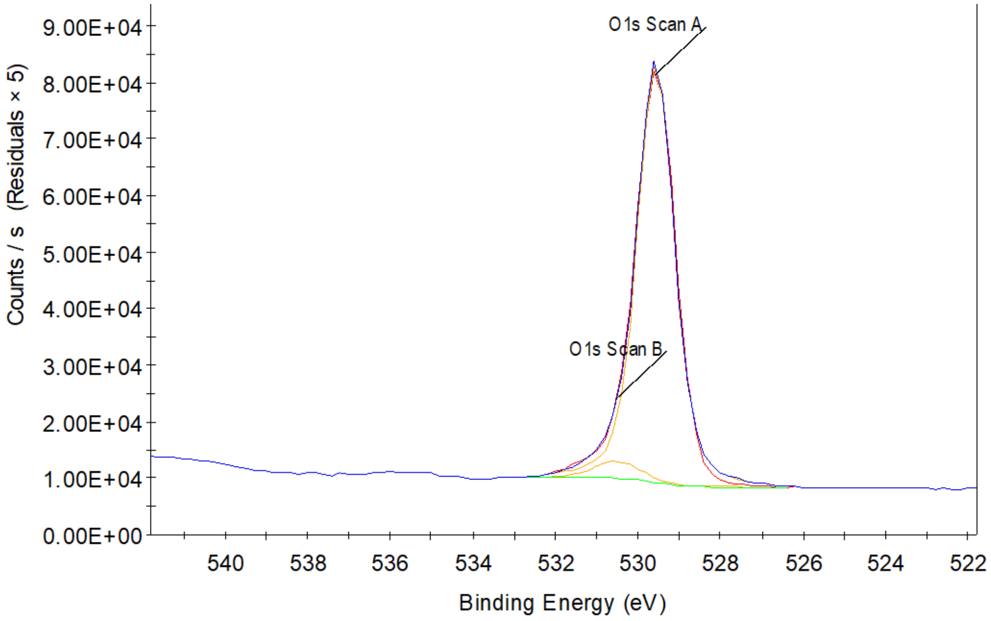

Figure 7.2.23. O1s scan for P25 NPs in pH 5.8 water, after 1 h of irradiation with simulated solar light.

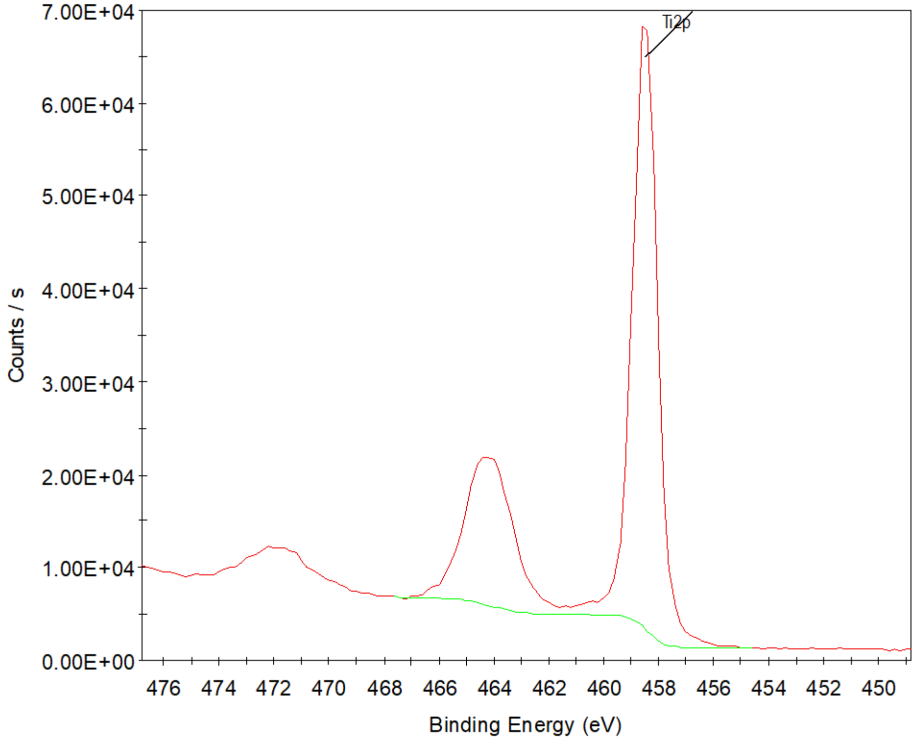

Figure 7.2.24. Ti2p scan for P25 NPs in pH 5.8 water, after 1 h of irradiation with simulated solar light.

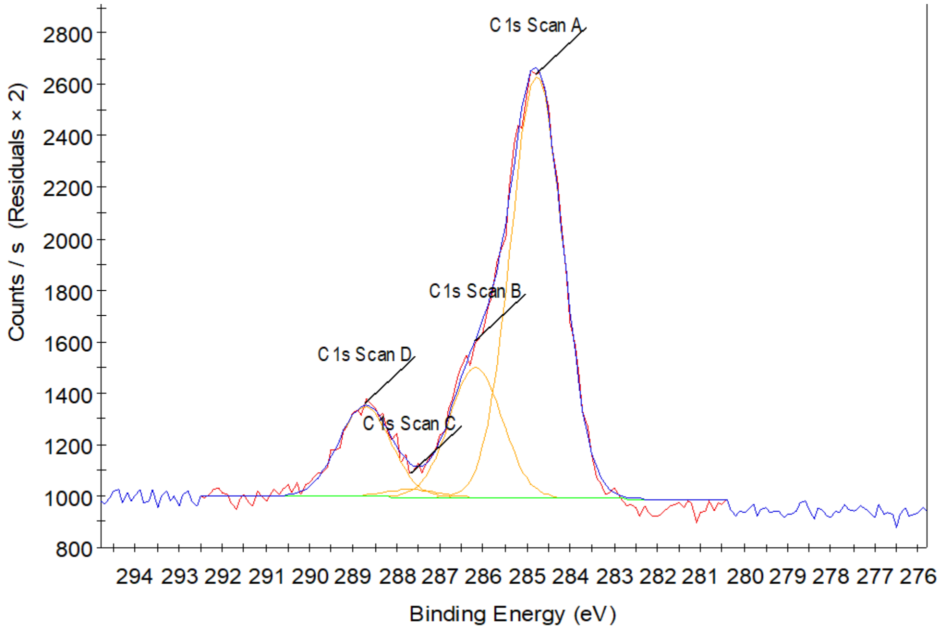

Figure 7.2.25. C1s scan for anatase NPs in pH 5.8 water, prior to irradiation.

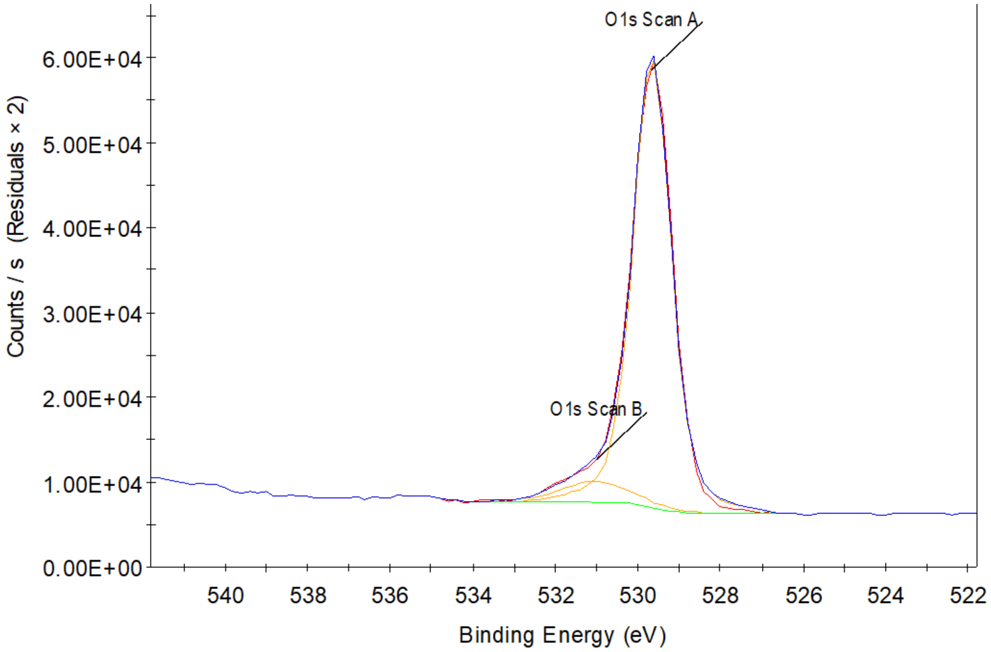

Figure 7.2.26. O1s scan for anatase NPs in pH 5.8 water, prior to irradiation.

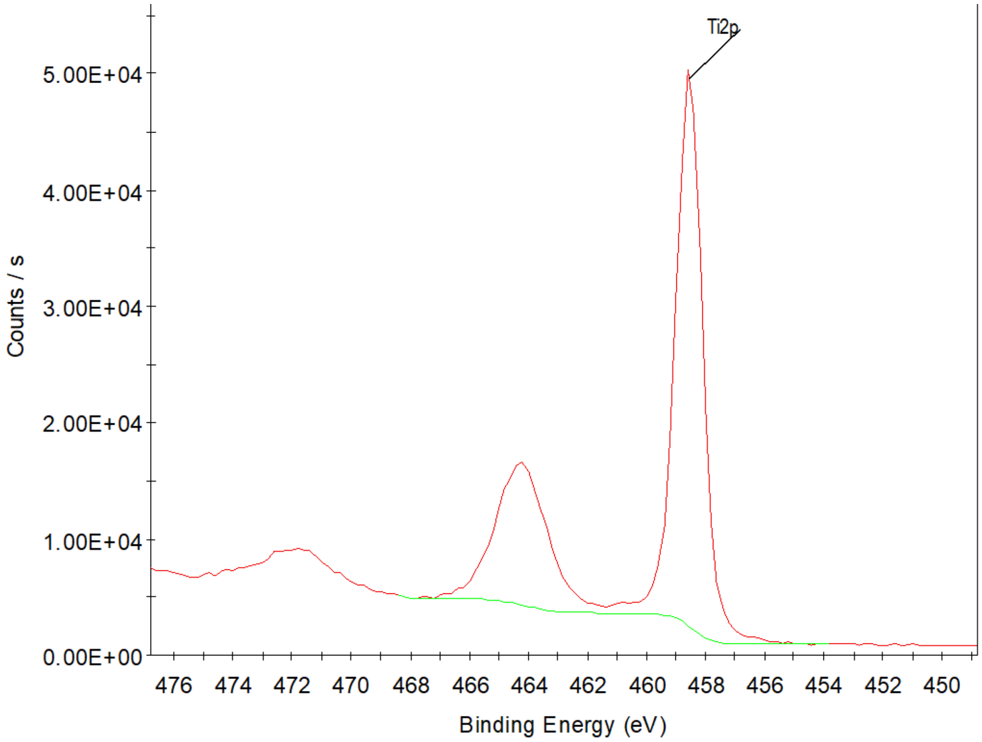

Figure 7.2.27. Ti2p scan for anatase NPs in pH 5.8 water, prior to irradiation.

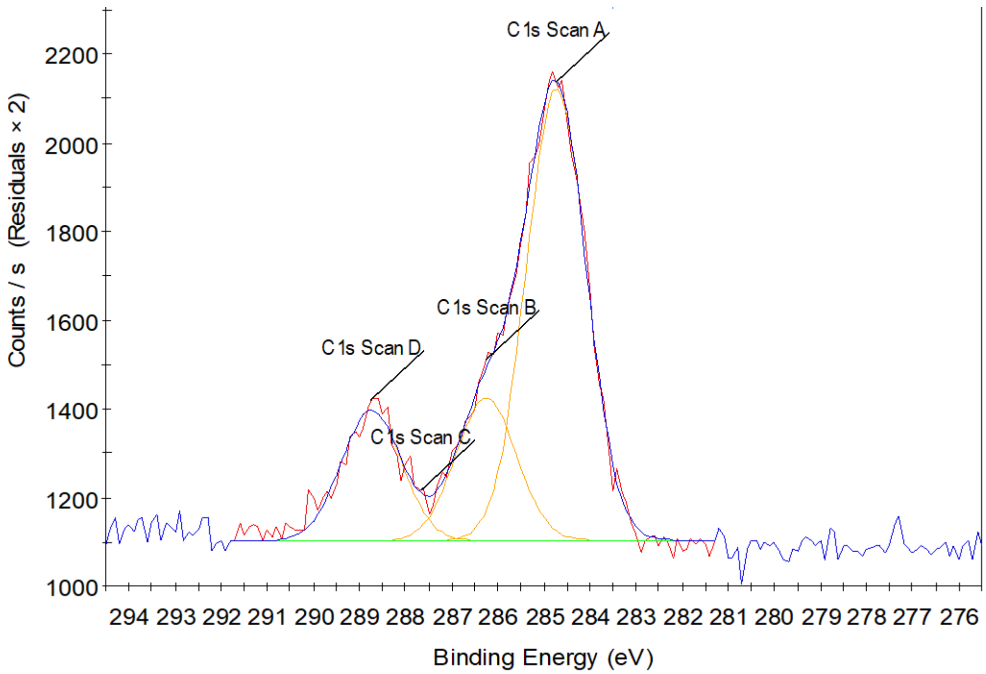

Figure 7.2.28. C1s scan for anatase NPs in pH 5.8 water, after 1 h of irradiation with simulated solar light.

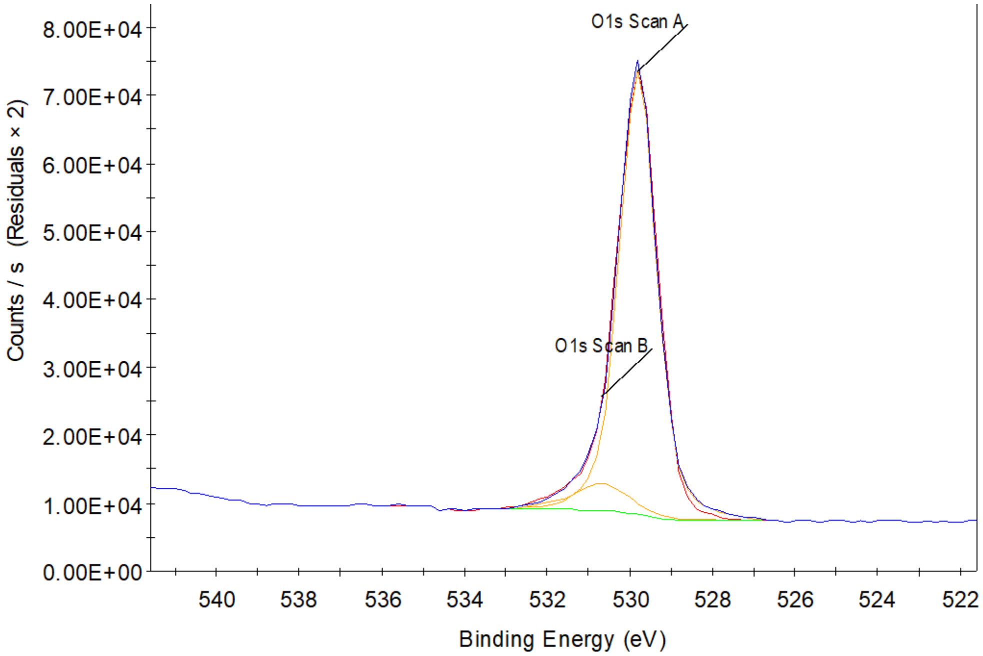

Figure 7.2.29. O1s scan for anatase NPs in pH 5.8 water, after 1 h of irradiation with simulated solar light.

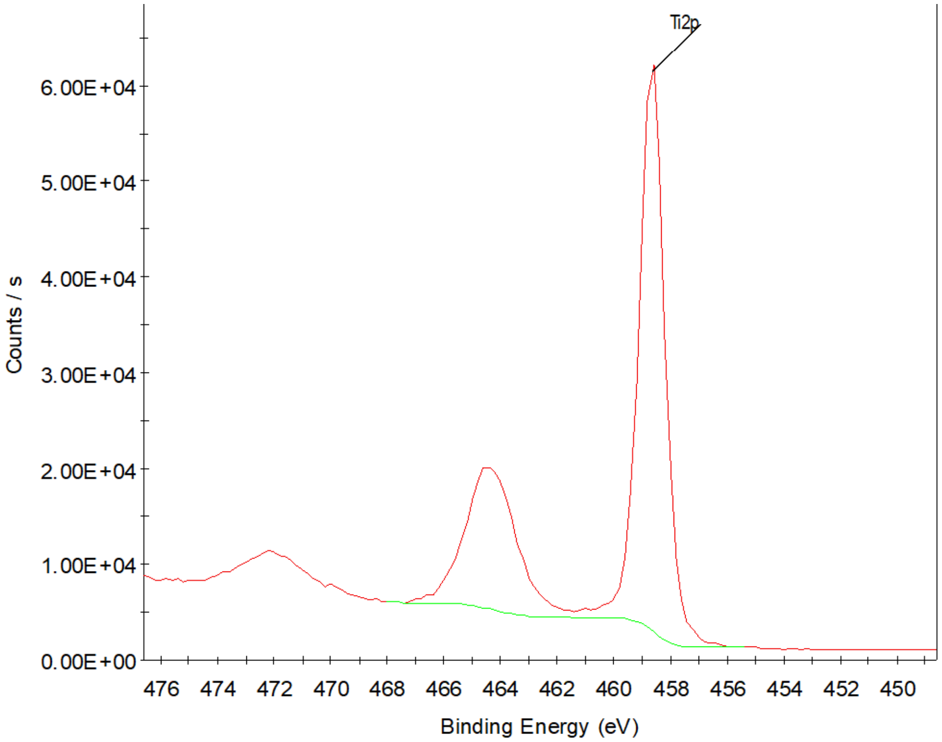

Figure 7.2.30. Ti2p scan for anatase NPs in pH 5.8 water, after 1 h of irradiation with simulated solar light.

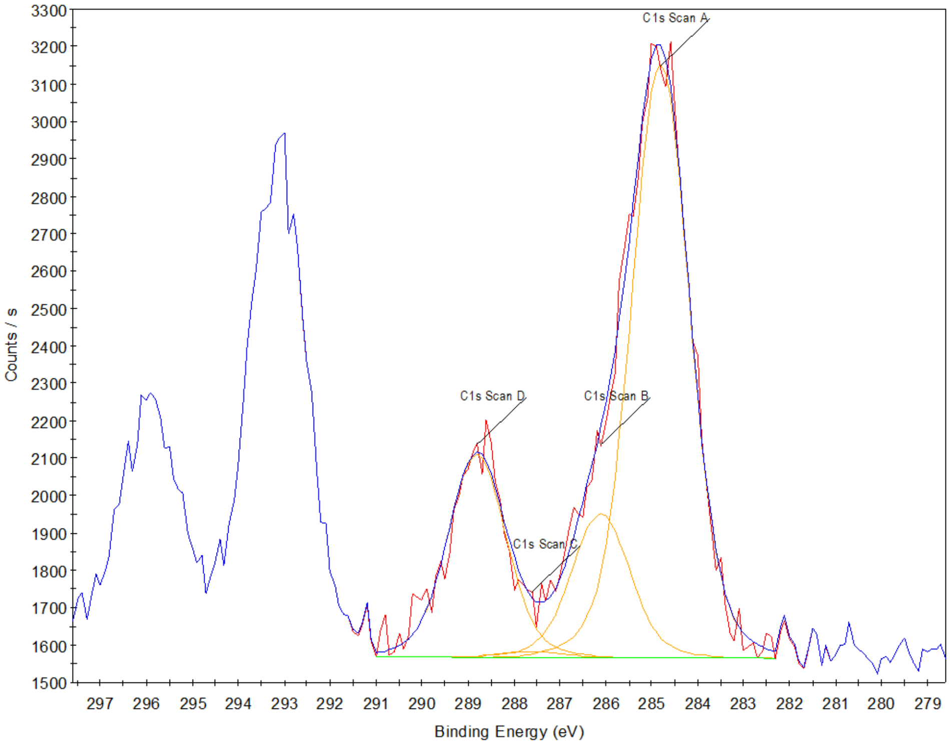

Figure 7.2.31. C1s scan for P25 NPs in pH 7.4 water, prior to irradiation. The additional unlabeled peaks from 292-297 eV are assigned to potassium, and are not included in the analysis of C1s.

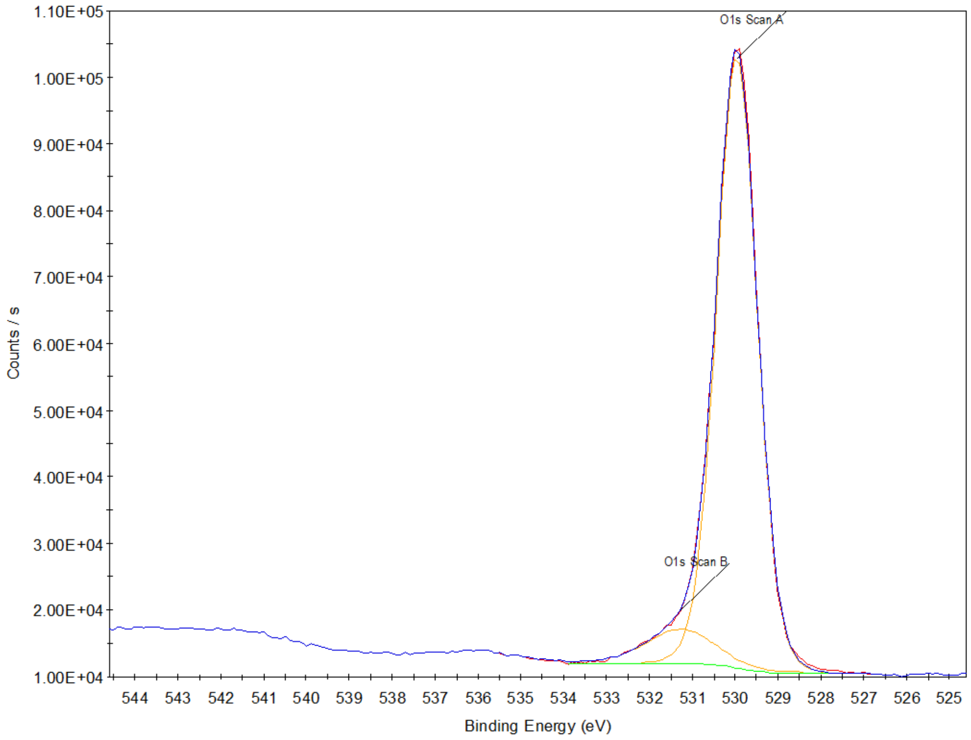

Figure 7.2.32. O1s scan for P25 NPs in pH 7.4 water, prior to irradiation.

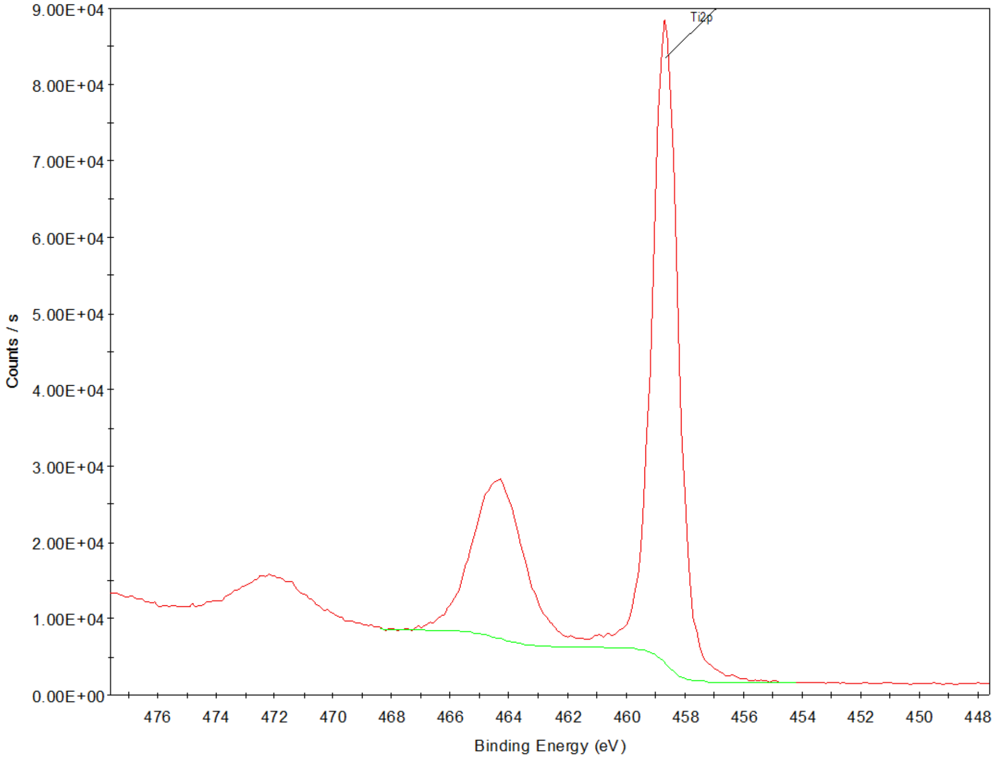

Figure 7.2.33. Ti2p scan for P25 NPs in pH 7.4 water, prior to irradiation.

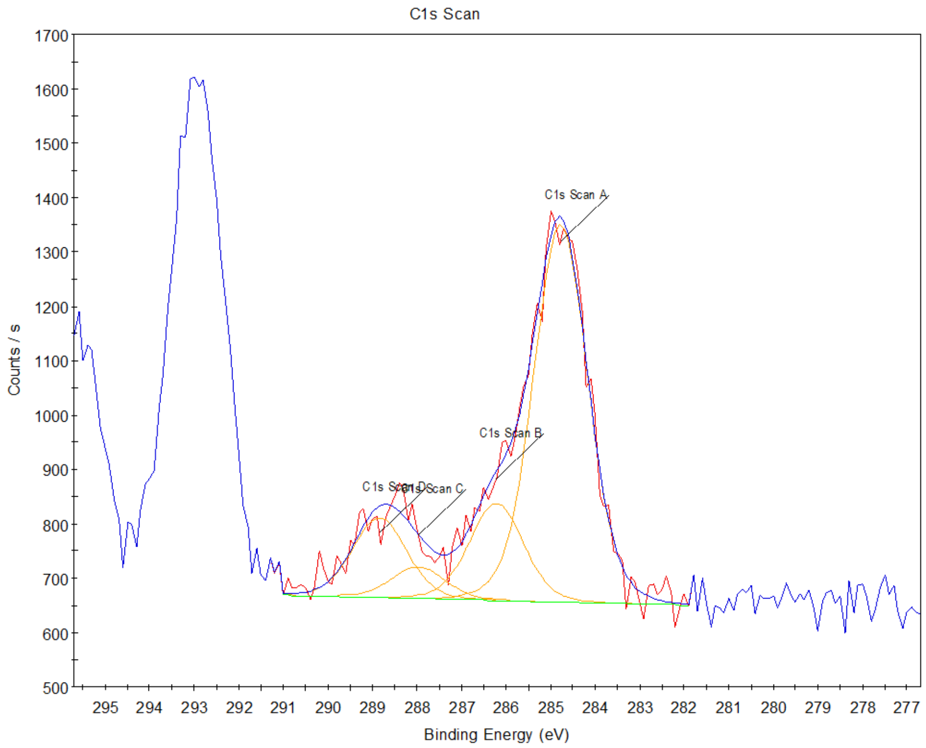

Figure 7.2.34. C1s scan for P25 NPs in pH 7.4 water, after 1 h of irradiation with simulated solar light. The additional unlabeled peaks from 292-297 eV are assigned to potassium, and are not included in the analysis of C1s.

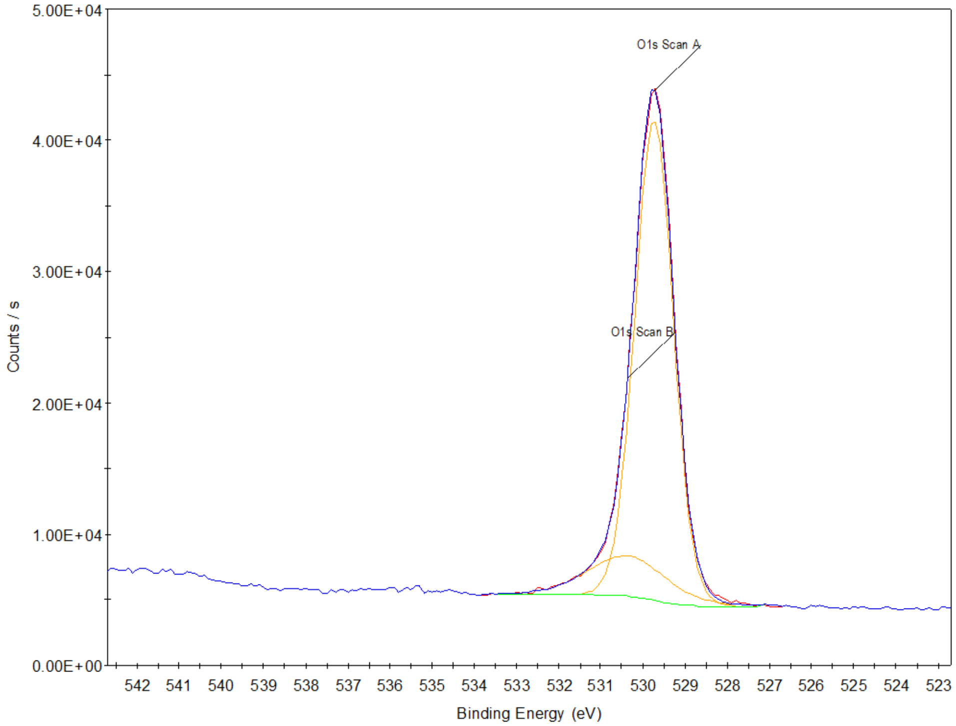

Figure 7.2.35. O1s scan for P25 NPs in pH 7.4 water, after 1 h of irradiation with simulated solar light.

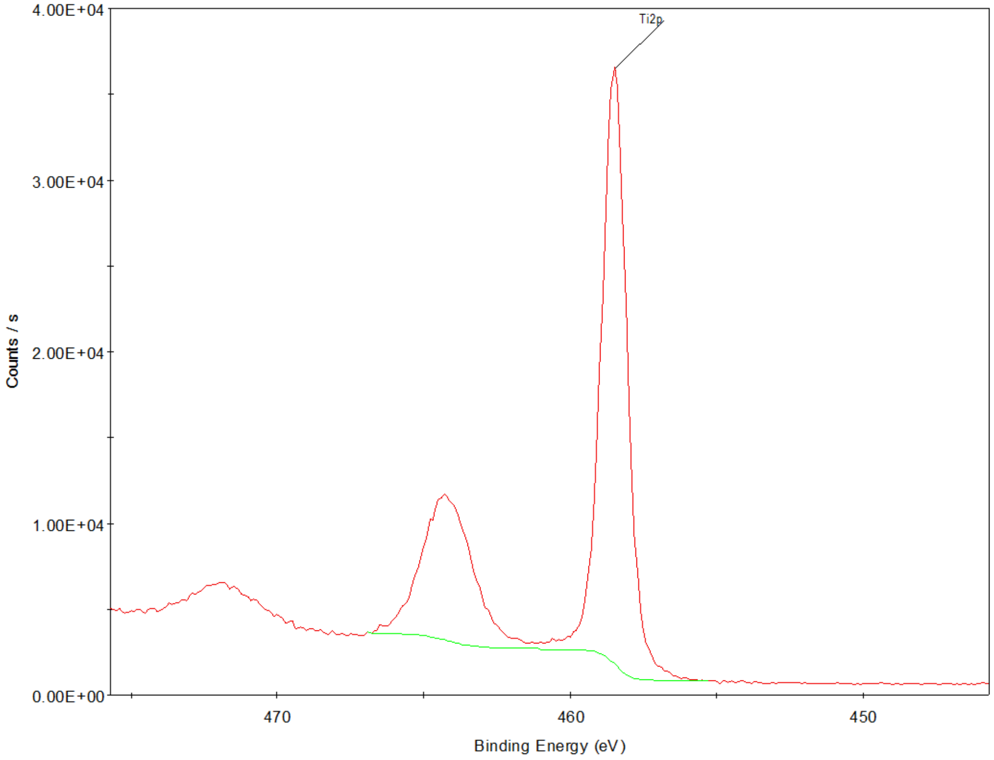

Figure 7.2.36. Ti2p scan for P25 NPs in pH 7.4 water, after 1 h of irradiation with simulated solar light.

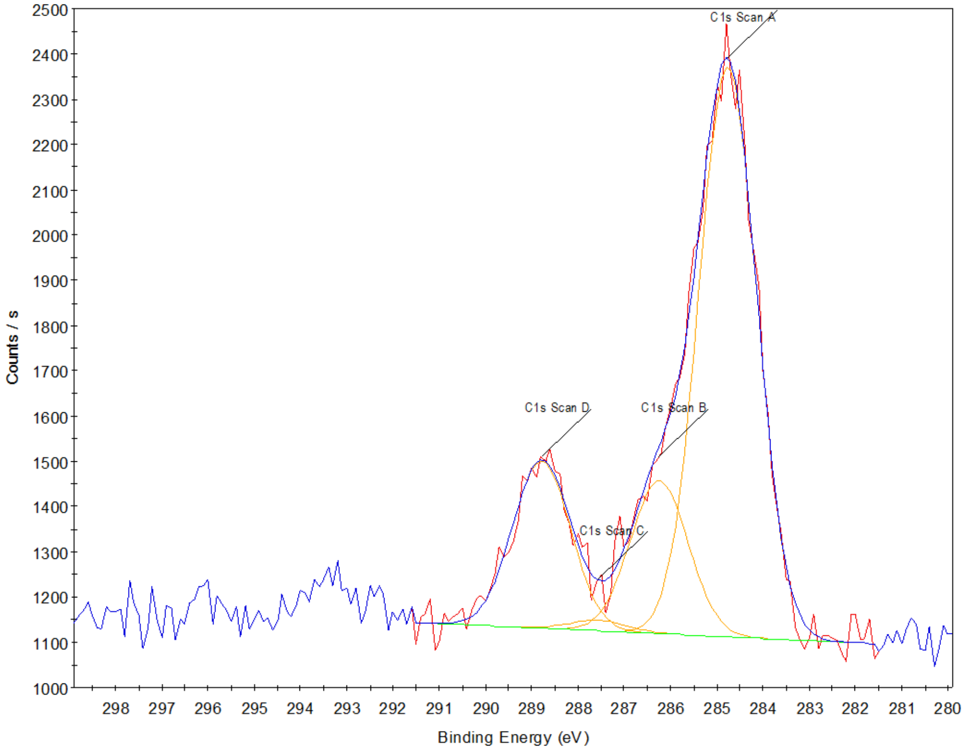

Figure 7.2.37. C1s scan for anatase NPs in pH 7.4 water, prior to irradiation.

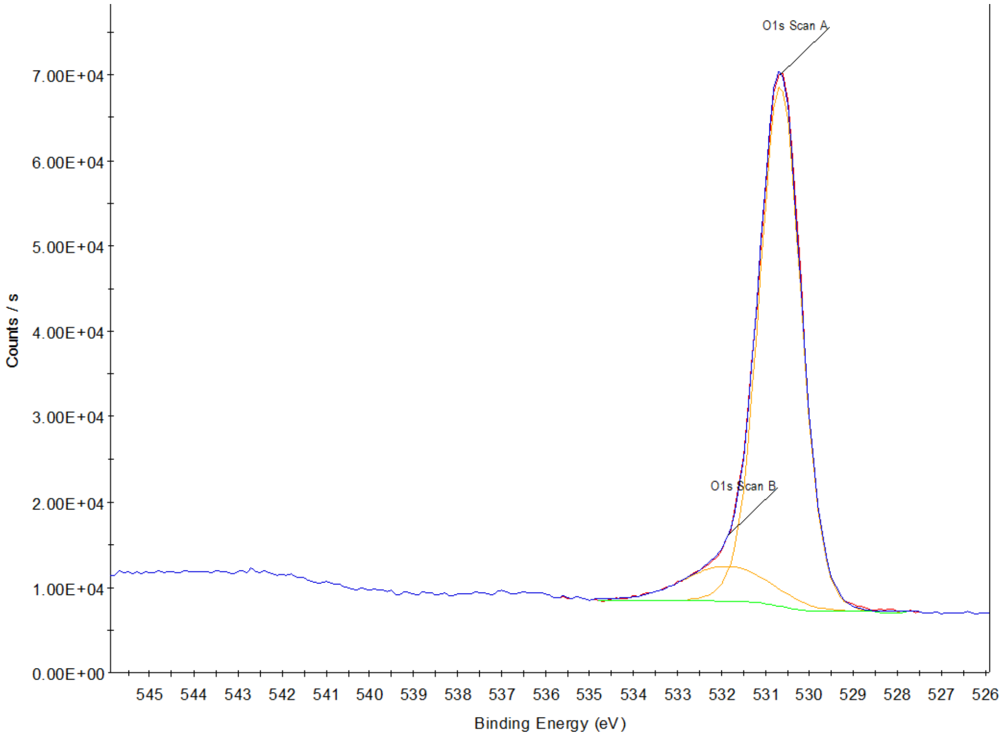

Figure 7.2.38. O1s scan for anatase NPs in pH 7.4 water, prior to irradiation.

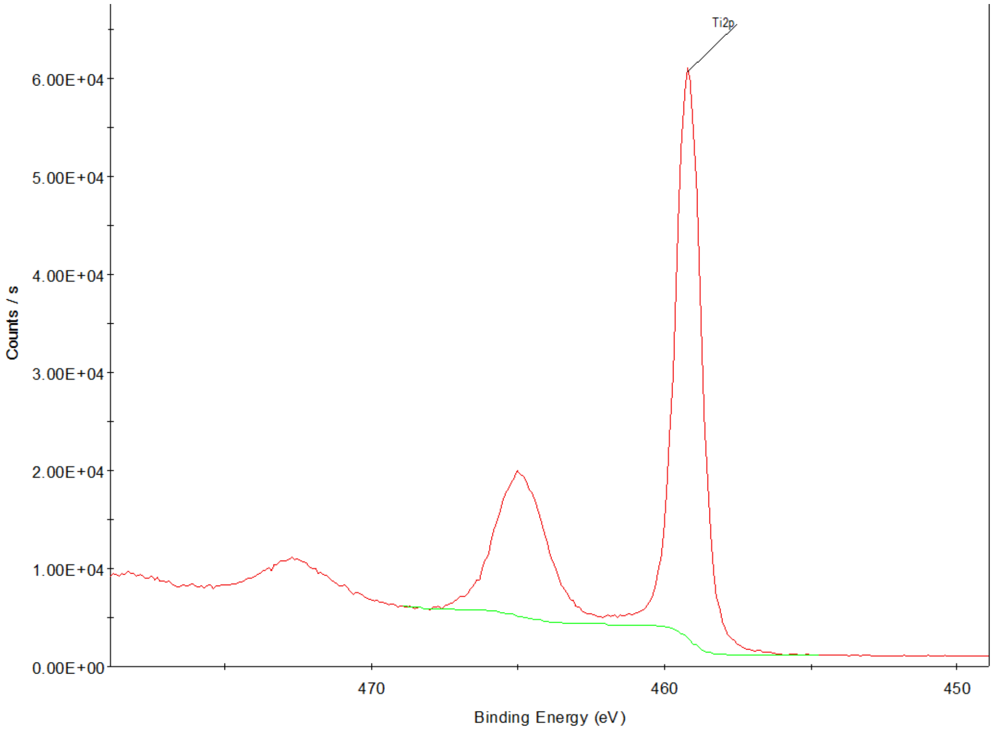

Figure 7.2.39. Ti2p scan for anatase NPs in pH 7.4 water, prior to irradiation.

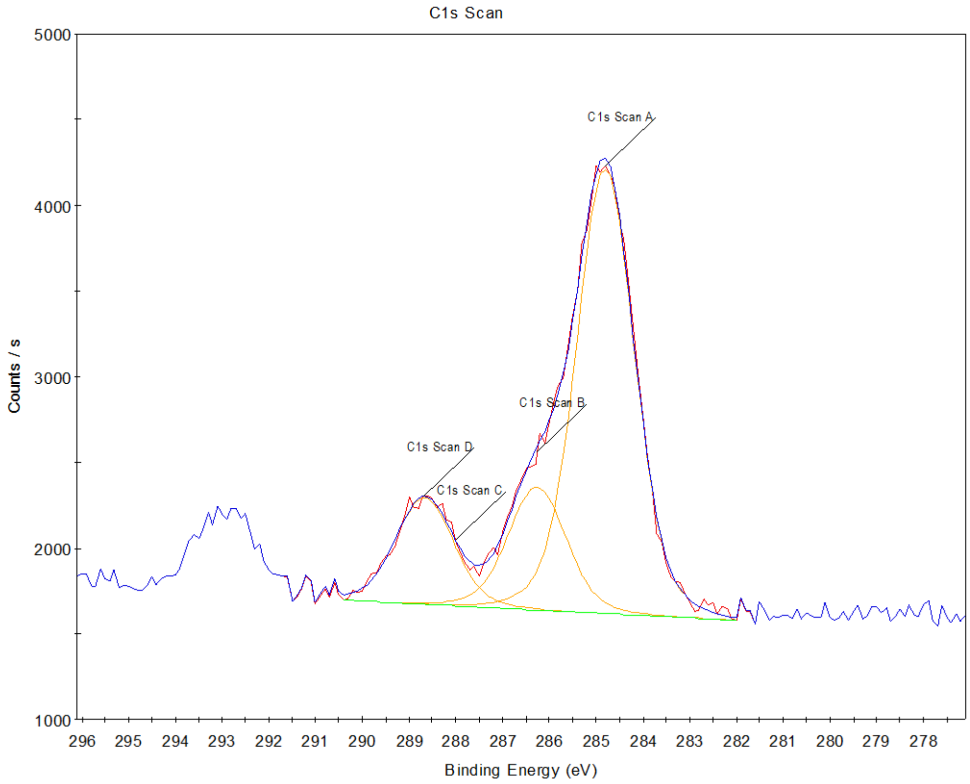

Figure 7.2.40. C1s scan for anatase NPs in pH 7.4 water, after 1 h of irradiation with simulated solar light.

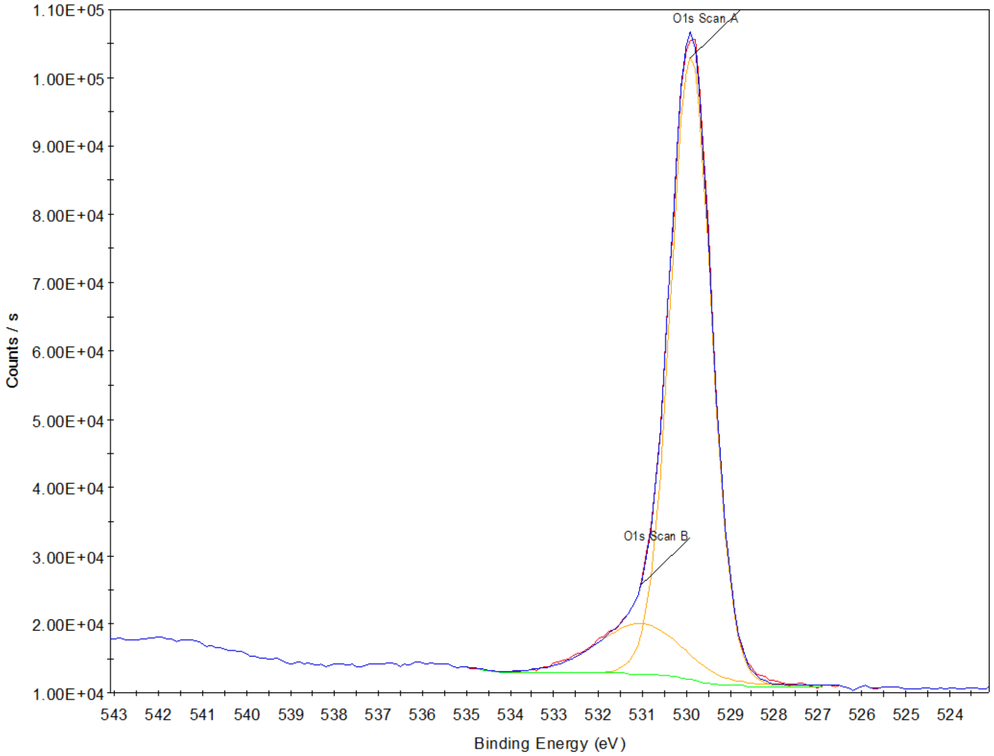

Figure 7.2.41. O1s scan for anatase NPs in pH 7.4 water, after 1 h of irradiation with simulated solar light.

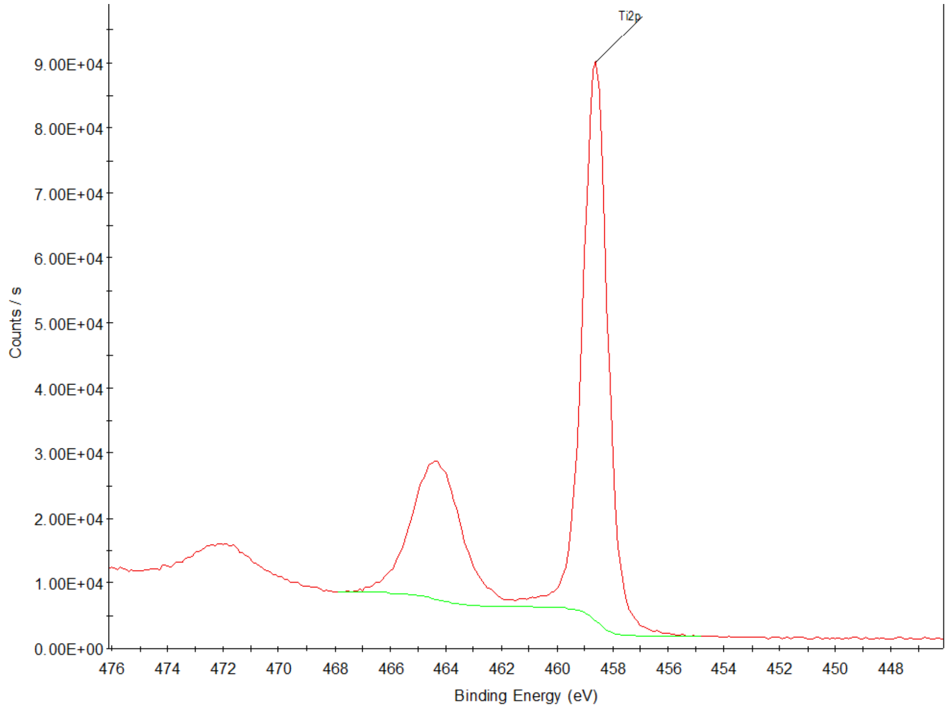

Figure 7.2.42. Ti2p scan for anatase NPs in pH 7.4 water, after 1 h of irradiation with simulated solar light.

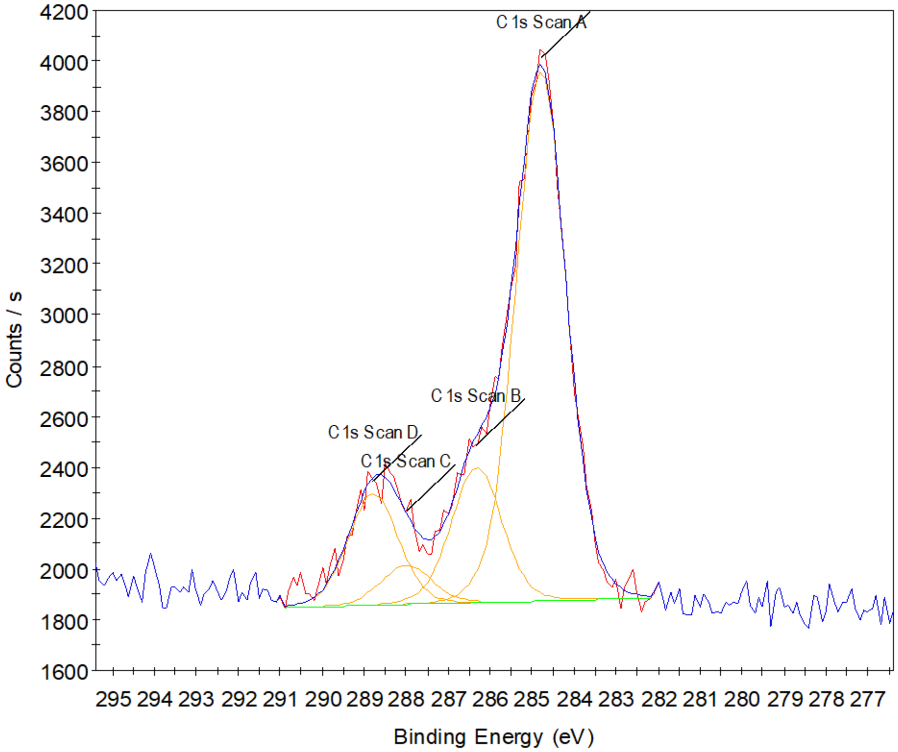

Figure 7.2.43. C1s scan for P25 NPs in PBS media water, prior to irradiation. Samples were centrifuged washed in DDI water twice prior to XPS sample preparation.

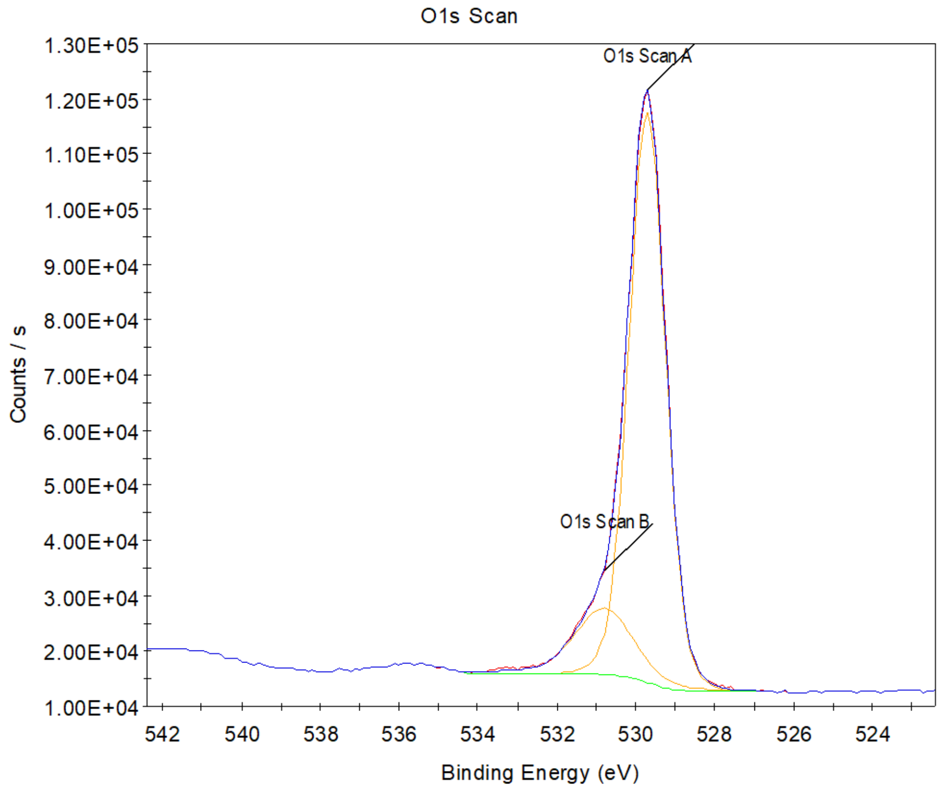

Figure 7.2.44. O1s scan for P25 NPs in PBS media water, prior to irradiation. Samples were centrifuged washed in DDI water twice prior to XPS sample preparation.

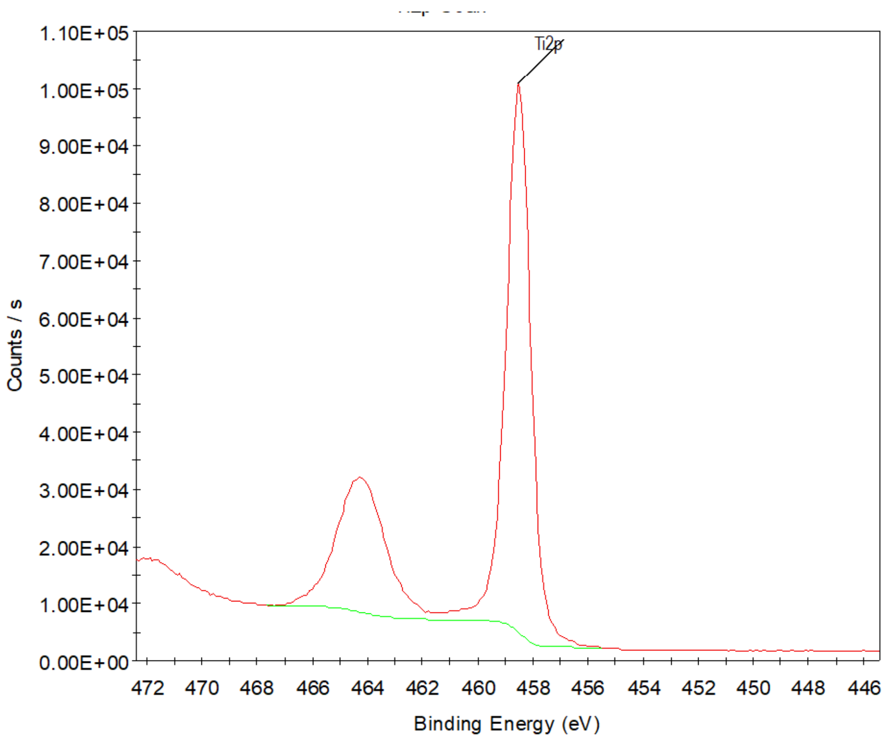

Figure 7.2.45. Ti2p scan for P25 NPs in PBS media water, prior to irradiation. Samples were centrifuged washed in DDI water twice prior to XPS sample preparation.

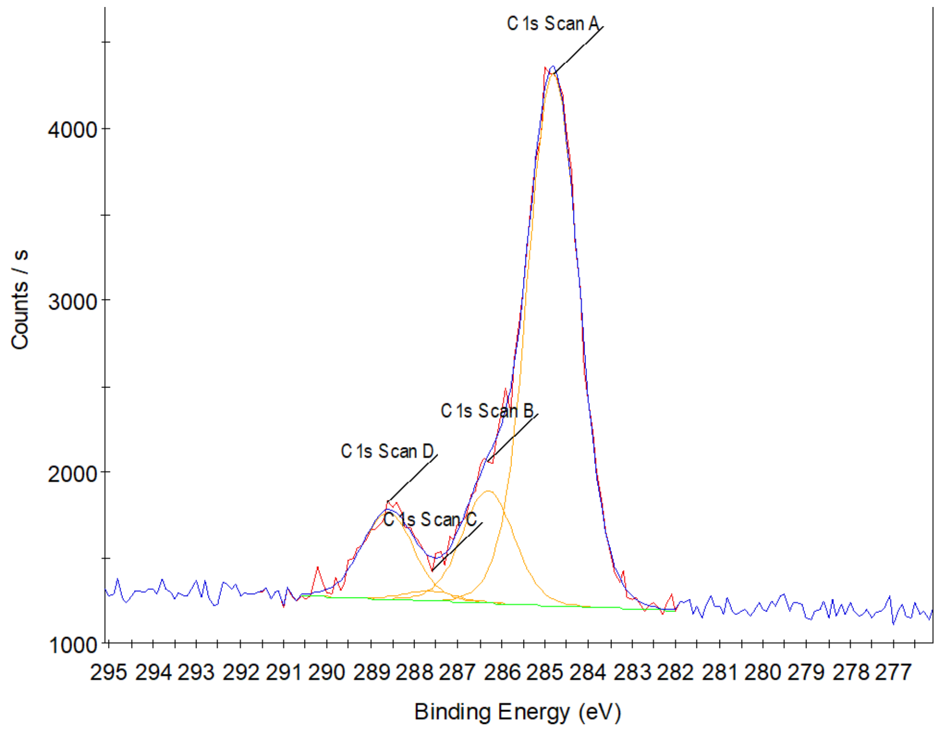

Figure 7.2.46. C1s scan for P25 NPs in PBS media water, after 1 h of irradiation with simulated solar light. Samples were centrifuged washed in DDI water twice prior to XPS sample preparation

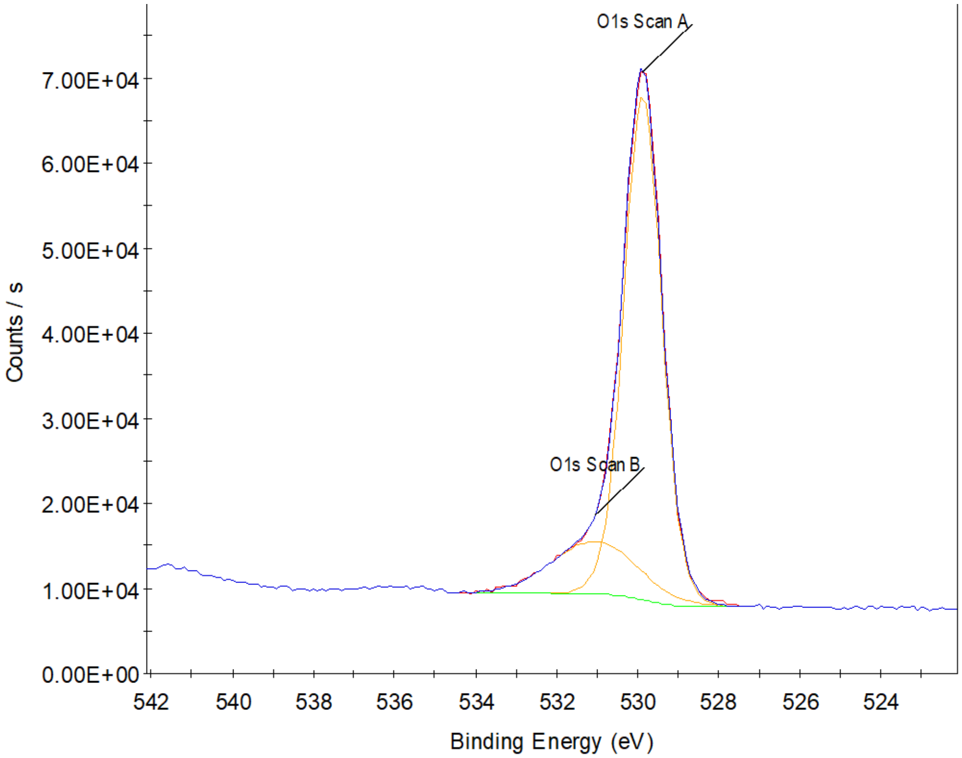

Figure 7.2.47. O1s scan for P25 NPs in PBS media water, after 1 h of irradiation with simulated solar light. Samples were centrifuged washed in DDI water twice prior to XPS sample preparation.

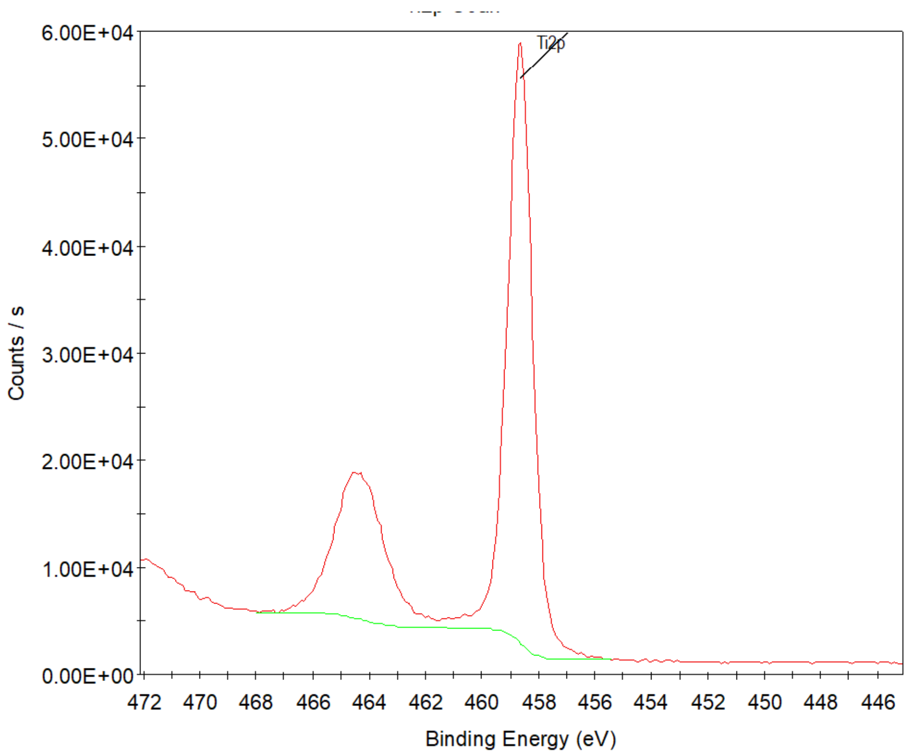

Figure 7.2.48. Ti2p scan for P25 NPs in PBS media water, after 1 h of irradiation with simulated solar light. Samples were centrifuged washed in DDI water twice prior to XPS sample preparation.

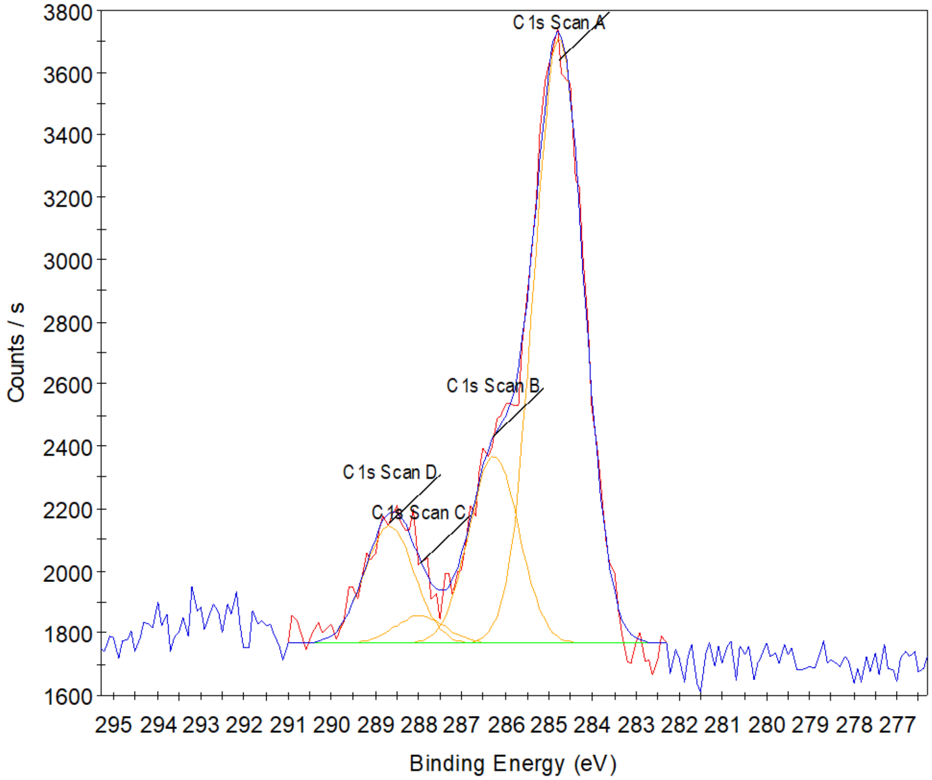

Figure 7.2.49. C1s scan for anatase NPs in PBS media water, prior to irradiation. Samples were centrifuged washed in DDI water twice prior to XPS sample preparation.

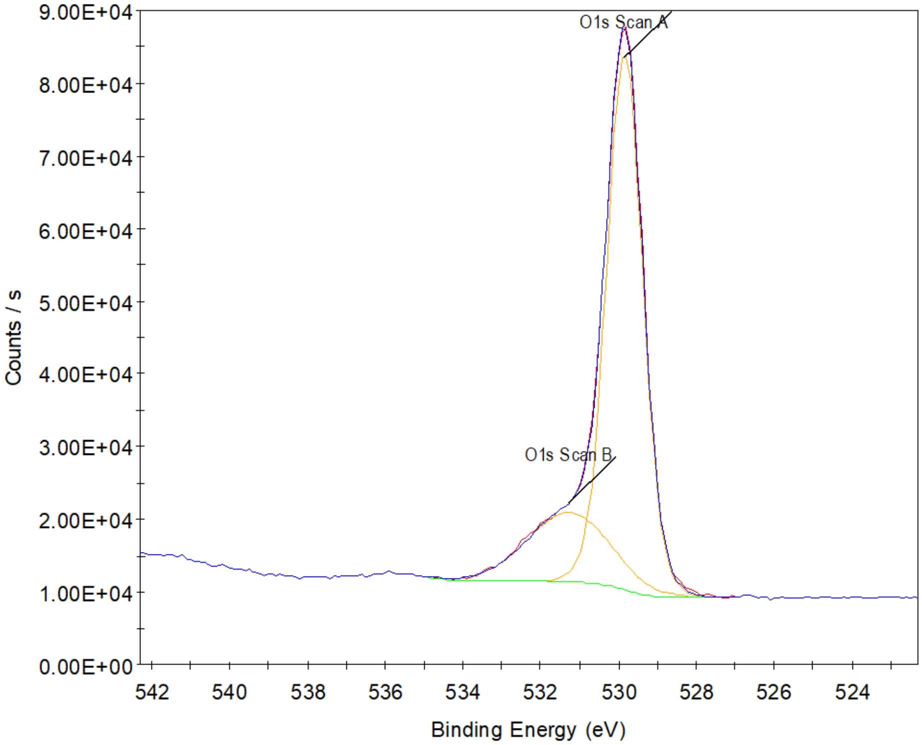

Figure 7.2.50. O1s scan for anatase NPs in PBS media water, prior to irradiation. Samples were centrifuged washed in DDI water twice prior to XPS sample preparation.

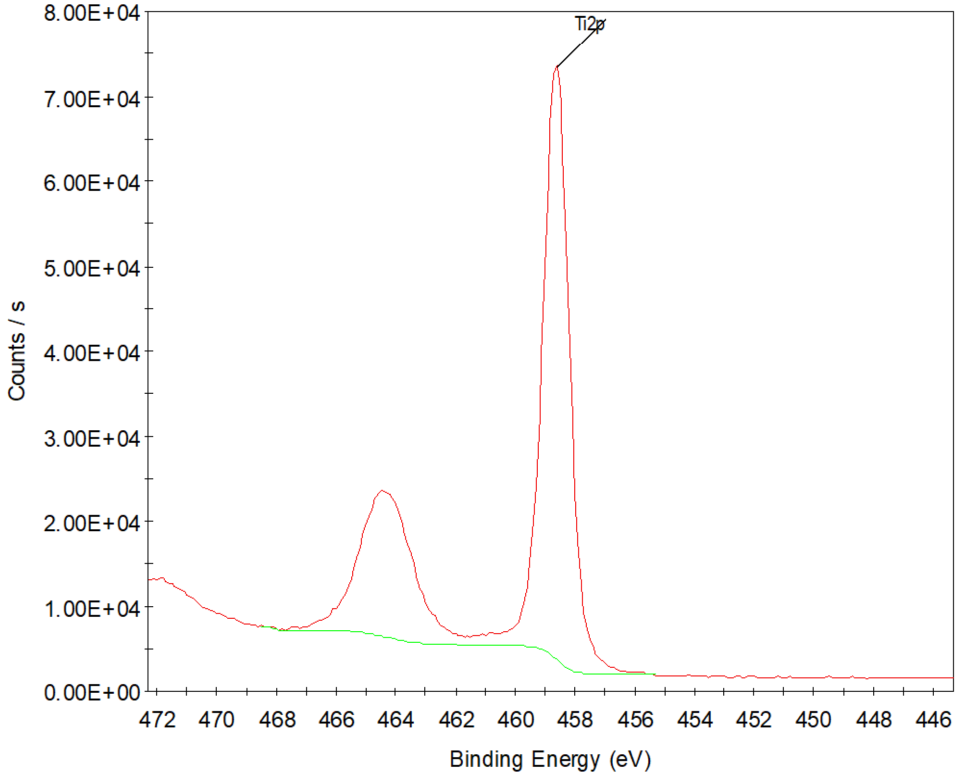

Figure 7.2.51. Ti2p scan for anatase NPs in PBS media water, prior to irradiation. Samples were centrifuged washed in DDI water twice prior to XPS sample preparation.

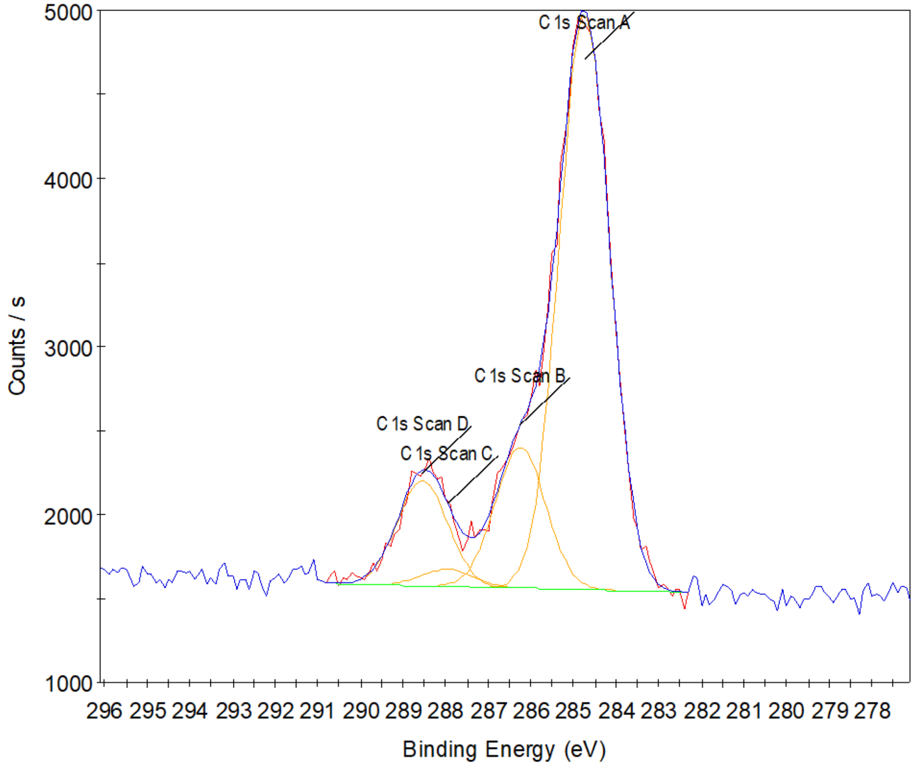

Figure 7.2.52. C1s scan for anatase NPs in PBS media water, after 1 h of irradiation with simulated solar light. Samples were centrifuged washed in DDI water twice prior to XPS sample preparation.

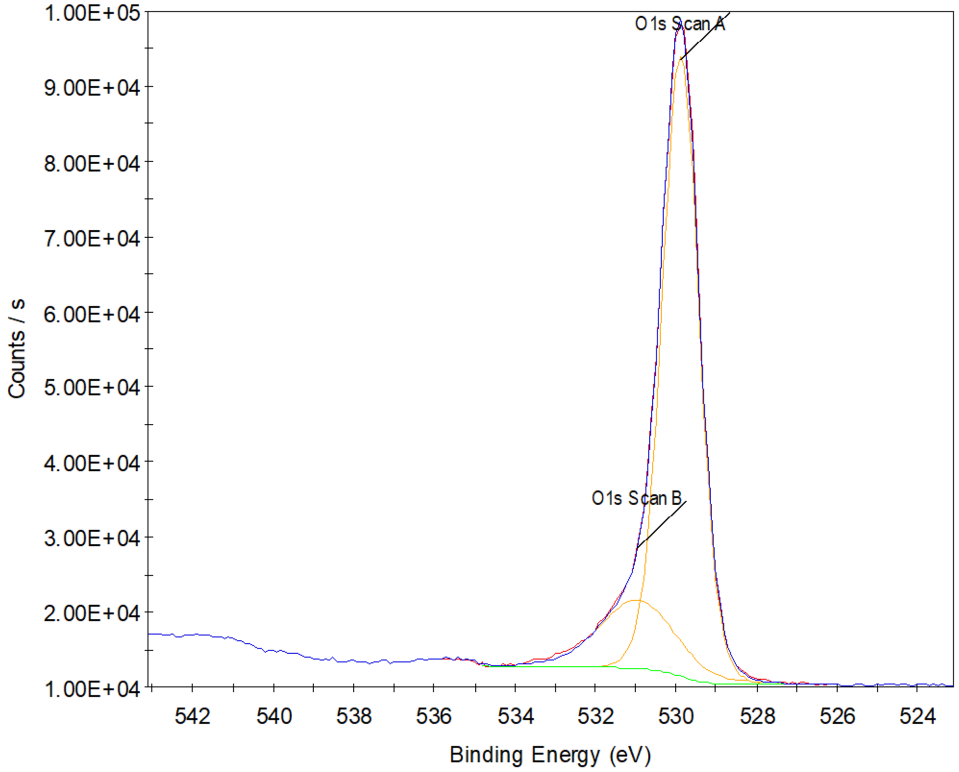

Figure 7.2.53. O1s scan for anatase NPs in PBS media water, after 1 h of irradiation with simulated solar light. Samples were centrifuged washed in DDI water twice prior to XPS sample preparation.

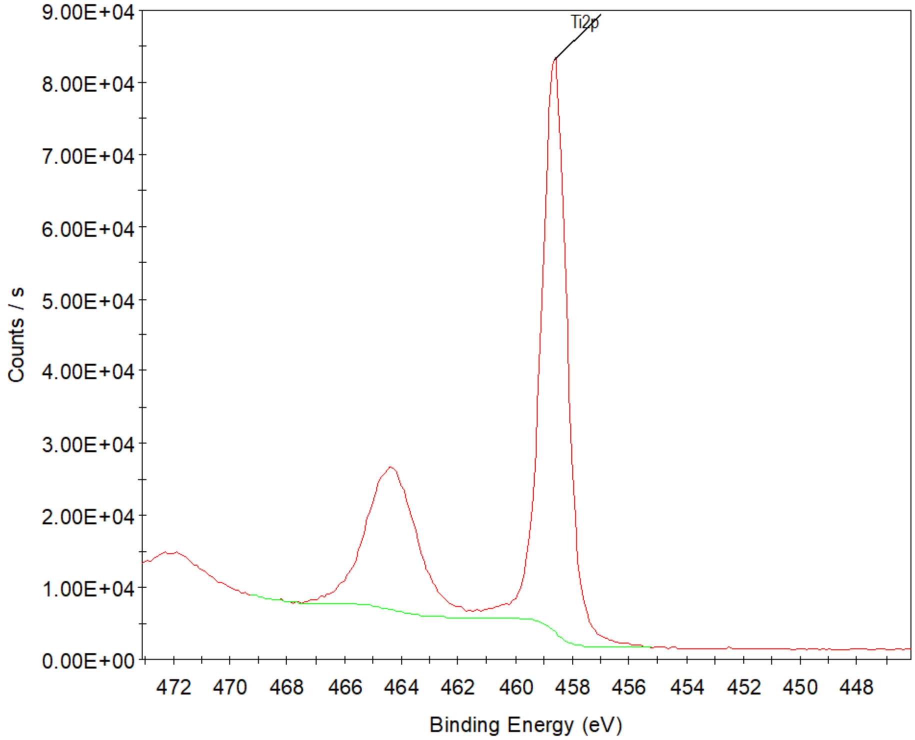

Figure 7.2.54. Ti2p scan for anatase NPs in PBS media water, after 1 h of irradiation with simulated solar light. Samples were centrifuged washed in DDI water twice prior to XPS sample preparation.

MB Dye Standard Curve

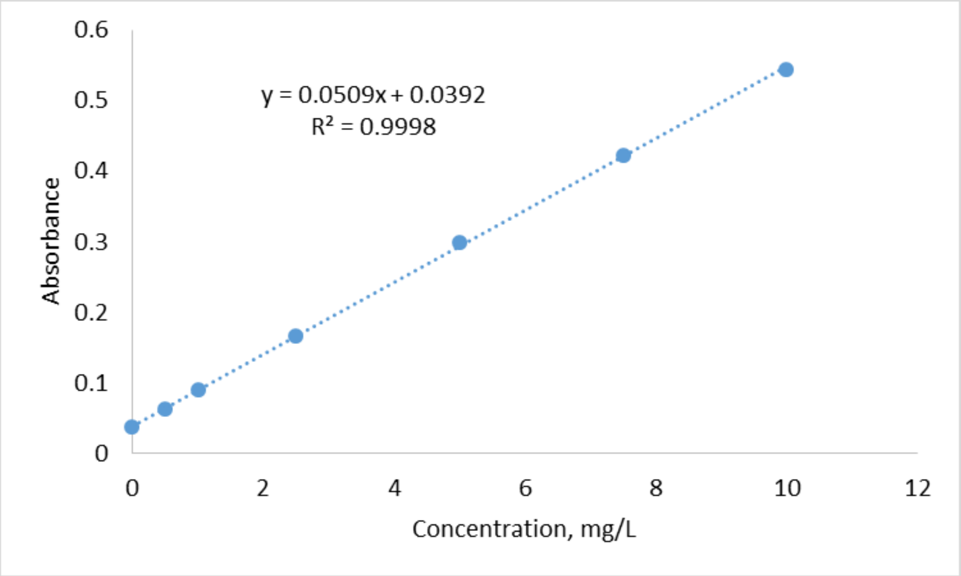

Figure 7.2.55. MB dye standard curve.

pH, Temperature, and Dissolved Oxygen of Samples in MB Dye Degradation Experiments

Table 7.2.13. Summary of pH, temperature, and dissolved oxygen values from MB dye degradation experiments. Values are presented as average ± standard deviation.

		Ambient			After 1 h Irradiation		
		pH	T, °C	D.O., mg/L	pH	T, C	D.O., mg/L
pH 5.8	P25	5.79 ± 0.03	21.3 ± 0.4	8.73 ± 0.15	5.34 ± 0.04	36.8 ± 0.7	6.94 ± 0.20
	Anatase	5.80 ± 0.03	21.2 ± 0.5	8.65 ± 0.11	5.55 ± 0.05	37.2 ± 1.8	6.99 ± 0.25
pH 7.4	P25	7.40 ± 0.04	21.1 ± 0.3	8.42 ± 0.12	6.35 ± 0.05	37.9 ± 1.1	7.01 ± 0.23
	Anatase	7.39 ± 0.02	21.2 ± 0.3	8.40 ± 0.06	6.58 ± 0.10	36.8 ± 1.9	7.32 ± 0.27
PBS	P25	7.41 ± 0.01	21.5 ± 0.5	8.19 ± 0.07	7.39 ± 0.03	39.1 ± 0.8	6.48 ± 0.11
	Anatase	7.42 ± 0.02	21.3 ± 0.6	8.06 ± 0.04	7.41 ± 0.02	38.2 ± 0.7	6.67 ± 0.09

Thermal Degradation of MB Dye

Table 7.2.14. Percent degradation of MB dye as a result of thermal exposure. Experiments were performed using 500 mg/L concentrations of TiO_2, with the glass jars entirely covered by aluminum foil to block out irradiation.

		Average	Std. Dev
pH 5.8	P25	0.87	0.77
	Anatase	1.55	0.69
pH 7.4	P25	1.82	0.42
	Anatase	2.41	0.86
PBS	P25	1.34	0.79
	Anatase	2.03	0.6